HIGH TEMPERATURE SOLID OXIDE CELLS

EDITED BY: Junwei Wu, Dong Ding, Jae-ha Myung and Tenglong Zhu
PUBLISHED IN: Frontiers in Chemistry and Frontiers in Energy Research

frontiers Research Topics

frontiers

ISSN 1664-8714
ISBN 978-2-88966-963-9
DOI 10.3389/978-2-88966-963-9

About Frontiers

Frontiers is more than just an open-access publisher of scholarly articles: it is a pioneering approach to the world of academia, radically improving the way scholarly research is managed. The grand vision of Frontiers is a world where all people have an equal opportunity to seek, share and generate knowledge. Frontiers provides immediate and permanent online open access to all its publications, but this alone is not enough to realize our grand goals.

Frontiers Journal Series

The Frontiers Journal Series is a multi-tier and interdisciplinary set of open-access, online journals, promising a paradigm shift from the current review, selection and dissemination processes in academic publishing. All Frontiers journals are driven by researchers for researchers; therefore, they constitute a service to the scholarly community. At the same time, the Frontiers Journal Series operates on a revolutionary invention, the tiered publishing system, initially addressing specific communities of scholars, and gradually climbing up to broader public understanding, thus serving the interests of the lay society, too.

Dedication to Quality

Each Frontiers article is a landmark of the highest quality, thanks to genuinely collaborative interactions between authors and review editors, who include some of the world's best academicians. Research must be certified by peers before entering a stream of knowledge that may eventually reach the public - and shape society; therefore, Frontiers only applies the most rigorous and unbiased reviews.
Frontiers revolutionizes research publishing by freely delivering the most outstanding research, evaluated with no bias from both the academic and social point of view. By applying the most advanced information technologies, Frontiers is catapulting scholarly publishing into a new generation.

What are Frontiers Research Topics?

Frontiers Research Topics are very popular trademarks of the Frontiers Journals Series: they are collections of at least ten articles, all centered on a particular subject. With their unique mix of varied contributions from Original Research to Review Articles, Frontiers Research Topics unify the most influential researchers, the latest key findings and historical advances in a hot research area! Find out more on how to host your own Frontiers Research Topic or contribute to one as an author by contacting the Frontiers Editorial Office: frontiersin.org/about/contact

HIGH TEMPERATURE SOLID OXIDE CELLS

Topic Editors:
Junwei Wu, Harbin Institute of Technology, Shenzhen, China
Dong Ding, Idaho National Laboratory (DOE), United States
Jae-ha Myung, Incheon National University, South Korea
Tenglong Zhu, Nanjing University of Science and Technology, China

Citation: Wu, J., Ding, D., Myung, J.-h., Zhu, T., eds. (2021). High Temperature Solid Oxide Cells. Lausanne: Frontiers Media SA. doi: 10.3389/978-2-88966-963-9

Table of Contents

frontiers in Chemistry

EDITORIAL
published: 21 September 2021
doi: 10.3389/fchem.2021.719826

Editorial: High Temperature Solid Oxide Cells

Junwei Wu[1]*, *Jae-ha Myung*[2]*, *Dong Ding*[3]* and *Tenglong Zhu*[4]*

[1]Harbin Institute of Technology, Shenzhen, China, [2]Department of Materials Science and Engineering, Incheon National University, Incheon, South Korea, [3]Idaho National Laboratory (DOE), Idaho Falls, ID, United States, [4]Nanjing University of Science and Technology, Nanjing, China

Keywords: solid oxide cells, solid oxide fuel cells, Perovskite, modeling, cathode

Editorial on the Research Topic

High Temperature Solid Oxide Cells

In recent decades, the extensive use of fossil fuels has led to global warming, increasing pressure on environmental protection. Solid oxide cells (SOCs) are promising electrochemical energy conversion and storage devices used at high temperatures (600–1,000°C). SOCs can be operated in fuel cell mode (solid oxide fuel cells or SOFCs mode), where they produce electricity from hydrogen or other energy resources such as hydrocarbons, CO, etc., or they can be operated in electrolysis mode (solid oxide electrolysis cells or SOECs mode), where they produce hydrogen or syngas, etc., from H_2O and CO_2 when the electricity is supplied. When operated in both SOFC and SOEC modes reversibly, these can be termed as reversible solid oxide cells or RSOCs.

Fundamentally, two types of SOCs have been developed, the tubular and the planer design. The tubular-type SOFC has long-term stability, whereas the planar-type SOFC has high power density compared to the tubular-type SOFC, which shows favorable properties such as high volumetric power densities and low electrical resistance. Xi et al. estimated various physical parameters inside the planar-type SOFC. The model was constructed in detail to include gas flow, heat transfer, mass transfer, and an electrochemical reaction. Therefore, planar-type SOFCs' performance is affected by structural parameters (Xi et al.).

In addition, the operating temperature of SOFCs plays a critical role in aspects of catalytic activity, stability, electrical efficiency, fuel flexibility, and durability of the materials. It operates at high temperatures (500–900°C), which has the advantage that it can operate with a wide range of fuels, including hydrogen, methane, syngas, ethanol, biogas, and so on. It is possible to maximize the efficiency over 80% through the combination of heat and power generation (CHP). Xi et al. developed a biomass gasification (BG)-SOFC-CHP system with a power generation of 100 kW. The results showed a significant energy-saving effect. The major goals of this work were analyzing the advantages of the CHP system compared to the traditional energy system (Xi et al.).

The operating temperature of SOFCs can affect the physical and chemical process taking place in the cell. These processes are also influenced by the microstructure. Thornton et al. calculated the impedance data for characterizing the microstructure of a SOFC cathode. They found the effective tortuosity of the microstructure of a SOFC cathode by using electrochemical impedance spectroscopy (EIS) data (Thornton et al.). In the aspect of the catalytic activity of the electrode, the high temperature operation favors the use of a non-precious metal catalyst. Xia et al. conducted theoretical calculations and experiments of the hydrogen oxidation process on Ni-CeO_2 material. The presence of nickel enhanced H_2 adsorption and lowered the energy barrier that

OPEN ACCESS

Edited by:
Wenping Sun,
Zhejiang University, China

Reviewed by:
Sivaprakash Sengodan,
Imperial College London,
United Kingdom

***Correspondence:**
Junwei Wu
junwei.wu@hit.edu.cn
Jae-ha Myung
mjaeha@inu.ac.kr
Dong Ding
dong.ding@inl.gov
Tenglong Zhu
zhutenglong@njust.edu.cn

Specialty section:
This article was submitted to Electrochemistry, a section of the journal Frontiers in Chemistry

Received: *03 June 2021*
Accepted: *23 June 2021*
Published: *21 September 2021*

Citation:
Wu J, Myung J, Ding D and Zhu T (2021) Editorial: High Temperature Solid Oxide Cells. Front. Chem. 9:719826. doi: 10.3389/fchem.2021.719826

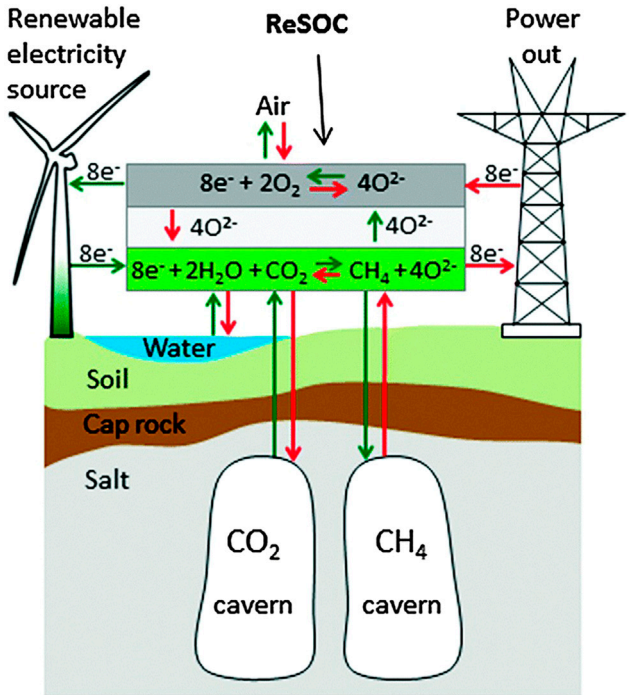

FIGURE 1 | Schematic diagram of the proposed large-scale electricity conversion and storage system.

allowed the separated hydrogen to combine with the surface oxygen of CeO_2 and form H_2O. The ECR experiments showed that the H_2 oxidation rate at the surface was increased with the longer deposition time of Ni, corresponding with the theoretical results (Xia et al.). This provides critical insight into the interface reaction between the catalyst and MIEC substrate. However, the advantages of high temperature SOFC are limited due to cost-ineffectiveness and thermal degradation of materials. To solve this problem, Kim et al. studied electrochemical properties of layered perovskite, changing the chemical compositions. They showed the relationship between the electrochemical properties and chemical composition in an $SmBa_{1-x}Ca_xCo_2O_{5+\delta}$ (SBCCO, x = 0.01, 0.03, 0.1, and 0.2) oxide system. The electrical conductivity of SBCCO was about 460 S/m at 500°C which is an excellent value for lower operating temperature (Kim et al.). Kim et al. also studied layered perovskite with A-site deficiency, and they verified that the electrical conductivity was affected by the stoichiometric compositions. They used $Sm_{1-x}BaCo_2O_{5+\delta}$ (x = 0, 0.01, 0.02, 0.03, 0.04, 0.05, 0.10, and 0.15) oxide systems as the cathode materials of SOFC. $Sm_{0.90}BaCo_2O_{5+\delta}$ (SBCO_0.90) displayed the lowest area-specific resistance (ASR) values, and metal-insulator transition (MIT) electrical conductivity occurred in all samples (Kim et al.). Finally, the authors also considered a crystal structure able to increase electrical conductivity.

Recently, to improve the catalytic activity at an intermediate operating temperature, the *in-situ* exsolution technique has been proposed. The exsolution method was used to grow a nano catalyst from the perovskite system, and the exsolved nanoparticles were socketed onto the perovskite surface. Sun et al. prepared an Ni-Co alloy decorated with lanthanum chromite oxide (LSC-NiCo) *via* an *in-situ* exsolution process and evaluated its electrochemical performance. They introduced A-site deficiency to maximize the exsolution of the B-site. The electrolyte-supported cell decorated with the Ni-Co nano-alloy showed a maximum power density of 320 mW/cm^2 in H_2 at 850°C (Sun et al.). The above performance was higher than a single Ni-doped electrode because Co facilitates the exsolution process in LSC-NiCo. This result indicates the versatile functionality of the materials by showing carbon deposition resistance in a syngas atmosphere.

We collected a number of articles and summarized their subjects as follows: various physical parameters, energy efficiency, impedance, hydrogen oxidation reaction of an anode, compositional change for high conductivity materials, and *in-situ* exsolution technique. This research topic shows the valuable contributions of research in the field of high-temperature SOFCs and provides a new insight for the future developments of a high-performance SOFC system.

In the future, renewable energy will need a huge capacity of energy conversion and storage technology because most of the renewable energy will be available as electricity from the most abundant, but intermittent, renewable energy sources, namely electricity from photovoltaic solar cells and wind turbines. By storing the produced gas in existing natural gas grids, the system can create a strong and efficient link between the electricity and gas markets (Jensen et al., 2015; Butera et al., 2019), as shown in **Figure 1**. In addition, the system is able to operate reversibly using gas from the grid to satisfy the electric power demand. Therefore, more and more research and development will focus on SOECs and RSOCs, including but not limited to, novel materials, design and modeling, operation modes, and so on, which are critical to realize the wide applications of SOC systems.

AUTHOR CONTRIBUTIONS

All authors listed have made a substantial, direct, and intellectual contribution to the work and approved it for publication.

ACKNOWLEDGMENTS

Prof. Myung would like to acknowledge Incheon National University (International Cooperative) Research Grant in 2018.

REFERENCES

Butera, G., Jensen, S. H., and Clausen, L. R. (2019). A Novel System for Large-Scale Storage of Electricity as Synthetic Natural Gas Using Reversible Pressurized Solid Oxide Cells. *Energy* 166, 738–754. doi:10.1016/j.energy.2018.10.079

Jensen, S. H., Graves, C., Mogensen, M., Wendel, C., Braun, R., Hughes, G., et al. (2015). Large-scale Electricity Storage Utilizing Reversible Solid Oxide Cells Combined with Underground Storage of CO2 and CH4. *Energy Environ. Sci.* 8, 2471–2479. doi:10.1039/c5ee01485a

Conflict of Interest: The authors declare that the research was conducted in the absence of any commercial or financial relationships that could be construed as a potential conflict of interest.

Publisher's Note: All claims expressed in this article are solely those of the authors and do not necessarily represent those of their affiliated organizations, or those of the publisher, the editors and the reviewers. Any product that may be evaluated in this article, or claim that may be made by its manufacturer, is not guaranteed or endorsed by the publisher.

frontiers in Chemistry

ORIGINAL RESEARCH
published: 22 January 2021
doi: 10.3389/fchem.2020.609338

Multiphysics Coupling Simulation and Parameter Study of Planar Solid Oxide Fuel Cell

Zheng Dang[1]*, *Xin Shen*[1,2], *Jinyan Ma*[1,2], *Zhaoyi Jiang*[1,2] and *Guang Xi*[1]

[1]Department of Fluid Machinery and Engineering, School of Energy and Power Engineering, Xi'an Jiaotong University, Xi'an, China, [2]Department of Civil Engineering, School of Human Settlement and Civil Engineering, Xi'an Jiaotong University, Xi'an, China

In this paper, a numerical model of gas flow, heat transfer, mass transfer and electrochemical reaction multi-physics field coupling of a planar SOFC is established and solved. According to the calculation results, the distribution of velocity, temperature and concentration inside the SOFC cell is analyzed. The influence of cathode inlet flow rate, porosity, rib width and other parameters on the performance of SOFC is also discussed. The results show that within a certain range, increasing the cathode inlet flow rate can significantly increase the average current density of the cell. Increasing the porosity of the electrode can improve the gas diffusion of the porous electrode, thereby increasing the rate of the electrochemical reaction. Increasing the width of the ribs will result in a significant decrease in cell performance. Therefore, the rib width should be reduced as much as possible within the allowable range to optimize the working performance of the cell.

Keywords: solid oxide fuel cells, multiphysics coupling, physical fields distribution, parameter study, work performance

OPEN ACCESS

Edited by:
Tenglong Zhu,
Nanjing University of Science and Technology, China

Reviewed by:
Daifen Chen,
Jiangsu University of Science and Technology, China
Yunfei Bu,
Nanjing University of Information Science and Technology, China

***Correspondence:**
Zheng Dang
zdang@mail.xjtu.edu.cn

Specialty section:
This article was submitted to Electrochemistry, a section of the journal Frontiers in Chemistry

Received: *23 September 2020*
Accepted: *14 December 2020*
Published: *22 January 2021*

Citation:
Dang Z, Shen X, Ma J, Jiang Z and Xi G (2021) Multiphysics Coupling Simulation and Parameter Study of Planar Solid Oxide Fuel Cell. Front. Chem. 8:609338. doi: 10.3389/fchem.2020.609338

INTRODUCTION

As a new energy technology, anode supported planar solid oxide fuel cell (SOFC) has attracted much attention in recent years (Kong et al., 2016; Wang et al., 2018a; Wang et al., 2018b). Compared with other types of fuel cells, SOFC has the advantages of diversified fuel selection, high power generation efficiency, and no need for precious metal catalysis (Zheng et al., 2015; Presto et al., 2018; Zhang et al., 2018; Futamura et al., 2019; Hagen et al., 2019; Sahli et al., 2019). In order to further improve the performance of SOFC, a detailed understanding of its specific working process is required (Kong et al., 2020). The operation of SOFC involves a variety of physical processes such as heat transfer, material transport, fluid flow and chemical and electrochemical reactions. These physical processes are highly coupled and interact with each other, and their internal velocity field, temperature field and electric field are extremely complex. In general, experimental methods for SOFC are costly and time-consuming because of its multiscale feature of the porous electrodes. In contrast, the numerical simulation based upon computational fluid dynamics (CFD) method is much cheaper and more efficient, which can easily change various parameters of SOFC and analyze their impact on SOFC performance. Therefore, numerical simulation method for SOFC is widely used.

Ferguson et al. (1996) established three-dimensional mathematical models of SOFC of flat and tubular structures, and studied and analyzed the effects of three different flow modes, namely, codirectional flow, reverse flow and cross flow, on electric field, temperature field and concentration field. Iwata et al. (2000) designed a quasi-two (co-flow and counter-flow) and quasi-three (cross-flow) dimensional simulation program considering mass, charge and heat balance, and obtained the

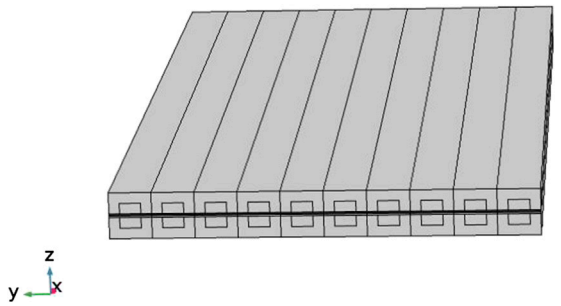

FIGURE 1 | Schematic figure of the SOFC model.

TABLE 1 | SOFC cell geometry (Iman, 2017).

Geometry parameter	Value/mm
Gas channel width	2
Gas channel height	1
Interconnector height	2
Width of interconnect	2
Gas channel length	100
Anode thickness	0.15
Electrolyte thickness	0.1
Cathode thickness	0.1

temperature and current density distribution along the flow direction and perpendicular to the electrolyte membrane. Jeon et al. (2006) established a two-dimensional reaction interval model containing a complete single channel, and optimized the width ratio of the flow channel and the interconnector through the research results. Stygar et al. (2012) established a 3-dimensional corrugated SOFC model, and studied the influence of the unit geometry on the temperature distribution and heat transfer rate in the interconnector. The influence of co-current and counter-current on temperature distribution is considered in the simulation. The results show that the temperature gradient is relatively low and the temperature distribution is relatively uniform during counter-flow, which has a significant impact on the electrical conductivity, corrosion performance and durability of the connector. Yuan et al. (Andersson et al., 2012) comprehensively considered the physical processes such as heat transfer, mass transfer, fluid flow, charge transport, internal reforming reaction of fuel and electrochemical reaction, and coupled multiple physical fields to build a numerical model of SOFC single channel at medium temperature. The effects of ion and electron transport resistance in the electrode as well as operating temperature and excessive airflow on the cell performance were studied. Zhang et al. (2015) established an anode-supported three-dimensional SOFC single channel model based on computational fluid dynamics (CFD), and compared the calculated results with the experimental results, which were well verified. The distribution of temperature, reactant velocity, current density and reactant concentration in different flow modes is explained in detail by comparing three different flow modes (co-, counter- and cross-flow). It is found that the output power of the current and counter-flow mode is much higher than that of the cross-flow mode when other operating parameters are kept constant. Dong (2019) established a complete SOFC multi-physics coupling model based on the open-source fuel cell code, and used the model to predict the performance of the cell, and discussed the transmission phenomenon and electrochemical characteristics inside the cell. Zeng et al. (2018) developed a three-dimensional model of the solid oxide fuel together with the optimized interconnection design. The results show that the current density and thermal stress are related to the shape of the interconnection tip and the depth of the cathode. Compared with rectangular and quadrilateral tip interconnects, triangular tip interconnects have the best electrochemical performance. With the increase of the tip depth, the current density will increase accordingly, and only the current density of the trapezoidal ribs decreases with the increase of the tip depth. Wang et al. (2018a), Wang et al. (2018b) established a three-dimensional model of a planar anode supported solid oxide fuel cell, and the influence of working pressure on the cell performance was studied. The results indicate that increasing the operating pressure can improve the cell performance by increasing the open circuit voltage and reducing the activation overpotential, and enhance the electrochemical reaction near the electrolyte. Lee et al. (2017) presented a three-dimensional model of a reversible solid oxide fuel cell, and the effects of different geometric structures and operating parameters (electrode support layer thickness; interconnector rib size; fuel gas composition) on current-potential characteristics and round-trip efficiency were studied. The results show that due to the uneven distribution of the reactants, the size of the ribs has a significant impact on the cell performance, especially when the support layer is thin. Li et al. (2018) proposed a three-dimensional model that couples mass transfer, electron transport, and electrochemical reactions based on a solid oxide fuel cell with porous electrodes and gas channels, the results show that the current density distribution is significantly related to the gas composition distribution. Meanwhile, the simulation results also indicate that, the ridgeline of the interconnection line will limit the mass transfer inside the cell and negatively affect the electrochemical reaction.

However, the current research rarely involves the influence of the rib width parameter of the cell on the cell performance. Only the research by Li et al. (2018) considered the rib width parameter without considering the effect of temperature field in the simulation. The present work discussed the influence of rib width with models coupled with temperature field. In this research, a three-dimensional multi-physics model of planar SOFC is established to study the physical fields distribution in the cell. And the effect of some operation parameters such as cathode inlet flow rate, inlet temperature on the cell is discussed based on the model. Meanwhile, the cell performance under different structural parameters (porosity and rib width) was studied, the rib width is an important cell structural parameter.

MODEL GEOMETRY

A three-dimensional planar SOFC cell is shown in **Figure 1**. It contains 10 fuel and air channels. The flow direction of air and fuel in this cell are counter-flow.

This model was established for result verification and parameter study and its geometry parameters are selected based on the work by Khazaee et al. (Iman, 2017), as defined in **Table 1**.

TABLE 2 | Input parameters of electrochemical model (Hajimolana et al., 2011).

Input parameters	Anode	Cathode
k_e	6.54×10^{11}	2.35×10^{11}
$E_a/10^3 \times \mathrm{J{\cdot}mol^{-1}}$	140	137
n	2	4
A_v	5×10^5	5×10^5
V_{YSZ}	0.42	0.42
V_{Ni}/V_{LSM}	0.28	0.28
ε	0.4	0.4
τ	10	10

GOVERNING EQUATIONS

Electrochemical Model

For hydrogen fuel cells, hydrogen and oxygen are fed into the anode and cathode channels of the cell respectively. When hydrogen and oxygen pass through the electrode surface, they diffuse to the electrode/electrolyte interface through the porous electrode structure, and the oxygen is at the cathode and electrolyte interface. Obtain electrons to form oxygen ions. The oxygen ions are transferred to the anode/electrolyte interface through the solid electrolyte layer, and chemically react with the hydrogen on it, and chemically react with the hydrogen on it to generate water vapor, while the oxygen ions lose electrons; The external circuit conducts from the anode to the cathode, forming a closed loop and generating current at the same time. The electrochemical reactions occurring at the anode and cathode of the cell are as follows:

Anode :

$$\mathrm{H_2 + O^{2-} \rightarrow H_2O + 2e^-} \tag{1}$$

Cathode :

$$\frac{1}{2}\mathrm{O_2 + 2e^- \rightarrow O^{2-}} \tag{2}$$

The electrical energy output by the solid oxide fuel cell is converted from the chemical energy of the fuel. It can be known from the thermodynamic formula that when the temperature and pressure remain unchanged, the maximum output electrical work of the SOFC is equal to the decrease in Gibbs free energy. Thus, the open circuit voltage (EOCV) of SOFC can be obtained, that is, the Nernst potential is as the following:

$$\begin{aligned} E_{Nernst} &= -\frac{\Delta G(T,P)}{2F} = -\frac{\Delta G(T,P_0)}{2F}\ln\left(\frac{P_{H_2}P_{O_2}^{0.5}}{P_{H_2O}}\right) \\ &= E_{Nernst}^0 + \frac{RT}{2F}\ln\left(\frac{P_{H_2}P_{O_2}^{0.5}}{P_{H_2O}}\right) \end{aligned} \tag{3}$$

where E_{Nernst} denotes Nernst potential(V), $\Delta G(T,P)$ denotes Gibbs free energy under the condition of temperature T and pressure P, P_{H_2} denotes hydrogen partial pressure at the three-phase interface (Pa), P_{O_2} denotes oxygen partial pressure at the three-phase interface, P_{H_2O} denotes the partial pressure of water vapor at the three-phase interface.

In the actual working process of SOFC, there are some resistances that make the actual cell output voltage less than the ideal voltage E_{Nernst}. This voltage loss phenomenon is called polarization. The main polarization losses are divided into three types, namely activation polarization, concentration polarization and ohmic polarization, defined as follows:

$$\eta_{act} = \frac{2RT}{nF}\sin h^{-1}\left(\frac{i}{2i_0}\right) \tag{4}$$

$$\eta_{conc,a} = \frac{RT}{2F}\ln\left(\frac{P_{H_2}^0 P_{H_2O}^{tpb}}{P_{H_2}^{tpb}P_{H_2O}^0}\right) \tag{5}$$

$$\eta_{conc,c} = \frac{RT}{4F}\ln\left(\frac{P_{O_2}^0}{P_{O_2}^{tpb}}\right) \tag{6}$$

$$\eta_{ohm} = i \cdot R \tag{7}$$

$$i = i_0\left\{\exp\left(\frac{\alpha nF}{RT}\eta_{act}\right) - \exp\left(\frac{-(1-\alpha)nF}{RT}\eta_{act}\right)\right\} \tag{8}$$

where η_{act} denotes activation polarization, $\eta_{conc,a}$ denotes concentration polarization of anode, $\eta_{conc,c}$ denotes concentration polarization of cathode, η_{ohm} denotes ohmic polarization, and i denotes the local current density ($\mathrm{A{\cdot}m^{-2}}$), i_0 denotes the reference exchange current density ($\mathrm{A{\cdot}m^{-2}}$). i_0 can be expressed by **Equation (8)**, where k_e is the pre-exponential factor, E_a is the activation energy.

$$i_0 = \frac{RT}{nF}\cdot k_e \cdot \exp\left(\frac{-E_a}{RT}\right) \tag{9}$$

The actual working potential of SOFC is defined as follows:

$$V_{op} = E_{Nernst} - \eta_{act} - \eta_{conc} - \eta_{ohm} \tag{10}$$

where V_{op} denotes the actual working potential.

During the operation of SOFC, the charge is transferred in the electrodes, electrolytes and interconnectors in the form of electronic current and ionic current. The transport equations of electron current and ion current are expressed as follows:

$$\nabla \cdot i_k = \nabla\left(-\sigma_k^{eff}\nabla\varphi_k\right) = S_{current} \tag{11}$$

$$S_{current} = A_v \cdot i \tag{12}$$

where $S_{current}$ denotes a general source term, k denotes an index that is *el* for the electrode or *io* for the electrolyte, A_v denotes surface area to volume ratio/$\mathrm{m^2{\cdot}m^{-3}}$, φ_k the potential (SI unit: V) and σ_k^{eff} denotes the effective conductivity (SI unit: S/m) which can be calculated as:

$$\sigma_{s,a}^{eff} = \frac{9.5 \times 10^7}{T} \cdot \exp\left(\frac{-1150}{T}\right) \cdot \frac{V_{Ni,a}}{\tau_{Ni,a}} \quad (13)$$

$$\sigma_{s,c}^{eff} = \frac{4.2 \times 10^7}{T} \cdot \exp\left(\frac{-1200}{T}\right) \cdot \frac{V_{LSM,c}}{\tau_{LSM,c}} \quad (14)$$

$$\sigma_{l,el}^{eff} = 3.34 \times 10^4 \cdot \exp\left(\frac{-10300}{T}\right) \cdot \frac{V_{YSZ,el}}{\tau_{YSZ,el}} \quad (15)$$

where V is the volume fraction for the specific materials in the electrodes and t is the structure-dependent tortuosity factors. **Table 2** shows the input parameters of the electrochemical model.

Mass Transport

The material transport process is mainly composed of diffusion and convection. Factors such as concentration gradients, temperature gradients, pressure gradients, etc. will drive the transfer of gas components. At present, there are mainly three models used to describe the mass transfer process, namely the Fick model, the Maxwell–Stefen model and the Dusty gas model. The mass transfer model used in this paper is the Maxwell–Stefen model, which is expressed as follows:

$$\nabla\left(-\rho \cdot \omega_i \sum D_{eff,ij} \cdot \nabla x_j + \left(x_j - \omega_j\right)\frac{\nabla p}{p} \cdot \vec{u} - D_i^T \cdot \frac{\nabla T}{T}\right) + \rho \cdot \vec{u} \cdot \nabla \omega_j = S_i \quad (16)$$

$$S_i = -\frac{i}{2F} M_i \quad (17)$$

where ω_i denotes the mass fraction of material i, D_i^T the thermal diffusion coefficient (assumed to be zero at this work), S_i the source term, M_i the molar mass of material i, and $D_{eff,ij}$ is the effective diffusion coefficients, which can be calculated as follows:

$$D_{eff,ij} = \varepsilon^{\tau} \cdot D_{ij} \quad (18)$$

where D_{ij} denotes the binary diffusion coefficient, and can be expressed by **Eq. (16)**:

$$D_{ij} = \frac{k_d \cdot T^{1.75} \cdot \left(\frac{1}{M_i} + \frac{1}{M_j}\right)^{0.5}}{p \cdot \left(v_i^{\frac{1}{3}} + v_j^{\frac{1}{3}}\right)^2} \quad (19)$$

Momentum Transport

The Navier–Stokes equation is usually used to describe the flow process in the flow channel in SOFC. The combination of the N–S equation and the continuity equation can be expressed as:

$$\left(\rho\vec{u} \cdot \nabla\right)\vec{u} = -\nabla p + \nabla \cdot \left[\mu\left(\nabla\vec{u} + \left(\nabla\vec{u}\right)^T\right) - \frac{2}{3}\mu\left(\nabla \cdot \vec{u}\right)I\right]\nabla\left(\rho\vec{u}\right) \quad (20)$$

$$\nabla \cdot \left(\rho\vec{u}\right) = 0 \quad (21)$$

where ρ denotes density (kg m^{-3}), μ the viscosity coefficient of fluid (kg m^{-1} s^{-1}).

TABLE 3 | Input parameters.

Parameters	Symbol	Value
Anode thermal conductivity/W m^{-1} K^{-1}	$k_{s,a}$	11
Cathode thermal conductivity/W m^{-1} K^{-1}	$k_{s,c}$	6
Electrolyte thermal conductivity/W m^{-1} K^{-1}	$k_{s,el}$	2.7
Interconnect thermal conductivity/W m^{-1} K^{-1}	k_{int}	20
Anode specific heat/J kg^{-1} K^{-1}	$C_{p,a}$	450
Cathode specific heat/J kg^{-1} K^{-1}	$C_{p,c}$	430
Electrolyte specific heat/J kg^{-1} K^{-1}	$C_{p,el}$	470
Interconnect specific heat/J kg^{-1} K^{-1}	$C_{p,\text{int}}$	550
Anode density/kg m^{-3}	ρ_a	3.31 × 10^3
Cathode density/kg m^{-3}	ρ_c	3.03 × 10^3
Electrolyte density/kg m^{-3}	ρ_{el}	5.16 × 10^3
Interconnect density/kg m^{-3}	ρ_{int}	3.03 × 10^3
Operating pressure/Pa	p_0	1.01 × 10^5
Operating temperature/K	$T_{operate}$	1,073
Inlet air velocity/m·s^{-1}	u_a	3
Inlet fuel velocity/m s^{-1}	u_c	0.4
Hydrogen inlet mass fraction	ω_{H_2}	0.4
Oxygen inlet mass fraction	ω_{O_2}	0.15
Inlet temperature/K	T_{in}	1,073

The momentum transfer in porous media can be described by the Darcy–Brinkman equation. The combination of Brinkman equation and continuity equation can be expressed as:

$$\frac{\mu}{\kappa}\vec{u} = -\nabla p + \nabla \cdot \frac{1}{\varepsilon}\left[\mu\left(\nabla\vec{u} + \left(\nabla\vec{u}\right)^T\right) - \frac{2}{3}\mu\left(\nabla \cdot \vec{u}\right)I\right] \quad (22)$$

$$\nabla \cdot \left(\rho\vec{u}\right) = S_i \quad (23)$$

where κ is the permeability of the porous medium (m^2), S_i the source term.

Heat Transport

To accurately simulate the actual working process of the SOFC, thereby optimizing cell performance and improving thermal stability, the internal energy transfer process of the SOFC must be considered.

For the solid area (electrolyte and connecting body), only heat conduction needs to be considered, the thermal energy equation can be expressed as:

$$\nabla \cdot (-k\nabla T) = S \quad (24)$$

For the flow channel, heat conduction and convection heat transfer need to be considered at the same time, the thermal energy equation can be expressed as:

$$\nabla \cdot \left(-k\nabla T + C_f C_p T\vec{u}\right) = S \quad (25)$$

For the porous electrode area, the local thermal equilibrium assumption is generally adopted, that is, the temperature of the porous medium material in the local area is equal to the temperature of the fluid, so the energy governing equation is:

$$\rho_g \cdot \varepsilon \cdot C_{p,g} \cdot \vec{u} \cdot \nabla T = \nabla \cdot \left(k_{eff}\nabla T\right) + S \quad (26)$$

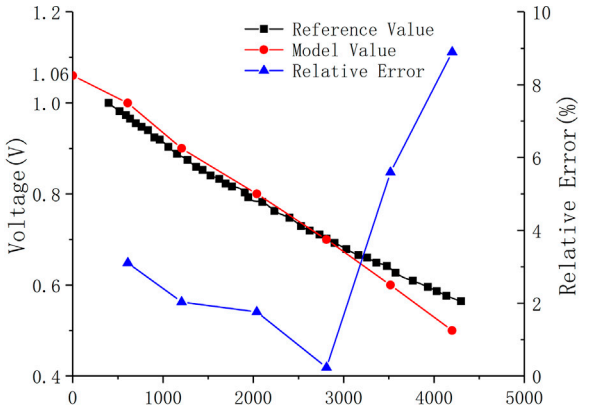

FIGURE 2 | Comparison of the model-predicted V–I curve with experimental data at the same operating condition.

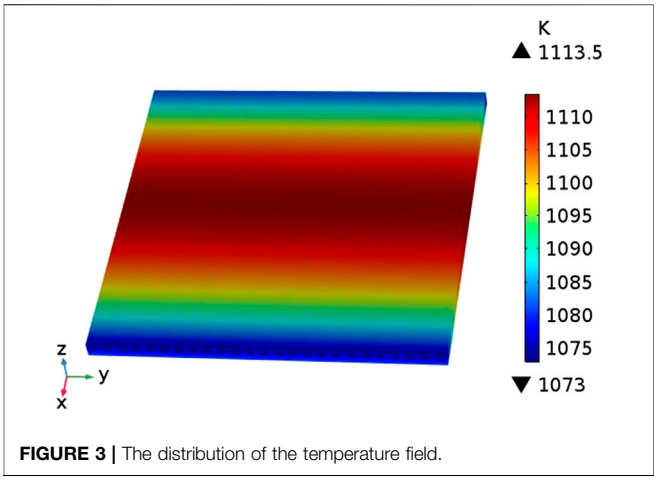

FIGURE 3 | The distribution of the temperature field.

where C_f is the molar concentration of fluid, $C_{p,g}$ the specific heat of gas mixture, ρ_g the density of gas mixture, S the source term, and k_{eff} effective thermal conductivity.

The source term S for the thermal energy equation due to the electrochemical reactions can be expressed as:

$$S = |i| \cdot \left(\frac{T \cdot |\Delta S|}{nF} + |\eta_{act}| + \eta_{conc} \right) + \sum \frac{i^2}{\sigma} \tag{27}$$

Input Parameters and Boundary Conditions

The operating conditions and input parameters for the developed model are listed in **Table 3**. The potential at the anode current collector is set to zero and at of the cathode current collector is as the cell operating voltage. All other external boundaries and interfaces are insulated.

RESULT AND DISCUSSION

In order to prove the correctness of the model built in this paper, the simulated calculation results are compared with the experimental data provided by Yakabe et al. (2001). in the literature. The comparison results of the volt-ampere characteristic curves are shown in **Figure 2**. The results show that the calculation results of the planar SOFC model established in this paper are in good agreement with the experimental data given in the literature, and the maximum error is less than 10%. Therefore, the model can be used to study the performance of SOFC.

Physical Fields Distribution

Temperature Distribution

The distribution of the temperature field inside the cell in the case of counter-flow is shown in **Figure 3**. It can be seen that the cell has a low temperature (1073 K) at both ends and a high temperature (around 1110 K) in the middle. This is because the fuel gas and air in the model are in a reverse flow mode, and the inflow temperature is both 1073 K. With the continuous inflow of fuel gas and air Inside the cell, the heat generated by the electrochemical reaction continues to accumulate, and the cell temperature rises accordingly, reaching a maximum near the middle of the cell. At both ends of the cell, the high-temperature gas flowing out of the cell exchanges heat with the gas flowing into the other side of the cell, and the temperature gradually drops.

Velocity Field Distribution

It can be seen from **Figures 4A, B** that the inlet velocity of the anode fuel gas is 0.4 m s^{-1}. After entering the cell, the boundary layer is formed first, and the flow velocity rapidly increases to about 0.58 m s^{-1}. At a relatively stable level, along the fuel flow direction, the hydrogen flow velocity in the anode flow channel hardly changes; while the cathode air inlet velocity is 3 m s^{-1} at the inlet. After entering the cell, the boundary layer is also formed. The flow velocity rapidly increased to about 4.5 m s^{-1}, and then the gas flow velocity in the cathode flow channel decreased continuously along the air flow direction. There is a difference in the velocity field distribution of the cathode and anode flow channels. This is because the anode consumes 1 mol of hydrogen and generates 1 mol of water vapor, while the total molar flow rate of the mixed gas inside the anode remains unchanged, so the velocity is almost unchanged; The continuous consumption of the flow direction causes the total molar flow of the cathode gas to be continuously reduced, and therefore the flow rate of cathode fluid is continuously reduced.

Concentration Field Distribution

The oxygen concentration distribution on the cross section of the cell are shown in **Figure 5**. It can be seen from **Figure 5** that the oxygen concentration in the flow channel has been maintained at a high level (around 0.1). The oxygen concentration inside the porous electrode directly in contact with the flow channel is also relatively high, but the oxygen concentration in the cell ribs (the part of the porous electrode directly in contact with the interconnector) is very low (less than 0.01). There are three main reasons for this phenomenon: First, It is because the oxygen concentration in the flow channel is low

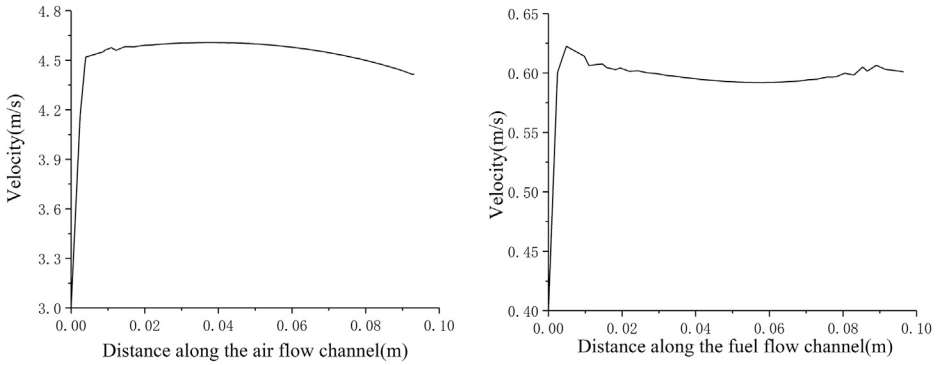

FIGURE 4 | Velocity distribution in flow channel.

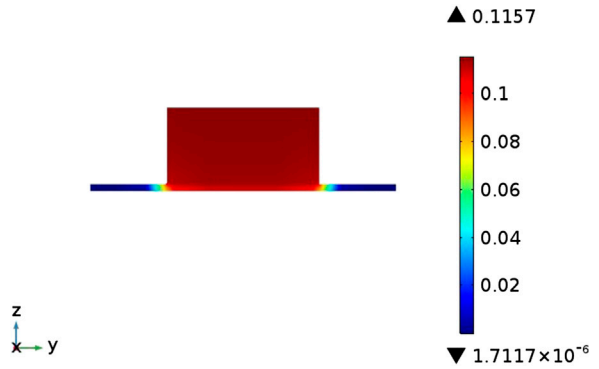

FIGURE 5 | Oxygen concentration distribution in anode flow channel.

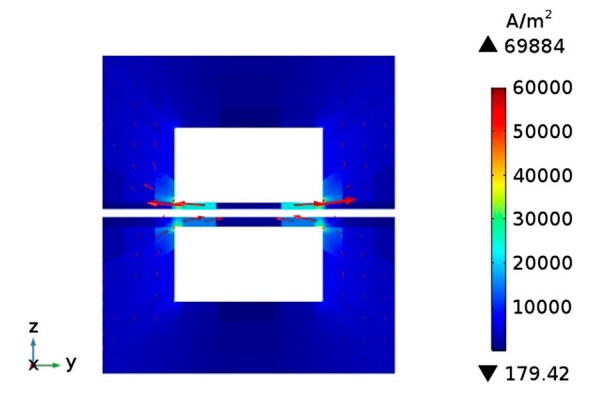

FIGURE 6 | Current density distribution on the cross section of the cell.

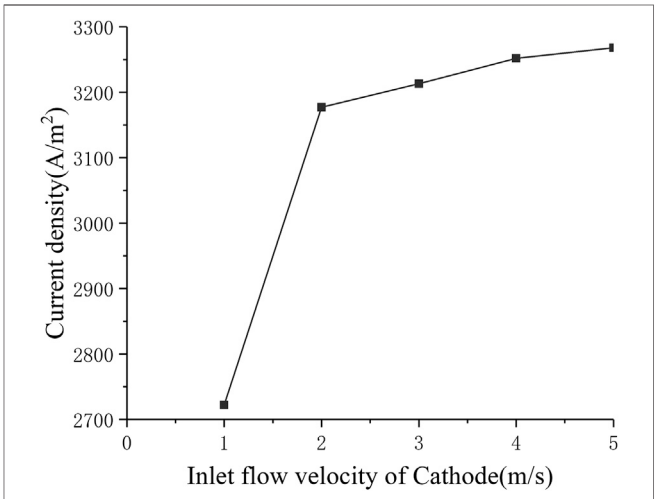

FIGURE 7 | The relationship between current density and cathode inlet flow rate.

(the oxygen inlet mole fraction is 0.14); secondly, the rib area does not directly contact the flow channel, so its oxygen transportation mainly depends on diffusion, and the binary diffusion coefficient of oxygen is lower than other gas in SOFC, which is not conducive to the diffusion of oxygen, and for common anode-supported SOFCs, the thickness of the cathode is generally thin, which will also make the diffusion of oxygen more difficult. The imbalance of the oxygen concentration distribution will lead to the imbalance of the electrochemical reaction, resulting in uneven temperature distribution inside the cell.

Concentration Field Distribution

Figure 6 shows the current density distribution on the cross section of the flow channel. The arrow direction represents the direction of current flow. It can be known that the current density distribution on the entire cross-section is relatively uniform and the values are relatively small (less than 1×10^5 A m^{-2}), but near the contact surface of the flow channel and the interconnector, the current density has a maximum value around 7×10^5 A m^{-2}. This is because the electronic current in the electrode can only pass through the interconnector part, and always takes the shortest path, but the flow channel is not conductive, therefore, the electronic current generated by the porous electrode part will be transmitted laterally to both sides of the

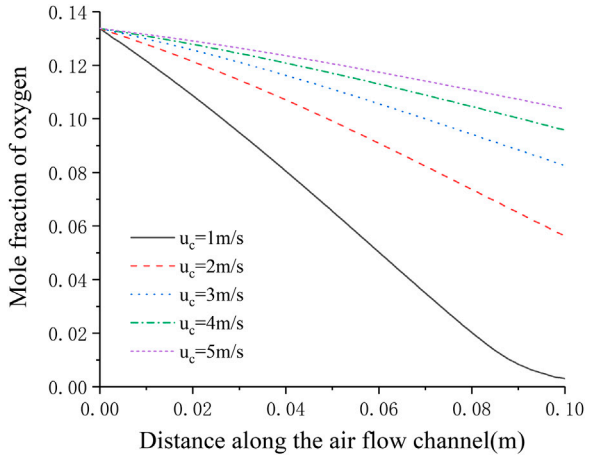

FIGURE 8 | Distribution of oxygen concentration in the cathode flow channel under different cathode inlet flow rates.

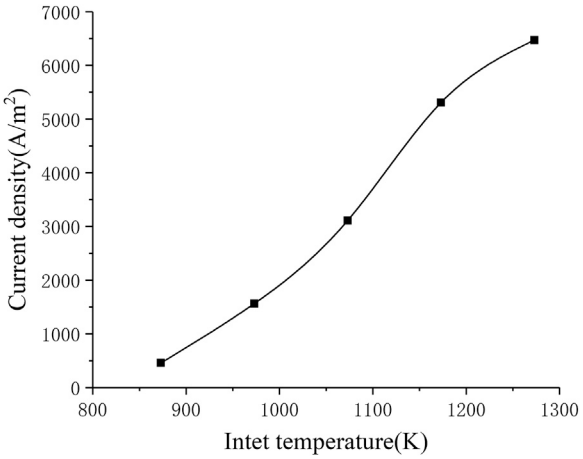

FIGURE 9 | The relationship between inlet temperature and current density.

flow channel, and flows into the interconnector at the position where he flow channel is in contact with interconnector.

Parameter Study

The change of SOFC's working parameters and structural parameters will affect the distribution of physical fields inside the cell. This part mainly studies the influence of the several parameters on the performance of SOFC. The research results are calculated under the condition of output voltage V_{op} = 0.7 V.

Influence of Cathode Inlet Flow Rate

In order to study the influence of the cathode inlet flow rate on the performance of SOFC, the multi-physical field distribution of the cathode flow rate from 1 to 5 m s^{-1} was calculated. **Figure 7** shows the change in current density when the cathode inlet flow rate changes (the standard operating condition is the cathode inlet flow rate u_c = 3 m s^{-1}). It can be seen that when the cathode flow rate increases from 1 to 2 m s^{-1}, the current density increases rapidly from around 2700 A m^{-2} to around 3200 A m^{-2}. When the cathode inlet flow rate continues to increase, the increase in current density gradually slows down. This is because the initial air inlet flow is too small, so the oxygen in the back of the cell is exhausted. The main reason for limiting the cell performance is insufficient supply of reactants. At this time, increasing the cathode air flow will increase the current density significantly. As the cathode inlet flow rate continues to increase, the air on the cathode side gradually becomes excessive, but the electrochemical reaction in the cell has already obtained enough reactants, so the improvement of cell performance is not obvious, When the inlet flow velocity of Cathode increases from 2 to 5 m s^{-1}, the current density only increases by less than 100 A m^{-2}.

Figure 8 shows the distribution of oxygen concentration in the flow channel under different cathode inlet flow rates. It can be seen that the lower the cathode inlet flow rate, the longer the oxygen stays in the cell, and the more oxygen is consumed. When the cathode flow rate is 1 m s^{-1}, the downward trend of the oxygen mole fraction at the outlet has a significant slowdown, and

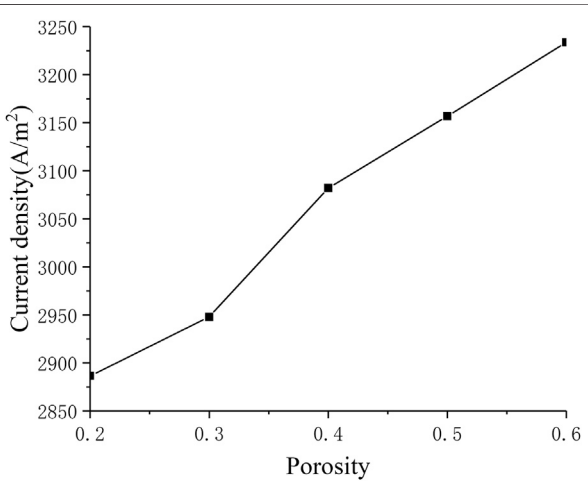

FIGURE 10 | The relationship between porosity and current density.

is close to 0, indicating that the flow rate of oxygen is not enough under this flow rate condition. On the other hand, with the continuous increase of the cathode inlet flow rate, the consumption of oxygen in the flow channel is getting lower and lower, and **Figure 7** shows that the current density is continuously increasing, which shows that after sufficient reactants are provided, increasing the oxygen flow rate mainly improves the diffusion process of oxygen in the porous medium, thereby increasing the current density and improving the cell performance.

Influence of Inlet Temperature

The electrochemical reaction process in the SOFC working process is greatly affected by temperature. In order to study the influence of the inlet temperature on the performance of the SOFC, In the range of 873–1273 K, every 100 K is selected as a

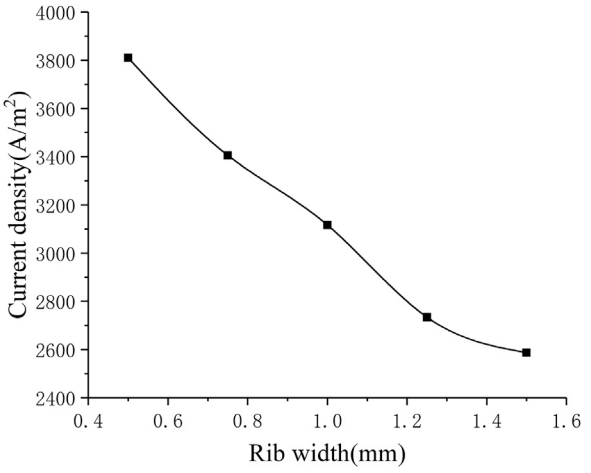

FIGURE 11 | The relationship between rib width and current density.

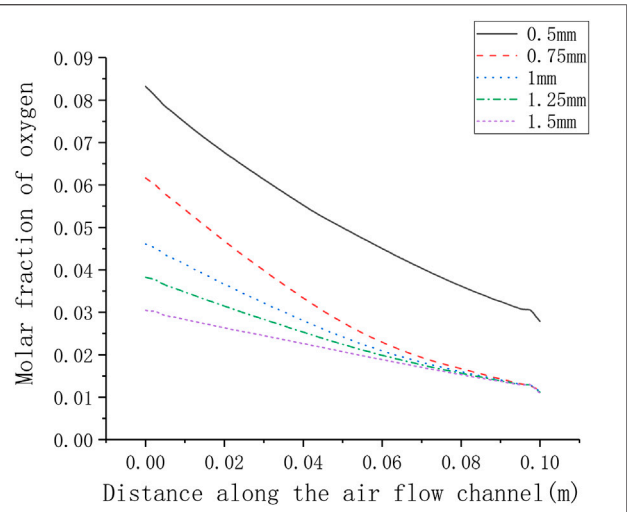

FIGURE 12 | Distribution of oxygen concentration in the rib under different rib width.

working condition point, a total of five inlet temperature conditions are solved separately. **Figure 9** shows the corresponding relationship between inlet temperature and current density. It can be seen that the current density increases significantly as the inlet temperature increases (from around 500 A m^{-2} to around 6500 A m^{-2}). This is consistent with the formula given in the electrochemical model, that is, as the temperature rises, the local current density will increase, thereby increasing the average current density of the cell.

Influence of Porosity

Porosity is the microstructure parameter of the porous electrode, which reflects the difficulty of gas transfer in the porous medium. **Figure 10** describes the corresponding relationship between current density and porosity. It can be seen that as the porosity continues to increase, the current density also increases (from around 2900 A m^{-2} to around 3200 A m^{-2}). This is because the porosity improves the diffusion characteristics of the electrode, making the diffusion of oxygen and hydrogen inside the porous electrode easier, thereby improving cell performance.

Influence of Rib Width

The different rib width parameters selected for numerical calculation are 0.5, 0.75, 1.25, 1.5 mm. **Figure 11** shows the corresponding relationship between rib width and current density. It can be seen that as the rib width increases, the current density gradually decreases (from around 3800–2600 A m^{-2}). In order to understand the gas transport situation of the cell ribs, a straight line is selected as the calculation area on the center plane of the cathode ribs, and the distance between the straight line and one side of the rib is 0.1 times of the whole rib width. For different rib widths, the oxygen concentration distribution on the straight line is shown in **Figure 12**. Generally, as the rib width increases, the average oxygen concentration in the rib area becomes lower. When the rib width is 0.5 mm, the oxygen mole fraction at the cathode exit is about 3%, and when the rib width is other values, the oxygen mole fraction at the cathode exit is very close, both being about 1%. This is because when the rib width is greater than 0.75 mm, the oxygen concentration near the exit is too low, which is close to the lower limit of concentration preset in the simulation. It can be considered that the oxygen has been completely consumed at this time and has no contribution to the electrochemical reaction. Meanwhile, the larger the rib width, the lower the oxygen concentration at the entrance, that is, the smaller the total contribution of the entire rib area to the cell performance. Therefore, increasing the rib width is equivalent to increasing the area of the adverse reaction zone, on the other hand, increasing the rib width makes the oxygen transmission path in the porous electrode longer, and it is more difficult for oxygen to transport to the middle of the rib. In addition, increasing the rib width will also lengthen the current transmission length in the cathode, which increases the ohmic polarization. Combining the above three factors, increasing the rib width will reduce the performance of the cell. Correspondingly, the performance of the cell can be improved by reducing the rib width. However, the rib width is restricted by the manufacturing process and cost. Considering all factors, reducing the rib width as much as possible can improve the working performance of the cell.

CONCLUSION

In this paper, a numerical model of multi-physics coupling of a planar SOFC is established and solved. According to the calculation results, the distribution of various physical parameters inside the SOFC cell is analyzed. The influence of cathode inlet flow rate, porosity, rib width and other parameters on the performance of SOFC is discussed with a fully coupled models. The following conclusions are mainly drawn:

(1) Due to the thinner cathode porous electrode and the smaller oxygen binary diffusion coefficient, the oxygen concentration in the electrode area directly in contact with the flow channel is much greater than the oxygen concentration in the electrode area (rib) directly in contact with the interconnector. The concentration varies greatly between the electrode area covered by channel and the electrode area covered by the ribs. This uneven concentration distribution will affect the electrochemical reaction rate; the current density distribution inside the SOFC is not uniform, and its maximum value is located near the interface between the cathode ribs and the flow channel
(2) When the cathode inlet flow rate is less than a certain value, the oxygen flowing into the cathode will be exhausted before it reaches the cell outlet. In this range, increasing the cathode inlet flow rate can significantly improve the working performance of the cell. When the cathode inlet flow rate is greater than the critical value, the inlet air can meet the needs of the electrochemical reaction, and it is difficult to increase the inlet flow rate to significantly improve the cell performance.
(3) Increasing the porosity can improve the gas diffusion inside the porous electrode and reduce the concentration polarization, thereby increasing the output voltage of SOFC; Increasing the rib width will extend the gas diffusion path and the electron transmission path in the porous electrode. In order to improve the working performance of the cell, the rib width should be reduced as much as possible within the range allowed by objective conditions such as the manufacturing process.

DATA AVAILABILITY STATEMENT

The original contributions presented in the study are included in the article/Supplementary Material, further inquiries can be directed to the corresponding author.

AUTHOR CONTRIBUTION

ZD responsible for the overall organization, conception and writing of the paper. XS responsible for model construction, data analysis, and paper writing. JM responsible for data processing and assist in writing of the paper, ZJ responsible for data processing and assist in writing of the paper. GX responsible for paper conception and method guidance.

FUNDING

This paper is only funded by the National Key Research and Development Program, the sponsor is the Ministry of Science and Technology of the People's Republic of China. The Ministry of Science and Technology of the People's Republic of China through the key research and development plan (2018YFB1502200) funded authors to carry out the research work of the establishment of the multi-physics coupling model of the kW-level SOFC reactor. The National Key Research and Development Program funded all open access publication fees (2950USD). The study is supported by the National Key R&D Program of China 2018YFB1502200.

REFERENCES

Andersson, M., Yuan, J. L., and Sundén, B. (2012). SOFC modeling considering electrochemical reactions at the active three phase boundaries. *Int. J. Heat Mass Transf.* 55 (4), 773–788. doi:10.1016/j.ijheatmasstransfer.2011.10.032

Dong, H. J. (2019). Computational fluid dynamics simulation of anode-supported solid oxide fuel cells with implementing complete overpotential model. *Energy* 13, 1621. doi:10.3390/en13071621

Ferguson, J. R., Fiard, J. M., and Herbin, R. (1996). Three-dimensional numerical simulation for various geometries of solid oxide fuel cells. *J. Power Sources* 58 (2), 109–122.

Futamura, S., Muramoto, A., Tachikawa, Y., Matsuda, J., Lyth, S. M., Shiratori, Y., et al. (2019). SOFC anodes impregnated with noble metal catalyst nanoparticles for high fuel utilization. *Int. J. Hydrogen Energy* 44, 8502–8518. doi:10.1016/j.ijhydene.2019.01.223

Hagen, A., Langnickel, H., and Sun, X. (2019). Operation of solid oxide fuel cells with alternative hydrogen carriers. *Int. J. Hydrogen Energy* 44, 18382–18392. doi:10.3390/en13236173

Hajimolana, S. A., Hussain, M. A., Daud, W. A. W., Soroush, M., and Shamiri, A. (2011). Mathematical modeling of solid oxide fuel cells: a review. *Renew. Sustain. Energy* 15, 1893–1917. doi:10.1016/j.rser.2010.12.011

Iman, K. A. R. (2017). Numerical simulation of the performance of solid oxide fuel cell with different flow channel geometries. *Energy* 119, 235–244. doi:10.3390/en11030473

Iwata, M., Hikosaka, T., Morita, M., Iwanari, T., Ito, K., Onda, K., et al. (2000). Performance analysis of planar-type unit SOFC considering current and temperature distributions. *Solid State Ionics Diffus. React.* 132 (3), 297–308. doi:10.1016/s0167-2738(00)00645-7

Jeon, D. H., Nam, J. H., and Kim, C. J. (2006). Microstructural optimization of anode-supported solid oxide fuel cells by a comprehensive microscale model. *J. Electrochem. Soc.* 153 (2), 406–417. doi:10.3390/en20200427

Kong, W., Zhang, W., Zhang, S., Zhang, Q., and Su, S. (2016). Residual stress analysis of a micro-tubular solid oxide fuel cell. *Int. J. Hydrogen Energy* 41, 16173–16180. doi:10.1016/j.ijhydene.2016.05.256

Kong, W., Zhen, H., Siyu, L., Xiang, G., and Xiaorong, W. (2020). A novel interconnector design of SOFC. *Int. J. Hydrogen Energy* 45 (39), 20329–20338. doi:10.1021/acsami.6b12157

Lee, S. J., Jung, C. Y., and Yi, S. C. (2017). Computational analysis on the electrode geometric parameters for the reversible solid oxide cells. *Electrochim. Acta* 242, 86–99. doi:10.3390/en13205468

Li, X. L., Shi, W. Y., and Han, M. F. (2018). Optimization of interconnect flow channels width in a planar solid oxide fuel cell. *Int. J. Hydrogen Energy* 43 (46), 21524–21534. doi:10.1016/j.ijhydene.2019.11.069

Presto, S., Kumar, P., Varma, S., Viviani, M., and Singh, P. (2018). Electrical conductivity of NiMoebased double perovskites under SOFC anodic conditions. *Int. J. Hydrogen Energy* 43, 4528–4533. doi:10.3390/en13143659

Sahli, Y., Ben Moussa, H., and Zitouni, B. (2019). Optimization study of the produced electric power by SOFCs. *Int. J. Hydrogen Energy* 44, 22445–22454. doi:10.1016/j.ijhydene.2018.08.162

Stygar, M., Brylewski, T., and Rękas, M. (2012). Effects of changes in MOLB-type SOFC cell geometry on temperature distribution and heat transfer rate in interconnects. *Int. J. Heat Mass Transf.* 55 (15), 4421–4426. doi:10.1007/s11434-016-1146-3

Wang, C., Yang, J. J., Huang, W., Zhang, T., Yan, D., Pu, J., et al. (2018a). Numerical simulation and analysis of thermal stress distributions for a planar solid oxide fuel cell stack with external manifold structure. *Int. J. Hydrogen Energy* 43, 20900–20910. doi:10.1016/j.ijhydene.2018.08.076

Wang, Y., Zhan, R. B., Qin, Y. Z., Zhang, G. B., Du, Q., and Jiao, K. (2018b). Three-dimensional modeling of pressure effect on operating characteristics and performance of solid oxide fuel cell. *Int. J. Hydrogen Energy* 43 (43), 20059–20076. doi:10.1016/j.ijhydene.2018.09.025

Yakabe, H., Ogiwara, T., Hishinuma, M., and Yasuda, I. (2001). 3-D model calculation for planar SOFC. *J. Power Sources* 102 (1–2), 144–154. doi:10.1016/S0378-7753(01)00775-3

Zeng, S. M., Zhang, X. Q., Chen, J. S., Li, T. S., and Andersson, M. (2018). Modeling of solid oxide fuel cells with optimized interconnect designs. *Int. J. Heat Mass Transf.* 125, 506–514. doi:10.3390/en13236404

Zhang, X., Yu, G., Zeng, S., Parbey, J., Xiao, S., Li, B., et al. (2018). Mechanism of chromium poisoning the conventional cathode material for solid oxide fuel cells. *J. Power Sources* 381, 26–29. doi:10.1016/j.jpowsour.2018.01.072

Zhang, Z. G., Yue, D. T., Yang, G. G., Chen, J. F., Zheng, Y. F., Miao, H., et al. (2015). Three-dimensional CFD modeling of transport phenomena in multi-channel anode-supported planar SOFCs. *Int. J. Heat Mass Transf.* 84, 942–954. doi:10.1016/j.ijheatmasstransfer.2015.01.097

Zheng, K., Zhang, Y., Li, L., and Ni, M. (2015). On the tortuosity factor of solid phase in solid oxide fuel cell electrodes. *Int. J. Hydrogen Energy* 40, 665–669. doi:10.1016/j.ijhydene.2014.10.111

Conflict of Interest: The authors declare that the research was conducted in the absence of any commercial or financial relationships that could be construed as a potential conflict of interest.

SYMBOL DESCRIPTION

A_v Surface area to volume ratio/$m^2 \cdot m^{-3}$

C_p Specific heat/$J \cdot mol^{-1} \cdot K^{-1}$

$D_{eff,ij}$ Effective binary diffusion/$m^2 \cdot s^{-1}$

E_a Activation energy/$J \cdot mol^{-1}$

E_{Nernst} Open circuit Nernst voltage/V

F Faraday constant/$C \cdot mol^{-1}$

M Molar mass/$kg \cdot mol^{-1}$

R General gas constant/$J \cdot mol^{-1} \cdot K^{-1}$

S Source term

T Temperature/K

V_{op} Output voltage/V

V Volume fraction

i_0 Exchange current density/$A \cdot m^{-2}$

k Thermal conductivity/$W \cdot m^{-1} \cdot K^{-1}$

n Number of species (in the gas-phase species transport governing equation)

u Velocity/$m \cdot s^{-1}$

ε Porosity

η Polarization/V

κ Permeability/m^2

μ Dynamic viscosity/$kg \cdot m^{-1} \cdot s^{-1}$

ρ Density/$kg \cdot m^{-3}$

σ Ion/Electron conductivity/$S \cdot m^{-1}$

τ Tortuosity factor

φ Electric potential/V

frontiers in Chemistry

ORIGINAL RESEARCH
published: 25 January 2021
doi: 10.3389/fchem.2020.628813

$SmBa_{1-x}Ca_xCo_2O_{5+d}$ Layered Perovskite Cathodes for Intermediate Temperature-operating Solid Oxide Fuel Cells

*Kyeong Eun Song[1], Sung Hun Woo[1], Seung Wook Baek[2], Hyunil Kang[3], Won Seok Choi[3], Jun Young Park[4] and Jung Hyun Kim[1]**

[1]Department of Advanced Materials Science and Engineering, Hanbat National University, Daejeon, South Korea, [2]Interdisciplinary Materials Measurement Institute, Korea Research Institute of Standards and Science (KRISS), Daejeon, South Korea, [3]Department of Electrical Engineering, Hanbat National University, Daejeon, South Korea, [4]Department of Nanotechnology and Advanced Materials Engineering, HMC, Sejong University, Seoul, South Korea

In $SmBa_{1-x}Ca_xCo_2O_{5+d}$ (x = 0.01, 0.03, 0.1, and 0.2, SBCCO) oxide systems calcined at 1100°C for 8 h, the XRD patterns of the SBCCO single phase were maintained in the cases of $SmBa_{0.97}Ca_{0.03}Co_2O_{5+d}$ (SBCCO-0.97) and $SmBa_{0.99}Ca_{0.01}Co_2O_{5+d}$ (SBCCO-0.99) compositions. In $SmBa_{0.8}Ca_{0.2}Co_2O_{5+d}$ (SBCCO-0.8) and $SmBa_{0.9}Ca_{0.1}Co_2O_{5+d}$ (SBCCO-0.9), $CaCoSmO_4$ existed with the pattern SBCCO. SBCCO structures were identified as orthorhombic crystal structures because they showed splitting of the X-ray diffraction (XRD) peaks at 23.4°, 47.9°, and 59.1°.Typical metallic conduction behaviors were found in all measured compositions except SBCCO-0.8, which showed a metal-insulator transition (MIT) behavior. Compared to other $SmBa_{1-x}Ca_xCo_2O_{5+d}$ compositions, SBCCO-0.8 showed the highest electrical conductivity of 460 S/cm at 500°C. In particular, SBCCO-0.9 was found to have an excellent ASR characteristic of about 0.077 Ωcm^2 at 700°C. The activation energy of SBCCO-0.9 was the lowest among SBCCO oxide systems with a value of 0.77 eV.

Keywords: intermediate temperature-operating solid oxide fuel cell, cathode, electrical conductivity, area specific resistance, layered perovskite

OPEN ACCESS

Edited by:
Jae-ha Myung, Incheon National University, South Korea

Reviewed by:
Aniruddha Pramod Kulkarni, Commonwealth Scientific and Industrial Research Organisation (CSIRO), Australia
Porun Liu, Griffith University, Australia

****Correspondence:***
Jung Hyun Kim
jhkim2011@hanbat.ac.kr

Specialty section:
This article was submitted to Electrochemistry, a section of the journal Frontiers in Chemistry

Received: *13 November 2020*
Accepted: *28 December 2020*
Published: *25 January 2021*

Citation:
Song KE, Woo SH, Baek SW, Kang H, Choi WS, Park JY and Kim JH (2021) $SmBa_{1-x}Ca_xCo_2O_{5+d}$ Layered Perovskite Cathodes for Intermediate Temperature-operating Solid Oxide Fuel Cells. Front. Chem. 8:628813. doi: 10.3389/fchem.2020.628813

RESEARCH HIGHLIGHTS

SBCCO-0.8: The highest electrical conductivity value of 329.7 S/cm at 700°C.
The lowest ASR value of SBCCO-0.9: 0.077 Ωcm^2 at 700°C.
The lowest activation energy of SBCCO-0.9: 0.77 eV.
The tendency of ASR was similar to that of unit cell volume.

INTRODUCTION

Solid Oxide Fuel Cells (SOFC) are energy devices that directly convert the chemical energy of hydrogen and oxygen into electrical energy; these devices have higher efficiency than do other energy conversion devices. Significantly, SOFCs operate in a high-temperature range of 650–1000°C. They have many advantages in terms of fuel and material selectivity.

However, the advantages of SOFCs in high temperature conditions may be limited by certain disadvantages: thermal degradation of ceramic materials and metal materials inside SOFCs occurs because of the high temperature conditions (Koide et al., 2000; Andersson et al., 2013; Jin et al., 2017)

To solve these issues, many researchers and institutes have focused on the development of Intermediate Temperature-operating Solid Oxide Fuel Cells (IT-SOFCs), which have lowered operation temperatures.

In particular, research has been conducted on cathode materials that exhibit fast oxygen reduction properties at relatively lower temperatures. The typical cathode material used for IT-SOFCs is a simple perovskite having a chemical composition of ABO_3 (A: lanthanide, B: transition metal). In addition, a complex perovskite of $AA'BB'O_3$ composition, in which various kinds of elements are substituted for the simple A-site and B-site of perovskite (Complex perovskite) has been found to have excellent electrochemical properties as well as electrical conductivities.

However, complex perovskites can exhibit dis-ordering due to substitution of various materials and decreases of coulomb potential, elastic potential and oxygen mobility (Chen et al., 2003; Hashimoto et al., 2005; Taskin et al., 2007).

To solve these problems, studies of layered perovskites showing chemical composition of $AA'B_2O_{5+d}$ are being conducted. Layered perovskites occupy many vacancies in the oxide lattice, because oxygen ions are partially removed or completely removed in the $[Ln\text{-}O]_x$ layer. These oxygen vacancies prevent spin glass behavior and enhance the behavior and induce superior 2surface kinetic property (Tarancon et al., 2007; Frontera et al., 2003).

Our research group reported that synthesized layered perovskite, $SmBa_{0.5}Sr_{0.5}Co_2O_{5+d}$ (SBSCO), showed an excellent Area Specific Resistance (ASR) of 0.092 Ωcm^2 at 700°C and could be used as a cathode material of IT-SOFC (Kim et al., 2009b).

However, the Sr contained in SBSCO causes segregation on the surface, causing problems such as reduction of electrochemical properties and long-term performance (Liu et al., 2014; Zhao et al., 2014).

Based on these results, the goal of this study is to investigate the phase synthesis and electrochemical properties of $SmBa_{1-x}Ca_xCo_2O_{5+d}$ (SBCCO) oxide systems in which elemental Ba and Ca elements were substituted into the A'-site of the layered perovskite. Especially, the generation of a secondary phase was investigated in the synthesis process of SBCCO, and not only the effect of the secondary phase on the electrical conductivity, but also its relationship to the crystal structure and electrochemical properties were studied.

EXPERIMENTAL

Sample Preparation and X-Ray Diffraction (XRD)

Samarium Oxide (Sm_2O_3, 99.9%. Alfa Aesar), Barium Carbonate ($BaCO_3$, 99.0%, Alfa Aesar), Calcium Carbonate (CaO, 99.5%, Alfa Aesar), and Cobalt Oxide (Co_3O_4, 99.9%, Alfa Aesar) powder were used for the synthesis of $SmBa_{1-x}Ca_xCo_2O_{5+d}$ (SBCCO, x = 0.01, 0.03, 0.1, and 0.2) by solid state synthesis (SSR). Each powder was accurately weighed according to its chemical composition, and mixed using an agate mortar with a pestle and ethanol. The mixtures were placed in an oven and maintained at 78°C for 12 h to evaporate the ethanol. Mixtures were calcined for 6 h at 1000°C as a first calcination step to decompose all the carbonate. After that, materials were crushed by the agate mortar with the pestle and ball mill; then, a secondary calcination step was carried out for 8 h in an electric furnace at 1100°C in air atmosphere.

TABLE 1 | Abbreviations of $SmBa_{1-x}Ca_xCo_2O_{5+d}$ (SBCCO, x = 0.01, 0.03, 0.1, and 0.2) oxide systems.

Chemical compositions	Abbreviations
$SmBa_{0.8}Ca_{0.2}Co_2O_{5+d}$	SBCCO-0.8
$SmBa_{0.9}Ca_{0.1}Co_2O_{5+d}$	SBCCO-0.9
$SmBa_{0.97}Ca_{0.03}Co_2O_{5+d}$	SBCCO-0.97
$SmBa_{0.99}Ca_{0.01}Co_2O_{5+d}$	SBCCO-0.99

The chemical compositions and abbreviations in $SmBa_{1-x}Ca_xCo_2O_{5+d}$ (SBCCO, x = 0.01, 0.03, 0.1, and 0.2) of cathode materials are summarized in **Table 1**.

X-ray diffraction (XRD) patterns of the synthesized $SmBa_{1-x}Ca_xCo_2O_{5+d}$ (SBCCO, x = 0.01, 0.03, 0.1, and 0.2) oxide systems were obtained on a Model D/Max 2500, Rigaku (45Kv, 200mA, Cu kα radiation); the obtained data were matched with reference data for the phase synthesis and analyzed using the MDI JADE six program.

Electrical Conductivity Analysis

To measure the electrical conductivity of the synthesized cathode materials, pellets were prepared by pressing of rectangular-shaped bars (25 × 6 × 3 mm). Then, pellets for the electrical conductivity measurement were sintered at 1100°C for 3 h. The electrical conductivities were measured using the DC four probe method with a Keithley 2400 Source Meter over a temperature range of 50–900°C at steps of 50°C and a heating rate of 5°C/min.

Electrochemical Characterization

For fabrication of the electrolytes, individual samples of 2.5 g of $Ce_{0.9}Gd_{0.1}O_2$ (CGO91, Rhodia) powder were pressed into disc shaped metal molds at 2×10^3 kg/m^2. The CGO91 electrolytes were sintered at 1450°C for 6 h and the final geometry of the sintered electrolyte pellets was approximately 22.18 mm in diameter and 0.97 mm in thickness. Inks of single-phase and composite cathodes were prepared using mixtures of $SmBa_{1-x}Ca_xCo_2O_{5+d}$ (SBCCO) cathode powders, Alpha-terpineol (KANTO CHEMICAL), Butvar (SIGMA Aldrich) and acetone. These mixtures were stirred for 1 week with a magnetic bar. Then, $Ce_{0.9}Gd_{0.1}O_2$ (CGO91, Rhodia) was mixed with the cathode powder at a mass ratio of 1:1 to sustain the decrease in area specific resistance (ASR). After the prepared inks were applied to the electrolytes using screen printing to fabricate symmetrical half cells, samples were heat-treated at 1000°C for 1 h at a heating rate of 5°C/min.

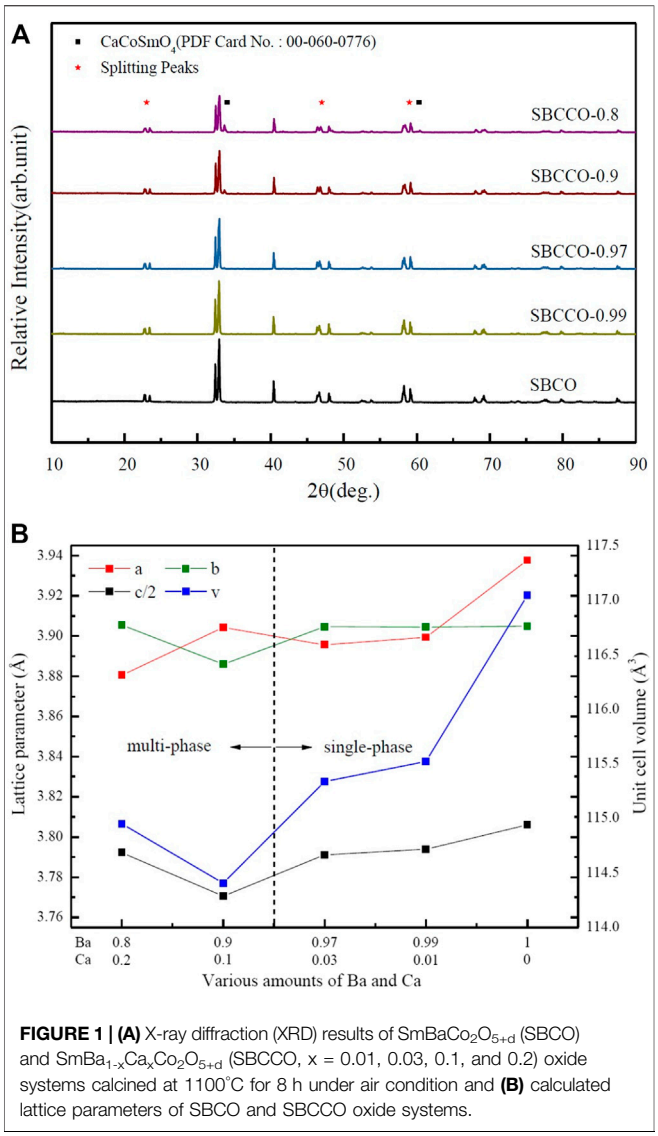

FIGURE 1 | (A) X-ray diffraction (XRD) results of $SmBaCo_2O_{5+d}$ (SBCO) and $SmBa_{1-x}Ca_xCo_2O_{5+d}$ (SBCCO, x = 0.01, 0.03, 0.1, and 0.2) oxide systems calcined at 1100°C for 8 h under air condition and **(B)** calculated lattice parameters of SBCO and SBCCO oxide systems.

The area specific resistances (ASRs) of the half cells were measured using an AC impedance analyzer (Model nStat, HS Technologies); the measurements were performed in a frequency range of 0.05 Hz–2.5 MHz and temperature range of 900°C–650°C with 50 C steps in air atmosphere.

The cathode ASR was determined from the difference between the first and second intercepts of the impedance curves, divided by 2.

RESULTS AND DISCUSSION

X-Ray Diffraction (XRD) Analysis of Layered Perovskite Oxide Systems

X-ray diffraction (XRD) results of $SmBa_{1-x}Ca_xCo_2O_{5+d}$ (hereafter SBCCO, x = 0.01, 0.03, 0.1 and 0.2) substituted with Barium (Ba) and Calcium (Ca) in the $A^{/}$-site of the layered perovskite $SmBaCo_2O_{5+d}$ (SBCO) are shown **Figure 1A**.

As can be seen in **Figure 1A**, $SmBa_{0.97}Ca_{0.03}Co_2O_{5+d}$ (SBCCO-0.97) and $SmBa_{0.99}Ca_{0.01}Co_2O_{5+d}$ (SBCCO-0.99) can be identified as single because typical peaks were found at about 23.4°, 33.0°, 40.4°, 46.4°, 59.1°, 69.2° and 78.0°, which can be considered typical of layered perovskite.

The XRD patterns are the same as those of $SmBaCo_2O_{5+d}$ (SBCO), reported by our group as a single phase. Therefore, it can be determined that SBCCO-0.97 and SBCCO-0.99 were synthesized as single phase (Kim et al., 2009b).

On the other hand, additional peaks caused by $CaCoSmO_4$ (PDF no. 00-060-0776) were measured in the vicinity of 34.0° and 60.3° in the XRD results for $SmBa_{0.8}Ca_{0.2}Co_2O_{5+d}$ (SBCCO-0.8) and $SmBa_{0.9}Ca_{0.1}Co_2O_{5+d}$ (SBCCO-0.9).

That is, it can be confirmed that the single phase of the layered perovskite and $CaCoSmO_4$ coexist in SBCCO-0.8 and SBCCO-0.9.

$CaCoSmO_4$ has been reported in the literature to improve the electrical conductivity (Taguchi et al., 2007); the relationship between the appearance of $CaCoSmO_4$ and the electrical conductivity will be further explained in the section on Electrical Conductivity Analysis of Layered Perovskite.

In addition, the relative intensity of $CaCoSmO_4$ increased as the amount of Ca substitution increased, which means that the concentration of $CaCoSmO_4$ increased in SBCCO-0.8 compared to SBCCO-0.9.

Through these results, it is possible to find the composition conditions for synthesis of a single phase depending on the amount of Ca substitution in the composition of $SmBa_{1-x}Ca_xCo_2O_{5+d}$ (x = 0.01, 0.03, 0.1 and 0.2). The compositions of x = 0.01 and 0.03 in the $SmBa_{1-x}Ca_xCo_2O_{5+d}$ oxide system appropriate conditions. In other words, single phase $SmBa_{1-x}Ca_xCo_2O_{5+d}$ oxide systems can be synthesized when elemental Ca which can be substituted at the $A^{/}$-site, exists only in a limited range (x = 0.01 and 0.03).

This can be explained by the difference in the ionic radii of Ba and Ca. When Ca, having a relatively small ionic radius compared to that of Ba, is replaced with $SmBa_{1-x}Ca_xCo_2O_{5+d}$ oxide systems, a much larger distortion is observed due to the difference of the ionic radii, leading to distortion of the structure of the sublattice. These distortions are not found in SBCO, SBCCO-0.99 or SBCCO-0.97, but can be observed in SBCCO-0.9 and SBCCO-0.8 (Olsson et al., 2017; Wu et al., 2020).

In addition, the peaks measured at 23°, 47° and 59° (2θ) split from the other compositions of $SmBa_{1-x}Ca_xCo_2O_{5+d}$ (SBCCO, x = 0.01, 0.03, 0.1 and 0.2), as can be seen in **Figure 1A**. This shows the same behavior as the splitting peaks at 23°, 47° and 59° of $SmBa_{0.5}Sr_{0.5}Co_2O_{5+d}$ (SBSCO), SBCO and $GdBaCo_2O_{5+d}$ (GBCO), previously reported as orthorhombic crystal structures. As a result, the $SmBa_{1-x}Ca_xCo_2O_{5+d}$ (x = 0.01, 0.03, 0.1, and 0.2) oxide systems were determined to have an orthorhombic crystalline structure with different lattice parameters. (Kim et al., 2009b; Aksenova et al., 2010; Marrero-Jerez et al., 2014).

The calculated lattice parameters and unit cell volumes of the $SmBa_{1-x}Ca_xCo_2O_{5+d}$ (x = 0.01, 0.03, 0.1 and 0.2) oxide systems obtained using the program JADE six are summarized in

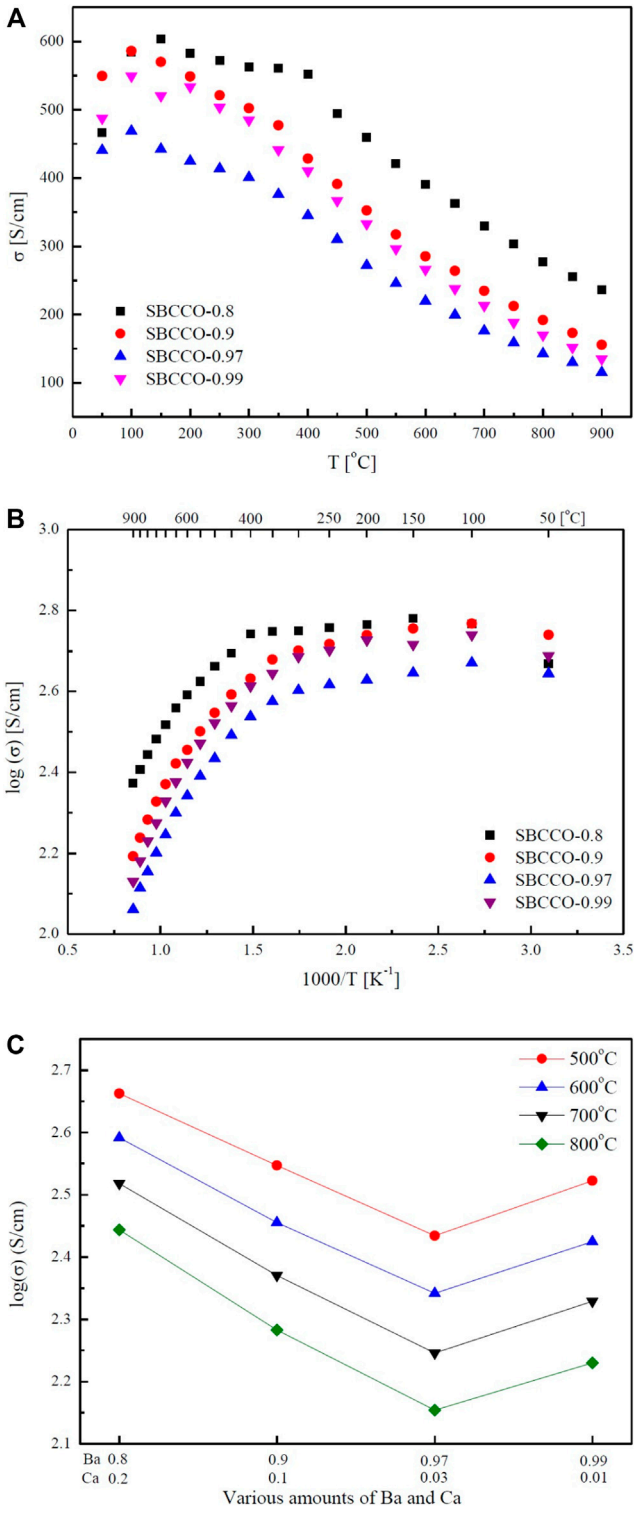

FIGURE 2 | Electrical conductivities of $SmBa_{1-x}Ca_xCo_2O_{5+d}$ (SBCCO, x = 0.01, 0.03, 0.1, and 0.2) Layered perovskite oxide systems with respect to the temperature: **(A)** electrical conductivity vs. T (°C), **(B)** logarithm of electrical conductivity vs. 1000/T (K^{-1}), and **(C)** electrical conductivity results with respect to various amounts of Ba (Barium) and Ca (Calcium).

Figure 1B, which shows the specific crystallographic characteristics.

For SBCCO-0.97, SBCCO-0.99 and SBCO, considered to be single phase, it was confirmed that the unit cell volumes and lattice parameters decreased as the substitution amount of Ba decreased. This behavior can be explained as stemming from the difference in ionic radii of Ba and Ca substituted into the A'-site in the chemical composition of $AA'B_2O_{5+d}$ (A: Lanthanide, A': Ba and Ca): the ionic radius of Ba (1.35 Å) is considerably larger than that of Ca (0.99 Å).

When considering a crystal in which Ba and Ca are substituted into the layered structure, layered perovskite has a structure in which [Ln-O] and [A'-O] layers appear along the c-axis. As a result Ca can replace Ba at the A'-site when the substitution amount of Ba decreases. As the substitution amount of Ca increases in the $SmBa_{1-x}Ca_xCo_2O_{5+d}$ (x = 0.01, 0.03, 0.1, and 0.2) oxide systems, the distance between the [Ln-O] layer and the [A'-O] layer decreases; these relationships result in decreased lattice parameters and, accordingly, the unit cell volume also decreases (Ahrens, 1952; Pauling, 1931; Kim and Manthiram, 2015).

Electrical Conductivity Analysis of Layered Perovskite

Electrical conductivity results of $SmBa_{1-x}Ca_xCo_2O_{5+d}$ (x = 0.01, 0.03, 0.1 and 0.2) oxide systems with respect to the composition and temperature are summarized in **Figure 2**. From **Figure 2A**, the maximum electrical conductivities in these materials can be observed to be in the lower temperature ranges; the minimum values are measured in the higher temperature ranges. The maximum and minimum electrical conductivity values with respect to the temperature are summarized in **Table 2**.

According to **Figure 2A** and **Table 2**, the maximum electrical conductivity value (603 S/cm) of SBCCO-0.8 is the highest of all compositions tested and the maximum electrical conductivity value decreases when the substitution amount of Ca decreases in $SmBa_{1-x}Ca_xCo_2O_{5+d}$ (x = 0.01, 0.03, 0.1 and 0.2) oxide systems. In addition, SBCCO-0.8 shows its maximum electrical conductivity value at 150°C, but other compositions show maximum conductivity at 100°C.

The value of electrical conductivity in $SmBa_{0.5}Sr_{0.5}Co_2O_{5+d}$ (SBSCO), at about 1280 S/cm at 50°C, is better than the values of $SmBaCo_2O_{5+d}$ (SBCO, 500 S/cm) and SBCCO-0.8 (466 S/cm). However, the value of electrical conductivity in SBCCO-0.8 was 330 S/cm at 700°C, which was lower than that of SBSCO (430 S/cm) but higher than that of SBCO (270 S/cm) (Kim et al., 2010; Kim, 2014).

The overall electrical conductivity behaviors can be identified in **Figure 2B**, which shows the conductivity results at logarithmic scale; the $SmBa_{1-x}Ca_xCo_2O_{5+d}$ oxide systems show typical metallic behavior, in which the electrical conductivity decreases with increasing temperature, except for the $SmBa_{0.8}Ca_{0.2}Co_2O_{5+d}$ (SBCCO-0.8) composition (Kim et al., 2010).

All of the compositions used in this conductivity measurement showed relatively higher electrical conductivity values from

TABLE 2 | Maximum and minimum conductivities and temperatures of $SmBa_{1-x}Ca_xCo_2O_{5+d}$ (SBCCO, x = 0.01, 0.03, 0.1, and 0.2).

Chemical compositions	Maximum conductivity (S/cm)	Temperature(°C)	Minimum conductivity (S/cm)	Temperature(°C)
SBCCO-0.8	603	150	236	900
SBCCO-0.9	586	100	156	900
SBCCO-0.97	469	100	115	900
SBCCO-0.99	549	100	135	900

relatively lower temperature ranges (50–300°C) and a rapid decrease from 300 to 900°C, which implies that metal–insulator transition (MIT) behavior is observed in $SmBa_{1-x}Ca_xCo_2O_{5+d}$ (x = 0.01, 0.03, 0.1, and 0.2) oxide systems (Kim, 2014).

SBCCO-0.8 showed the same MIT behavior; however, the temperature at which the maximum conductivity value is measured is relatively lower compared to the other compositions; the electrical conductivity increased in the 50–150°C range and decreased at temperatures above 200°C in SBCCO-0.8.

The electrical conductivity is relatively high in the low temperature range in the composition of $SmBa_{1-x}Ca_xCo_2O_{5+d}$ (SBCCO, x = 0.01, 0.03, 0.1 and 0.2), as shown in **Figure 2B**. This is the concentration of Co^{4+} that causes small polaron hopping, which is relatively higher than the case for Co^{3+}, in the state where Co^{3+} and Co^{4+} coexist (Kim et al., 2010). The effect of these Co^{4+} concentrations on the electrical conductivity in the low temperature range was reported in our group (Kim et al., 2010).

On the other hand, the decreased electrical conductivity values in the range of 300–900°C are caused by the decreased concentration of Co^{4+}. Further, the concentration of oxygen vacancies increases as a function of temperature in these oxide systems. This can also result in decreases in electrical conductivity. For example, the movement of charge carriers can be limited due to oxygen vacancies, which increase rapidly in the range of 300–350°C; at the same time, the electrical conductivity decreases rapidly (Kim, 2014). It can be seen in the literature results of Thermogravimetric Analysis (TGA) and Differential Scanning Calorimetry (DSC) of $SmBa_{0.5}Sr_{0.5}Co_2O_{5+d}$ (SBSCO) that weight decreases rapidly from 300 to 350°C; the same tendency was found for the electrical conductivity in this study (Kim, 2014).

The results of the electrical conductivity according to the composition of $SmBa_{1-x}Ca_xCo_2O_{5+d}$ (SBCCO, x = 0.01, 0.03, 0.1 and 0.2) oxide systems from 500 to 700°C are presented in **Figure 2C**. The electrical conductivity of SBCCO-0.8 was the highest at the measured temperature and composition. The value of electrical conductivity in SBCCO-0.8 is highest, at about 460 S/cm, from 500°C, better than the values of $SmBa_{0.9}Ca_{0.1}Co_2O_{5+d}$ (SBCCO-0.9, 352 S/cm), $SmBa_{0.97}Ca_{0.03}Co_2O_{5+d}$ (SBCCO-0.97, 272 S/cm) and $SmBa_{0.99}Ca_{0.01}Co_2O_{5+d}$ (SBCCO-0.99, 333 S/cm). In other words, the compositions in which the single phase and $CaCoSmO_4$ (PDF no. 00-060-0776) coexist generally have higher electrical conductivity than the compositions of single phase. Therefore, it can be considered that this result was affected by the increase in concentration of $CaCoSmO_4$.

According to the literature, $CaCoSmO_4$ improves the electrical conductivity as the temperature increases. This effect can also be confirmed for SBCCO-0.8, which contains the most $CaCoSmO_4$, and has the highest electrical conductivity (Taguchi et al., 2007).

In addition, it can be seen that the electrical conductivity of SBCCO-0.97, which has the lowest value of electrical conductivity among all compositions, is higher than 100 S/cm, which is the minimum electrical conductivity required for IT-SOFC (Boehm et al., 2003). Therefore, all compositions of $SmBa_{1-x}Ca_xCo_2O_{5+d}$ (SBCCO, x = 0.01, 0.03, 0.1 and 0.2) are applicable as cathode material of IT-SOFC.

Electrochemical Characterization

To investigate the area specific resistances (ASRs) of $SmBa_{1-x}Ca_xCo_2O_{5+d}$ (SBCCO, x = 0.01, 0.03, 0.1 and 0.2), impedance spectroscopy was carried out using symmetrical half cells in a temperature range of 650–850°C; the results are shown in **Figure 3A**.

ASR was compared by considering the surface area of the cathode after sintering at high temperature. Since all half cells are screen printed with the same size mesh, there is little difference in surface area.

The results of ASR have the ohmic resistance removed to allow comparison with the ASR of SBCCO. The ASR values of SBCCO-0.97 and SBCCO-0.99 were 0.11 Ωcm^2 and 0.72 Ωcm^2 at 700°C. The ASRs of SBCCO-0.8 and SBCCO-0.9 were 0.26 Ωcm^2 and 0.07 Ωcm^2 at 700°C. The SBCCO-0.9 cathode material showed the lowest ASR value at 700°C. In addition, the ASR of SBCCO-0.9 was found to be 0.12 Ωcm^2 at 650°C; this is the lowest ASR value among the oxide systems used in this experiment.

When comparing the ASR value (0.12 Ωcm^2) of SBCCO-0.9 with the 0.244 Ωcm^2 value of $SmBa_{0.5}Sr_{0.5}Co_2O_{5+d}$ (SBSCO), 0.13 Ωcm^2 value of $SmBaCo_2O_{5+d}$ (SBCO) and 0.558 Ωcm^2 value of $GdBa_{0.5}Sr_{0.5}Co_2O_{5+d}$ (GBSCO) at 650°C, SBSCO-0.9 showed the lowest ASR value, which indicates that the oxygen reduction processes in Ca-substituted SBSCO-0.9 occurs faster than in Sr-substituted layered perovskites (Kim et al., 2009a; Kim et al., 2009b; Song et al., 2018).

The activation energies of $SmBa_{1-x}Ca_xCo_2O_{5+d}$ (SBCCO, x = 0.01, 0.03, 0.1 and 0.2) oxide systems were calculated from Arrhenius plots of the fitted line and their values are also summarized in **Figure 3A**. SBSCO-0.9 showed the lowest activation energy (0.77 eV) and SBSCO-0.97 showed a relatively low activation energy of 0.93 eV.

However, the activation energies of SBCCO-0.99 and SBCCO-0.8 are 1.06 and 1.29 eV; these values are higher than those of SBSCO-0.9 and SBSCO-0.97. It can be seen that SBCCO-0.9 exhibits lower activation energy even when compared with the

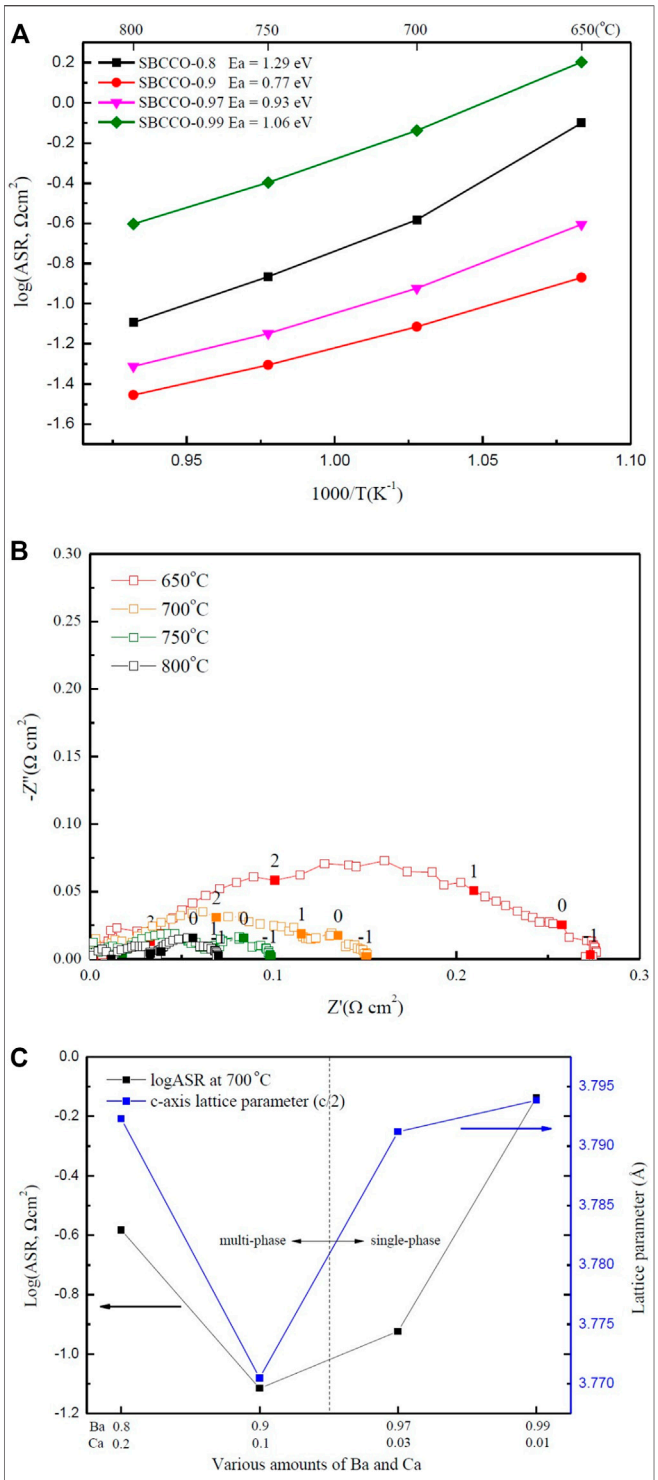

FIGURE 3 | (A) Area specific resistances (ASRs) of $SmBa_{1-x}Ca_xCo_2O_{5+d}$ (SBCCO, x = 0.01, 0.03, 0.1, and 0.2) oxide systems measured from 650 to 800°C in air condition, **(B)** Impedance plots of SBCCO-0.9 oxide system measured at 650, 700, 750, and 800°C in air on dense CGO91 electrolyte and **(C)** Relationships between ASRs measured at 700°C and calculated c-axis lattice parameters of SBCCO oxide systems.

activation energy of the Sr-substituted layered perovskites because SBSCO, SBCO and GBSCO have activation energies of 1.23, 1.11 and 1.22 eV. This means that the energy to activate the reactions for SBCCO-0.9 is smaller than those for SBSCO, SBCO and GBSCO (Kim et al., 2009a; Kim et al., 2009b; Song et al., 2018)

The activation energies of Sr-substituted perovskite $La_{0.6}Sr_{0.4}Co_{0.2}Fe_{0.8}O_3$ (LSCF) and $Ba_{0.5}Sr_{0.5}Co_{0.2}Fe_{0.8}O_3$ (BSCF) are 0.44 and 0.38 eV, lower than that of SBCCO-0.9 (Shen and Lu, 2018). However, SBCCO-0.9 has the advantage of compatibility with lower case Yttria-stabilized zirconia (YSZ) electrolyte without interlayer. The cathode substituted Sr uses an interlayer between the cathode and YSZ electrolyte to prevent segregation (Cai et al., 2012; Wang et al., 2016). SBCCO substitutes Ca instead of Sr, so it will be compatible with YSZ electrolyte without interlayer.

Figure 3B shows ASR results of SBCCO-0.9. The composition of SBCCO-0.9 has ASR values of 0.13, 0.07, 0.04 and 0.03 Ωcm^2 at 650, 700, 750 and 800°C. These values are all lower than 0.15 Ωcm^2, which is the ASR required of cathodes of IT-SOFC at 650°C (Steele, 1996).

Figure 3C shows the correlation between the lattice parameters and the ASRs. The SBCCO-0.9 composition showed the lowest ASR, with the lowest lattice parameter on the c-axis. Therefore, the decrease in ASR was affected by the decrease in c-axis lattice parameter due to the increase in amount of Ca. The SBCCO-0.9 composition comprised of multi phases shows the lowest ASR property among all $SmBa_{1-x}Ca_xCo_2O_{5+d}$ (SBCCO, x = 0.01, 0.03, 0.1, and 0.2) layered perovskites and is directly related with the crystallographic properties caused by the decrease of the c-axis lattice parameters.

CONCLUSION

In this research, we have investigated the phase synthesis and electrochemical properties of $SmBa_{1-x}Ca_xCo_2O_{5+d}$ (SBCCO, x = 0.01, 0.03, 0.1 and 0.2) layered perovskites by substituting Ca for Ba as possible cathode material for IT-SOFC.

The XRD results of the $SmBa_{1-x}Ca_xCo_2O_{5+d}$ oxide system reveal that single phases were found in the compositions of SBCCO-0.97 (x = 0.03) and SBCCO-0.99 (x = 0.01). However, compositions such as SBCCO-0.8 and SBCCO-0.9 included secondary phases of $CaCoSmO_4$. The electrical conductivities of SBCCO-0.8 and SBCCO-0.9 were about 460 S/m and 352 S/cm at 500°C; these values are superior to those of the single-phase cathode. In addition, SBCCO-0.9 has excellent ASR values of 0.13 and 0.07 Ωcm^2 at 650 and 700°C.

DATA AVAILABILITY STATEMENT

The original contributions presented in the study are included in the article/Supplementary Material, further inquiries can be directed to the corresponding author.

AUTHOR CONTRIBUTIONS

KS and JK contributed ideas, designed the work and wrote the manuscript. SW and KS performed experiments and data analysis. SB, HK, WC, and JP contributed to discussing this project, providing laboratory platform, editing the manuscript and financial support.

FUNDING

This work was supported by the National Research Foundation of Korea (NRF) grant funded by the Korean government (MSIT) (No. 2019R1A2C1087534) and the research fund of Hanbat National University in 2019.

REFERENCES

Ahrens, L. H. (1952). The use of ionization potentials Part 1. Ionic radii of the elements. *Geochem. Cosmochim. Acta* 2, 155–169. doi:10.1016/0016-7037(52)90004-5

Aksenova, T. V., Gavrilova, L. Y., Yaremchenko, A. A., Cherepanov, V. A., and Kharton, V. V. (2010). Oxygen nonstoichiometry, thermal expansion and high-temperature electrical properties of layered $NdBaCo_2O_{5+d}$ and $SmBaCo_2O_{5+d}$. *Mater. Res. Bull.* 45 (9), 1288–1292. doi:10.1016/j.materresbull.2010.05.004

Andersson, M., Yuan, J., and Sunden, B. (2013). SOFC modeling considering hydrogen and carbon monoxide as electrochemical reactants. *J. Power Sources* 232, 42–54. doi:10.1016/j.jpowsour.2012.12.122

Boehm, E., Bassat, J. M., Dordor, P., Mauvy, F., and Grenier, J. C. (2003). Oxygen transport properties of $La_2Ni_{1-x}Cu_xO_{4+\delta}$ mixed conducting oxides. *Solid State Sci.* 5 (7), 973–981. doi:10.1016/S1293-2558(03)00091-8

Cai, Z., Kubicek, M., Fleig, J., and Yildiz, B. (2012). Chemical heterogeneities on $La_{0.6}Sr_{0.4}CoO_{3-\delta}$ thin films-correlations to cathode surface activity and stability. *Chem. Mater.* 24, 1116–1127. doi:10.1021/cm203501u

Chen, W., Wen, T., Nie, H., and Zheng, R. (2003). Study of $Ln_{0.6}Sr_{0.4}Co_{0.8}Mn_{0.2}O_3$ (Ln = La, Gd, Sm, or Nd) as the cathode materials for intermediate temperature SOFC. *Mater. Res. Bull.* 38 (8), 1319–1328. doi:10.1016/S0025-5408(03)00143-0

Frontera, C., Garcia-Munoz, J. L., Llobet, A., Manosa, L., and Aranda, M. A. G. (2003). Selective spin-state and metal-insulator transitions in GdBaCo2O5.5. *J. Solid State Chem.* 171 (1-2), 349–352. doi:10.1016/S0022-4596(02)00232-3

Hashimoto, S., Kammer, K., Larsen, P. H., Poulsen, F. W., and Mogensen, M. (2005). A study of $Pr_{0.7}Sr_{0.3}Fe_{1-x}Ni_xO_{3-\delta}$ as a cathode material for SOFCs with intermediate operating temperature. *Solid State Ionics* 176 (11-12), 1013–1020. doi:10.1016/j.ssi.2004.09.010

Jin, S. B., Kim, K. S., Baek, S. W., Kim, H. S., Kang, H. I., Choi, W. S., et al. (2017). Characterization of layered perovskite nanofibers using electrospinning for cathode materials of low temperature-operating solid oxide fuel cell. *New. Renew. Energy* 13 (2), 50–58. doi:10.7849/ksnre.2017.6.13.2.050

Kim, J. H., Cassidy, M., Irvine, J. T. S., and Bae, J. M. (2009a). Advanced electrochemical properties of $LnBa_{0.5}Sr_{0.5}Co_2O_{5+d}$ (Ln = Pr, Sm, and Gd) as cathode materials for IT-SOFC. *J. Electrochem. Soc.* 156 (6), B682–B689. doi:10.1149/1.3110989

Kim, J. H., Kim, Y. M., Connor, P. A., Irvine, J. T. S., Bae, J. M., and Zhou, W. (2009b). Structural, thermal and electrochemical properties of layered perovskite $SmBaCo_2O_{5+d}$, a potential cathode material for intermediate-temperature solid oxide fuel cells. *J. Power Sources* 194 (2), 704–711. doi:10.1016/j.jpowsour.2009.06.024

Kim, J. H., Cassidy, M., Irvine, J. T. S., and Bea, J. M. (2010). Electrochemical investigation of composite cathodes with $SmBa_{0.5}Sr_{0.5}Co_2O_{5+d}$ cathodes for intermediate temperature operating solid oxide fuel cell. *Chem. Mater.* 22 (3), 883–892. doi:10.1021/cm901720w

Kim, J. H. (2014). Comparison of electrical conductivities in complex perovskites and layered perovskite for cathode materials of intermediate temperature-operating solid oxide fuel cell. *J. Korean Ceram. Soc.* 51 (4), 295–299. doi:10.4191/kcers.2014.51.4.295

Kim, J. H., and Manthiram, A. (2015). Layered $LnBaCo_2O_{5+d}$ perovskite cathodes for solid oxide fuel cells: and overview and perspective. *J. Mater. Chem. A.* 3, 24195–24210. doi:10.1039/C5TA06212H

Koide, H., Someya, Y., Yoshida, T., and Maruyama, T. (2000). Properties of Ni/YSZ cermet as anode for SOFC. *Solid State Ionics* 132 (3-4), 253–260. doi:10.1016/S0167-2738(00)00652-4

Liu, Y., Chen, K., Zhao, L., Chi, B., Pu, Jian., Jiang, S. P., et al. (2014). Performance stability and degradation mechanism of $La_{0.6}Sr_{0.4}Co_{0.2}Fe_{0.8}O_{3-\delta}$ cathodes under solid oxide fuel cells operation conditions. *Int. J. Hydrogen Energy* 39 (28), 15868–15876. doi:10.1016/j.ijhydene.2014.03.077

Marrero-Jerez, J., Peña-Martínez, J., and Núñez, P. (2014). Study of the oxygen desorption from $GdBa_{1-x}Sr_xCo_2O_{5+\delta}$ (x = 0, 0.25, 0.5 and 1): effect of the Sr-content on the oxidation state of cobalt ions. *J. Alloys Compd.* 606 (5), 269–272. doi:10.1016/j.jallcom.2014.04.021

Olsson, E., Aparicio-Angle, X., and Leeuw, N. H. (2017). A computational study of the electronic properties, ionic conduction, and thermal expansion of $Sm_{1-x}A_xCoO_3$ and $Sm_{1-x}A_xCoO_{3-x/2}$ (A = Ba^{2+}, Ca^{2+}, Sr^{2+}, and x = 0.25, 0.5) as intermediate temperature SOFC cathodes. *Phys. Chem. Chem. Phys.* 19, 13960–13969. doi:10.1039/C7CP01555K

Pauling, L. (1931). The nature of the chemical bond. *J. Am. Chem. Soc.* 53 (4), 1367–1400. doi:10.1021/ja01355a027

Shen, F., and Lu, K. (2018). Comparison of different perovskite cathodes in solid oxide fuel cells. *Fuel Cells* 18 (4), 457–465. doi:10.1002/fuce.201800044

Song, S. W., Choi, W. S., Kang, H., Baek, S. W., Azad, A. K., Park, J. Y., et al. (2018). Synthesis and electrochemical properties of layered perovskite substituted with heterogeneous lanthanides for intermediate temperature-operating solid oxide fuel cell. *Int. J. Hydrogen Energy* 43 (24), 11378–11385. doi:10.1016/j.ijhydene.2018.04.011

Steele, B. C. H. (1996). Survey of materials selection for ceramic fuel cells II. Cathodes and anodes. *Solid State Ionics* 86-88 (2), 1223–1234. doi:10.1016/0167-2738(96)00291-3

Taguchi, H., Nakade, K., and Hirota, K. (2007). Synthesis and characterization of K_2NiF_4-type $CaLnCoO_4$ (Ln = Sm and Gd). *Mater. Res. Bull.* 42, 649–656. doi:10.1016/j.materresbull.2006.08.004

Tarancon, A., Skinner, S. J., Chater, R. J., Hernández-Ramírez, F., and Kilner, J. A. (2007). Layered perovskites as promising cathodes for intermediate temperature solid oxide fuel cells. *J. Mater. Chem.* 17, 3175–3181. doi:10.1039/B704320A

Taskin, A. A., Lavrov, A. N., and Ando, Y. (2007). Fast oxygen diffusion in A-site ordered perovskites. *Prog. Solid State Chem.* 35 (2-4), 481–490. doi:10.1016/j.progsolidstchem.2007.01.014

Wang, H., Yakal-Kremski, K. J., Yeh, T., Rupp, G. M., Limbeck, A., Fleig, J., et al. (2016). Mechanisms of performance degradation of $(La,Sr)(Co,Fe)O_{3-d}$ solid oxide fuel cell cathodes. *J. Electrochem. Soc.* 163 (6), F581–F585. doi:10.1149/2.0031607jes

Wu, X., Gu, C., Cao, J., Miao, L., Fu, C., and Liu, W. (2020). Investigations on electrochemical performance of $La_2NiO_{4+\delta}$ cathode material doped at A site for solid oxide fuel cells. *Mater. Res. Express.* 7 (6), 065507. doi:10.1088/2053-1591/ab9c60

Zhao, L., Drennan, J., Kong, C., Amarasinghe, S., and Jiang, S. P. (2014). Insight into surface segregation and chromium deposition on $La_{0.6}Sr_{0.4}Co_{0.2}Fe_{0.8}O_{3-\delta}$ cathodes of solid oxide fuel cells. *J. Mater. Chem. A.* 2, 11114–11123. doi:10.1039/C4TA01426J

Conflict of Interest: The authors declare that the research was conducted in the absence of any commercial or financial relationships that could be construed as a potential conflict of interest.

frontiers in Chemistry

ORIGINAL RESEARCH
published: 01 February 2021
doi: 10.3389/fchem.2020.595608

Perovskite Chromite With *In-Situ* Assembled Ni-Co Nano-Alloys: A Potential Bifunctional Electrode Catalyst for Solid Oxide Cells

Zhishan Li[1†], *Lin Cui*[2†], *Jingli Luo*[2], *Jianhui Li*[3] *and Yifei Sun*[1*]

[1]College of Energy, Xiamen University, Xiamen, China, [2]Department of Chemical and Materials Engineering, University of Alberta, Edmonton, Canada, [3]National Engineering Laboratory for Green Chemical Productions of Alcohols, Ethers and Esters, College of Chemistry and Chemical Engineering, Xiamen University, Xiamen, China

Solid oxide fuel cell (SOFC) is an advanced electricity generation device with attractive fuel flexibility and conversion efficiency. As its reversed process, solid oxide electrolysis cell (SOEC) can efficiently electrolyze notorious CO_2 to valuable chemical product such as CO, by utilizing renewable energy. To achieve long-term operation, the development of catalytically active electrode materials in both SOFC/SOEC modes is highly desirable, yet still challenging. In this research, an A-site deficient perovskite oxide (lanthanum chromite) decorated with *in-situ* exsolved Ni-Co nano-alloy has been fabricated and applied as a potential fuel electrode for both SOFC/SOEC. The influences of A-site non-stoichiometry and B-site dopant concentration on structural properties and *in-situ* exsolution process have been elaborately studied from various aspects. Diverse characterizations collectively confirm that the existence of A-site deficiency helps the formation of oxygen vacancies and stimulates the exsolution of B-site cations. In addition, the synergistic effect between the dopants of Co and Ni manipulates the reducibility and promotes carbon deposition resistance of the material. The electrolyte-supported SOFC with self-assembled Ni-Co nano-alloy electrode has shown maximum power densities of 329 mW/cm^2 (in H_2) and 258 mW/cm^2 (in syngas, H_2 + CO) at 850 °C, which are 50% better than those of the fuel cell with the exsolved Ni nanoparticles only. Also, the nano-alloy decorated electrode catalyst promotes a 30% increase in SOEC performance for CO_2 electrolysis with prominently enhanced resistance against carbon deposition, suggesting the versatile functionality of the materials.

Keywords: solid oxide cells, in-situ exsolution, perovskite oxide, nano alloy, carbon deposition resistance

OPEN ACCESS

Edited by:
Tenglong Zhu,
Nanjing University of Science and Technology, China

Reviewed by:
Jun Zhou,
Xi'an Jiaotong University, China
Zhihong Du,
University of Science and Technology Beijing, China

***Correspondence:**
Yifei Sun
yfsun@xmu.edu.cn

[†]*These authors contributes equally to this work*

Specialty section:
This article was submitted to Electrochemistry, a section of the journal Frontiers in Chemistry

Received: *17 August 2020*
Accepted: *23 December 2020*
Published: *01 February 2021*

Citation:
Li Z, Cui L, Luo J, Li J and Sun Y (2021) Perovskite Chromite With In-Situ Assembled Ni-Co Nano-Alloys: A Potential Bifunctional Electrode Catalyst for Solid Oxide Cells. Front. Chem. 8:595608. doi: 10.3389/fchem.2020.595608

INTRODUCTION

The rapid growth of the world's fossil fuel consumption in recent years has led to some severe environmental concerns such as greenhouse effect (Pérez-Lombard et al., 2008). Therefore, many advanced technologies have been developed by researchers to alleviate these challenges. Fuel cell (FC) is a device that directly converts chemical energy to electricity beyond the limitation of Carnot cycle (O'hayre et al., 2016). This process is also done in an eco-friendly manner with significant environmental advantages in terms of its low pollutant emission.

Working in the temperature range from 500 to 800 °C, the solid oxide fuel cell (SOFC) has been considered as the most efficient fuel cell with flexible fuel option including hydrocarbon fuels (Stambouli and Traversa, 2002). Additionally, the high operation temperature accelerates the kinetics of fuel oxidation, thus avoiding the use of noble metal catalysts and significantly decreasing the overall cost of system. Unfortunately, the current technology for SOFC is still difficult to achieve large scale commercialization mainly due to the unsatisfied fuel electrode (anode) performance and stability (Da Silva and de Souza, 2017). Fuel electrodes usually require high catalytic activities, good conductivities, high porosities, and compatibilities with electrolytes as well as interconnectors. Previously, the composite of Ni-YSZ cermet has been widely investigated as an anode for SOFC, which provides excellent ionic and electronic conductivities. However, its poor redox stability and rapid deactivation owing to carbon deposition still hinder its applications (Prakash et al., 2014).

An alternative candidate to substitute Ni-YSZ is perovskite oxide family which has an excellent stability at high temperature, wide structural tunability, as well as good compatibility with the commercial electrolyte material (Sunarso et al., 2017). As a representative, the lanthanum chromite perovskite oxide, $LaCrO_{3-\delta}$, has an excellent chemical, mechanical and thermodynamic stability. The doping of the bivalent element including Sr or Ca at the A site leads to Cr^{3+} to Cr^{4+} transition, which creates more electronic holes in the valence band and thus improves the electronic conductivity. Meanwhile, the as-formed oxygen vacancies give rise to ionic conductivity by charge compensation, (i.e. maintain electrical neutrality of the system) (Setz et al., 2015; Sarno et al., 2018).

However, the application of lanthanum chromite in SOFC is still hindered by its low catalytic activity, mainly due to lack of reactive sites. To solve this problem, catalytically active metal nanoparticles were incorporated onto perovskite surface by wet impregnation (infiltration) or chemical deposition (Sfeir et al., 2001). However, the agglomeration of the nanoparticles will inevitably occur after long-term operation due to the weak metal-oxide adhesion, resulting in the irreversible cell degradation (Jiang, 2006).

Alternatively, the *in-situ* exsolution method has been proposed to overcome this barrier in catalyst fabrication. The main conception of *in-situ* exsolution is to dissolve catalytic transition metals into the perovskite structure (at B sites) during the air preparation process (an oxidizing atmosphere), and force them to partially exsolve out of the lattice in a reducing atmosphere. Such process introduces the array of highly uniform dispersed nanoparticles on the perovskite support. Compared to infiltration method, the nanoparticles produced by *in-situ* exsolution were socketed into perovskite matrix, illustrating a stable metal particle/oxide support interface (Kwon et al., 2020). Also, according to the study by Neagu et al., the *in-situ* exsolved particles are expected to maintain higher redox stability and better carbon deposition resistance while operating in hydrocarbon fuels (Neagu et al., 2015).

Besides fabrication methodology, introducing a second metal (guest metal) to construct a nano-alloy active site is expected to effectively manipulate the properties of metal/oxide catalyst. For example, Ni based alloys were confirmed to better suppress the formation of carbon fibers than pure Ni (An et al., 2011). Takanabe et al. demonstrated that the catalytic activity of Ni-Co alloy catalyst gradually increases with the increased Ni content, while the coke resistance rises in proportion to the amount of Co content (Takanabe et al., 2005). Grgicak et al. studied Ni-Co alloy in comparison to single Ni metal and pointed out that the Ni-Co alloy exhibited a highly stable activity as well as promoted the electrochemical activity in carbon containing environment over a wide range of temperature (500–900 °C) (Grgicak et al., 2008). Therefore, a proper ratio of Ni and Co needs to be considered for the tradeoff between reaction activity and coking resistance.

Based on the above consideration, in this work, a Ni-Co alloy assembled lanthanum chromite perovskite (LSC-NiCo) was prepared and the influences of Ni/Co content and cation deficiency on structural and chemical properties were systematically studied. The electrochemical performance of the electrode with exsolved Ni-Co alloy was evaluated in both SOFC and SOEC modes. Results show that the LSC-NiCo can be a promising candidate for reversible solid oxide cells.

TABLE 1 | designation of bimetallic doping ratio experiment.

Abbreviation	Composition
LSC-6315NiCo	$(La_{0.6}Sr_{0.3})$ $(Cr_{0.85}NiCo(3:1)_{0.15})O_{3-\delta}$
LSC-6312NiCo	$(La_{0.6}Sr_{0.3})$ $(Cr_{0.88}NiCo(3:1)_{0.12})O_{3-\delta}$
LSC-6309NiCo	$(La_{0.6}Sr_{0.3})$ $(Cr_{0.91}NiCo(3:1)_{0.09})O_{3-\delta}$
LSC-6306NiCo	$(La_{0.6}Sr_{0.3})$ $(Cr_{0.94}NiCo(3:1)_{0.06})O_{3-\delta}$
LSC-6303NiCo	$(La_{0.6}Sr_{0.3})$ $(Cr_{0.97}NiCo(3:1)_{0.03})O_{3-\delta}$
LSC-6309Ni	$(La_{0.6}Sr_{0.3})$ $(Cr_{0.91}Ni_{0.09})O_{3-\delta}$
LSC-7309NiCo	$(La_{0.7}Sr_{0.3})$ $(Cr_{0.91}NiCo(3:1)_{0.09})O_{3-\delta}$

EXPERIMENT METHODOLOGY

Synthesis of Cell Materials

Experimental Procedure of Electrode Fabrication

A citric acid and ethylene diamine tetra acetic acid (EDTA) complexing combustion method was applied to prepare the electrode materials. The precursor solution is formed by dissolving stoichiometric amounts of metal nitrates in deionized water with additive of citric acid ($C_6H_8O_7$) and EDTA ($C_{10}H_{16}N_2O_8$) as the co-chelating agents. Metal nitrates include lanthanum (III) nitrate hexahydrate ($La(NO_3)_3{\cdot}6H_2O$), strontium nitrate anhydrous ($Sr(NO_3)_2$), chromium (III) nitrate nona hydrate ($Cr(NO_3)_3{\cdot}9H_2O$), nickel (II) nitrate hexahydrate ($Ni(NO_3)_2{\cdot}6H_2O$), and cobalt (II) nitrate hexahydrate ($Co(NO_3)_2{\cdot}6H_2O$). The molar ratio of metal nitrate, EDTA and citric acid is 1 : 1 : 1.5. Then, the pH of solution is adjusted to ~8 using ammonium hydroxide (NH_4OH) for a better chelating result. The solution is subsequently stirred and heated at 80°C until the gel is formed. The gel is heated to 300°C rapidly and kept at 300°C for 0.5–1 h so that an auto combustion process of the gel will take place to form precursor powder (as-prepared powder). The precursor powders are then grounded and

sintered at 1,200°C for 5 h to form the single phase of targeted perovskite oxide. The designation of the materials is shown in **Table 1**.

The cathode of LSCF ($(La_{0.60}Sr_{0.40})_{0.95}Co_{0.20}Fe_{0.80}O_{3-\delta}$) was purchased from Fuel Cell Materials used as the air electrode in this work.

Fabrication of Solid Oxide Cells

Electrode ink was fabricated by thoroughly mixing the electrode powder, the GDC10 power (10% gadolinium doped ceria oxide, Fuel Cell materials) and the electrode glue at the weight ratio of 1.5 : 1.5 : 1.7 in the milling machine for 2 h. The GDC buffer layers introduced at the electrode and electrolyte interfaces were made by mixing the GDC10 powder with the electrode glue at 1.7: 3 weight ratio. Buffer layers were painted on the two sides of the electrolyte (25 mm diameter, 0.3 mm thickness, 8 mol% yttrium doped zirconia oxide, Fuel Cell Materials). Buffer layers were dried in an air-drying oven (at 90°C for 15 min) and sintered with the electrolyte at 1,300°C for 5 h. Then the fuel electrode ink was painted on one side of the buffer layer with the painting area of 0.965 cm^2. After air-drying the ink, the fuel electrode LSC was sintered at 1,200°C for 5 h. The air electrode LSCF was painted on the other side of the cell, then sintered at 950°C for 4 h in the furnace to obtain good adhesion between the electrode and electrolyte. Au paste was painted on both sides of the electrode as the current collector.

Electrochemical Test Setup for SOFC

The well fabricated cells were placed in an electrochemical test setup shown in **Supplementary Figure S1**. The fabricated cell was sealed on a home-made coaxial alumina two-tube setup by a ceramic sealant (Ceramabond 552, Aremco Products) to separate air and fuel gas injected into the different chambers. The current collectors for the two electrodes were connected to the electrochemical workstation (potentiostat) by 0.5 mm diameter silver wires. The volumetric flow meters were used to control the flow rate of inlet gases, and the outlet gases flowing at the cathode and anode were removed from the system to carry away the generated products and thus allow the reaction to continue. Once the ceramic sealant was cured at room temperature in air, this set-up would be placed in the Thermolyne tubular furnace and then heated to 70 and 260°C for 1 h with a ramping rate of 1°C min^{-1}. Finally, it was heated to the operating temperature with a ramping rate of 2°C min^{-1} for testing. The electrochemical performance was evaluated using the electrochemical workstation with a Solartron 1,287 potentiostat and a Solartron 1,255 frequency response analyzer to collect data and measure the produced powers from SOFC operations (**Supplementary Figure S1**).

Material Characterizations

The phase of the catalyst was analyzed by powder X-Ray diffraction (XRD) using a Rigaka D/max-2500 X-ray diffractometer with a Cu Kα radiation at room temperature and the data were analyzed with Jade and Xpert Highscore Plus Software. The microstructure and morphology of the catalysts, cross sectional and surface images of the cells as well as the material composition by SEM-EDS analysis were obtained at room temperature by Zeiss Sigma 300VP-FESEM equipment. Thermogravimetric (TGA) Analysis of the materials was performed using a Q600 (TA instrument) instrument in different atmospheres. The temperature program oxidation (TPO) was carried out using a TG-Mass Spectrometry (thermostat QMS 200) instruments (TG-MS). The hydrogen-temperature program reduction (H_2-TPR) analysis was performed using a home-made temperature program setup equipped with a Hewlett Packard 5,890 Series II gas chromatograph. The X-ray photoelectron spectra were collected on a Thermo fisher Scientific K-Alpha$^+$ instrument. The C1s XPS peak was calibrated to 284.6 eV, as shown in **Supplementary Figure S2**.

RESULTS

The powder X-ray diffraction (XRD) was used to confirm the crystalline structures of the fabricated materials. According to the study on the materials with different Co/Ni percentages, the optimal concentration of B-site dopant was confirmed as 9 mol% (**Supplementary Figure S3**), and higher doping content will lead to co-existence of NiO impurity. Furthermore, we manipulated the compositions of the material by varying the A-site deficiency and Ni/Co ratio. **Figures 1A,B** show the corresponding XRD patterns. The three materials, LSC-6309NiCo, LSC-6309Ni and LSC-7309NiCo all successfully formed the single phase of LSC perovskite oxide as marked by the asterisk (*) (Pudmich et al., 2000). Moreover, some minor peak shift could be identified by analyzing peak position in detail (**Figure 1B**). The (104) diffraction peaks for LSC-6309NiCo, LSC-6309Ni and LSC-7309NiCo were at 32.75°, 32.85°, and 32.65° (2θ), respectively. According to Bragg Law ($n\lambda = 2d\sin\theta$), the LSC-6309Ni should have the smallest d-spacing and cell parameter while LSC-7309NiCo has the largest unit cell. The evolution of cell volume can be preliminarily explained by the different ion radius of dopants. The ionic radii for 6-fold coordination B-site Cr^{3+}, Ni^{2+} and Co^{2+} are 0.615, 0.69 and 0.745 Å respectively (Sebastian, 2010). Thus, it is reasonable to expect that the bimetallic Ni-Co doping has the increased unit cell volume. Also, the decrease of the unit cell volume of LSC-6309NiCo compared with LSC-7309NiCo is mainly caused by the A-site cation non-stoichiometry, which is in agreement with the literature results of A. V. Kovalevsky et al. (Kovalevsky et al., 2014).

With *in-situ* exsolution treatment on various samples, the metallic particles are expected to be small in size (nanoscale) and uniformly decorated on the surface of the LSC parent. The tendency of the exsolution of metal particles can be partially predicted by the Gibbs free energy. The values of Gibbs free energy of the reduction reaction of each cation were calculated using HSC 6.0 software and shown in **Supplementary Figure S4**. Only Co and Ni are thermodynamically favorable to exsolve under the high temperature from 600 to 900 °C, since only the reductions of Co_3O_4 and NiO have the negative Gibbs free energies. For example, at 800 °C, the reduction of Co_3O_4 to Co

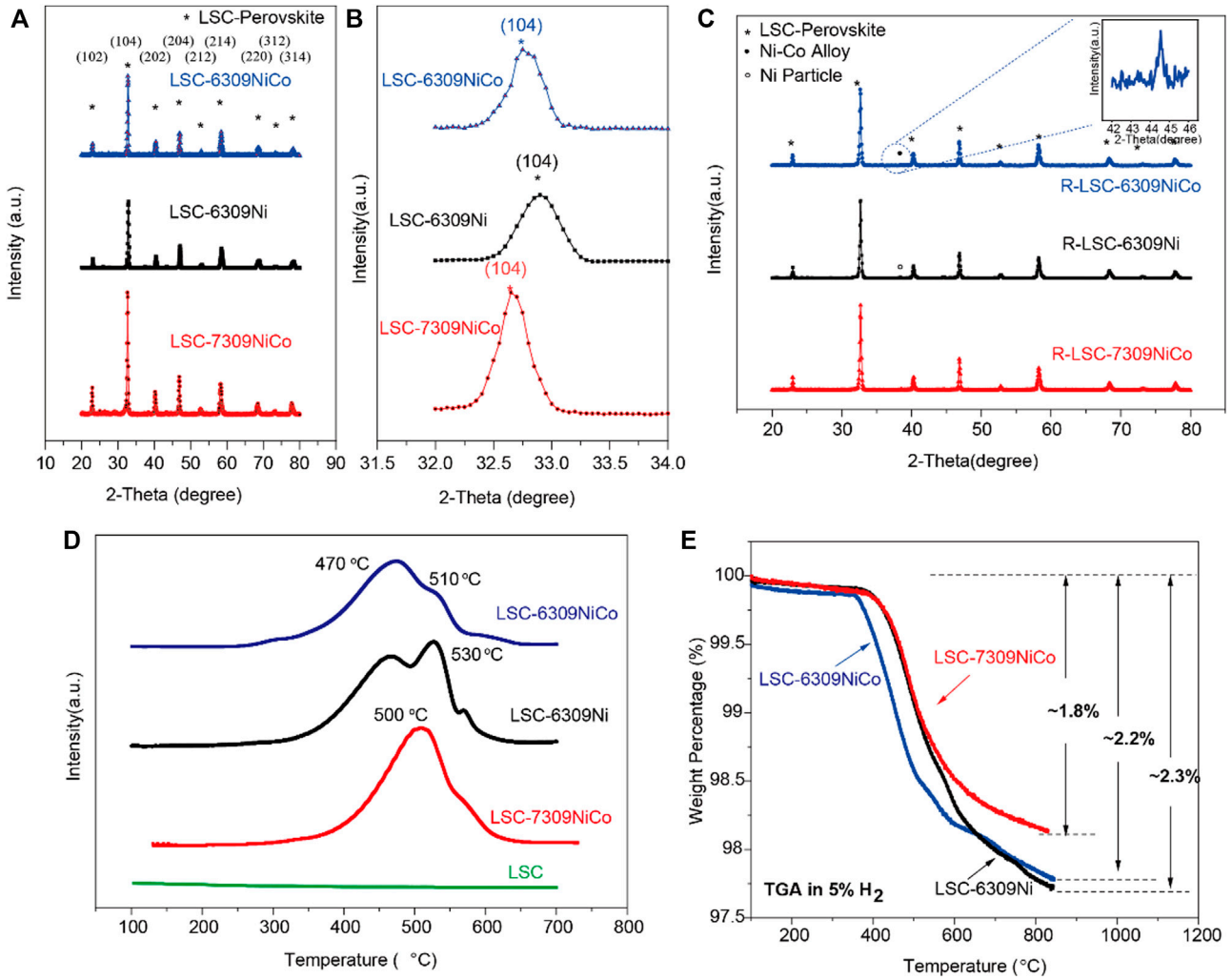

FIGURE 1 | A) XRD patterns and **B)** the partial enlarged detail for perovskite oxide LSC-6309NiCo, LSC-6309Ni and LSC-7309NiCo, **C)** XRD patterns for the reduced samples R-LSC-6309NiCo, R-LSC-6309Ni and R-LSC-7309NiCo, **D)** H_2-TPR curves of the fresh LSC, LSC-6309NiCo, LSC-6309Ni and LSC-7309NiCo, and **E)** TGA diagram in 5%H_2/N_2 for LSC-6309NiCo, LSC-6309Ni and LSC-7309NiCo.

has a Gibbs free energy of −256.91 kJ/mol and that of NiO to Ni is −46.646 kJ/mol, while all other elements still show positive values. In addition, the exsolved Ni and Co metallic particles are expected to form a Ni-Co alloy phase during the high temperature *in-situ* exsolution treatment on the surface of perovskite. Theoretically, it is known that Co and Ni are adjacent to each other in the periodic table and satisfy the Hume-Rothery rule, indicating that they can easily form a solid solution phase (alloy) with various ratios (Janghorban et al., 2001). Thus, it is tentatively suggested that the formation of Ni-Co alloy during the exsolution process in this experiment is favorable.

Based on these theoretical estimations, all the samples were reduced at 800 °C for 3 h in 5% H_2/N_2 atmosphere during which the dopants (Ni, Co) should be *in-situ* exsolved out of the bulk LSC and get uniformly dispersed on the surface. The XRD patterns for reduced samples R-LSC-6309NiCo, R-LSC-6309Ni and R-LSC-7309NiCo, and their detailed exsolution peak positions are illustrated in **Figure 1C**. All of the reduced samples have successfully maintained the main LSC structure after the high temperature reduction process as indicated by asterisk-marked peaks. The diffraction peak labeled as hollow circle has been detected for LSC-6309Ni, indicative of the formation of metallic Ni. In addition, a clear diffraction peak labeled as solid circle has been detected for both R-LSC-6309NiCo and R-LSC-7309NiCo, which can be assigned to Ni-Co alloy (Kwon et al., 2018).

To investigate the reducibility of this series of materials and the synergistic effect between Co and Ni, hydrogen temperature programmed reduction (H_2-TPR) tests were carried out. As shown in **Figure 1D**, there is no obvious H_2 consumption peak occurring in the pattern of LSC perovskite, indicating that LSC might not have exsolved nanoparticles in a reducing atmosphere with increasing temperature. This result is consistent with the Gibbs free energy diagram as mentioned before. Doping

of active metals Ni and Co has made a great improvement on the reducibility of the material. Clear H_2 consumption peaks are observed for both LSC-6309NiCo and LSC-6309Ni. The curve of LSC-6309Ni has two clear H_2 consumption peaks at ~470 °C and 530 °C. Based on the previous studies (Rida et al., 2012; Jahangiri et al., 2013), the first peak (α peak) of LSC-6309Ni corresponds to the reduction of Ni^{3+} to Ni^{2+} (around 500 °C), while the second peak (β peak) represents the reduction from Ni^{2+} to metallic Ni^0 (before 600 °C). The Ni^{2+} to Ni^0 transformation consumes a large amount of hydrogen, which can be confirmed from the area of the β peak because the usage of samples for H_2-TPR measurement is the same. The LSC-6309NiCo material has a similar shape of α peak at ~470 °C, but with a much lower β peak at 510 °C. The material with different B-site concentration shows similar shape of TPR plots (**Supplementary Figure S5**). This phenomenon indicates that the formation of the Ni-Co solutions significantly changes the reduction behavior of the material. A previous study indicated that the main H_2-TPR peak for Co_3O_4 occurs at 433 °C, which just overlapped with α peak of Ni.[21] That can also explain the wider range of α peak in LSC-6309NiCo than in LSC-6309Ni. The β peak for LSC-7309NiCo has moved to a lower temperature and partially merged with the α peak. This result means that the exsolution process of LSC-7309NiCo requires higher energy than LSC-6309NiCo for both Ni^{3+} to Ni^{2+} and Ni^{2+} to Ni^0 transformations. The TPR result clearly proves that the addition of the second metal Co can significantly facilitate the reduction of materials. The existence of A-site deficiency could also accelerate the reduction to generate more Ni-Co nanoparticles.

As the *in-situ* exsolution proceeds, the coordinated lattice oxygen ions surrounding the cations escape from the LSC perovskite oxide as well. The non-stoichiometric oxygen ions have introduced fair amount of oxygen vacancies (δ) into the structure. The quantity of oxygen vacancies plays a significant role in the ionic conductivity and electrochemical catalytic activity of a perovskite material. In this experiment, the TGA was performed to measure the weight losses of the materials with increasing temperature in the reducing atmosphere. As stated by previous studies, the primary weight loss in the curve is due to the formation of oxygen vacancies (He et al., 2014; Konsolakis et al., 2015). The TGA was operated for different materials from 100 to 850 °C at a heating rate of 20 °C per minute in 5% H_2/N_2. **Figure 1E** shows the comparison of TGA curves for LSC-6309NiCo, LSC-6309Ni, and LSC-7309NiCo, and the weight losses for them are ~2.2%, ~2.3%, and ~1.8%, respectively. LSC-6309NiCo had a similar weight loss to that of LSC-6309Ni, but had an obvious lower onset temperature and a larger weight loss in stage two and the first half of stage three (similar as LSC-6303NiCo and LSC-6306NiCo shown in **Supplementary Figure S6**). Stages two and three are the main steps to introduce oxygen vacancies into the structure, and LSC-6309NiCo started at 380 and 510 °C while LSC-6309Ni at 420 and 580 °C. At the last part of stage three, at around 600 °C, the weight loss of LSC-6309Ni increased, resulting in a similar increased amount for LSC-6309NiCo. This result indicates that A-site deficient material, both from monometallic doping and bimetallic doping, shall introduce a similar amount of oxygen vacancies into the structure, but bimetallic doped perovskite demonstrates a facilitated exsolution process. In comparison, LSC-7309NiCo has a smaller amount of weight loss than both LSC-6309NiCo and LSC-6309Ni, and the starting temperatures for stage two and three are around 420 and 580 °C, which are higher than that for LSC-6309NiCo. By comparing the result of these TGA curves, it can be inferred that the introduction of A-site deficiency and bimetallic doping of Ni and Co can facilitate the formation of oxygen vacancies into the structure, thereby improving ionic conductivity and catalytic activity.

The identification for the exsolution is further analyzed by SEM microstructure images. **Figure 2A** shows the SEM image of fresh LSC-6309NiCo powder sample. Clearly, no exsolution of metallic nanoparticles could be found on the surface of fresh sample with the particle size of around 500 nm. In comparison, numerous amounts of exsolved nanoparticles are observed on the reduced sample R-LSC-6309NiCo, which was pre-treated in 5% H_2-N_2 at 800 °C for 4 h, as shown in **Figure 2B**. The exsolved particles are uniformly dispersed on the surface of bulk. **Figures 2C,D** are the point scanning results for R-LSC-6309NiCo. The bulk phase in **Figure 2C** is marked as point 1) and the exsolved particle is marked as point (2). From **Figure 2D**, La is detected at 0.5, 4.7, 5.1 and 5.9 keV, Sr at 1.8 keV, and Cr at 0.25 and 5.4 keV for both the bulk and exsolved particle. Moreover, distinct Co and Ni peaks are detected at point 2) at 7 and 7.5 keV, respectively, while the peaks for point 1) are weak at these positions. Similar method was also applied to confirm the formation of Ni nanoparticle in R-LSC-6309Ni (see **Supplementary Figure S7**). It is concluded that the exsolution particles from R-LSC-6309NiCo base are indeed Ni-Co alloy. The TEM images in **Figure 3** further confirms the Ni-Co alloy structure of exsolved particle on the surface of R-LSC-6309NiCo. Herein, the exsolved particle is marked as point (3).

To understand the evolution of element composition and valence state of samples before and after the exsolution, the X-ray photoelectron spectroscopy spectra (XPS) were further employed. As shown in **Figure 4A**, the Ni2p XPS spectra are similar to that of NiO, suggesting its major composition of Ni^{2+} (Du et al., 2015). After exsolution treatment, the peak positions of Ni2p1/2 and Ni2p3/2 both shift to lower binding energy regime by 0.61 eV, which suggests a significant valence decrease of Ni after reduction and the formation of metallic state Ni (Liu et al., 2016). The O1s XPS spectra of different samples are shown in **Figure 4B**. The percentage of oxygen species obtained by XPS peak fitting is shown in **Supplementary Table S1**. There are huge differences in the O1s XPS spectra of the samples before and after the exsolution. The high resolution O1s spectrum can be deconvoluted into four peaks at 532.8, 530.1, 530.3 and 528.8 eV, which can be ascribed to surface absorbed molecular oxygen species, surface adsorbed oxygen/hydroxyl group, surface adsorbed oxygen/hydroxyl group and lattice oxygen species, respectively. After exsolution, the R-LSC-6309NiCo represents enhanced concentration of O_2/OH (38.58%) and O_2^{2-}/O^- (21.50%), suggesting the higher content of oxygen vacancy (Zhu et al., 2016). The larger amount of oxygen vacancies on the samples may also contribute to the ionic diffusion and facilitate the catalytic reaction. Similar to Ni2p XPS spectra,

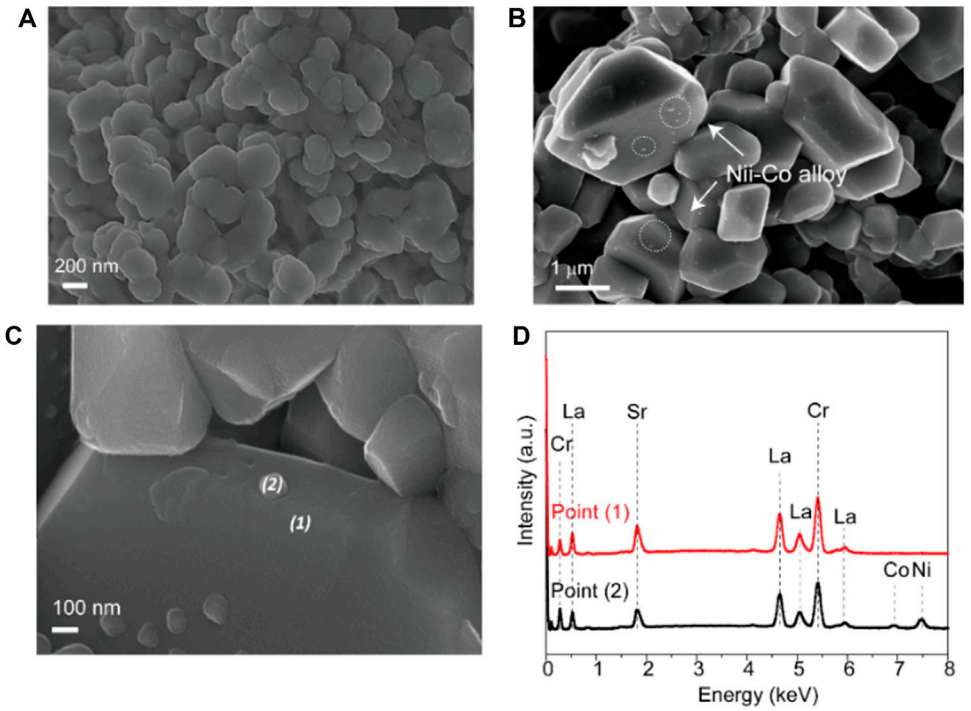

FIGURE 2 | SEM images of **(A)** fresh LSC-6309NiCo microstructure, **(B)** reduced sample R-LSC-6309NiCo, and **(C–D)** the correlated EDS point scanning results.

the Co2p3/2 and Co2p1/2 XPS spectra of samples after reduction have a blue shift by 0.55 eV. The data collected from XPS are consistent with the characterization of XRD and SEM, confirming the formation of Ni-Co alloy.

The SEM image of the cross-section microstructure for the tested cell is shown in **Figure 5A**. The dense YSZ electrolyte with a thickness of 300 μm can be observed, and two 15 μm GDC buffer layers were introduced between the electrode and the electrolyte. The fuel and air electrode layers with the thickness of approximately 30 μm were applied above the GDC layers. **Figure 5B** shows the j-V curve for LSC-6309NiCo and LSC-6309Ni (anode) cells at 850 °C in pure H_2 gas. The tested cells were reduced with 5% H_2/N_2 gas for 2 h before the test to trigger the *in-situ* exsolution of Ni-Co alloy. In H_2 gas, the OCV values for LSC-6309NiCo and LSC-6309Ni cells were 1.15 and 1.13 V, respectively. The high values of OCV observed indicated that negligible gas leakage was present in the cell. The LSC-6309NiCo cell can generate a maximum power density of 329 mW/cm^2 with a current density of 599 mA/cm^2, while the LSC-6309Ni cell only had a maximum power output of 237 mW/cm^2 with a current density of 441 mA/cm^2. **Figure 5C** illustrates the electrochemical performance for LSC-6309NiCo and LSC-6309Ni cells in syngas at 850 °C. The OCV values of 1.11 and 1.14 V were determined as expected for LSC-6309NiCo and LSC-6309Ni, respectively, in syngas. LSC-6309NiCo cell produced a maximum power density of 258 mW/cm^2 with current density of 455 mA/cm^2, as compared to the LSC-6309Ni cell having a maximum power density of 170 mW/cm^2 and with a current density of 307 mA/cm^2. These results demonstrate that the Ni-Co alloy doped LSC cell can maintain the promoted catalytic activity for both H_2 and syngas oxidations.

Supplementary Figure S8A illustrates the EIS performance of both LSC-6309NiCo and LSC-6309Ni cells from 10^6 to 0.1 Hz under open circuit voltage condition with H_2 gas at 850 °C. The curves intersections with the real axis (*x*-axis) at high frequencies represent their ohmic resistance, which is mainly caused by the electrolyte material (Fabbri et al., 2008). LSC-6309NiCo and LSC-6309Ni cells have shown the similar ohmic resistances of 0.54 and 0.56 Ω, which are reasonable with the 300 μm thickness of YSZ electrolyte. The difference between the two intersections at high frequency and low frequency with the *x*-axis represents the activation polarization resistance, which is the sum of the electrode (anode and cathode) reaction resistances (Zuo et al., 2006). The real parts of the impedance at low frequency for LSC-6309NiCo and LSC-6309Ni are partially compared at 10, 1 and 0.1 Hz as marked by the dashed lines in the figure. LSC-6309NiCo cell has shown a clear reduction of the real impedance compared to LSC-6309Ni at the identical frequencies. This result has demonstrated the lower polarization resistance of LSC-6309NiCo cell compared with the LSC-6309Ni cell. The lower value of polarization resistance for the LSC-6309NiCo also clarifies its better electrochemical performance. **Supplementary Figure S8B** is the EIS diagram for LSC-6309NiCo and LSC-6309Ni cells for syngas oxidation at 850 °C under OCV condition. Compared with the H_2 oxidation EIS diagram, no significant increase of ohmic resistances are found in syngas atmosphere. In addition, the real impedance values of each cell are compared at 10, 1 and 0.1 Hz. Apparently, LSC-6309Ni has an obvious larger

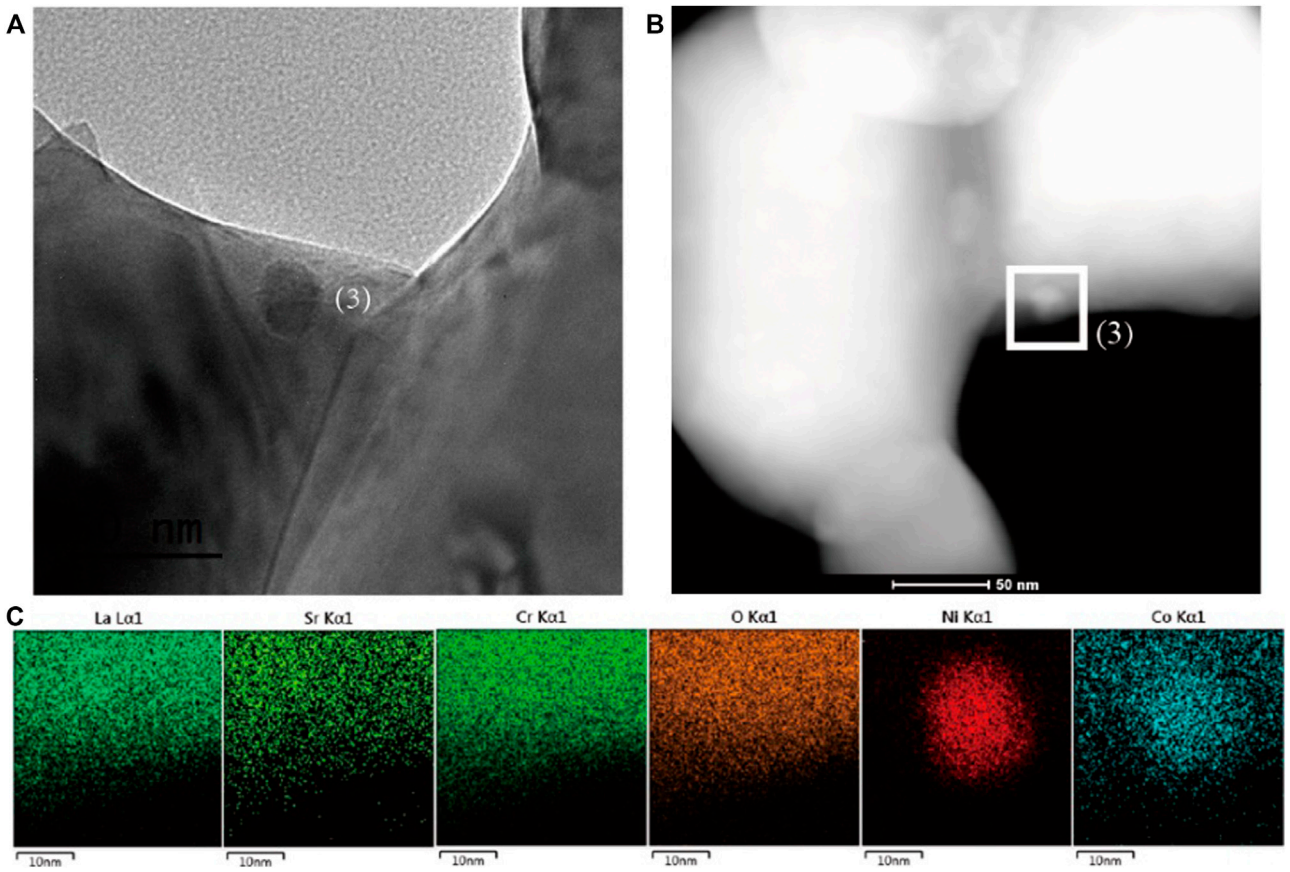

FIGURE 3 | (A) TEM and **(B)** STEM-HAADF images of the reduced sample R-LSC-6309NiCo, and **(C)** the correlated elemental mapping of La, Sr, Cr, O, Ni and Co for point (1) in **(B)**, which is represented by cyan, lime, green, orange, red and blue, respectively.

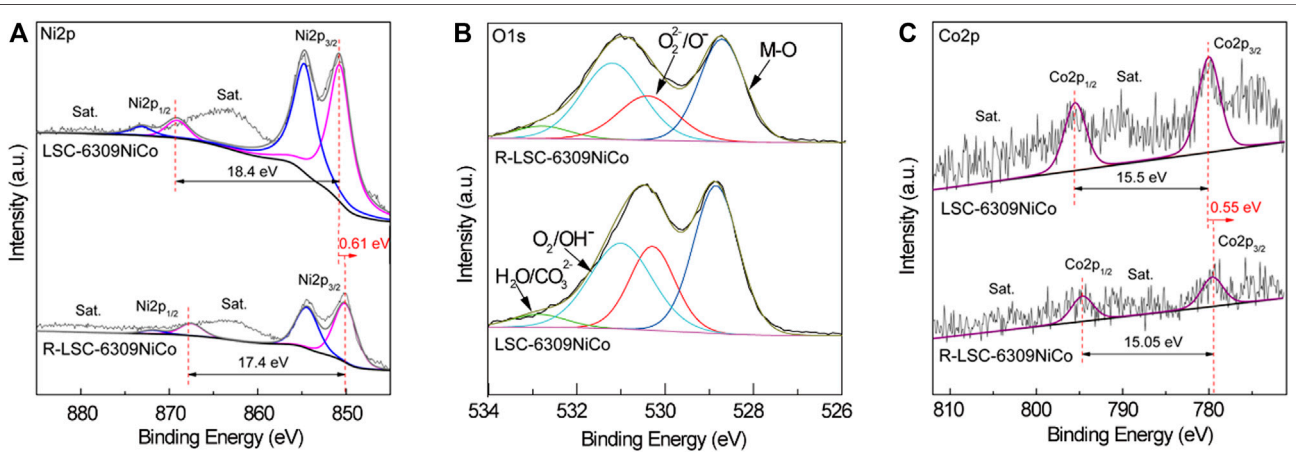

FIGURE 4 | XPS spectra of LSC-6309NiCo and R-LSC-6309NiCo samples: **(A)** Ni2p, **(B)** O1s and **(C)** Co2p.

value of real impedance than LSC-6309NiCo under each frequency.

Furthermore, the electrochemical performances of SOEC using LSC-6309NiCo and LSC-6309Ni cathodes were evaluated at 850 °C in CO_2/CO atmosphere at the ratio of 70 : 30. CO gas was added into fuel gas CO_2 during the electrochemical test to prevent the oxidation of exsolved particles. The cells were tested mainly under electrolysis mode

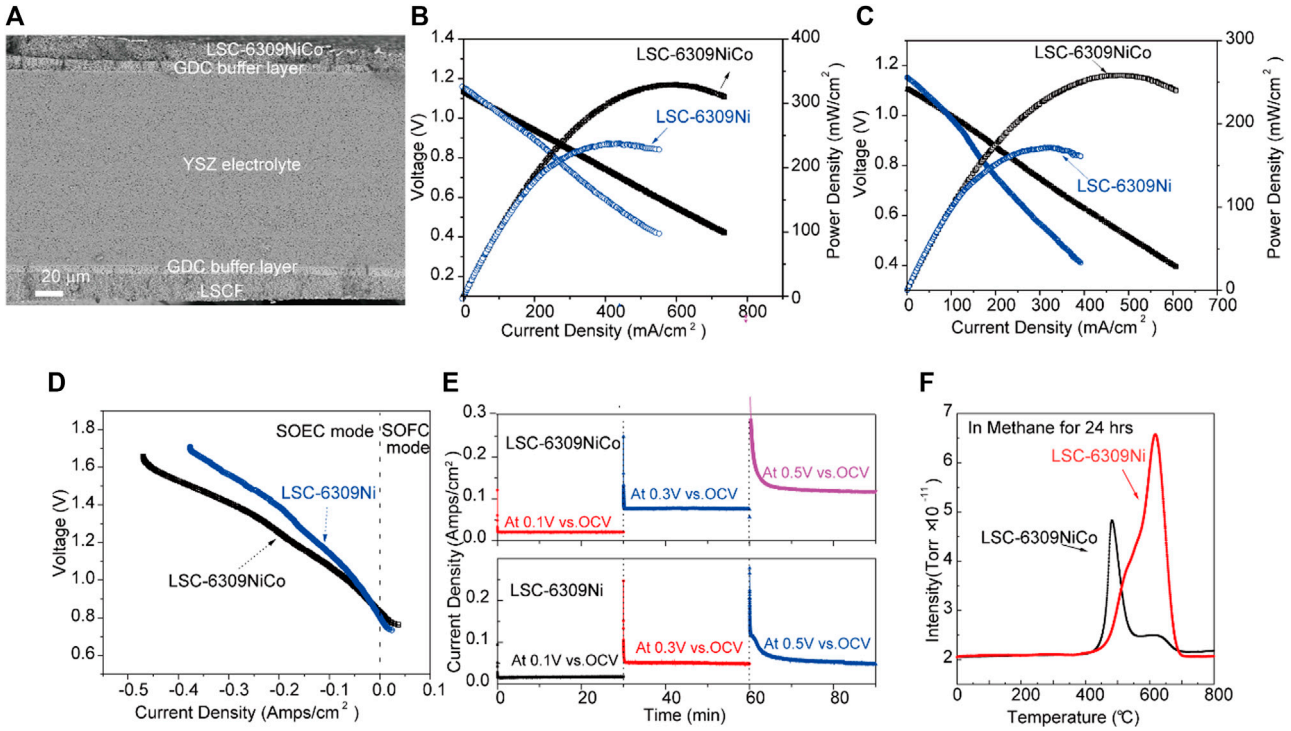

FIGURE 5 | (A) SEM image of the cross-section area of the cell, **(B)** j-V curves of LSC-6309NiCo and LSC-6309Ni at 850 °C in pure H_2 gas and **(C)** in syngas, **(D)** j-V curves of LSC-6309NiCo and LSC-6309Ni at 850 °C in 70% CO_2/30%CO, **(E)** Short term stabilities of the electrolysis cells with LSC-6309NiCo and LSC-6309Ni cathodes at 850 °C at various applied voltages, and **(F)** TPO curves for CH_4 treated LSC-6309NiCo and LSC-6309Ni.

(negative current density) with applied voltages from 0 to 0.9 V (vs. OCV). **Figure 5D** illustrates the j-V curve of SOEC equipped with LSC-6309Ni and LSC-6309NiCo cathodes. The OCV values for both cells are 0.84–0.82 V, which are close to the theoretical values in 70% CO_2/30% CO atmosphere. As depicted, the LSC-6309NiCo cell has current densities of 0.039, 0.136 and 0.245 mA/cm^2 at the applied voltages of 0.1, 0.3 and 0.5 V, respectively, while LSC-6309Ni has corresponding current densities of 0.027, 0.089 and 0.179 mA/cm^2. The LSC-6309NiCo cell has expressed a better performance than the LSC-6309Ni cell in CO_2/CO atmosphere at all applied voltages, which demonstrates that the bimetal doped LSC cell has a better catalytic property in the CO_2 reduction process.

Short term operating stabilities for LSC-6309NiCo and LSC-6309Ni electrolysis cells were tested in 70% CO_2/30% CO at 850 °C with various applied voltages and plotted in **Figure 5E**. Both cells were run in the SOEC mode for 30 min at constant voltages of 0.1, 0.3 and 0.5 V (vs. OCV). The LSC-6309NiCo electrolysis cell shows good stabilities under all voltages and the current densities of the cell with increasing applied voltage. In contrast, the LSC-6309Ni electrolysis cell expresses good stabilities at the applied voltages of 0.1 and 0.3 V. A significant degradation of the LSC-6309Ni cell was detected at 0.5 V applied voltage. The possible reason for this degradation might be the influence from carbon deposition on Ni particles from the over reduction in CO_2/CO atmosphere (Li et al., 2015). As a result, the stable operating potential for LSC-6309Ni can be inferred as 0.3 V vs. OCV. The morphology of bulk LSC materials is maintained after short-term tests, as presented in **Supplementary Figure S9**. Overall, the bimetallic doped LSC perovskite has shown better stability than the Ni doped LSC in an SOEC atmosphere at various applied potentials.

Previous studies have indicated the poor carbon deposition resistance of Ni particle doped fuel electrodes operating in coal gases. The coal derived fuel gas applied to solid oxide cells such as hydrocarbons, syngas, and even CO_2 gas can cause carbon deposition and lead to performance degradation of the cell (Chen et al., 2011). Therefore, carbon deposition resistance is another important parameter for catalytic activity analysis of the electrode. The carbon deposition resistance of Ni and Ni-Co LSC perovskite oxide was studied in this work by O_2-TPO analysis. The samples were sintered with CH_4 gas at 850 °C for 24 h. After the treatment with CH_4 gas, the samples were inserted for the TGA test from 0 to 850°C in air. The gas outlet of the TGA was connected with the MS, therefore, the specific amount of produced CO_2 at different temperatures could be measured. The O_2-TPO profile measured by MS is shown in **Figure 5F**. The CO_2 peak areas for LSC-6309NiCo and LSC-6309Ni were 4.21×10^{-9} and 5.30×10^{-9}, respectively. From this result, it can be concluded that compared with Ni doped catalytic material, the addition of Co into the catalyst can effectively suppress the formation of carbon deposition on the electrode material as studied by K. Takanabe et al. (Takanabe et al., 2005). Moreover, the CO_2 peak position of LSC-6309Ni electrode

material is at around 620 °C, while the peak position for LSC-6309NiCo is around 470 °C. The lower operating temperature for LSC-6309NiCo electrode material indicates a smaller energy required for redox treatment. Compared to LSC-6309Ni, LSC-6309NiCo shows higher carbon deposition resistance and lower required recovery temperature. This is because the formation of surface Ni-Co alloy can effectively suppress the bonding of undesired carbon and preferentially oxidize the carbon atom into gas phase. The monometallic Ni is more likely to facilitate the formation of carbon-carbon bonds (Nikolla et al., 2009), resulting in poor carbon deposition resistance of LSC-6309Ni.

CONCLUSION

The LSC-based perovskite oxides were prepared in this work as a potential electrode material for SOFC and SOEC. The roles of A-site stoichiometry and B-site dopant concentration on material properties were studied by XRD, TPR, TPO, TGA, XPS and SEM. LSC-6309NiCo and LSC-6309Ni were selected for the electrochemical performance tests in SOFC and SOEC. The following conclusions can be drawn based on the experimental results:

- The Ni and Co doped LSC perovskite oxide were fabricated by combustion process with the saturation doping level up to 9 mol%.
- The introduction of A-site deficiency is the key driving force to trigger the exsolution of Nano Ni-Co alloy particles. The exsolution process was found to be facilitated by Co incorporation.
- The Ni-Co alloy decorated materials delivered better electrochemical performance in both SOFC and SOEC modes. Meanwhile, the formation of Ni-Co alloy has efficiently reduced the carbon deposition in the cell while operating in SOEC mode.

DATA AVAILABILITY STATEMENT

The original contributions presented in the study are included in the article/**Supplementary Material**, further inquiries can be directed to the corresponding author.

AUTHOR CONTRIBUTIONS

YS, JL and JL designed this work. LC and ZL conducted the experiments. All authors discussed the manuscript.

FUNDING

This work is supported by the National Natural Science Foundation of China (No.21773195). This research is financially supported by the Natural Sciences and Engineering Research Council of Canada-Discovery Grant (GRPIN–2016–05494), and Alberta Innovates Technology Futures Research Grant.

ACKNOWLEDGMENTS

YS acknowledges the support from the Nanqiang Young Top-notch Talent Fellowship from Xiamen University. As a part of the University of Alberta's Future Energy Systems research initiative, this research was made possible in part thanks to funding from the Canada First Research Excellence Fund.

SUPPLEMENTARY MATERIAL

The Supplementary Material for this article can be found online at: https://www.frontiersin.org/articles/10.3389/fchem.2020.595608/full#supplementary-material.

REFERENCES

An, W., Gatewood, D., Dunlap, B., and Turner, C. H. (2011). Catalytic activity of bimetallic nickel alloys for solid-oxide fuel cell anode reactions from density-functional theory. *J. Power Sources* 196, 4724–4728. doi:10.1016/j.jpowsour.2011.01.007

Chen, T., Wang, W. G., Miao, H., Li, T., and Xu, C. (2011). Evaluation of carbon deposition behavior on the nickel/yttrium-stabilized zirconia anode-supported fuel cell fueled with simulated syngas. *J. Power Sources* 196, 2461–2468. doi:10.1016/j.jpowsour.2010.11.095

Da Silva, F. S., and de Souza, T. M. (2017). Novel materials for solid oxide fuel cell technologies: a literature review. *Int. J. Hydrogen Energy.* 42, 26020–26036. doi:10.1016/j.ijhydene.2017.08.105

Du, X., Ding, Y., and Li, C. (2015). Morphology-controlled self-assembly and nanostructured NiO: an efficient and robust photocatalytic water-oxidation catalystcient and robust photocatalytic water-oxidation catalyst. *ChemCatChem* 7, 2370–2376. doi:10.1002/cctc.201500308

Fabbri, E., Pergolesi, D., D'Epifanio, A., Di Bartolomeo, E., Balestrino, G., Licoccia, S., et al. (2008). Design and fabrication of a chemically-stable proton conductor bilayer electrolyte for intermediate temperature solid oxide fuel cells (IT-SOFCs). *Energy Environ. Sci.* 1, 355–359. doi:10.1039/b806655h

Grgicak, C. M., Pakulska, M. M., O'Brien, J. S., and Giorgi, J. B. (2008). Synergistic effects of Ni1−xCox-YSZ and Ni1−xCux-YSZ alloyed cermet SOFC anodes for oxidation of hydrogen and methane fuels containing H2S. *J. Power Sources* 183, 26–33. doi:10.1016/j.jpowsour.2008.05.002

He, W., Huang, H., Chen, M., Gao, J.-F., and Chen, C.-S. (2014). Stability and oxygen transport property of La0.8Sr0.2Cr0.5Fe0.5O3-δ. *Solid State Ionics* 260, 86–89. doi:10.1016/j.ssi.2014.03.018

Jahangiri, A., Aghabozorg, H., and Pahlavanzadeh, H. (2013). Effects of Fe substitutions by Ni in La-Ni-O perovskite-type oxides in reforming of methane with CO2 and O2. *Int. J. Hydrogen Energy* 38, 10407–10416. doi:10.1016/j.ijhydene.2013.05.080

Janghorban, K., Kirkaldy, J. S., and Weatherly, G. C. (2001). The Hume-Rothery size rule and double-well microstructures in gold-nickel. *J. Phys. Condens. Matter* 13, 8661. doi:10.1088/0953-8984/13/38/309

Jiang, S. P. (2006). A review of wet impregnation-An alternative method for the fabrication of high performance and nano-structured electrodes of solid oxide fuel cells. *Mater. Sci. Eng., A.* 418, 199–210. doi:10.1016/j.msea.2005.11.052

Konsolakis, M., Sgourakis, M., and Carabineiro, S. A. C. (2015). Surface and redox properties of cobalt-ceria binary oxides: on the effect of Co content and pretreatment conditions. *Appl. Surf. Sci.* 341, 48–54. doi:10.1016/j.apsusc.2015.02.188

Kovalevsky, A. V., Yaremchenko, A. A., Populoh, S., Weidenkaff, A., and Frade, J. R. (2014). Effect of A-site cation deficiency on the thermoelectric performance of donor-substituted strontium titanate. *J. Phys. Chem. C.* 118, 4596–4606. doi:10.1021/jp409872e

Kwon, O., Joo, S., Choi, S., Sengodan, S., and Kim, G. (2020). Review on exsolution and its driving forces in perovskites. *J. Phys. Energy* 2, 032001. doi:10.1088/2515-7655/ab8c1f

Kwon, O., Kim, K., Joo, S., Jeong, H. Y., Shin, J., Han, J. W., et al. (2018). Self-assembled alloy nanoparticles in a layered double perovskite as a fuel oxidation catalyst for solid oxide fuel cells. *J. Mater. Chem.* 6, 15947–15953. doi:10.1039/c8ta05105d

Li, W., Shi, Y., Luo, Y., Wang, Y., and Cai, N. (2015). Carbon deposition on patterned nickel/yttria stabilized zirconia electrodes for solid oxide fuel cell/solid oxide electrolysis cell modes. *J. Power Sources* 276, 26–31. doi:10.1016/j.jpowsour.2014.11.106

Liu, Y., Fu, N., Zhang, G., Lu, W., Zhou, L., and Huang, H. (2016). Ni@NiO core/shell dendrites for ultra-long cycle life electrochemical energy storage. *J. Mater. Chem.* 4, 15049–15056. doi:10.1039/c6ta05508g

Neagu, D., Oh, T. S., Miller, D. N., Ménard, H., Bukhari, S. M., Gamble, S. R., et al. (2015). Nano-socketed nickel particles with enhanced coking resistance grown *in situ* by redox exsolution. *Nat. Commun.* 6, 8120–8128. doi:10.1038/ncomms9120

Nikolla, E., Schwank, J., and Linic, S. (2009). Direct electrochemical oxidation of hydrocarbon fuels on SOFCs: improved carbon tolerance of Ni alloy anodes. *J. Electrochem. Soc.* 156, B1312–B1316. doi:10.1149/1.3208060

O'hayre, R., Cha, S. W., Colella, W., and Prinz, F. B. (2016). *Fuel cell fundamentals*. New Jersey, NJ, United States: John Wiley and Sons.

Pérez-Lombard, L., Ortiz, J., and Pout, C. (2008). A review on buildings energy consumption information. *Energy Build.* 40, 394–398. doi:10.1016/j.enbuild.2007.03.007

Prakash, B. S., Kumar, S. S., and Aruna, S. (2014). Properties and development of Ni/YSZ as an anode material in solid oxide fuel cell: a review. *Renew. Sustain. Energy Rev.* 36, 149–179. doi:10.1016/j.rser.2014.04.043

Pudmich, G., Boukamp, B. A., Gonzalez-Cuenca, M., Jungen, W., Zipprich, W., and Tietz, F. (2000). Chromite/titanate based perovskites for application as anodes in solid oxide fuel cells. *Solid State Ionics* 135, 433–438. doi:10.1016/S0167-2738(00)00391-X

Rida, K., Peña, M. A., Sastre, E., and Martinez-Arias, A. (2012). Effect of calcination temperature on structural properties and catalytic activity in oxidation reactions of LaNiO3 perovskite prepared by Pechini method. *J. Rare Earths* 30, 210–216. doi:10.1016/S1002-0721(12)60025-8

Sarno, C., Luisetto, I., Zurlo, F., Licoccia, S., and Di Bartolomeo, E. (2018). Lanthanum chromite based composite anodes for dry reforming of methane. *Int. J. Hydrogen Energy* 43, 14742–14750. doi:10.1016/j.ijhydene.2018.06.021

Sebastian, M. T. (2010). *Dielectric materials for wireless communication*. Amsterdam, Netherlands: Elsevier.

Setz, L. F. G., Santacruz, I., León-Reina, L., De la Torre, A. G., Aranda, M. A. G., Mello-Castanho, S. R. H., et al. (2015). Strontium and cobalt doped-lanthanum chromite: characterisation of synthesised powders and sintered materials. *Ceram. Int.* 41, 1177–1187. doi:10.1016/j.ceramint.2014.09.046

Sfeir, J., Buffat, P. A., Möckli, P., Xanthopoulos, N., Vasquez, R., Joerg Mathieu, H., et al. (2001). Lanthanum chromite based catalysts for oxidation of methane directly on SOFC anodes. *J. Catal.* 202, 229–244. doi:10.1006/jcat.2001.3286

Stambouli, A. B., and Traversa, E. (2002). Solid oxide fuel cells (SOFCs): a review of an environmentally clean and efficient source of energy. *Renew. Sustain. Energy Rev.* 6, 433–455. doi:10.1016/S1364-0321(02)00014-X

Sunarso, J., Hashim, S. S., Zhu, N., and Zhou, W. (2017). Perovskite oxides applications in high temperature oxygen separation, solid oxide fuel cell and membrane reactor: a review. *Prog. Energy Combust. Sci.* 61, 57–77. doi:10.1016/j.pecs.2017.03.003

Takanabe, K., Nagaoka, K., and Aika, K.-I. (2005). Improved resistance against coke deposition of titania supported cobalt and nickel bimetallic catalysts for carbon dioxide reforming of methane. *Catal. Lett.* 102, 153–157. doi:10.1007/s10562-005-5848-4

Zhu, Y., Zhou, W., Yu, J., Chen, Y., Liu, M., and Shao, Z. (2016). Enhancing electrocatalytic activity of perovskite oxides by tuning cation deficiency for oxygen reduction and evolution reactions. *Chem. Mater.* 28, 1691–1697. doi:10.1021/acs.chemmater.5b04457

Zuo, C., Zha, S., Liu, M., Hatano, M., and Uchiyama, M. (2006). Ba(Zr0.1Ce0.7Y0.2)O3-δ as an electrolyte for low-temperature solid-oxide fuel cells. *Adv. Mater.* 18, 3318–3320. doi:10.1002/adma.200601366

Conflict of Interest: The authors declare that the research was conducted in the absence of any commercial or financial relationships that could be construed as a potential conflict of interest.

frontiers in Chemistry

ORIGINAL RESEARCH
published: 01 February 2021
doi: 10.3389/fchem.2020.591322

Hydrogen Oxidation Pathway Over Ni–Ceria Electrode: Combined Study of DFT and Experiment

Yunan Jiang[1], Shuang Wang[1], Jun Xu[2], Minghao Zheng[1], Yi Yang[1], Xiaojun Wu[1,3] and Changrong Xia[1]**

[1] Chinese Academy of Sciences (CAS) Key Laboratory of Materials for Energy Conversion, Department of Materials Science and Engineering, University of Science and Technology of China, Hefei, China, [2] Department of Materials Science and Engineering, University of Science and Technology of China, Hefei, China, [3] Hefei National Laboratory for Physical Science at the Microscale, University of Science and Technology of China, Hefei, China

Ni–ceria cermets are potential anodes for intermediate-temperature solid oxide fuel cells, thanks to the catalytic activity and mixed conductivities of ceria-based materials associated with the variable valence states of cerium. However, the anodic reaction mechanism in the Ni–ceria systems needs to be further revealed. Via density functional theory with strong correlated correction method, this work gains insight into reaction pathways of hydrogen oxidation on a model system of Ni_{10}-CeO_2(111). The calculation shows that electrons tend to be transferred from Ni_{10} cluster to cerium surface, creating surface oxygen vacancies. Six pathways are proposed considering different adsorption sites, and the interface pathway proceeding with hydrogen spillover is found to be the prevailing process, which includes a high adsorption energy of −1.859 eV and an energy barrier of 0.885 eV. The density functional theory (DFT) calculation results are verified through experimental measurements including electrical conductivity relaxation and temperature programmed desorption. The contribution of interface reaction to the total hydrogen oxidation reaction reaches up to 98%, and the formation of Ni–ceria interface by infiltrating Ni to porous ceria improves the electrochemical activity by 72% at 800°C.

Keywords: Ni-ceria cermet, anode reaction kinetics, solid oxide fuel cell, density functional theory, hydrogen spillover

OPEN ACCESS

Edited by:
Dong Ding,
Idaho National Laboratory (DOE), United States

Reviewed by:
Chao Su,
Curtin University, Australia
San Ping Jiang,
Curtin University, Australia
Ling Zhao,
China University of Geosciences Wuhan, China

****Correspondence:***
Changrong Xia
xiacr@ustc.edu.cn
Xiaojun Wu
xjwu@ustc.edu.cn

Specialty section:
This article was submitted to Electrochemistry, a section of the journal Frontiers in Chemistry

Received: *04 August 2020*
Accepted: *28 October 2020*
Published: *01 February 2021*

Citation:
Jiang Y, Wang S, Xu J, Zheng M, Yang Y, Wu X and Xia C (2021) Hydrogen Oxidation Pathway Over Ni–Ceria Electrode: Combined Study of DFT and Experiment. Front. Chem. 8:591322. doi: 10.3389/fchem.2020.591322

INTRODUCTION

As a device that efficiently transfers chemical fuel energy into electricity, solid oxide fuel cell (SOFC) is given a competitive edge in long-term stability, fuel flexibility, and sustainable energy in the future (Ormerod, 2003). One of the key steps in the electrochemical energy conversion process is the fuel oxidation reaction at the anode, where the fuel molecule such as H_2 and CO combines with an oxygen ion $O_O^{\times}$ meanwhile releasing electrons and forming an oxygen ion vacancy $V_O^{\bullet\bullet}$. In the case where hydrogen or reform gas is supplied as the fuel, the hydrogen oxidation reaction at the anode can be written as Equation (1).

$$H_2(g) + O_O^{\times} \rightarrow H_2O(g) + V_O^{\cdot\cdot} + 2e' \quad (1)$$

The equation shows that the anodic reaction usually takes place at the three-phase boundaries (3PB), where the fuel gas, the electrons, and oxygen ions are all available (Sun and Stimming, 2007).

This is the case for the state-of-the-art Ni–yttrium-stabilized zirconia (YSZ) cermet anodes, which have been widely used in intermediate- and high-temperature SOFCs that operate at temperature up to 1,000°C (Horita et al., 2006). In the Ni–YSZ cermet, the reaction occurs only at the Ni–YSZ–gas 3PB since YSZ is a pure oxygen ion conductor that transport oxygen ions and oxygen vacancies while metallic nickel plays the role of both electronic conductor and electrocatalyst.

Different from YSZ, ceria-based oxygen ion conductors also have electronic conductivities due to the facile conversion between Ce^{3+} and Ce^{4+} oxidation states in the anodic conditions of low oxygen partial pressure and high temperature. The variable oxidation state dedicates ceria to catalyze the fuel oxidation reaction and facilitates the formation of additional oxygen vacancies. The character of mixed conductivity makes it possible to electrochemically oxidize the fuel on the ceria surfaces. Thus, replacing zirconia with ceria will extend the reaction sites from 3PB to the whole surface of the cermet anode within the effective reaction zone and consequently increase the electrode performance. In addition, the oxygen ionic conductivities of ceria-based electrolytes such as samaria-doped ceria (SDC) are several times higher than those of zirconia-based electrolytes like YSZ. The high conductivity increases the availability of oxygen ions, thus enlarging the electrochemically effective zone. Comprehensively, compared with Ni–YSZ, ceria-based cermets exhibit much higher anodic activity, especially at intermediate temperatures below 800°C (Kašpar et al., 1999; Fergus, 2006). Besides, when hydrocarbon fuel is supplied to the anode, Ni–ceria cermets show higher resistance to carbon deposition than Ni–YSZ since carbon can be removed through combining with oxygen from ceria due to the capability of changing oxidation states (Ramirez-Cabrera et al., 2000; Laosiripojana et al., 2005).

While Ni–ceria shows many advantages, its anode reaction mechanism is not understood as clearly as that of Ni–YSZ. Hydrogen oxidation occurs only at the 3PB in the system of Ni–YSZ, and the kinetic pathway for such reaction could be subdivided into three parts: hydrogen adsorption on Ni, hydrogen spillover to the Ni–YSZ interface, and water formation and desorption at 3PB (Shishkin and Ziegler, 2009; Cucinotta et al., 2011). For the Ni–ceria cermets, the reaction takes place not only at 3PB but also at the ceria surface due to the higher availability of surface oxygen vacancy. By comparing the electronic properties of Ni–YSZ and Ni–CeO_2 interfaces, Shishkin and Ziegler demonstrate that the formation of the surface vacancy is much easier in the case of Ni–CeO_2, while oxygen vacancy can only exists at 3PB for Ni–YSZ (Shishkin and Ziegler, 2014). Calculation on Ni–CeO_2(111) system reveals that the surface oxygen vacancy is energetically more favored than the interfacial oxygen vacancy (Shishkin and Ziegler, 2010a). Furthermore, Hahn et al. suggest that oxygen vacancy is affected by the position of reduced Ce^{3+} sites in CeO_2 and the quantum number of their occupied *f*-type orbitals (Hahn et al., 2015). Although some properties in Ni–CeO_2 system are studied through theoretical calculations, the overall reaction pathway of hydrogen oxidation is still uncovered. In this work, we adopt density functional theory with strong correlated correction (DFT + U) method to evaluate different molecular pathways of H_2 oxidation on Ni–CeO_2(111) surface. Possible H_2 oxidation mechanisms with different pathways is unveiled and demonstrated systematically. The energetically favored pathway is concluded from theoretical calculations and further shown *via* experimental approaches.

COMPUTATIONAL METHODS

All spin-polarized calculations were accomplished by DFT method implemented in the Vienna *ab initio* simulation package (VASP) (Kresse and Furthmüller, 1996). The generalized gradient approximation (GGA) with the Perdew–Burke–Ernzerhof (PBE) functional was used (Blochl et al., 1994; Perdew et al., 1996; Hammer et al., 1999). To accurately describe the strongly corrected electrons of the localized Ce 4f orbitals, GGA + U with U_{eff} = 5 eV for Ce ions was adopted (Nolan et al., 2005; Andersson et al., 2007). The projector-augmented wave (PAW) method was carried out to deal with the interaction between ionic core electrons and valence electrons with Ce($[Xe]4f^1 5d^1 6s^2$), Ni($[Ar]3d^8 4s^2$), O($1s^2 2s^2 2p^4$), and H($1s^1$) (Blochl et al., 1994; Perdew et al., 1996). The force on atom was smaller than 0.03 eV/Å for the geometric optimization. It was set at 400 eV for the kinetic energy cutoff and the convergence criteria was 10^{-4} eV for the electronic structure calculations. The low-index (111) surface of CeO_2 is the most stable surface, which was selected as the substrate (Conesa, 1995).

On the basis of the Monkhorst–Pack scheme, the Brillouin zone was sampled with a 6 × 6 × 6 *k*-point grid for CeO_2 bulk. The optimized lattice parameter of ceria was 5.437 Å, consistent with the experimental result of 5.411 Å (Kümmerle and Heger, 1999). The CeO_2(111) with a 4 × 4 slab was simulated by using two O–Ce–O triple layers of which atoms in the bottom O–Ce–O layer were fixed as their bulk positions. The thickness of vacuum was set to 15 Å to avoid the interslab interaction between two neighboring slabs along the direction perpendicular to the surface. The Ni_{10} cluster and the bond lengths of the H_2 and O_2 molecules have been previously optimized within a 15-Å cubic box. The evaluated that the bond lengths of the H_2 and O_2 molecule agree with our previous research (Wang et al., 2016). The energy of triple oxygen was utilized for all the calculations. The detailed location of H_2 oxidation reaction and energy of the transition state (TS) were simulated with the climbing image nudged elastic band (CI-NEB) method. In the reaction pathway diagrams (**Figures 3–6**), ΔE_x represents the energy difference of structures between two neighboring reaction stages, which is equal to the energy of the *x*th stage minus the energy of the previous stage. ΔE_{TSx} represents the energy barrier of the transition state.

EXPERIMENTAL

Electrical Conductivity Relaxation Measurement

The reaction kinetics was measured using the electrical conductivity relaxation (ECR) method (Wang et al., 2012). CeO_2 powder was prepared using the carbonate coprecipitation

method with cerium nitrate hexahydrate [$Ce(NO_3)_3{\cdot}6H_2O$, ≥99.9%] as the precursors (Ding et al., 2008). The powder was uniaxially dry pressed under 320 MPa into rectangular bars and sintered at 1,550°C for 5 h in air. The bar density was 96.8%, measured using the Archimedes method. The bar size was about $30.0 \times 5.20 \times 0.52$ mm^3. Ni film was deposited on the bar surface using nickel target (4 N purity, Kejing Materials Technology) by a sputter coater (JFC-1600, JEOL) at 20 mA and under a vacuum of 8 Pa. Afterwards, the bar was heated at a rate of 3°C min^{-1} to 800°C for 2 h in reducing atmosphere to form Ni particles on the bar surface. The deposition was conducted for 20, 40, and 80 s to vary the film thickness and, consequently, the amount of Ni particles per unit area. The surface microstructures were revealed using scanning electron microscopy (SEM, JSM-6700F, JEOL). The area covered by the Ni particles and the length of Ni–CeO_2 boundary were statistically determined using software Image J. The ECR experiments were conducted at 800°C with a digital multimeter (2001-785D, Keithley) using the four-probe technique (Wang et al., 2012). The atmosphere was switched from H_2/Ar (5:95) to H_2/Ar (10:90) to simulate the H_2 oxidation reaction. The gas was humidified within a moisture bottle at room temperature, containing about 3% H_2O, and the gas flowing rate was 200 ml min^{-1}.

Temperature Programmed Desorption/Reduction Tests

The reaction kinetics was further investigated using H_2-temperature programmed desorption (TPD), which was performed using Thermo Electron Corporation TPDRO1100 flow apparatus. The H_2 consumption was measured by a TCD detector. Before the TPD test, a pretreatment process for CeO_2 and Ni–CeO_2 bars was carried out using H_2/N_2 (5:95) gas mixture from room temperature to 150°C. Then, TPD signal was recorded while the samples were blown with N_2 at a flux of 20 ml min^{-1} and heated from room temperature to 1,000°C with a heating rate of 10°C min^{-1}.

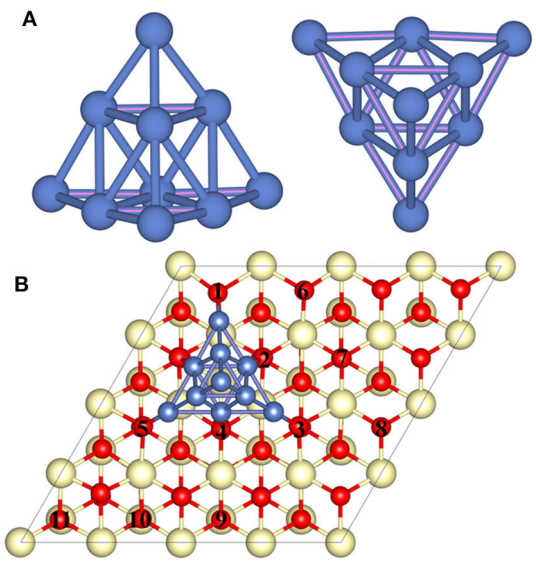

FIGURE 1 | The side and top views of the optimized geometry structure of **(A)** the free-standing Ni_{10} cluster and **(B)** the optimized Ni_{10} cluster placed on the stoichiometric CeO_2(111) with the lowest energy configuration. The dark blue, light yellow, and red balls refer to Ni, Ce, and O atoms, respectively. Numbers 1–5 refer to interface oxygen while 6–11 to surface oxygen.

Electrochemical Measurement

The electrochemical performance was investigated using symmetrical cells composed of YSZ (8 mol% yttria-stabilized zirconia) as the electrolyte substrates and porous CeO_2 impregnated with 8 wt% NiO as the electrodes. Dense YSZ substrates were fabricated by uniaxially pressing the 8 wt% YSZ powder (TZ-8Y, Tosoh Co., Japan) under 320 MPa followed by sintering at 1,500°C for 5 h in air. Porous CeO_2 was prepared using printing and sintering processes. The CeO_2 slurry was prepared by mixing the CeO_2 powder with α-terpineol as solvent and ethyl cellulose as the binder. The slurry was printed on both sides of the YSZ substrates and then heated with the substrates at 1,100°C for 2 h to form symmetric structures with the YSZ electrolyte sandwiched in two porous CeO_2 layers. Nickel was deposited by impregnation process. $Ni(NO_3)_2$ (≥99.9%) was dissolved in a mixture of water and ethanol (1:1 volume ratio) with a concentration of 0.5 mol L^{-1}. The solution was dropped on the porous electrodes, dried and heated at 800°C in air for 1 h to form NiO particles within the porous CeO_2 backbones. NiO was *in situ* reduced to Ni and thus forming the Ni–CeO_2 cermet electrodes. The volume ratio of Ni to CeO_2 was 5.5:100. The Solartron Frequency Response Analyzer 1260 and a Solartron Electrochemical Interface 1287 were used for electrochemical measurements. Ag paste (SRISR DAD-87) was used as electron collector layer, and Ag wires (≥99.9%, Xiyu Electrical and Mechanical Technology) were used to ensure the electronic contact. The frequency range used was from 10^6 to10^{-2} Hz, and the AC amplitude is 10 mV. The impedance was measured in humidified H_2 (∼3% H_2O).

RESULTS AND DISCUSSION

Electron Redistribution at Ni_{10}-CeO_2(111) by Computation

A previous study has revealed that the trigonal pyramid-shaped Ni_{10} cluster with T_d symmetry is the most stable structure (Lu et al., 2011; Song et al., 2011; Rodríguez-Kessler and Rodríguez-Domínguez, 2015), and the low-index (111) surface of CeO_2 is the most stable surface, so that CeO_2(111) surface is selected as the substrate to represent CeO_2 (Conesa, 1995). To simplify the calculation process, the effect of electrochemical environment such as potential is not considered in this work since the real reaction condition is too complicated to simulate precisely. Similar to previous studies of the metal–CeO_2 systems, we focus on the effect of heterogeneous structure of the CeO_2-supported metals, while the diffusion of metal particles is not considered (Kim and Henkelman, 2012; Kim et al., 2012; Kishimoto et al., 2014; Liu et al., 2016). Based on this, the pyramid-shaped Ni_{10} cluster is constructed on the CeO_2(111) surface to illustrate the properties of Ni–CeO_2 cermet for the H_2 reaction process.

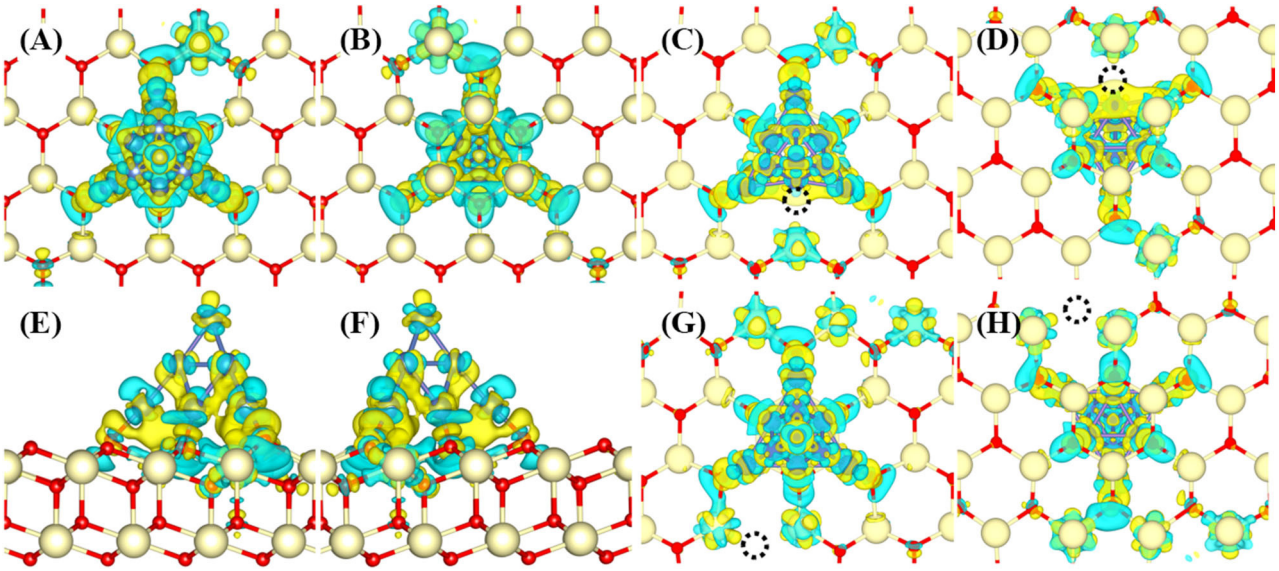

FIGURE 2 | Charge density difference profiles for Ni_{10}-CeO_2(111) **(A–D)** without and **(E–H)** with oxygen vacancy. The views without vacancy are **(A)** from top to bottom, **(B)** from bottom to top, and **(C,D)** side. The views with an interface oxygen vacancy (V4) are **(E,F)** while **(G,H)** refer to surface oxygen vacancy (V10). The views **(E,G)** are from top to bottom while **(F,H)** from bottom to top. The dark blue, light yellow, red balls, and black dotted circle refer to Ni, Ce, O atoms, and oxygen vacancy, respectively. The isosurface value is 0.004 a.u. The yellow and blue colors refer to the positive and negative values, respectively.

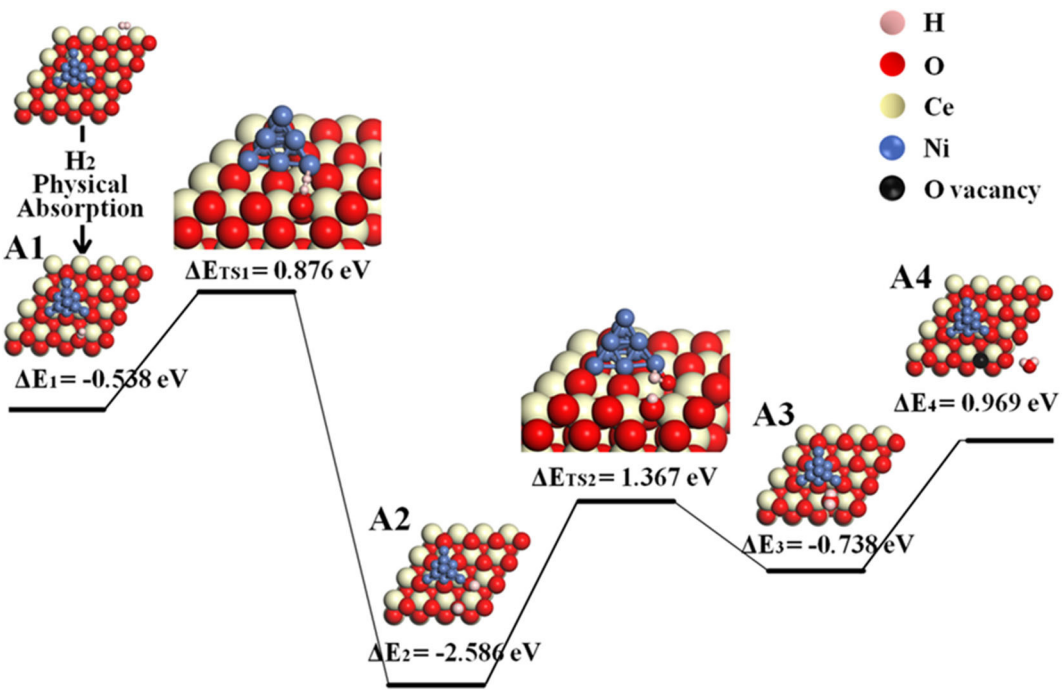

FIGURE 3 | Molecular pathway of H_2 oxidation reaction in Ni_{10}-CeO_2(111) system with hydrogen adsorption on ceria surface and oxidation reaction at 3PB (pathway II).

Various positions for Ni_{10} cluster on CeO_2(111) surface are investigated, and the configuration with the lowest energy is displayed in **Figure 1**, which will be used as the model to study the reaction process.

The interaction between Ni_{10} cluster and CeO_2(111) substrate is essential to elucidate the H_2 oxidation pathways and electrochemical catalytic properties since the charge transfer between Ni_{10} and CeO_2(111) determines the chemical activity of

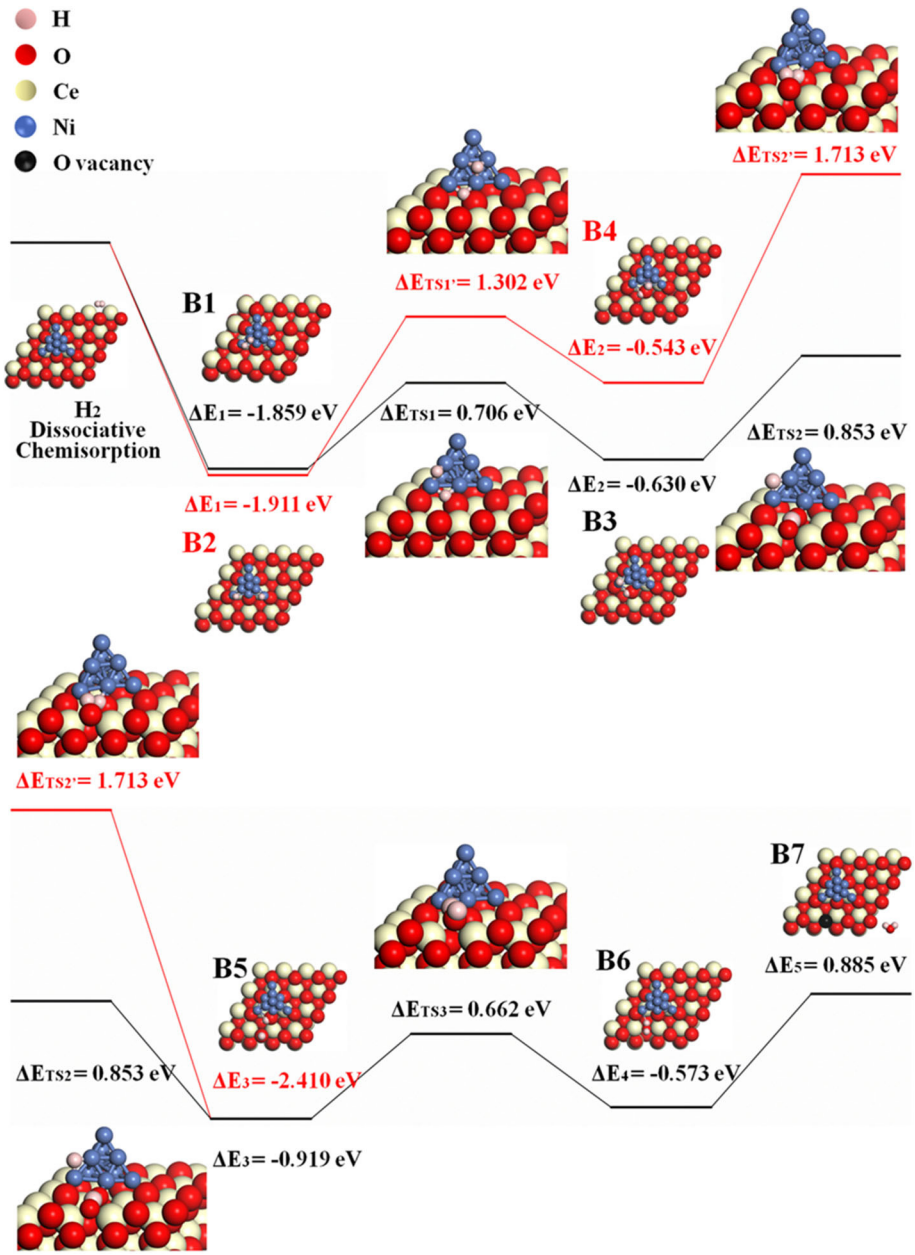

FIGURE 4 | The H-spillover pathways of H_2 oxidation in the Ni_{10}-CeO_2(111) system with hydrogen adsorption on Ni_{10} and oxidation reaction at 3PB (pathway III in black lines and pathway IV in red lines).

the substrate to a great extent. Bader charge analysis indicates that ~1.07 electrons are transferred from Ni_{10} cluster to CeO_2(111) surface (**Supplementary Figure 1**). The redistributed charge density [i.e., the charge density difference between CeO_2(111) with and without Ni_{10} cluster, is displayed in **Figure 2**]. It is found that the valence states of four Ce ions are reduced from Ce^{4+} to Ce^{3+} with three Ce ions under the Ni_{10} cluster and one adjacent to Ni_{10} cluster (**Figures 2A–D**). Such remarkable charge transfer from Ni_{10} cluster to CeO_2(111) surface indicates that there is a strong interaction at the interface between Ni_{10} cluster and CeO_2(111) surface, resulting in a partially positively charged Ni_{10} cluster on negatively charged CeO_2(111) surface. Such structure also indicates that Ni can facilitate the formation of oxygen vacancy on the ceria surface.

It is known that oxygen defects may alter the electronic structure and thus influence the H_2 oxidation reaction (Wu et al., 2015). Similar to previously reported configurations (Shishkin and Ziegler, 2010a,b), two types of oxygen vacancies are investigated (**Supplementary Figure 2**). The first type is the interface oxygen vacancy (labeled as V_4), created by removing

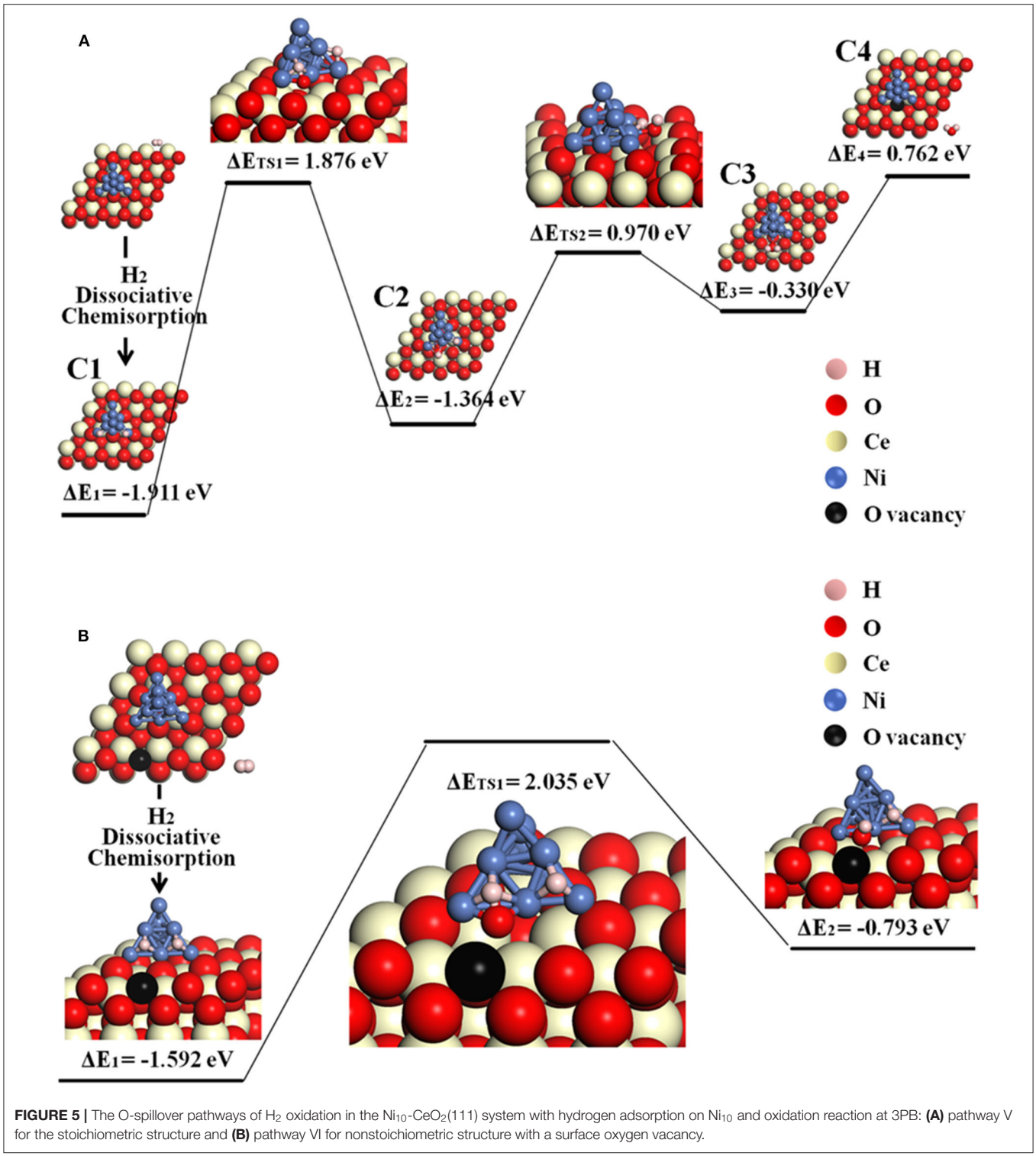

FIGURE 5 | The O-spillover pathways of H_2 oxidation in the Ni_{10}-CeO_2(111) system with hydrogen adsorption on Ni_{10} and oxidation reaction at 3PB: **(A)** pathway V for the stoichiometric structure and **(B)** pathway VI for nonstoichiometric structure with a surface oxygen vacancy.

one oxygen atom at the interface of Ni_{10} and CeO_2. The second type is the surface oxygen vacancy (labeled as V_{10}), formed by removing one oxygen atom at the CeO_2 surface away from Ni_{10}. For model V_4, the Bader charge analysis indicates that about 0.93 electrons are transferred from the Ni_{10} cluster to the CeO_2 surface, which is smaller than that on the perfect CeO_2(111) surface (1.07*e*). Although the presence of interface oxygen vacancy reduces the charge transferred from the Ni_{10} cluster to the CeO_2 surface, still five Ce ions are found to be reduced to lower valences. As illustrated in **Figures 2E,F**,

TABLE 1 | Adsorption energy and highest energy barrier for H_2 oxidation reaction at Ni_{10}-CeO_2 (111) *via* various pathways.

	Adsorption energy (eV)	Highest energy barrier (eV)	Energy Balance (eV)
Pathway I, adsorption and reaction at bare ceria [Wang et al., 2016].	−0.035	2.399	−0.178
Pathway II, adsorption on ceria and reaction at interface	−0.538	1.367	−0.650
Pathway III, adsorption on Ni, hydrogen spillover, and reation at 3PB	−1.859	0.885	−0.875
Pathway IV, adsorption on Ni, hydrogen spillover, and reation at 3PB	−1.911	1.713	−0.875
Pathway V, adsorption on Ni, oxygen spillover, and reation at 3PB	−1.911	1.876	0.003
Pathway VI, adsorption on Ni, oxygen spillover, and reation at 3PB with surface oxygen vacancy	−1.592	2.035	−0.350

the transferred electrons are mainly located at two Ce ions neighboring to the Ni_{10} cluster, and the remaining three Ce ions are underneath the Ni_{10} cluster. However, for model V_{10}, more charges are transferred from the Ni_{10} cluster to the reduced vacancy defect. The Bader charge analysis indicates that about 1.58 electrons are transferred from Ni_{10} cluster to the reduced CeO_2(111) surface with surface oxygen vacancy (V_{10}), which is significantly larger than those on the perfect and oxygen-defected CeO_2(111) surface with an interface oxygen vacancy. The plotted deformation charge density profiles, illustrated in **Figures 2G,H**, show that the transferred electrons are mainly situated on five reduced Ce ions adjacent to the Ni_{10} cluster, and the reduced valence states of three Ce ions underneath the Ni_{10} cluster are negligible. Therefore, both surface and interface oxygen vacancy significantly enhance the reduction in valence state of Ce ions on the surface. Besides, the electronic state of cerium, whether it is at the interface or surface, is obviously affected by the presence of nickel cluster under both conditions of oxygen-nonstoichiometric and perfect crystalline. Accordingly, the electrochemical performance on the ceria surface can be quite different from that at the Ni–ceria interface.

Computational Results of H_2 Oxidation Reaction Pathway on Ni_{10}-CeO_2(111)

Since ceria itself is catalytically active to hydrogen oxidation, the reaction on the Ni–ceria system may proceed in two different situations, one on bare ceria and the other with involvement of Ni. The first pathway (pathway I) occurs on the bare ceria surface, which has been studied in our previous work (Wang et al., 2016). Briefly, pathway I starts with a relatively weak hydrogen adsorption on the oxide surface with the adsorption energy of −0.035 eV. H_2 prefers to be adsorbed in parallel with the stoichiometric CeO_2(111) surface, subsequently dissociating into two hydrogen atoms over surface oxygen atoms while forming two hydroxyl groups by overcoming an energy barrier of 1.073 eV. Finally, the two –OH species form an adsorbed water molecule and a residual oxygen vacancy with an energy barrier of 2.399 eV, which is the most energy-consuming step.

The reaction processes with the participation of Ni are energetically preferred yet more complicated than that on the bare ceria surface. The initial step of hydrogen adsorption may happen either on ceria or Ni. In the first scenario where hydrogen is adsorbed on ceria, the possible reaction route (pathway II) is followed by disassociation of hydrogen molecule at the Ni–ceria interface and H_2O formation at 3PB as shown in the following steps A1–A4, where "sur" indicates ceria surface, and "inter" indicates the Ni–ceria interface.

$$H_2(g) \rightarrow H_2^*(ad, sur) \quad (A1)$$
$$H_2^*(ad, sur) \rightarrow H^*(O-inter) + H^*(O-sur) \quad (A1-A2)$$
$$H^*(O-inter) + H^*(O-sur) \rightarrow H^*(Ni) - OH^*$$
$$(V_O^{\cdot\cdot} - sur) \quad (A2-A3)$$
$$H^*(Ni) - OH^*(V_O^{\cdot\cdot} - sur) \rightarrow H_2O(g) + V_O^{\cdot\cdot}(sur) \quad (A3-A4)$$

According to the calculated results displayed in **Figure 3** for pathway II, the H_2 molecule is physically adsorbed on the ceria surface away from Ni in the first step (A1), with an adsorption energy of −0.538 eV. The H–H bond length of the adsorbed H_2 molecule is 0.754 Å (**Supplementary Figure 3**), slightly larger than the calculated equilibrium bond length of a free H_2 molecule (0.740 Å) (Wang et al., 2016). Then, the adsorbed H_2 dissociates into two separated hydrogen atoms: one adsorbed on interface oxygen, and the other adsorbed on the surface oxygen (A1–A2). This step includes an energy barrier of 0.876 eV, while the total energy difference from A1 to A2 is −1.710 eV, indicating that the formation of two –OH species is exothermic. In the next step, the two adsorbed –OH species combines to form an adsorbed H_2O on Ni_{10} cluster by overcoming a high energy barrier of 1.367 eV (A2–A3). The formation of adsorbed H_2O is endothermic with an energy difference of 0.629 eV. Finally, the adsorbed H_2O molecule is released as gas phase by overcoming an energy barrier of 0.969 eV. In short, the whole molecular pathway gives off 0.650 eV, and the highest energy barrier of this exothermic reaction is 1.367 eV, which is much smaller than 2.399 eV for the H_2 oxidation reaction on the bare CeO_2(111) (Wang et al., 2016).

In the second scenario, hydrogen is adsorbed on nickel rather than ceria in the initial step. According to a previous research, Ni not only functions as electron acceptor but also catalyzes the dissociation of hydrogen molecule into atoms. The hydrogen atoms formed on the Ni surface may spill over to the surface of oxides such as zirconia (Anderson and Vayner, 2006; Shishkin and Ziegler, 2009), LnO_x (Ln = Dy, Ho, Er, Yb, and Tb) (He et al., 2011), and gadolinia-doped ceria (Babaei et al., 2009).

The possible H-spillover pathway involves hydrogen adsorption and disassociation on Ni, hydrogen spillover, and water formation. The proposed steps are summarized as B1–B7.

$$H_2(g) \rightarrow H^{1*}(Ni) + H^{2*}(Ni) \quad (B1/B2)$$
$$H^{1*}(Ni) + H^{2*}(Ni) \rightarrow H^{1*}(O-inter)$$
$$+H^{2*}(Ni) \quad (B1-B3/B2-B4)$$
$$H^{1*}(O-inter) + H^{2*}(Ni) \rightarrow H^{1*}(O-inter)$$
$$+H^{2*}(O-sur) \quad (B3-B5/B4-B5)$$
$$H^{1*}(O-inter) + H^{2*}(O-sur) \rightarrow H^{1*}(O-inter)$$
$$-OH^{2*}(V_O^{\cdot\cdot}) \quad (B5-B6)$$
$$H^{1*}(O-inter) - OH^{2*}(V_O^{\cdot\cdot}) \rightarrow H_2O(g) + V_O^{\cdot\cdot} \quad (B6-B7)$$

Because H_2O may form either at the ceria surface or at 3PB of Ni–ceria–gas interface, two possible H-spillover pathways are distinguished as illustrated in **Figure 4**. Pathway III is labeled with black line, which proceeds with steps of B1, B3, and B5–B7, while red line refers to pathway IV that goes through B2, B4, and B5–B7. Both initial structures are dissociated H_2 molecule on the Ni_{10} cluster surface (B1/B2). In pathway III, one dissociative H (H^1) atom is adsorbed on the edge between the top and interlayer of Ni_{10} cluster, while the other H (H^2) atom is adsorbed on the edge between the interlayer and contact layer of Ni_{10} cluster (B1). Then, H^1 slightly moves and combines with an interface oxygen near the Ni_{10} cluster, while H^2 spills over to the ceria surface away from the Ni_{10} cluster to combine with a surface oxygen. Thus, two hydroxyl groups are generated in this process, overcoming an energy barrier of 0.853 eV (B3–B5). After that, H^1 is attracted to the hydroxyl group containing H^2, forming one H_2O molecule (B5–B6) and a surface oxygen vacancy (B6–B7) with energy barriers of 0.662 and 0.885 eV, respectively. In pathway IV, H atoms are adsorbed on two edges between the interlayer and the contact layer of Ni_{10} cluster in structure B2, which is slightly more stable than structure B1. In the following steps, H atoms migrate from the Ni_{10} cluster to the ceria surface and react with the oxygen atoms at interface and surface to form two –OH species, overcoming the energy barriers of 1.302 and 1.713 eV, respectively. In general, pathway III (black line) is more favorable compared to pathway IV (red line), since the highest energy barrier for pathway III (0.885 eV for B6–B7) is much lower than that for pathway IV (1.713 eV for B4–B5).

The possible O-spillover pathways include hydrogen adsorption and dissociation on Ni, oxygen spillover from ceria to Ni cluster, and formation of H_2O molecule, summarized as C1–C4 and illustrated in **Figure 5A** for pathway V.

$$H_2(g) \rightarrow H^{1*}(Ni) + H^{2*}(Ni) \quad (C1)$$
$$O(inter) \rightarrow O^*(Ni) + V_O^{\cdot\cdot}(inter), O^*(Ni)$$
$$+H^{1*}(Ni) \rightarrow OH^{1*}(Ni) \quad (C2)$$
$$H^{2*}(Ni) + OH^{1*}(Ni) \rightarrow H_2O(Ni) \quad (C2-C3)$$
$$H_2O(Ni) \rightarrow H_2O(g) \quad (C3-C4)$$

The initial structure C1 is for the disassociation of hydrogen molecule. In the following step, an oxygen atom at the Ni_{10}-CeO_2 interface spill overs from the oxide surface toward the metal cluster, then reacts with the hydrogen atom to form a hydroxyl group while leaving an interface oxygen vacancy (C1–C2). This is the most energy-consuming step, as it contains the highest energy barrier of 1.876 eV. Next, the hydroxyl group reacts with H atom, forming an adsorbed H_2O on the Ni_{10} cluster by overcoming an energy barrier of 0.970 eV (C2–C3). In the final step, it consumes 0.762 eV to release the adsorbed H_2O molecule to the gas phase. As a whole, this O-spillover process is endothermic with a negligible energy of 0.003 eV, and the rate-limiting process is H_2 oxidation.

Besides, the situation where an oxygen vacancy is created on the ceria surface is also considered, as illustrated in **Figure 5B** for pathway VI. In this case, the adsorption energy for the first step (H_2 disassociation on Ni_{10} cluster) is −1.592 eV, which is less stable than the C1 structure. Next, interface O atom migrates to the Ni surface and reacts with one H atom to form an –OH species by overcoming a large energy barrier of 2.035 eV. Doubtlessly, it takes more energy to achieve a O-spillover step when a surface oxygen vacancy exists on the ceria.

In conclusion, six possible pathways are proposed for the oxidation reaction on the Ni–ceria system. Pathway I takes place on the bare ceria surface and is entirely unrelated to the Ni–ceria interface. The other five pathways are all 3PB related since the reaction steps are either linking directly to the interface oxygen atoms (positions 1–5 in **Figure 1**) or to the surface oxygen atoms (positions 6–11 in **Figure 1**), noting that surface atoms are also affected by the nickel cluster as mentioned in the previous discussion. In addition, the surface atoms in our Ni–CeO_2(111) model at the atomic scale could be regarded as the interface atoms in real electrochemical system, since the electrode is often characterized in a much larger scale such as nanoscale. Thus, it is reasonable to treat pathways II–VI as the possible reaction processes for the hydrogen oxidation reaction at the Ni–ceria interface while only pathway I as the pathway on the ceria surface.

Table 1 lists the hydrogen adsorption energy, highest energy barrier, and total energy balance of each pathway. The hydrogen adsorption energy differs enormously depending on the location. The energy for adsorption on bare ceria in pathway I is only −0.035 eV, while the adsorption energy in the Ni_{10} cluster in pathways III, IV, and V are around −1.9 eV. Besides, the adjacent Ni_{10} cluster in pathway II promptly increases the adsorption energy on the surface site, from −0.035 to −0.538 eV. Thus, the enhancement of hydrogen adsorption by Ni particles is quite obvious. Among the five pathways related to the Ni–ceria interface, the molecular pathway (pathway II) and the two H-spillover pathways (pathways III and IV) are all finished with formation of a surface oxygen vacancy rather than interface oxygen vacancy. Energetically speaking, pathway III is more favored than pathways II and IV. The highest energy barrier in pathway III is only 0.885 eV, about two-thirds of pathway II and one-half of pathway IV, while the energy balance is the lowest, −0.875 eV. In contrast, the highest energy barriers in pathways V and VI proceeding with oxygen spillover are more than twice as large as that in pathway III. Besides, the energy balance of pathway V

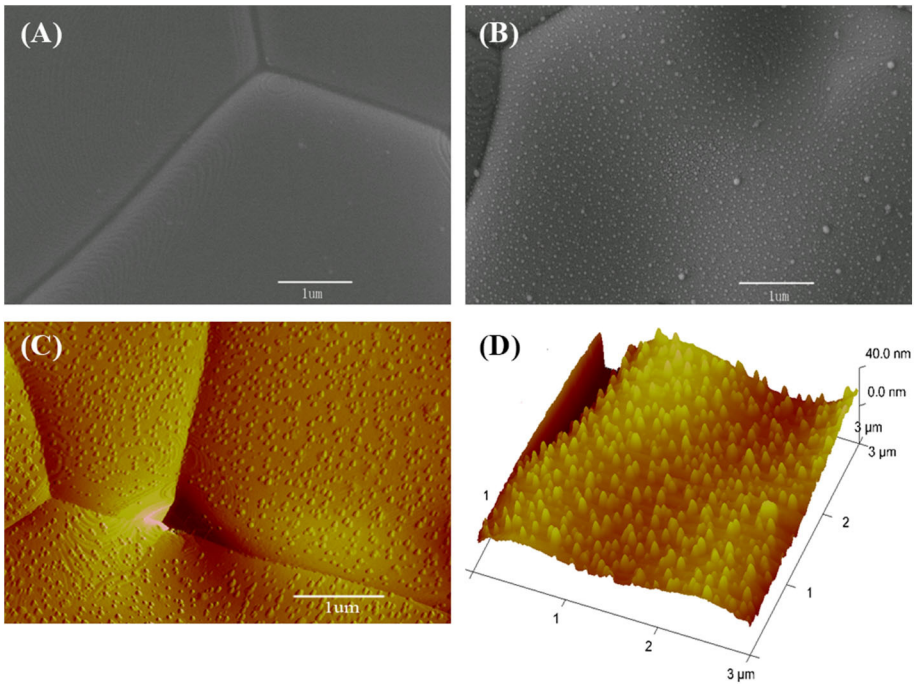

FIGURE 6 | Surface micrographs for **(A)** scanning electron microscopy (SEM) view of a bare CeO_2 bar, **(B)** SEM, **(C)** atomic force microscopy (AFM), and **(D)** three-dimensional AFM pictures for the bar with Ni particles prepared by 40 s deposition.

(0.003 eV) is contradictory to the thermodynamic prediction. Consequently, the oxygen spillover pathways rarely contribute to the overall anodic reaction, as they are unlikely to occur.

It is noted that the mechanism of hydrogen oxidation for Ni–CeO_2 system is quite different from that for Ni–YSZ system, although both are controlled by the reaction at 3PB. For Ni–YSZ, the energetically favored pathway is hydrogen spillover from Ni to the Ni–YSZ interface with formation of an interface vacancy, while hydrogen spillover from the interface to YSZ surface with formation of a surface vacancy is very unfavorable because interfacial vacancy formation is much easier than the latter (Shishkin and Ziegler, 2014). However, due to facile formation of the surface vacancy at the CeO_2(111) surface, the hydrogen oxidation for the Ni–CeO_2 system tends to proceed with hydrogen spillover to the CeO_2(111) surface and finish with the formation of a surface oxygen vacancy. This result is obvious for the energetically most favored route (pathway III).

As a result, assumption could be made that the reaction rate for interface process that mainly occurs following pathway III should be much higher than that for the ceria surface of pathway I, although both of them could exist in practical situations. Besides, the contribution from the surface reaction to the total electrode reaction could be very small, and the total reaction rate may be controlled by the interface length (i.e., the length of 3PB). The surface and interface reaction rates and their contributions will be further compared in *Experimental*, with the perspective of reaction kinetics.

Experimental Results and Discussion

The hydrogen oxidation reaction catalyzed by ceria can be represented using Kroger–Vink notations as

$$\mathbf{H_2\,(g) + O_O^{\times} + 2Ce_{Ce}^{\times}(Ce^{+4}) \rightarrow H_2O\,(g) + V_O^{\cdot\cdot} + 2Ce_{Ce}'(Ce^{+3})} \quad (2)$$

Equation (2) can also be considered as the ceria reduction reaction. Comparing Equations (1, 2), it is found that the ceria reduction reaction is equivalent to the anodic H_2 oxidation reaction (Wang et al., 2012). Thus, ECR method is adopted to simulate the anodic reaction. By increasing the H_2 partial pressure, the equilibrium in Equation (2) shifts toward the right. Meanwhile, Ce^{4+} is reduced to Ce^{3+}, and the conductivity increases. The conductivity change is tested with dense bar samples.

The CeO_2 bar consists of grains several micrometers in size (**Figure 6A**). When Ni is deposited, the surface clearly presents fine particles (**Figure 6B**). These fine particles are Ni as formed in the sputtering–heating process, in which the sputtering results in a thin nickel film while the heating turns the film into particles. The fine particles are isolated and evenly distributed. The non-connected Ni particles do not influence the ground conductivity of the ceria bar. The Ni particle number per unit area increases with the sputtering time (**Supplementary Figure 4**). The diameter and vertical height of Ni particles are about 20 and 13 nm, respectively, as shown from the three-dimensional AFM pictures (**Figures 6C,D**).

Figure 7 shows the curves of normalized conductivity measured at 800°C. The surface H_2 oxidation reaction rate for the

bare CeO_2 is very slow as the re-equilibrium time is over 12,000 s, which is much longer than that of doped ceria, about 7,000 s (Wang et al., 2013). When Ni particles are deposited on the ceria surface, however, the re-equilibrium time is sharply reduced. Besides, the re-equilibrium appears to be faster for the sample with longer deposition time of Ni. The re-equilibrium times for samples with 20, 40, and 80 s deposition are 2,171, 1,520, and 426 s, respectively. The accelerated re-equilibrium demonstrates enhanced surface reaction kinetics caused by Ni particles. The process of conductivity relaxation consists of the surface reaction to form oxygen ion vacancy and bulk diffusion of oxygen ions. Since the reaction is dominated by the surface process, the ECR data can be fitted with following formula (Yasuda and Hikita, 1994; Wang et al., 2013).

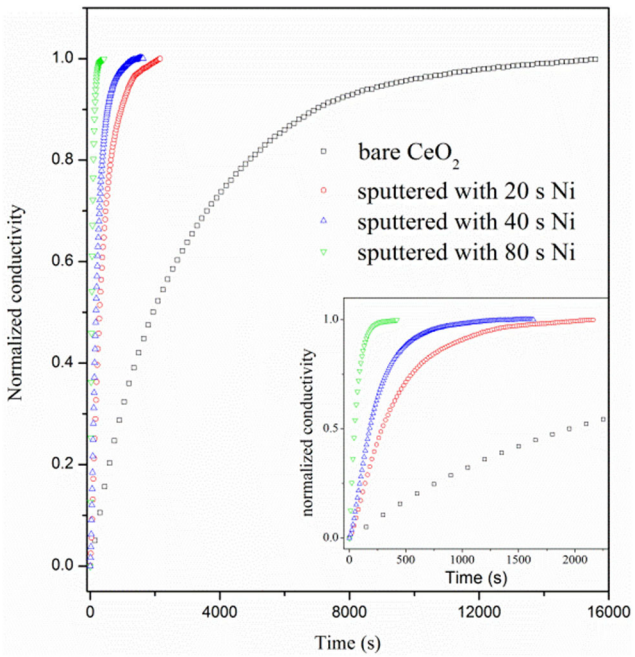

FIGURE 7 | Normalized conductivity curves vs. relaxation time for bare CeO_2 and CeO_2 with Ni particles, which are prepared by 20, 40, and 80 s deposition.

$$\frac{\sigma(t)-\sigma(0)}{\sigma(\infty)-\sigma(0)} = 1-\exp\left(-\frac{k_{chem}t}{a}\right) \quad (3)$$

where k_{chem} is the chemical surface exchange coefficient, which quantitatively represents the reaction rate of Equation (1), and the fitted k_{chem} values are listed in **Supplementary Table 1**. $\sigma(0)$ and $\sigma(\infty)$ are the equilibrated conductivities at the initial and final time of the relaxation curve. a is a constant and numerically equals half of the bar sample thickness. k_{chem} is 0.72×10^{-5} cm s^{-1} for the bare CeO_2 at 800°C, which equals to the reaction rate constant for hydrogen reduction on ceria surface, k_{ceria}. When Ni sputter is conducted for 20, 40, and 80 s, the k_{chem} dramatically increases to 6.03×10^{-5}, 10.3×10^{-5}, and 39.1×10^{-5} cm s^{-1}, respectively, proving that the surface reaction rate is remarkably accelerated by the involvement of Ni particles.

Physically, k_{chem} is contributed by the reaction on the bare ceria surface and the reaction related to the Ni particles, k_{Ni}

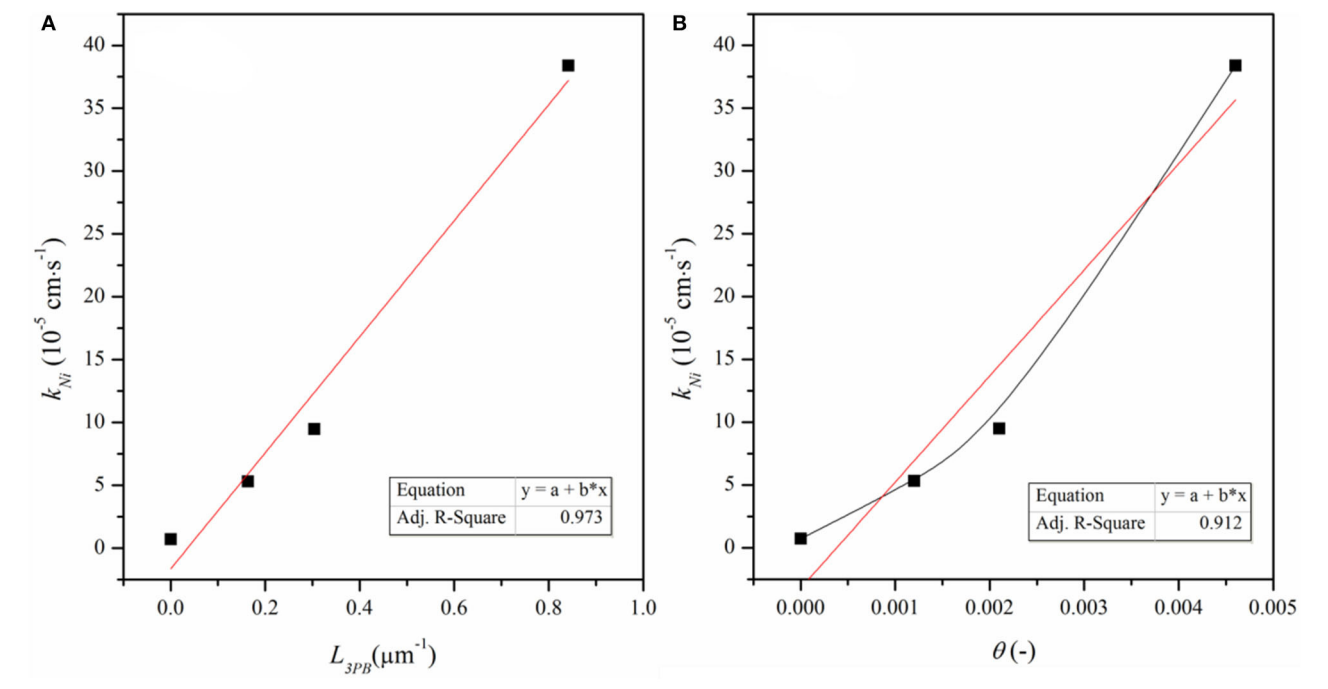

FIGURE 8 | k_{Ni} as a function of **(A)** density of 3PB (L_{3PB}) and **(B)** surface coverage of Ni particles, (θ).

(Wu et al., 2015)

$$k_{Ni} = k_{chem} - K_{ceria}(1-\theta) \quad (4)$$

k_{Ni} represents the nickel effect on the reaction, θ is the surface coverage of the Ni particles and $(1-\theta)$ is surface fraction of the bare ceria (**Supplementary Table 1**). **Figure 8** shows k_{Ni} as a function of θ and L_{3PB}, the length of Ni–CeO_2 interface (i.e., the length of 3PB boundaries). k_{Ni} increases linearly with L_{3PB}, suggesting that k_{Ni} represents the reaction that is limited by the step occurring at/near the Ni–CeO_2 interface rather than on the Ni–gas surface. According to the DFT analysis, the hydrogen reduction reactions are mostly favored by hydrogen-spillover-based pathway III, which is also limited to the Ni–CeO_2-gas 3PB. Thus, the DFT approach agrees well with the ECR conclusion that the Ni-related reaction mainly occurs at/near the Ni–CeO_2-gas 3PB.

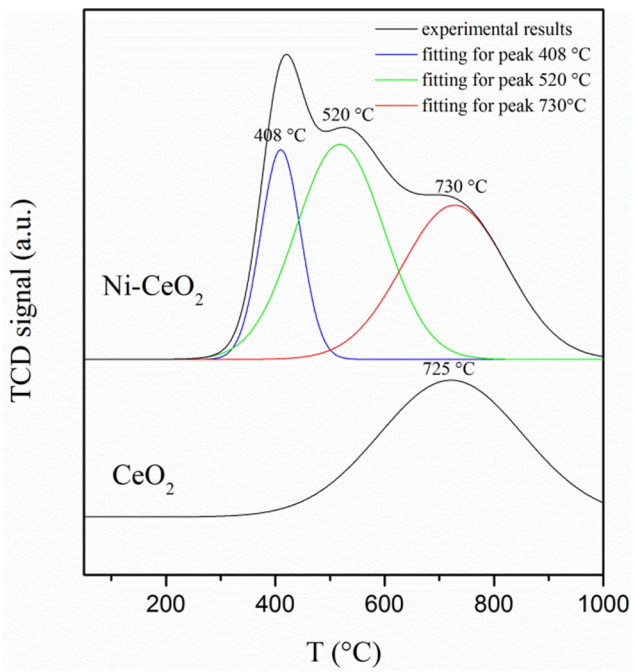

FIGURE 9 | Hydrogen temperature programmed desorption profiles for CeO_2 and Ni–CeO_2 powders.

According to the discussion based on DFT calculation, both reactions at the Ni-ceria interface and on the ceria surface may contribute to the H_2 oxidation. Under the ECR experimental conditions, the reaction rate constant k_{Ni} for H_2 oxidation at the interface is much higher than that on the ceria surface k_{ceria} (**Supplementary Table 1**). In addition, $\frac{k_{Ni}}{k_{ceria}}$ increases with L_{3PB} since a higher 3PB density means more active sites for the catalytic reaction. The highest $\frac{k_{Ni}}{k_{ceria}}$ value is about 53, demonstrating that the interface reaction is dominant although surface reaction exists. The ECR derived faster reaction rate at the interface than on the surface and is well-supported by the lower energy barrier in pathway III than pathway I as obtained by the DFT calculation.

The hydrogen adsorption/desorption on the ceria surface and Ni–ceria interface is compared with hydrogen-TPD measurement (**Figure 9**). The desorption curve for bare ceria shows only one desorption peak, which shows that the hydrogen desorption/adsorption on the ceria surface begins at about 450°C and reaches its highest rate at 725°C. Quite differently, the curve for the Ni-ceria includes two additional peaks at 408 and 520°C. These two peaks must be attributed to the adsorption on Ni particles. The additional adsorption on Ni as demonstrated with TPD analysis is well-consistent with the high adsorption energy for Ni_{10}-CeO_2(111) obtained from DFT calculation.

The electrochemical performance is compared with symmetrical cell using YSZ as the electrolyte substrates. **Figure 10** shows the impedance spectra measured at 800°C, where the response corresponding to the ohmic resistance is deducted to compare the electrode response clearly. The interfacial polarization resistance is 3.18 and 0.88 Ω cm^2 for

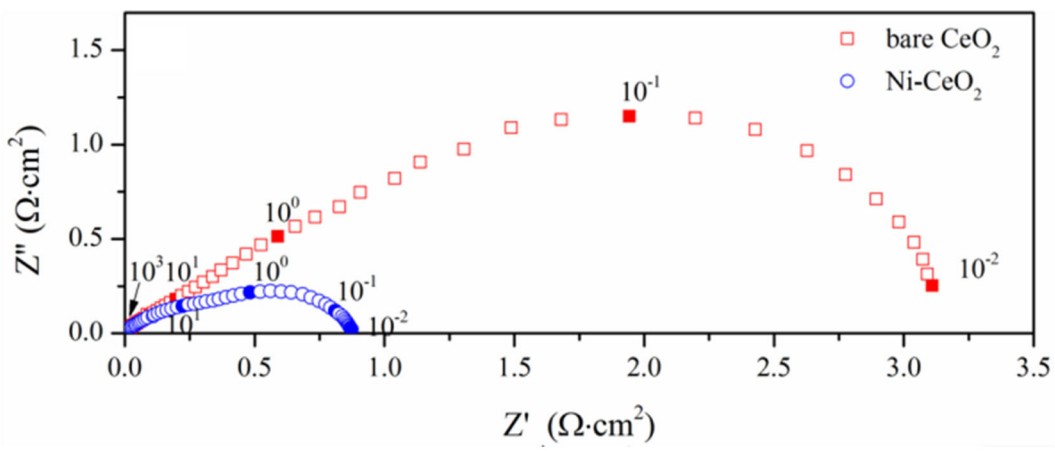

FIGURE 10 | Impedance spectra measured at 800°C.

the ceria and Ni-ceria electrodes, respectively. The reaction at the porous ceria electrode takes place at the ceria surface, while the Ni-ceria electrode provides additional reaction sites at the Ni-ceria interface. Since only 5.5% Ni is infiltrated to porous ceria to form the Ni-ceria electrode, the difference in electrode polarization resistance could roughly be attributed to the interface considering that the two electrodes have almost the same electronic conductivities and pore structures. Thus, the presence of the Ni-ceria interface in this work improves the electrochemical performance by 72.3%, proving that 3PB dominates the electrode reaction on Ni-ceria cermet anodes, which is possibly associated with the improved hydrogen adsorption capability and reduced energy barrier for hydrogen reduction.

CONCLUSION

Both theoretical calculations and experiments are conducted regarding Ni–CeO_2 as anode material for SOFCs. Via DFT + U computations, charge transfer between Ni_{10} cluster and CeO_2(111) surface proves the synergistic effects existing in the Ni-ceria system. Then, five possible hydrogen oxidation pathways over the Ni–CeO_2 electrode are proposed, including different sites for adsorption and reaction to evaluate the effects of Ni on CeO_2(111) surface. The results demonstrate that nickel can largely enhance H_2 adsorption on the ceria surface and lowers the energy barrier for disassociated hydrogens to combine with a surface oxygen of CeO_2 and form H_2O. The highest energy barrier decreases from 2.399 eV on pure CeO_2 to 0.885 eV at the Ni–CeO_2 interface in pathway III with hydrogen spillover mechanism, which can be concluded as the most energetically favored pathway. Furthermore, experimental results are found to be consistent with the theoretical calculations. ECR experiments demonstrate that surface reaction rate k_{Ni} increases linearly with the density of 3PB, and 98% of the total hydrogen oxidation is contributed by interface reaction at 3PB. H_2-TPD measurements also show enhanced hydrogen adsorption caused by Ni, as two additional and stronger desorption peaks appear at lower temperatures compared to bare ceria. Finally, EIS of ceria and Ni-ceria electrodes are measured to compare the electrochemical performance. The interfacial polarization resistance is remarkably reduced from 3.18 Ω cm^2 for pure ceria electrode to 0.88 Ω cm^2 for Ni-ceria electrode at 800°C.

DATA AVAILABILITY STATEMENT

The original contributions presented in the study are included in the article/**Supplementary Materials**, further inquiries can be directed to the corresponding author/s.

AUTHOR CONTRIBUTIONS

CX and XW conceived of the idea, designed the calculations and experiments, and analyzed the data. YJ and MZ carried out the electrochemical experiments. JX conducted the characterizations. SW performed the theoretical calculations. YY participated in the discussion of the results. YJ and SW wrote the paper. All authors commented on the manuscript.

FUNDING

The financial supports are from the National Natural Science Foundation of China (51972298) and Anhui Estone Materials Technology Co., Ltd. (2016340022003195).

ACKNOWLEDGMENTS

We gratefully acknowledge the financial supports from the National Natural Science Foundation of China (51972298) and Anhui Estone Materials Technology Co., Ltd. (2016340022003195). We acknowledge the Supercomputing Center of University Science and Technology of China for providing computational resources.

SUPPLEMENTARY MATERIAL

The Supplementary Material for this article can be found online at: https://www.frontiersin.org/articles/10.3389/fchem.2020.591322/full#supplementary-material

REFERENCES

Anderson, A. B., and Vayner, E. (2006). Hydrogen oxidation and proton transport at the Ni–zirconia interface in solid oxide fuel cell anodes: quantum chemical predictions. *Solid State Ionics* 177, 1355–1359. doi: 10.1016/j.ssi.2006.05.032

Andersson, D. A., Simak, S., Johansson, B., Abrikosov, I., and Skorodumova, N. V. (2007). Modeling of ce o 2, ce 2 o 3, and ce o 2– x in the lda+ u formalism. *Phys. Rev. B* 75:035109. doi: 10.1103/PhysRevB.75.035109

Babaei, A., Jiang, S. P., and Li, J. (2009). Electrocatalytic promotion of palladium nanoparticles on hydrogen oxidation on Ni/GDC anodes of SOFCs via spillover. *J. Electrochem. Soc.* 156, B1022–B1029. doi: 10.1149/1.3156637

Blochl, P. E., Jepsen, O., and Andersen, P. (1994). Improved tetrahedron method for Brillouin-zone integrations. *Phys. Rev. B Condensed Matter* 49, 16223–16233. doi: 10.1103/PhysRevB.49.16223

Conesa, J. (1995). Computer modeling of surfaces and defects on cerium dioxide. *Surface Sci.* 339, 337–352. doi: 10.1016/0039-6028(95)00595-1

Cucinotta, C. S., Bernasconi, M., and Parrinello, M. (2011). Hydrogen oxidation reaction at the Ni/YSZ anode of solid oxide fuel cells from first principles. *Phys. Rev. Lett.* 107:206103. doi: 10.1103/PhysRevLett.107.206103

Ding, D., Liu, B., Zhu, Z., Zhou, S., and Xia, C. (2008). High reactive Ce0. 8Sm0. 2O1. 9 powders via a carbonate co-precipitation method as electrolytes for low-temperature solid oxide fuel cells. *Solid State Ionics* 179, 896–899. doi: 10.1016/j.ssi.2007.11.015

Fergus, J. W. (2006). Electrolytes for solid oxide fuel cells. *J. Power Sources* 162, 30–40. doi: 10.1016/j.jpowsour.2006.06.062

Hahn, K. R., Seitsonen, A. P., Iannuzzi, M., and Hutter, J. (2015). Functionalization of CeO2 (1 1 1) by deposition of small Ni clusters: effects on CO_2 adsorption and O vacancy formation. *ChemCatChem* 7, 625–634. doi: 10.1002/cctc.201402906

Hammer, B., Hansen, L. B., and Nørskov, J. K. (1999). Improved adsorption energetics within density-functional theory using revised Perdew-Burke-Ernzerhof functionals. *Phys. Rev. B* 59:7413. doi: 10.1103/PhysRevB.59.7413

He, B., Wang, W., Zhao, L., and Xia, C. (2011). Ni–LnOx (Ln= Dy, Ho, Er, Yb and Tb) cermet anodes for intermediate-temperature solid oxide fuel cells. *Electrochim. Acta* 56, 7071–7077. doi: 10.1016/j.electacta.2011.05.117

Horita, T., Kishimoto, H., Yamaji, K., Xiong, Y., Sakai, N., Brito, M. E., et al. (2006). Materials and reaction mechanisms at anode/electrolyte interfaces for SOFCs. *Solid State Ionics* 177, 1941–1948. doi: 10.1016/j.ssi.2006.01.013

Kašpar, J., Fornasiero, P., and Graziani, M. (1999). Use of CeO_2-based oxides in the three-way catalysis. *Catalysis Today* 50, 285–298. doi: 10.1016/S0920-5861(98)00510-0

Kim, H. Y., and Henkelman, G. (2012). CO oxidation at the interface between doped CeO_2 and supported Au nanoclusters. *J. Phys. Chem. Lett.* 3, 2194–2199. doi: 10.1021/jz300631f

Kim, H. Y., Lee, H. M., and Henkelman, G. (2012). CO oxidation mechanism on CeO_2-supported Au nanoparticles. *J. Am. Chem. Soc.* 134, 1560–1570. doi: 10.1021/ja207510v

Kishimoto, H., Suzuki, A., Shimonosono, T., Nishi, M., Yamaji, K., Brito, M. E., et al. (2014). Effect of the oxide substrate on the nickel particle properties. *Solid State Ionics* 262, 403–406. doi: 10.1016/j.ssi.2014.01.004

Kresse, G., and Furthmüller, J. (1996). Efficient iterative schemes for ab initio total-energy calculations using a plane-wave basis set. *Phys. Rev. B* 54:11169. doi: 10.1103/PhysRevB.54.11169

Kümmerle, E., and Heger, G. (1999). The structures of C–Ce_2O_3+ δ, Ce_7O_{12}, and $Ce_{11}O_{20}$. *J. Solid State Chem.* 147, 485–500. doi: 10.1006/jssc.1999.8403

Laosiripojana, N., Sutthisripok, W., and Assabumrungrat, S. (2005). Synthesis gas production from dry reforming of methane over CeO_2 doped Ni/Al_2O_3: influence of the doping ceria on the resistance toward carbon formation. *Chem. Eng. J.* 112, 13–22. doi: 10.1016/j.cej.2005.06.003

Liu, B., Zhao, Z., Henkelman, G., and Song, W. (2016). Computational design of a CeO_2-supported Pd-based bimetallic nanorod for CO oxidation. *J. Phys. Chem. C* 120, 5557–5564. doi: 10.1021/acs.jpcc.6b00253

Lu, Q. L., Luo, Q., Chen, L., and Wan, J. (2011). Structural and magnetic properties of Ni n (n = 2–21) clusters. *Eur. Phys. J.* 61, 389–396. doi: 10.1140/epjd/e2010-10129-8

Nolan, M., Grigoleit, S., Sayle, D. C., Parker, S. C., and Watson, G. W. (2005). Density functional theory studies of the structure and electronic structure of pure and defective low index surfaces of ceria. *Surface Sci.* 576, 217–229. doi: 10.1016/j.susc.2004.12.016

Ormerod, R. M. (2003). Solid oxide fuel cells. *Chem. Soc. Rev.* 32, 17–28. doi: 10.1039/b105764m

Perdew, J. P., Burke, K., and Ernzerhof, M. (1996). Generalized gradient approximation made simple. *Phys. Rev. Lett.* 77:3865. doi: 10.1103/PhysRevLett.77.3865

Ramirez-Cabrera, E., Atkinson, A., and Chadwick, D. (2000). The influence of point defects on the resistance of ceria to carbon deposition in hydrocarbon catalysis. *Solid State Ionics* 136, 825–831. doi: 10.1016/S0167-2738(00)00507-5

Rodríguez-Kessler, P., and Rodríguez-Domínguez, A. (2015). Stability of Ni clusters and the adsorption of CH4: first-principles calculations. *J. Phys. Chem. C* 119, 12378–12384. doi: 10.1021/acs.jpcc.5b01738

Shishkin, M., and Ziegler, T. (2009). Oxidation of H2, CH4, and CO molecules at the interface between nickel and yttria-stabilized zirconia: a theoretical study based on DFT. *J. Phys. Chem. C* 113, 21667–21678. doi: 10.1021/jp905615c

Shishkin, M., and Ziegler, T. (2010a). The electronic structure and chemical properties of a Ni/CeO2 anode in a solid oxide fuel cell: A DFT+ U study. *J. Phys. Chem. C* 114, 21411–21416. doi: 10.1021/jp105316p

Shishkin, M., and Ziegler, T. (2010b). Hydrogen oxidation at the Ni/yttria-stabilized zirconia interface: a study based on density functional theory. *J. Phys. Chem. C* 114, 11209–11214. doi: 10.1021/jp1030575

Shishkin, M., and Ziegler, T. (2014). Direct modeling of the electrochemistry in the three-phase boundary of solid oxide fuel cell anodes by density functional theory: a critical overview. *Phys. Chem. Chem. Phys.* 16, 1798–1808. doi: 10.1039/C3CP53943A

Song, W., Lu, W.-C., Wang, C., and Ho, K. (2011). Magnetic and electronic properties of the nickel clusters Nin (n < 30). *Comput. Theoret. Chem.* 978, 41–46. doi: 10.1016/j.comptc.2011.09.028

Sun, C., and Stimming, U. (2007). Recent anode advances in solid oxide fuel cells. *J. Power Sources* 171, 247–260. doi: 10.1016/j.jpowsour.2007.06.086

Wang, S., Zheng, M., Li, M., Wu, X., and Xia, C. (2016). Synergistic effects towards H_2 oxidation on the Cu–CeO_2 electrode: a combination study with DFT calculations and experiments. *J. Mater. Chem. A* 4, 5745–5754. doi: 10.1039/C6TA00732E

Wang, Y., Wang, Y., and Xia, C. (2012). Surface process of doped ceria reduction by electrical conductivity relaxation. *J. Electrochem. Soc.* 159, F570–F576. doi: 10.1149/2.037209jes

Wang, Y., Zhu, Z., and Xia, C. (2013). Hydrogen oxidation at metal–ceria boundary by electrical conductivity relaxation method. *Electrochem. Commun.* 36, 10–13. doi: 10.1016/j.elecom.2013.08.026

Wu, X.-P., Gong, X.-Q., and Lu, G. (2015). Role of oxygen vacancies in the surface evolution of H at CeO_2 (111): a charge modification effect. *Phys. Chem. Chem. Phys.* 17, 3544–3549. doi: 10.1039/C4CP04766D

Yasuda, I., and Hikita, T. (1994). Precise determination of the chemical diffusion coefficient of calcium-doped lanthanum chromites by means of electrical conductivity relaxation. *J. Electrochem. Soc.* 141, 1268–1273. doi: 10.1149/1.2054908

Conflict of Interest: The authors declare that this study received funding from the National Natural Science Foundation of China (51972298) and Anhui Estone Materials Technology Co., Ltd. (2016340022003195). The funders were not involved in the study design, collection, analysis, interpretation of data, the writing of this article, or the decision to submit it for publication.

frontiers in Energy Research

ORIGINAL RESEARCH
published: 21 April 2021
doi: 10.3389/fenrg.2021.609534

Numerical Study on the Performance of a Cogeneration System of Solid Oxide Fuel Cell Based on Biomass Gasification

Zheng Dang[1], Zhaoyi Jiang[2], Jinyan Ma[1,2], Xin Shen[1,2] and Guang Xi[1]*

[1] Department of Fluid Machinery and Engineering, School of Energy and Power Engineering, Xi'an Jiaotong University, Xi'an, China, [2] Department of Civil Engineering, School of Human Settlement and Civil Engineering, Xi'an Jiaotong University, Xi'an, China

In order to solve the environmental pollution problem caused by winter heating of rural residential building in northern of China, in this paper a biomass gasification (BG)-solid oxide fuel cell (SOFC) combined heat and power (CHP) system has been establishedand numerically investigated. Taking a rural village around Xi'an which is an ancient city and located at central of northern China as the study object, according to heat and electricity output of the system and the heating and electrical load characteristics of the residential building of village, the energy saving ratio and economical efficiency of the CHP system under three different operation schemes compared with the traditional energy system have been analyzed. The results show that the operation scheme for heating designated rooms in rural buildings and meeting the average heat demand of users is the most energy-efficient and economical way. The primary energy saving rate and annual cost saving rate can reach 18.0% and 10.3%, respectively. When the user's heat and power load demand is clear, the closer the system's output heat and power ratio to the user's heat and power load ratio, the more significant the system's energy saving effect.

Keywords: biomass gasification, solid oxide fuel cell, combined heat and power system, operation scheme, performance analysis

OPEN ACCESS

Edited by:
Dong Ding,
Idaho National Laboratory (DOE), United States

Reviewed by:
Aleksey Yaremchenko, University of Aveiro, Portugal
Lei Bi, University of South China, China

****Correspondence:***
Zheng Dang
zdang@mail.xjtu.edu.cn

Specialty section:
This article was submitted to Fuel Cells, a section of the journal Frontiers in Energy Research

Received: *28 September 2020*
Accepted: *30 March 2021*
Published: *21 April 2021*

Citation:
Dang Z, Jiang Z, Ma J, Shen X and Xi G (2021) Numerical Study on the Performance of a Cogeneration System of Solid Oxide Fuel Cell Based on Biomass Gasification. Front. Energy Res. 9:609534. doi: 10.3389/fenrg.2021.609534

INTRODUCTION

With the intensification of global warming trends, increasing pressure on environmental protection, and the increasing scarcity of fossil energy sources, the use of renewable energy is becoming more and more popular in the world, which has become one of the promising energy sources supporting the sustainable development of human society. At present, there is generally

Abbreviations: PE*, total energy consumption of traditional system/kW· h; PE, total energy consumption of the CHP system/kW· h; σ_D , TER of user side; σ_{CHP} , TER of CHP system; $\eta_{th,B}$, boiler thermal efficiency; $\eta_{el,CHP}$, generation efficiency of CHP system; $\eta_{th,CHP}$, thermal efficiency of CHP system; $\eta_{el,PP}$, power plant efficiency; ΔP_{el}, user purchases electricity from the grid/kW; ξ_{el}, electricity traditional coefficient; ξ_{th}, heat traditional coefficient; C_{Sep}, the annual cost of using the traditional system/yuan; C_{CHP}, the annual cost of using the CHP system/yuan; C_{el}, local grid purchase price/yuan·kW^{-1}·h^{-1}; C_h, heat price when using waste heat boiler/yuan·kW^{-1}·h^{-1}; C_{inv}, initial investment cost of the traditional system/yuan; E_{el}, user's electricity consumption/kW·h; E_h, user's heat consumption/kW·h; R, capital recovery factor; i, annual interest rate; L, equipment life cycle; C_{Bio}, price of biomass fuel/yuan·kg^{-1}; C_B , cost of biomass required by the system/yuan; C_{invest} , initial investment cost of the CHP system/yuan; $C_{O\&M}$, system operation and maintenance costs (take 4% of initial installation costs); H_{Bio} , heating value of biomass fuel/kJ·kg^{-1}.

no advanced heating technology in rural of China. So far, distributed burning of coal is the main heating method for rural residential building, which has caused severe environmental pollution problems. For rural or remote places of northern of China, where buildings are not concentrated and traditional energy supply method for building is inefficient, therefore it is urgent to find an efficient and clean space heating techniques for this kind of rural buildings. On the other hand, there are a lot of biomass resources (mainly straw) in northern China, after the harvesting of crops how to deal with a large amount of straw become a big problem. In the past years, straw is often burning in the field, but now it is forbidden by the government because of the heavy air pollution. As we know, straw is a kind of biomass and biomass energy is a form of renewable energy. Generally, biomass energy is gotten through photosynthesis of plants by which solar energy is converted into chemical energy and stored in the body of biomass. Based on the heating technology needs in rural of northern of China, it is very important to seek to use straw as fuel for heating system development (Chen and Zhu, 2018; Yan et al., 2020).

Zhou et al. (2019) built a system of combined heating of solar energy and biomass energy with rural housing as a platform, and compared it with solar energy and auxiliary electric heating system to get good comfort and energy saving of the system. Zhang et al. (2017) built a biogas-based internal combustion engine CHP system, combined with rural user-side demand and supplemental heat sources, established a full-operation dynamic mathematical model, and conducted daily energy supply and demand balance analysis of the system throughout the year. The results show that the primary energy utilization rate of the system is 37.58%, compared with the traditional system, the primary energy saving rate is 17.12%. Li Y. et al. (2015) established a micro gas turbine CHP system, and analyzed the impact of the user's heat to power ratio (TER) and grid power purchase ratio on the energy saving potential of the CHP under the condition that the unit matched the user's load. The energy saving rate can reach 22.76%∼23.16%. Cong et al. (2018) analyzed the feasibility of applying biomass pyrolysis cogeneration technology in rural areas. The results show that the cogeneration technology is suitable for small central heating of about 200 households. The initial investment is generally not more than 3 million yuan, the investment recovery period is 4–5 years. Li G. et al. (2015) proposed a heating system based on a biomass particles forming fuel furnace, and compared with the traditional kang heating system. The results show that the heating effect of this system is better under intermittent heating conditions. Chen et al. (2014) used technical and economical analysis methods to compare two schemes for centralized heating and household heating of BG in a rural suburb of Tianjin, and gave the heating optimization plan for the village. Zhou et al. (2014) conducted an economical and environmental benefit analysis of the rural BG decentralized heating technology. The results show that the heating costs can be reduced to a reasonable level by means of segmented temperature control, temperature control in separate rooms, and energy-saving building renovation. From the above review of previous researches it can be concluded that, in northern of China, the utilization of rural biomass resources mainly includes the conversion of other biomass products into related energy products, direct combustion to provide heat, and combined use as fuel of cogeneration system. Among them, the development and utilization of biomass cogeneration technology has gradually become the main trend. However, in these works, heat engines are still used as the prime mover with exhaust pollution induced by burning.

Fortunately SOFC is a kind of device which can convert the chemical energy of fuel into electricity directly by electrochemical reaction and without burning process. If hydrogen is used as fuel the exhaust of SOFC is just water. If hydrocarbons including biomass are reformed, desulfurized, and fed as fuel, the exhaust of SOFC will still has zero oxynitride. Therefore SOFC is relatively more efficient, environmentally friendly than traditional burning system. In general straw can be used as a fuel for SOFC operation after a gasification and reforming process to construct rural building combined heat and power generation systems.

Different biomass raw materials and gasification gas production under different conditions will affect the performance of SOFC. Dey et al. (2014) studied the influence of different types of biomass raw materials on the BG-SOFC system, and the results showed that bagasse showed the best performance in the mixed system. Amiri et al. (2018) simulated the impact of fuel changes on the performance of the co-generation system by considering various fuel sources (such as natural gas, biogas, and syngas). The results show that fuel changes may seriously affect the consistency of the overall performance index of the system. All ideal results are obtained with a single fuel, so progressive multivariate and multi-objective optimization is required. Wan (2016) by integrating the gasification unit with the supercritical water unit to produce clean syngas for SOFC, the integrated system can achieve a power generation efficiency of 46.3%. Palomba et al. (2017) proposed a 630 kWh lignocellulose gasification solid oxide fuel cell cogeneration system simulation model. The results show that the primary energy consumption of the cogeneration system can be reduced by about 15 GW · H/y, CO_2 emission reduction is about 5,000 t/y. Jia et al. (2015) conducted energy analysis of the integration process of biomass gasification and SOFC, and gave a performance comparison of power systems for different gasification agents through thermodynamic method. The results show that when oxygen-enriched air is used as the gasification agent, the gasifier has the largest loss, and the total efficiency of the cogeneration is 29%. When steam is used as the gasification agent, the heat exchanger has the largest loss. The net electrical efficiency and efficiency of the system are 40 and 36%, respectively, which are higher than the efficiency when using oxygen-enriched air as the gasifying agent. Giarola et al. (2018) studied the energy efficiency indicators and economic performance of wastewater treatment facilities equipped with SOFC-CHP devices. Compared with traditional alternatives, they developed an optimization framework. The results show that both investment costs and operating costs of the combined supply system used in wastewater treatment

plants are reduced. Rokni (2018) proposed a solid oxide fuel cell absorption refrigeration tri-generation system based on municipal waste gasification. The system can maintain itself and does not need to rely on the grid for district heating and cooling. The results show that its system energy efficiency has exceeded 83%.

The researches in above literatures showed that SOFC has high power generation efficiency and can be accompanied by high-quality waste heat. As a prime mover of the distributed multi-supply system, it can effectively improve the efficiency of energy use and reduce energy consumption. At the same time, due to its higher operating temperature, hydrocarbon can be used as fuel, so they have a wide range of fuel adaptability. However, most of the researches are only focused on the performance and optimization of the SOFC-CHP system itself, but scarce work has been done to consider the characteristic of the heat and electrical load of particular building especially for the rural residential building of northern of China. Therefore, based on the actual demand situation in rural of northern of China, this paper designs and determines a BG-SOFC-CHP with a power generation of 100 kW for rural residential building around Xi'an City. Combining the heat and electricity output of the system and the heat and power load characteristics of rural buildings, analyze the advantages of this CHP system in terms of energy saving and economy compared to the traditional energy system under three different operating schemes. The results and conclusion will benefit the development of clean and efficient space heating techniques of rural residential building for northern of China.

SYSTEM CONSTRUCTION

System Model

Figure 1 shows the flowchart of the CHP system. The system mainly includes two parts: the biomass gasification part and the solid oxide fuel cell part. First of all, for the biomass gasification module, biomass is pyrolyzed and gasified to generate combustible gas, which is used as fuel to be introduced into the anode of SOFC. Since the operating pressure of the biomass gasification process is much greater than that of the solid oxide fuel cell, the produced gas is purified by desulfurization and other purification treatments and then decompressed through an expander. The outlet pressure of the expander is set to be consistent with the operating pressure of SOFC. Heat required for the gasification process is completely provided by the burner after SOFC stack. For the SOFC part, the gasification gas is mixed with the water pressurized by the water pump, and then is heated to the required inlet temperature of the SOFC by the hot exhaust gas from the burner. After being pressurized, air is also heated by the hot exhaust gas from the burner. Finally fuel and air are fed into anode and cathode of SOFC for electrochemical reaction to generate electricity. After two heat exchangers, the exhaust gas still has a relatively high temperature, and this

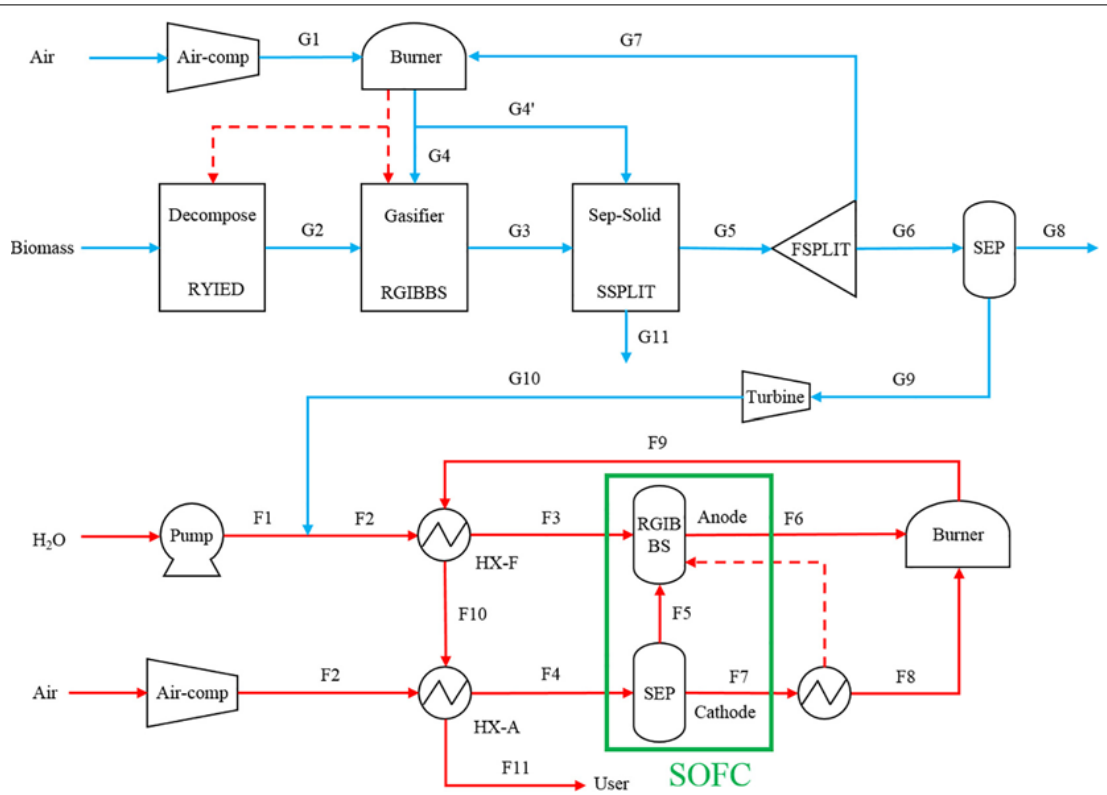

FIGURE 1 | BG-SOFC-CHP system flowchart. F, fuel; G, gas; HX, heat exchanger; SEP, separator; COMP, compressor; RGIBBS, Gibbs reactor.

part of the heat is recovered to provide space heating and hot water for living.

Chemical and Electrochemical Model

The fuel is natural gas, chemical reactions mainly include methane reforming and shift reaction as follows:

$$CH_4 + H_2O \rightarrow CO + 3H_2 \tag{1}$$

$$CO + H_2O \rightarrow CO_2 + H_2 \tag{2}$$

Because the rate of the oxidation reaction of carbon monoxide is much slower than that of the water vapor shift reaction, therefore, the oxidation reaction of carbon monoxide is ignored in the present research. The electrochemical reactions occurring at the anode and cathode of the SOFC are as follows:

Anode:

$$H_2 + O^{2-} \rightarrow H_2O + 2e^- \tag{3}$$

Cathode:

$$\frac{1}{2}O_2 + 2e^- \rightarrow O^{2-} \tag{4}$$

Total chemical reaction:

$$H_2 + \frac{1}{2}O_2 \rightarrow H_2O \tag{5}$$

For the methane reforming reaction rate, the Achenbach model is used to describe it (Achenbach, 1994):

$$r_{ref} = k_{CH_4} p_{CH_4} \exp\left(\frac{-E_{CH_4}}{RT}\right) \tag{6}$$

Here: k_{CH4}—reaction rate coefficient of CH_4/kJ·mol^{-1}; P_{CH4}—partial pressure of CH_4/bar;.E_{CH4}—activation energy of CH_4/mol·m^{-2}·bar^{-1}·s^{-1}.

For the water vapor shift reaction, because of its fast reaction rate, it can be considered that it reaches equilibrium quickly, and the equilibrium constant satisfies:

$$k_{shift} = \exp\left(-\frac{\Delta G}{RT}\right) = \frac{n_{CO_2} \cdot n_{H_2}}{n_{CO} \cdot n_{H_2O}} \tag{7}$$

Here: n_x—molar flow rate of component x/mol·s^{-1}; R—Gas mole constant/J·mol^{-1}·K^{-1}; T—Gas temperature /K.

Assuming that there is no volume change work during the electrochemical reaction process, that is, all the energy released by the chemical reaction is output in the form of electrical work, the maximum output work is equal to the Gibbs free energy change of the chemical reaction, which can be expressed as follows:

$$P_{max} = -\Delta G = n_e \cdot F \cdot E_N \tag{8}$$

Here: ΔG—Gibss free energy change of total cell reaction/W; n_e—The number of electrons transferred in a electrochemical reaction; F—Faraday constant/96485C·mol^{-1}; E_N—Nernst electromotive force/V.

Put into the cell reaction Eq. 5, the Nernst electromotive force can be expressed as:

$$E_N = -\frac{\Delta G_0}{n_e F} - \frac{RT}{n_e F} \cdot \ln\left[\frac{p_{H_2O}}{p_{H_2} \cdot \left(p_{O_2}\right)^{\frac{1}{2}}}\right] \tag{9}$$

Here: ΔG—Standard Gibbs Free Enthalpy Change/W; T—Reaction temperature/K; R—Universal gas constant/8.314J·mol^{-1}·K^{-1}; P_i—Partial pressure of each component /bar.

The current of the SOFC can be expressed as:

$$I = 2n_{H_2,consume} \cdot F \tag{10}$$

Here: $n_{H2,consume}$—The equivalent amount of hydrogen consumed/mol·s^{-1}.

The current density of the SOFC can be expressed as:

$$j = I/A \tag{11}$$

Here: A—Effective area of cell unit /m^2.

The output power can be expressed as:

$$P_{SOFC} = V_{cell} \cdot I = V_{cell} \cdot j \cdot A \tag{12}$$

Here: V_{cell}—Output voltage of fuel cell /V.

Loss Model

The voltage loss of SOFC mainly includes ohmic loss, activation loss and concentration loss. The ohmic loss is caused by the resistance of each component when the current flows through the components of the cell unit; the activation loss is caused by the lag of the electrochemical reaction on the electrode surface; the concentration loss is caused by the pressure drop on the porous electrodes. Considering that the concentration loss mainly plays a significant role under the high current density, and this research mainly focuses on the normal current density, the influence of the concentration loss is ignored in this paper. The final output voltage of the SOFCcan be expressed as follows:

$$V_{cell} = E_N - \underbrace{I \cdot \sum R_{ohm}}_{\sum \eta_{ohm}} - \underbrace{j \cdot \left(R_{act,a} + R_{act,c}\right)}_{\sum \eta_{act}} \tag{13}$$

Here: $R_{act,a}$—Equivalent activation resistance of anode/Ω·m^2; $R_{act,c}$—The equivalent activation resistance of the cathode/Ω·m^2.

The calculation of cell ohmic loss can be expressed as follows:

$$\sum \eta_{ohm} = I \cdot \sum R_{ohm} = I \cdot \sum \frac{\rho_i \cdot \delta_i}{S} = \frac{I}{S} \cdot \sum \rho_i \cdot \delta_i = j \cdot \sum \frac{\delta_i}{\sigma_i} \tag{14}$$

Here: ρ_i—Resistivity/Ω·m; δ_i—Electrode thickness/m; S—Effective area of cell/m^2; σ_i—Conductivity/Ω^{-1}·m^{-1}, The conductivity calculation formula of each component is shown in **Table 1**.

The calculation of activation loss refers to Achenbach's model, which is expressed as follows:

$$\frac{1}{R_{act,a}} = \frac{2F}{RT} \cdot k_A \cdot \left(\frac{p_{H_2}}{p^0}\right)^m \exp\left(\frac{-E_A}{RT}\right) \tag{15}$$

TABLE 1 | Conductivity of SOFC components (Braun, 2002).

Parts of the SOFC	Conductivity/$\Omega^{-1}\cdot m^{-1}$
Anode	$(95 \times 10^6/T)\exp(-1150/T)$
Cathode	$(42 \times 10^6/T)\exp(-1200/T)$
Electrolyte	$(3.34 \times 10^4/T)\exp(-10300/T)$
Connector	$(9.3 \times 10^6/T)\exp(-1100/T)$

$$\frac{1}{R_{act,c}} = \frac{4F}{RT} \cdot k_C \cdot \left(\frac{p_{O_2}}{p^0}\right)^m \exp\left(\frac{-E_C}{RT}\right) \tag{16}$$

Here: k_A—Activation coefficient of anode/A·m^2; k_C—Activation coefficient of cathode/A·m^2; E_A—Activation energy of anode/kJ·mol^{-1}; E_C—Activation energy of cathode/kJ·mol^{-1}; m—index /0.25.

Mathematical Model of Other Equipments

Compressor, water pump model.

The compressor and water pump pressurize the reactants to reach the pressure required for system operation. In this study, the method of isentropic compression is used. The power consumption of these devices during operation can be calculated by the following formula:

$$W = \frac{n}{n-1} RT_1 \left(1 - \pi^{\frac{n-1}{n}}\right) \tag{17}$$

Here: W—Power consumption of equipment/W; n—Polytropic index; T_1—Inlet temperature of compressor/K; π—Compression ratio.

Heat exchanger model.

The heat exchanger in this study uses a counter flow heat exchanger, and its thermodynamic calculation model is mainly based on the heat transfer equation and the energy balance equation, expressed as follows:

Heat transfer equation:

$$Q = k \cdot A \cdot \Delta t \tag{18}$$

Energy balance equation:

$$Q = q_{m1} c_1 \left(t_1^{'} - t_1^{''}\right) = q_{m2} c_2 \left(t_2^{'} - t_2^{''}\right) \tag{19}$$

Here: Q—Heat flow rate/kW; k—Heat transfer coefficient/W·m^{-2}·℃$^{-1}$; A—Heat exchanger area/m^2; Δt—Average heat exchange temperature difference/℃; q_{m1},q_{m2}—Mass flow of cold and hot fluid/kg·s^{-1}; c_1,c_2—specific heat capacity of cold and hot fluid/J·kg^{-1}·℃$^{-1}$; t_1',t_1''—Inlet and outlet temperature of cold fluid/℃; t_2',t_2''—Inlet and outlet temperature of hot fluid/℃.

Burner model.

In the SOFC system, the remaining fuel in the anode outlet and the excess air in the cathode outlet enter the combustion chamber again for full combustion. In this paper, it is assumed that the combustion chamber is under adiabatic conditions with no heat loss, and all remaining fuel in the anode tail gas reacts completely.

In the combustion chamber, the main components that can participate in the reaction are CH_4, H_2 and CO. The reaction equation of each component is as follows:

$$CH_4 + 2O_2 \rightarrow CO_2 + 2H_2O \tag{20}$$

$$H_2 + \frac{1}{2}O_2 \rightarrow H_2O \tag{21}$$

$$CO + \frac{1}{2}O_2 \rightarrow CO_2 \tag{22}$$

According to the mass conservation equation and energy conservation equation, the gas entering and leaving the combustion chamber satisfies the following relationship:

$$\sum n_{x,in} \cdot h_x(T_{in}) = \sum n_{x,out} \cdot h_x(T_{out}) \tag{23}$$

Here: $n_{x,in}$—The molar flow rate of component$_x$at the inlet of the combustion chamber/mol· s^{-1}; $n_{x,out}$—The molar flow rate of component$_x$at the outlet of the combustion chamber/mol· s^{-1}; T_{in}—Combustor inlet temperature/K; T_{out}—Outlet temperature of combustor /K.

Thermal storage tank model.

TABLE 2 | 100 kW BG-SOFC-CHP system parameters.

Parameters	Value
Biomass import flow/kg·h^{-1}	60
Material inlet temperature/℃	15
Air inlet flow (gasification)/kg·h^{-1}	137.26
Vaporization temperature/℃	900
Vaporization pressure/MPa	0.4
Combustion chamber exhaust gas split ratio/G4	0.3
Gasification recovery rate/G7	0.414
Expander outlet pressure/MPa	0.13
S/C	1
λ	3
Fuel cell system operating pressure/MPa	0.13
Anode inlet temperature/℃	800
Cathode inlet temperature/℃	850
SOFCoutlet temperature/℃	1112
Heat exchange of fuel heat exchanger/kW	26.44
Air heat exchanger heat exchange/kW	142.07
SOFC effective area/m^2	36
Current density/A·m^{-2}	3569
The output voltage/V	0.753
Exhaust temperature/℃	60
Net generating power/kW	100
Recovery of waste heat/kW	138
TER of system	1.38
Cell efficiency/%	47.29
System generation efficiency/%	39.45
System thermal efficiency/%	54.41
Cogeneration efficiency/%	93.86

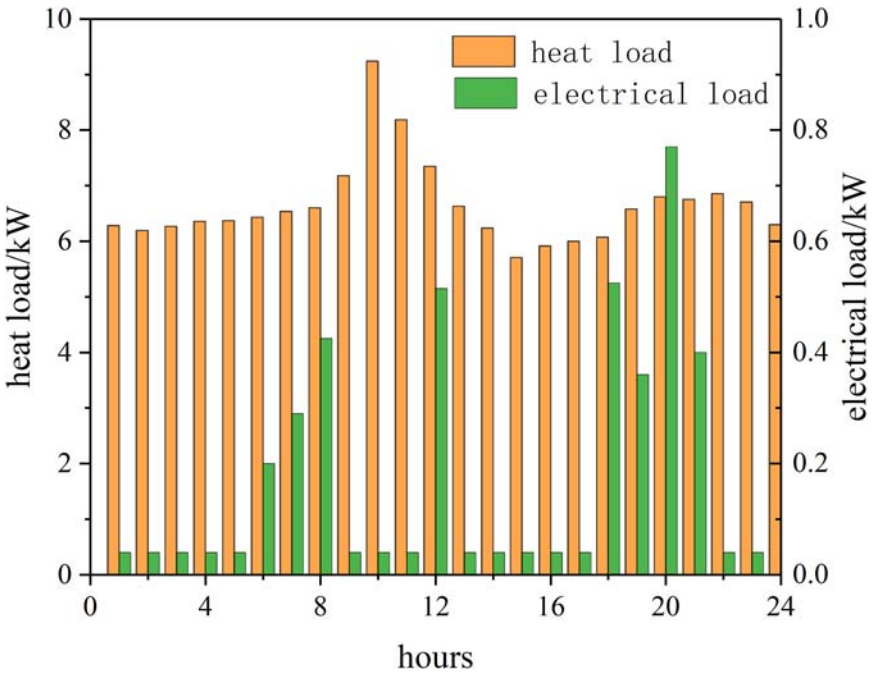

FIGURE 2 | Typical daily heat load and electric load in winter.

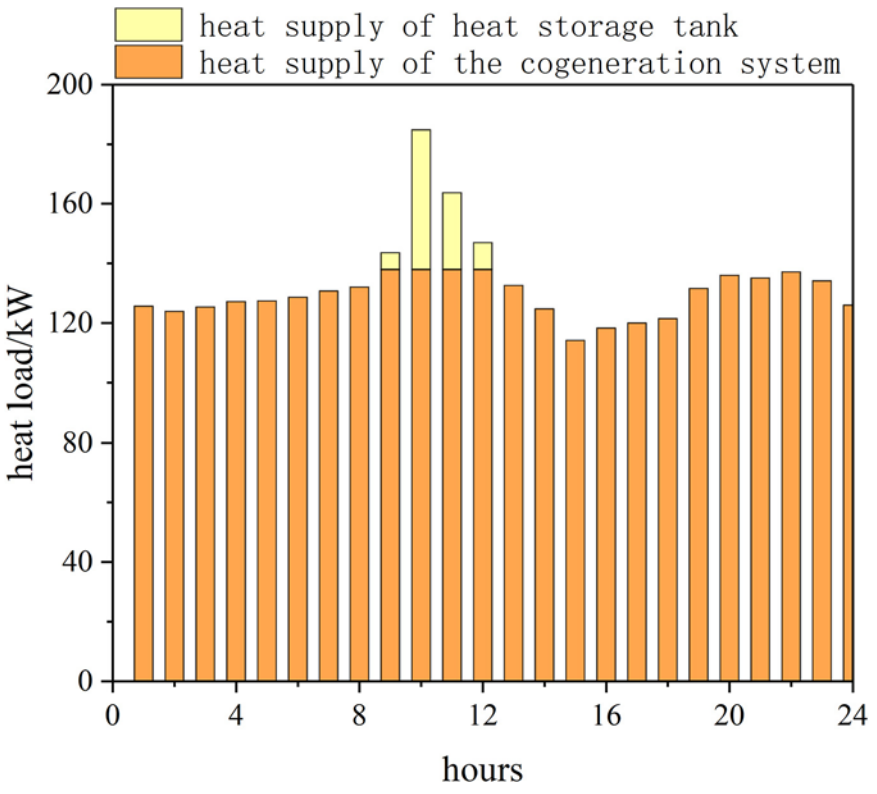

FIGURE 3 | Thermal energy supply on a typical winter day.

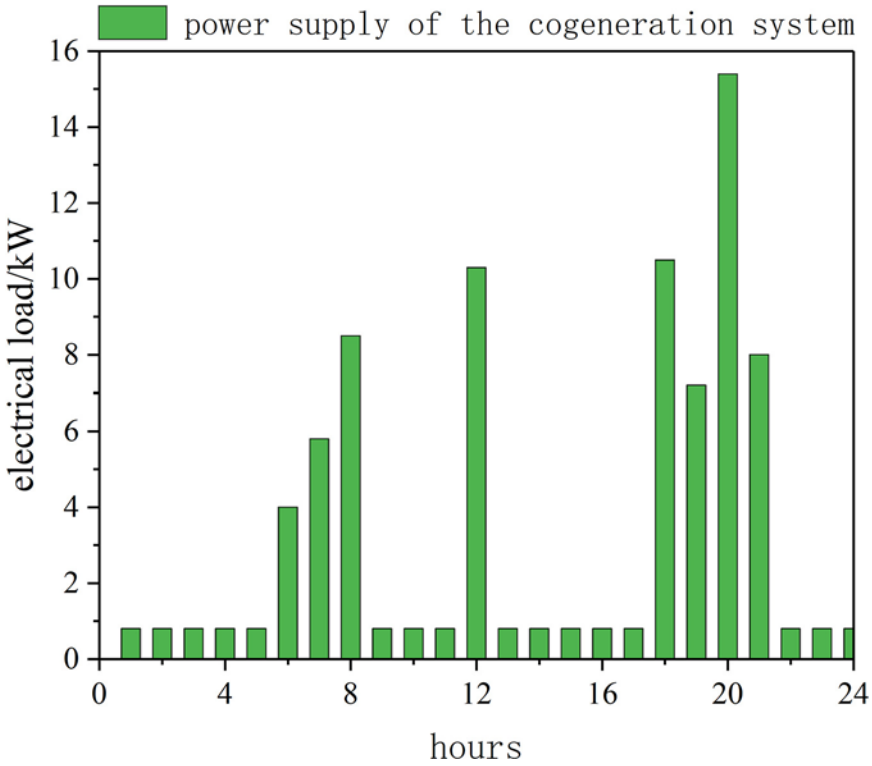

FIGURE 4 | Power supply on a typical winter day.

Rural households use water for periods of time, so the heat load during the day fluctuates. For the time period when the heat load demand is less than the heat produced by the cogeneration system, the heat storage tank is used to store this part of the heat. When the heat supply system is insufficient, the stored heat can be used to make up, and the capacity of the heat storage tank is determined according to the difference between the user's maximum heat load and the average heat load.

The amount of water in the thermal storage tank satisfies the following relationship:

$$m_t = m_{t-1} + m_t^{CHP} - m_t^{user} \tag{24}$$

Here: m_t—The amount of water in the thermal storage tank at time t/kg; m_{t-1}—The amount of water contained in the heat storage tank itself/kg; $m_t{}^{CHP}$—The amount of water produced and stored in the cogeneration system at time t/kg; $m_t{}^{user}$—User's water consumption at time t /kg.

The change of hot water temperature satisfies the following relationship:

$$m \cdot c\frac{dT}{dt} = Q_r - Q_{user} - Q_{loss} \tag{25}$$

Here: m—The quality of hot water/kg; c—Specific heat capacity of hot water/kJ·kg^{-1}·℃$^{-1}$; T—The temperature of the hot water/℃; Q_r—The heat storage tank absorbs the stored heat/kW; Q_{user}—Heat loss on the user side/kW; Q_{loss}—Heat loss of heat storage tank /kW.

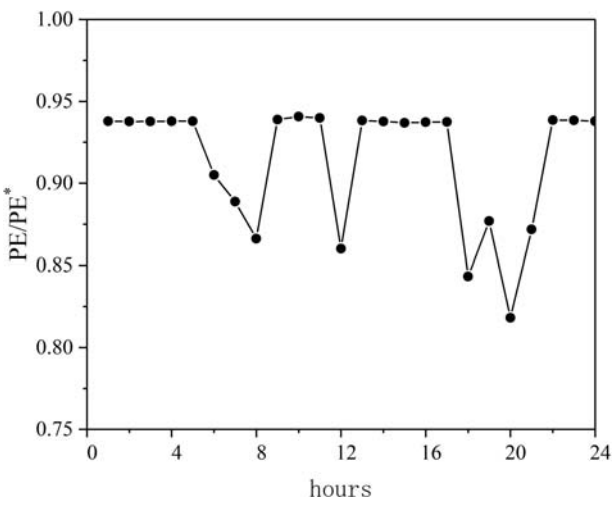

FIGURE 5 | Typical hourly energy consumption ratio in winter.

After studying the parameter conditions in the gasification process and the influences of parameter conditions on the SOFC and system performances, based upon the building power load demand, and set the 100 kW system net power generation as the design target, higher system cogeneration efficiency as the goals of system optimization, the design parameters of the biomass gasification solid oxide cogeneration system are

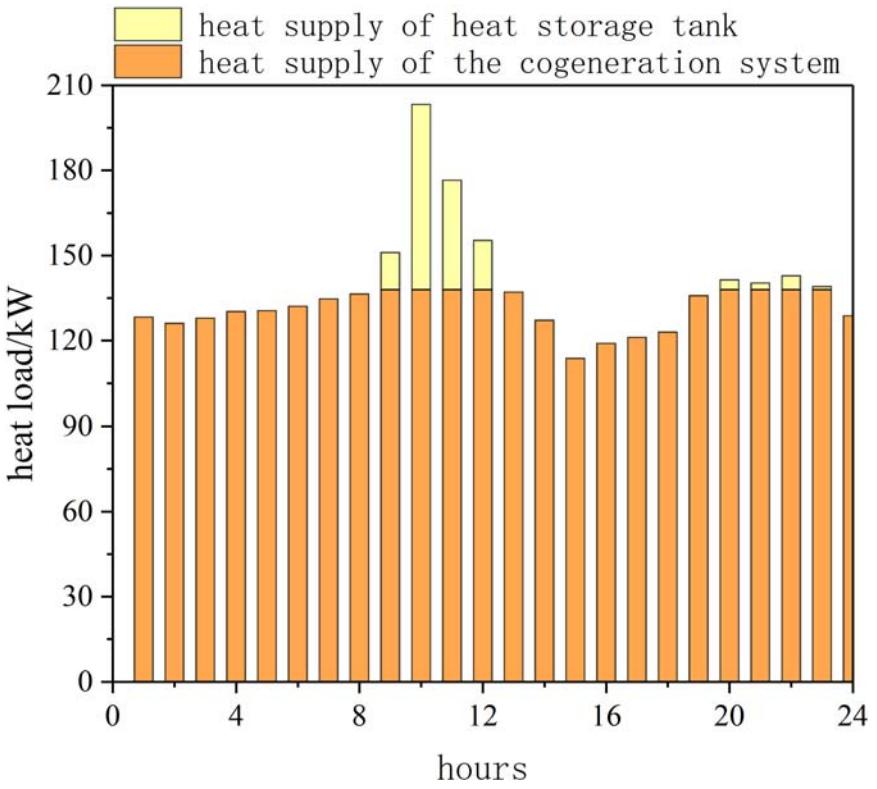

FIGURE 6 | Thermal energy supply on a typical winter day.

finally determined. **Table 2** are the results of modeling and parameter optimization using the approach described in the above subsection.

Calculation of Building Load

DeST (Designer's Simulation Toolkit) is a software platform (Tsinghua University, 2020) for building environment and HVAC system simulation developed by the Department of Building Technology Science, Tsinghua University. This paper uses this software to calculate the annual dynamic load of residential buildings.

This article takes a rural residential building in Xi'an as the research object. The building has two floors and a total area of 171 m^2. The DeST simulation software was used to calculate the hourly cooling and heating loads of the residential building throughout the year, and January 21 was selected as a typical winter day to study the hourly load changes of the building during the day. At the same time, the hot water load and electricity load of the building throughout the day are calculated according to the relevant standards in the "*Code for Design of Civil Building Electrical Appliances*" (JGJ 16-2008) and "*Code for Design of Building Water Supply and Drainage,*" and the simulation results of the building's heat and electrical load are shown in **Figure 2**.

System Evaluation Indicators

Primary Energy Saving Ratio (PESR) refers to the amount of primary energy consumed by the cogeneration system compared to the amount of primary energy consumed by the traditional energy supply system when meeting the user's same thermal and electric load demand. This paper takes PE/PE* the ratio of the primary energy consumption PE of the cogeneration system to the primary energy consumption PE* of the traditional energy system as the evaluation parameter, and the corresponding primary energy saving rate can be expressed as 1-PE/PE*. Calculated as follows:

$$PE^* = PE^*_{PP} + PE^*_B \tag{26}$$

$$PE = PE_{CHP} + PE_{PP} + PE_B - PE_{el,CHP,sur} - PE_{th,CHP,sur} \tag{27}$$

$$PESR = \frac{PE^* - PE}{PE^*} \tag{28}$$

Where: PE*—total energy consumption of the traditional energy system/kW·h; PE^*_{PP}—electric power purchased by the traditional system from the grid/kW·h; PE^*_B—primary energy consumption of the boiler in the traditional system/kW ·h; PE—the total energy consumption of the cogeneration system/kW·h; PE_{CHP}—the primary energy consumption of the cogeneration system/kW·h; PE_P—the electricity purchased by the cogeneration system from the grid/kW·h; PE_B—Primary energy consumption of the boiler in the cogeneration system/kW·h; $P_{el,CHP}$, sur—grid-connected power of the cogeneration system/kW·h; $P_{th,CHP}$, sur—storage heat of the cogeneration system/kW·h.

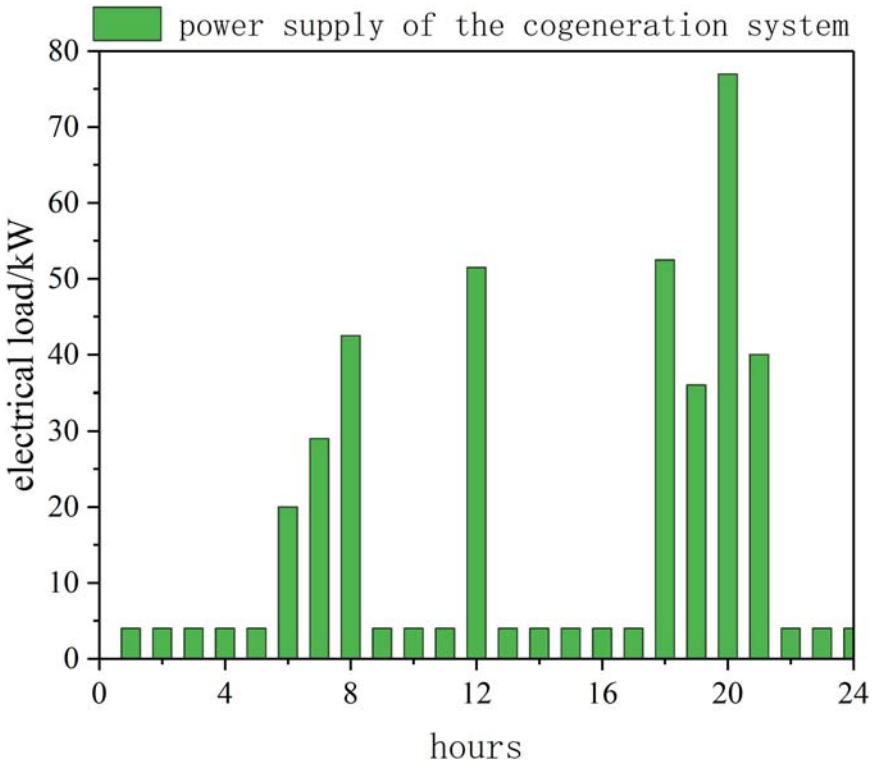

FIGURE 7 | Power supply on a typical winter day.

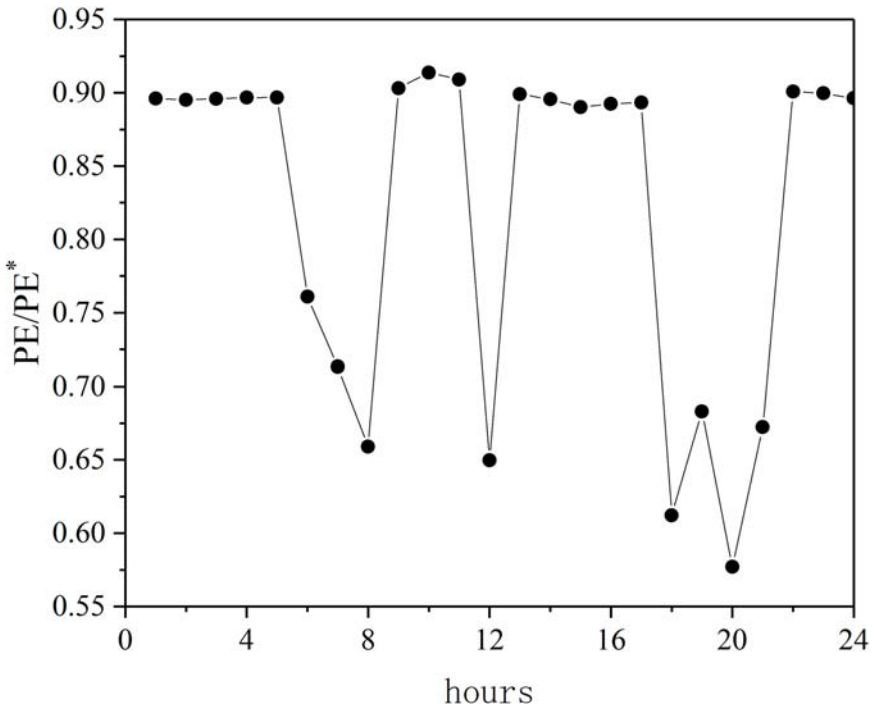

FIGURE 8 | Typical hourly energy consumption ratio in winter.

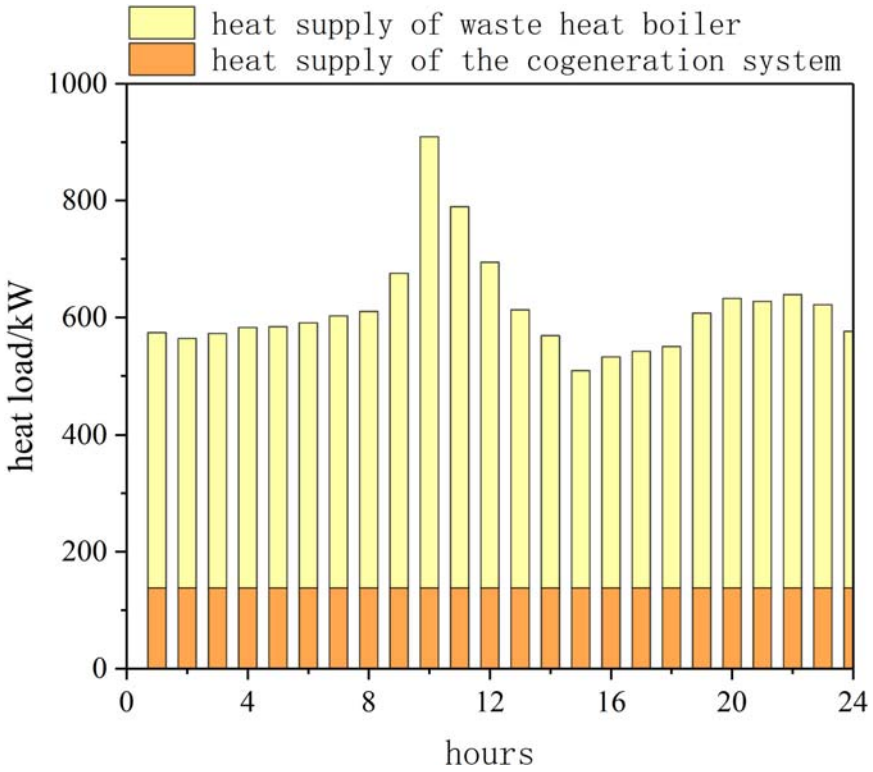

FIGURE 9 | Thermal energy supply on a typical winter day.

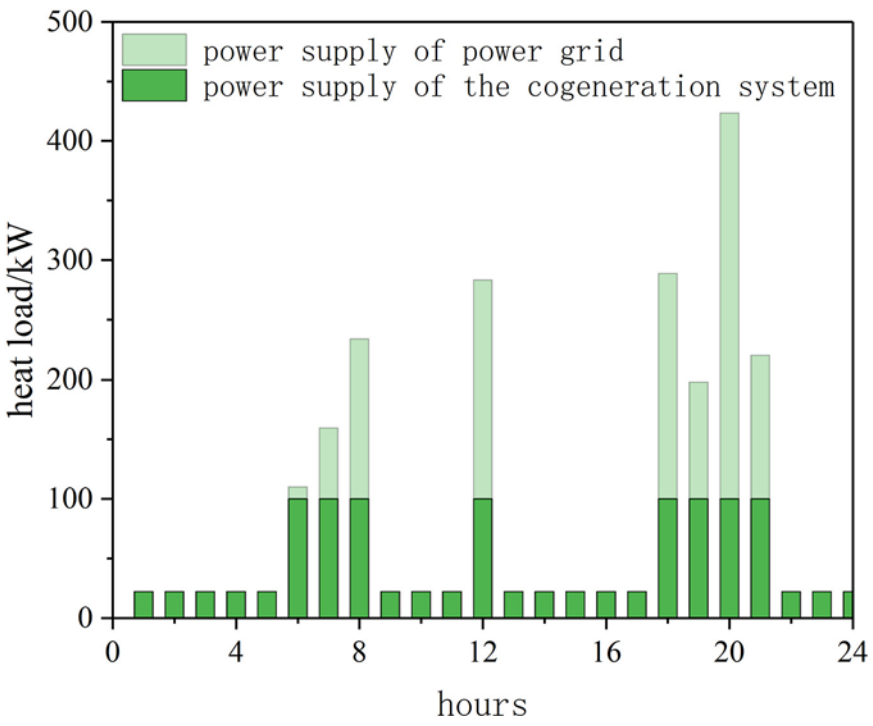

FIGURE 10 | Power supply on a typical winter day.

Considering that the thermal and electrical output of the system, the user's heat and electrical load demand cannot be completely matched, there will be a certain deviation, so according to the possible circumstances, the following three cases are discussed:

(1) The power generation and heat output of the combined supply system are used to meet the user's basic load supply, but do not exceed the user's electrical load and heat load demand. Combining the above formulas to obtain the primary energy saving rate calculation formula (Pohl and Diarra, 2014a,b):

$$PESR = 1 - \frac{1 + \frac{\sigma_D \eta_{th,B}}{\eta_{el,CHP}} \left[1 - \frac{\eta_{el,CHP}}{\eta_{th,B} \sigma_{CHP}} + \frac{\eta_{el,CHP}}{\eta_{el,PP}} \frac{\Delta P_{el}}{P_{el,D}} \left(1 - \frac{\eta_{el,PP}}{\eta_{el,CHP}} + \frac{\eta_{el,PP}}{\eta_{th,B} \sigma_{CHP}} \right) \right]}{1 + \frac{\sigma_D \eta_{th,B}}{\eta_{el,PP}}} \tag{29}$$

In the formula: σ_D—user-side electric heating ratio; σ_{CHP}—cogeneration system electric heating ratio; $\eta_{th,B}$—boiler thermal efficiency; ηel, CHP—cogeneration system power generation efficiency; $\eta_{el,PP}$—power generation efficiency of power plant; ΔP_{el}—User side purchases electricity from the grid/kW; $P_{el,D}$—User side electrical load/kW·h.

(2) The heat output of the combined supply system just meets the heat load demand of the user side, and the power generation capacity is surplus. Combining the above formulas to obtain the primary energy saving rate calculation formula:

$$PESR = 1 - \frac{\eta_{th,B} \left(1 - \xi_{el} \cdot \left[\frac{\sigma_{CHP} - \sigma_D}{\sigma_{CHP}} \right] \right)}{\eta_{th,CHP} \left(1 + \frac{\sigma_D \eta_{th,B}}{\eta_{el,PP}} \right)} \tag{30}$$

(3)The power generation of the combined supply system just meets the electric load demand of the user side, and the heat production has surplus. Combining the above formulas to obtain the primary energy saving rate calculation formula:

$$PESR = 1 - \frac{\eta_{el,PP} \left(1 - \xi_{th} \cdot \left[\frac{\sigma_D - \sigma_{CHP}}{\sigma_D} \right] \right)}{\eta_{el,CHP} \left(1 + \frac{\eta_{el,PP}}{\sigma_D \eta_{th,B}} \right)} \tag{31}$$

The annual cost rate reflects the economy of the joint supply system compared to the traditional system, and its expression is as follows (Ehyaei and Rosen, 2019; Sadat et al., 2019) :

$$ACSR = \frac{C_{Sep} - C_{CHP}}{C_{Sep}} \tag{32}$$

$$C_{Sep} = C_{el} \cdot E_{el} + C_h \cdot E_h + C_{inv} \cdot R \tag{33}$$

$$R = \frac{i(1+i)^L}{(1+i)^L - 1} \tag{34}$$

$$C_h = \frac{C_{Bio}}{\eta_{th,B} \cdot H_{Bio}} \tag{35}$$

$$C_{CHP} = C_{invest} \cdot R + C_B + C_{O\&M} \tag{36}$$

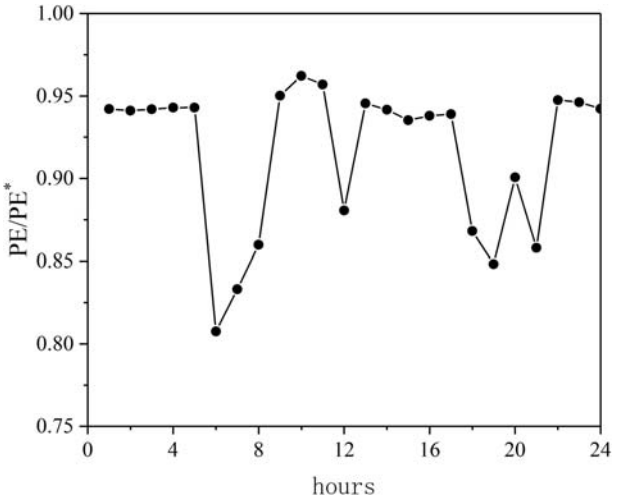

FIGURE 11 | Typical hourly energy consumption ratio in winter.

CHP SYSTEM SCHEME

Combining the heat and electricity output of the CHP system established in this paper and the heat load and electricity load requirements of residential buildings, this section mainly discusses the energy-saving and economy of the CHP system and the traditional system under different operation schemes.

Scheme One

According to the heat output and electricity output of the system, 20 residential users are used as heating objects. The composition of the user-side heat load and electricity load under this scheme can be obtained as shown in **Figures 3**, **4**, the primary energy saving rate of the system is shown in **Figure 5**.

It can be seen that under this scheme, the power generation of the joint supply system fully meets the user's electrical load demand, and there is still surplus. The excess power generation is used in the online sales mode. In addition to the large heat load demand of users between 9:00 and 12:00 during the day, the supply of the CHP system is insufficient, and the heat production of the CHP system can meet the user's heat load requirements in other periods. In this case, the corresponding heat storage tank is configured for the cogeneration supply system, and the excess heat is stored through the heat storage tank. When the heat generated by the system cannot meet the user's heat load demand, the stored heat is replenished to the user.

The largest values of system's primary energy saving rate occurred mainly around three periods of morning, noon, and evening, which is basically consistent with the trend of electrical load changes. This is because the user's electrical load is relatively increased at this time, and the heat load change is very small. The decrease in the heat to electricity ratio TER of user results in more significant energy savings. Compared with the traditional system, the primary energy saving

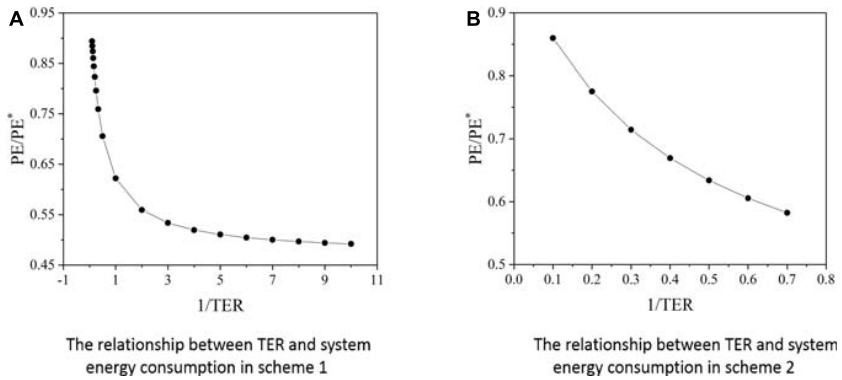

FIGURE 12 | Influence of user's TER on system energy saving. **(A)** The relationship between the TER and the system energy consumption in scheme 1. **(B)** The relationship between the TER and the system energy consumption in scheme 2.

efficiency under this scheme is about 8.6%, and the annual cost saving rate is 5.5%.

Scheme Two

Since the heat load demand of rural houses is much larger than the electricity load demand, according to the heat and power output of the designed 100 kW CHP system, it can only meet the heat demand of a small number of users, and there is a large surplus of power generation in the system. Combining the actual situation of heating in rural buildings in winter and the living habits of rural users, the actual heating area of a building generally includes only a few commonly used rooms, while other rooms are generally idle and there is no need for heating. Therefore, the heating area only selects the living room and master bedroom and secondary bedroom. Similarly, heating is performed in a manner that satisfies the average heat load of users. Combined with the system's thermal power output, 123 residential users are selected as heating objects, and the user's heat load, electricity load and the system's primary energy saving rate are calculated, as shown in **Figures 6–8**.

As can be seen from the results in the figure, except that the heat output of the CHP system between 9 o'clock and 12 o'clock and between 20 o'clock and 23 o'clock cannot meet the user's heat load demand, the heat supply of the CHP system can meet the user's needs at other times. And there is surplus heat. Similarly, it is processed by adding a heat storage tank as in the first scheme. Under this scheme, the change trend of the primary energy saving rate of the CHP system is basically the same as that in **Figure 5**, but the primary energy saving rate is greater. This is because compared with the first case, at this time the user's heat load is reduced, the electrical load remains unchanged, and the TER of user decreases, so the energy saving effect is more significant. Compared with the traditional system, the primary energy saving efficiency under this scheme is about 18.0%, and the annual cost saving rate is 10.3%.

Scheme Three

This section is also based on the actual heating situation in the countryside and operates according to the scheme that meets the user's daily average electrical load demand. The system can meet the average electricity load of the entire village. **Figures 9**, **10** show the user's heat and power load during the heating period, and the hourly energy consumption of the CHP system is shown in **Figure 11**.

It can be seen that under this scheme, the heat production of the CHP system can only meet a small part of the user's heat load demand, and most of the remaining heat load needs to be supplemented by the heat production of the waste heat boiler, in this case, the heat boiler provides heat source for the heat storage tank; except for morning, noon, and evening, the peak electricity consumption needs to be supplemented by purchasing electricity from the power grid. The electricity consumption load for the rest time is fully borne by the CHP system, and the excess power generation is sold online. The primary energy saving rate of the system is about 8.5%, and the annual cost saving rate of the system is about −20.2%.

CHP SYSTEM REGULATION

According to the analysis in Section "System Evaluation Indicators," the primary energy saving rate of the system is mainly related with the heat to electricity ratio on the user side. The relationship between the hourly energy consumption ratio of the CHP system and the user's TER has been discussed for the first and second operating modes, as shown in **Figure 12**.

It can be seen from the figure that when the heat and power output of the CHP system is fixed, the primary energy energy saving rate gradually decreases with the increase of the user's heat and power ratio TER; if the user's TER is closer to the system's TER, then the more significant the energy saving effect of the system. Under ideal conditions, when the heat and power output of the CHP system just exactly meets the heat and electricitiy load demand of the user side, that is, the system's heat to electricity ratio is equal to the user's TER, the system's energy saving effect reaches the best.

Since the heat load demand on the user side is basically stable, the energy saving effect of the system can be improved by

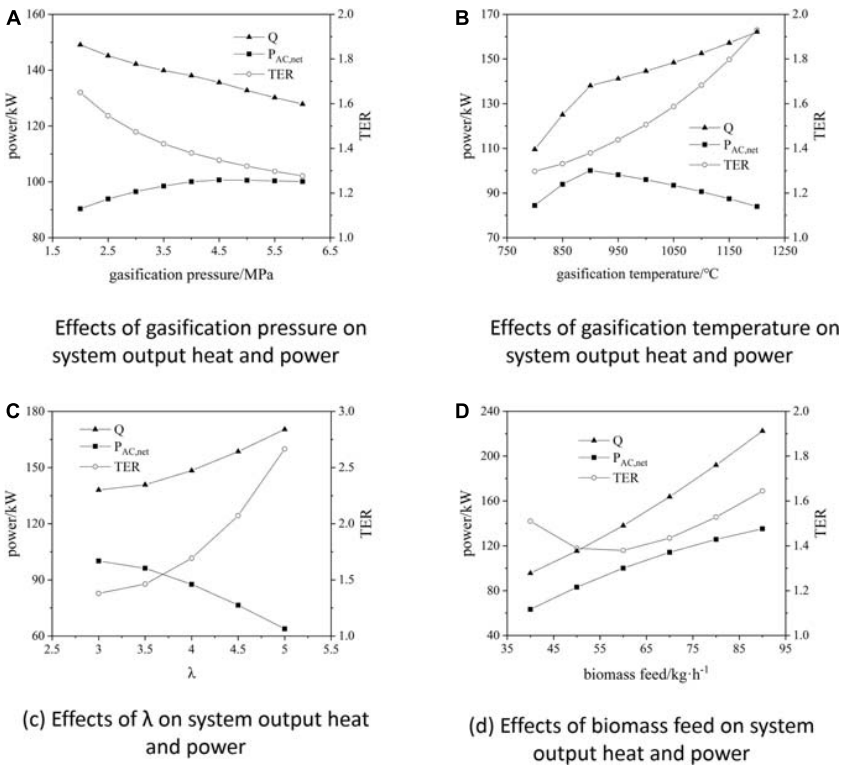

FIGURE 13 | Effect of input parameters on system output heat and power characteristics. **(A)** Effect of gasification pressure on system output heat and power. **(B)** Effect of gasification temperature on system output heat and power. **(C)** Effect of λ on the system output heat and power. **(D)** Effect of biomass feed on system output heat and power.

adjusting the heat and electricity output of the system. For the BG-SOFC-CHP system established in present study, different heat and power output characteristics of the system can be obtained by adjusting parameters such as biomass feed, gasification pressure, gasification temperature, and excess air coefficient, as shown in **Figure 13**.

It can be seen that as the gasification pressure decreases, the gasification temperature increases, the excess air coefficient increases, and the biomass feed increases, the TER of the system gradually increases; Among them, the influence of gasification temperature and excess air coefficient on the system's the TER is more significant, which can be used as the main means to adjust the system's TER. However, it should be noted that the parameters that affect the energy saving effect of the system also include the power generation efficiency and thermal efficiency of the system. The adjustment of the above system parameters will also affect the power generation efficiency and thermal efficiency of the system. At the same time, in order to ensure that the system can operate at a higher efficiency, the adjustment of various parameters should be controlled within a reasonable range.

CONCLUSION

Based on the BG-SOFC-CHP system with a net power generation capacity of 100 kW, the energy efficiency and economy of the CHP system compared to the traditional system under three different operating schemes have been studied. Through analysis, the following conclusions can be drawn:

1) In the case of heating all rooms in rural houses of northern China, the CHP system has certain energy-saving and economical characteristics but the energy-saving effect is not significant. This is mainly because the TER on the user side is much larger than the TER in the system. Therefore, the advantages of the cogeneration energy supply system cannot be fully utilized;
2) When considering the actual heating situation of rural residences in winter, the energy saving effect of the CHP system is more significant when the operation scheme that meets the average heat load demand of users is adopted, and it also has better economy;
3) When the operation scheme that meets the average electricity load demand of users is adopted, due to the small electricity consumption in rural areas and the strong time period fratures, the role of the CHP system cannot be played well at most times, resulting in the performance of energy saving is reduced, and it is not economical compared to the traditional system;
4) The primary energy savings rates of the three schemes are 8.6, 18.0, and 8.5%; the annual cost savings rates are 5.5, 10.3, and −20.2%; combined with the current situation that the

heat load demand in rural areas of northern of China is much greater than the electrical load demand, The second operation scheme is more reasonable and efficient;

5) The main factors affecting the energy efficiency of the CHP system are the system's heat to electricity ratio TER and the user's heat to electricity ratio TER. When the system's TER is constant, as the user's TER increases, the system's energy efficiency gradually decreases; when the system's TER is close to the user-side TER, the energy-saving effect of the system is more significant.

DATA AVAILABILITY STATEMENT

The raw data supporting the conclusions of this article will be made available by the authors, without undue reservation.

AUTHOR CONTRIBUTIONS

ZD: responsible for the overall organization, conception, and writing of the manuscript. ZJ: responsible for model construction, data analysis, and manuscript writing. JM: responsible for data processing and assist in writing of the manuscript. XS: responsible for data processing and assist in writing of the manuscript. GX: responsible for manuscript conception and method guidance. All authors contributed to the article and approved the submitted version.

FUNDING

The study was supported by the National Key R&D Program of China 2018YFB1502200.

REFERENCES

Achenbach, E. (1994). Three-dimensional and time-dependent simulation of a planar solid oxide fuel cell stack. *J. Power Sourc.* 49, 333–348. doi: 10.1016/0378-7753(93)01833-4

Amiri, A., Tang, S., Steinberger-Wilckens, R., and Tade, M. O. (2018). Evaluation of fuel diversity in solid oxide fuel cell system. *Int. J. Hydrogen Energy* 43, 23475–23487. doi: 10.1016/j.ijhydene.2018.10.192

Braun, R. J. (2002). *Optimal Design and Operation of Solid Oxide Fuel Cell Systems for Small-scale Stationary Applications.* Doctoral dissertation. Madison, WI: University of Wisconsin-Madison.

Chen, G., Xia, Z., Yan, B., Zhou, W., and Wang, Q. (2014). Technical and economic analysis of biomass gasification for heating in rural areas. *Renew. Energy Resour.* 32, 1395–1399.

Chen, Z., and Zhu, M. (2018). Prediction of residential heating gas demand of Hebei Province after "coal to gas"–based on micro-level survey data of rural household energy consumption. *China Prices* 7, 64–66.

Cong, H., Zhao, L., Meng, H., Yao, Z., Huo, L., Jia, J., et al. (2018). Applicability evaluation of biomass pyrolytic poly-generation technology on clean heating in northern rural of China. *Trans. Chin. Soc. Agric. Eng.* 34, 8–14. doi: 10.11975/j.issn.1002-6819.2018.01.002

Dey, T., Singdeo, D., Pophale, A., Bose, M., and Ghosh, P. C. (2014). SOFC power generation system by bio-gasification. *Energy Proc.* 54, 748–755. doi: 10.1016/j.egypro.2014.07.316

Ehyaei, M. A., and Rosen, M. A. (2019). Optimization of a triple cycle based on a solid oxide fuel cell and gas and steam cycles with a multiobjective genetic algorithm and energy, exergy and economic analyses. *Energy Convers. Manag.* 180, 689–708. doi: 10.1016/j.enconman.2018.11.023

Giarola, S., Forte, O., Lanzini, A., Gandiglio, M., Santarelli, M., and Hawkes, A. (2018). Techno-economic assessment of biogas-fed solid oxide fuel cell combined heat and power system at industrial scale. *Appl. Energy* 211, 689–704. doi: 10.1016/j.apenergy.2017.11.029

Jia, J., Abudula, A., Wei, L., Sun, B., and Shi, Y. (2015). Thermodynamic modeling of an integrated biomass gasification and solid oxide fuel cell system. *Renew. Energy* 81, 400–410. doi: 10.1016/j.renene.2015.03.030

Li, G., Liu, C., Li, X., and Chi, L. (2015). Test of heating effect of heating system based on biomass briquette stove in rural area. *Gas Heat* 35, 13–16. doi: 10.13608/j.cnki.1000-4416.2015.12.004

Li, Y., Ruan, Y., and Liu, Q. (2015). Performance analysis of micro combined heat and power system based on building load. *CIESC J.* 66, 364–370. doi: 10.11949/j.issn.0438-1157.20150709

Palomba, V., Prestipino, M., and Galvagno, A. (2017). Tri-generation for industrial applications: Development of a simulation model for a gasification-SOFC based system. *Int. J. Hydrogen Energy* 42, 27866–27883. doi: 10.1016/j.ijhydene.2017.06.206

Pohl, E., and Diarra, D. (2014a). A method to determine primary energy savings of CHP plants considering plant-side and demand-side characteristics. *Appl. Energy* 113, 287–293. doi: 10.1016/j.apenergy.2013.07.038

Pohl, E., and Diarra, D. (2014b). Assessment of primary energy savings by means of CHP systems in domestic energy supply. *Appl. Ther. Eng.* 71, 830–837. doi: 10.1016/j.applthermaleng.2013.12.021

Rokni, M. (2018). Design and analysis of a waste gasification energy system with solid oxide fuel cells and absorption chillers. *Int. J. Hydrogen Energy* 43, 5922–5938. doi: 10.1016/j.ijhydene.2017.10.123

Sadat, S. M. S., Lavasani, A. M., and Ghaebi, H. (2019). Economic and thermodynamic evaluation of a new SOFC based polygeneration system. *Energy* 175, 515–533. doi: 10.1016/j.energy.2019.03.093

Tsinghua University (2020). *Designer's Simulation Toolkit*. Available online at: https://update.dest.com.cn/

Wan, W. (2016). An innovative system by integrating the gasification unit with the supercritical water unit to produce clean syngas for solid oxide fuel cell (SOFC): system performance assessment. *Int. J. Hydrogen Energy* 41, 22698–22710. doi: 10.1016/j.ijhydene.2016.09.146

Yan, Y., Jiao, W., Wang, K., Huang, Y., Cheng, J., and Han, Q. (2020). Coal-to-gas heating compensation standard and willingness to make clean energy choices in typical rural areas of northern China. *Energy Policy* 145:111698. doi: 10.1016/j.enpol.2020.111698

Zhang, D., Li, J., and Zhang, H. (2017). All operation mathematical model and thermal performance analysis on combined heating power and biogas system. *CIESC J.* 68, 1998–2008. doi: 10.11949/j.issn.0438-1157.20161538

Zhou, R., Zhang, X., and Yan, R. (2019). Application of biomass energy-solar energy combined heating system in northern rural areas. *China Biogas* 37, 108–113.

Zhou, W., Chen, G., Ma, L., Yan, B., and Xia, Z. (2014). Economic and environmental benefits analysis of decentralized heating using biomass gasification gas in rural area. *Trans. Chin. Soc. Agric. Eng.* 30, 213–218. doi: 10.3969/j.issn.1002-6819.2014.14.027

Conflict of Interest: The authors declare that the research was conducted in the absence of any commercial or financial relationships that could be construed as a potential conflict of interest.

frontiers in Chemistry

ORIGINAL RESEARCH
published: 21 April 2021
doi: 10.3389/fchem.2021.633868

Enhanced Electrochemical Properties of Non-stoichiometric Layered Perovskites, $Sm_{1-x}BaCo_2O_{5+d}$, for IT-SOFC Cathodes

*Chan Gyu Kim[1], Sung Hun Woo[1], Kyeong Eun Song[1], Seung-Wook Baek[2], Hyunil Kang[3], Won Seok Choi[3] and Jung Hyun Kim[1]**

[1] Department of Advanced Materials Science and Engineering, Hanbat National University, Daejeon, South Korea, [2] Interdisciplinary Materials Measurement Institute, Korea Research Institute of Standards and Science (KRISS), Daejeon, South Korea, [3] Department of Electrical Engineering, Hanbat National University, Daejeon, South Korea

In this study, electrochemical properties of layered perovskites having non-stoichiometric compositions ($Sm_{1-x}BaCo_2O_{5+d}$, x = 0, 0. 01, 0.02, 0.03, 0.04, 0.05, 0.10, and 0.15) were analyzed for the direct application of cathode materials for Intermediate Temperature-operating Solid Oxide Fuel Cells (IT-SOFC). From the $Sm_{1-x}BaCo_2O_{5+d}$ oxide systems calcined at 1,100°C for 8 h, single phase ($SmBaCo_2O_{5+d}$, SBCO_1) was maintained only in the case of the x = 0 composition. In the compositions of x = 0.05–0.10, $BaCoO_{2.6}$ was mixed with the pattern of SBCO. In addition, in the composition of x = 0.15, it was confirmed that $BaCoO_{2.6}$ and CoO phases coexisted with SBCO. In the compositions of $Sm_{1-x}BaCo_2O_{5+d}$, the overall Area Specific Resistance (ASR) values decreased as the removal amount of Sm increased from x = 0–0.10; then, the values increased for compositions from x = 0.15. For example, the ASRs of SBCO_1, $Sm_{0.95}BaCo_2O_{5+d}$ (SBCO_0.95), $Sm_{0.90}BaCo_2O_{5+d}$ (SBCO_0.90), and $Sm_{0.85}BaCo_2O_{5+d}$ (SBCO_0.85) measured at 600°C were 0.301, 0.147, 0.119, and 0.179 Ω cm^2, respectively. In particular, SBCO_0.90 was found to have an excellent ASR property of about 0.035 Ω cm^2 at 700°C. Typical properties of the metal–insulator transition (MIT) electrical conductivity were shown in all measured compositions. The temperature at which MIT occurred increased as the non-stoichiometric composition increased.

Keywords: layered perovskite, cathode, intermediate temperature-operating solid oxide fuel cell, non-stoichiometric composition, area specific resistance, electrical conductivity

OPEN ACCESS

Edited by:
Junwei Wu,
Harbin Institute of Technology, China

Reviewed by:
Jun Zhou,
Xi'an Jiaotong University, China
Tae Ho Shin,
Korea Institute of Ceramic Engineering and Technology, South Korea

***Correspondence:**
Jung Hyun Kim
jhkim2011@hanbat.ac.kr;
jhkim1870@gmail.com

Specialty section:
This article was submitted to Electrochemistry, a section of the journal Frontiers in Chemistry

Received: *26 November 2020*
Accepted: *30 March 2021*
Published: *21 April 2021*

Citation:
Kim CG, Woo SH, Song KE, Baek S-W, Kang H, Choi WS and Kim JH (2021) Enhanced Electrochemical Properties of Non-stoichiometric Layered Perovskites, $Sm_{1-x}BaCo_2O_{5+d}$, for IT-SOFC Cathodes. Front. Chem. 9:633868. doi: 10.3389/fchem.2021.633868

HIGHLIGHTS

- $Sm_{1-x}BaCo_2O_{5+d}$ (x = 0, 0.01, 0.02, 0.03, 0.04, 0.05, 0.10, and 0.15) oxide systems having non-stoichiometric compositions were synthesized by solid state reaction.
- $BaCoO_{2.6}$ phase was identified from the composition of x = 0.05 or more in $Sm_{1-x}BaCo_2O_{5+d}$; CoO phase was also found to exist for the composition of $x = 0.15$

- All composition showed higher electrical conductivity values than 100 S/cm in the temperature ranges of 500–750°C.
- Area specific resistance (ASR) of $Sm_{1-x}BaCo_2O_{5+d}$ was 0.15 $\Omega \cdot cm^2$ or less at 650°C. SBCO_0.90 showed the lowest value of 0.119 $\Omega \cdot cm^2$ at 600°C

INTRODUCTION

As environmental problems such as global warming, caused by the indiscriminate use of fossil fuels since the beginning of the industrial revolution in the 19th century have recently emerged, interest in eco-friendly energy has been expanding (Wigley, 1998; Hoad, 2015). Accordingly, many countries around the world have been implementing nature-friendly policies and spurring green energy development. There are various nature-friendly energy generation methods, including wind, hydroelectric, and solar power However, these power generation systems have disadvantages such as restrictions on installation locations and high initial cost. Therefore, there is need for development of other energy methods that can replace these systems and mitigate their problems (Rodman and Meentemeyer, 2006; Kosnik, 2008; Ingole and Rakhonde, 2015).

Fuel cells or fuel cell systems based on hydrogen energy have been emerging as alternative energy conversion methods to replace the energy generating from fossil fuel. Especially, among various fuel cell types, solid oxide fuel cells (SOFC) are the focus of attention recently. An SOFC is an energy converting device that produces water and generates electricity via the chemical reaction of hydrogen and oxygen (Minh, 2004).

SOFCs are known to show higher values of energy efficiency and power density than those of other fuel cells. SOFCs, which are made of ceramics, are composed of a dense electrolyte and two porous electrodes (cathode and anode). The SOFC structure is simpler than those of other types of fuel cell. In addition, due to their high exchange current density and the kinetics characteristics that occur under relatively high temperature operating conditions, SOFCs do not require any precious or expensive catalysts for operation.

While SOFCs have advantages of high efficiency at high temperature and a stable ceramic structure, their high-temperature operating conditions can rather act as a disadvantage, causing problems such as thermal degradation of ceramic materials, sealing issues, and rapid oxidation of metal materials used as interconnectors. To solve these problems, research on Intermediate Temperature-operating Solid Oxide Fuel Cells (IT-SOFC) that feature lowered operating temperature in the intermediate temperature range (500–750°C) has been actively conducted. However, the main obstacle to this lowered-temperature-range SOFCs is the decreased electrochemical activity of the two electrodes (cathode and anode), as well as lowered ionic conductivity and increased ohmic resistance of the electrolyte. Significantly, the major source of voltage loss in IT-SOFCs is the cathode materials. Therefore, to achieve high power densities at the reduced temperatures, it is necessary to develop cathode materials that show excellent electrochemical reaction and enhanced/advanced low polarization resistance (Minh, 1993; Tu et al., 1997).

Recently, to replace existing IT-SOFC cathode materials, many research groups have investigated new concept-based cathode materials with a chemical composition of layered perovskite, because this structure yields superior oxide ionic diffusivity, excellent oxygen surface exchange coefficients, high oxygen transport properties, and higher electronic conductivity (Kim et al., 2010; Joung et al., 2013; Zhang et al., 2016). In this new perovskite structure ($A^{/}A^{//}B_2O_{5+d}$ chemical composition), various lanthanide atoms such as La, Pr, Nd, and Sm can be substituted into the $A^{/}$-site; Ba can be replaced in the $A^{//}$-site; and transition metal ions of Co, Mn, and Fe can be located at the B-site.

The first application of a layered perovskite structure as cathode of SOFC (Zhou et al., 1993) showed that a difference in coordination number occurs due to the difference in ion radius between the $A^{/}$ and $A^{//}$ ions; thus, oxygen vacancies are formed, yielding excellent electrochemical properties (Akahoshi and Ueda, 2001; Frontera et al., 2003; Kim et al., 2007, 2010; Kim and Manthiram, 2015). The layered perovskite structure into which elemental Co was substituted on the B-site is comprised of a stacked structure with $[CoO_2]$-$[BaO]$-$[CoO_2]$-$[LnO_6]$ on the c-axis.

In the $[LnO_6]$ layer, there is a large difference between the ionic radius of Ln and the ionic radius of Ba^{2+}, resulting in a pyramid structure of CO_5 and an octahedral structure of CO_6. Finally, oxygen vacancies are generated in the $[LnO_6]$ layer due to this structural feature. Accordingly, structure is known to exhibit higher electrochemical properties because it has excellent oxygen mobility properties and at the same time shows excellent surface diffusion properties. For example, according to Ding et al., who investigated the composition of $PrBa_{0.5}Sr_{0.5}Co_2O_{5+d}$, this composition exhibited remarkable properties in the 500–700°C temperature range and showed an area specific resistance (ASR) value of 0.23 $\Omega \cdot cm^2$ at 650°C (Ding and Xue, 2010). In additional, the $SmBaCo_2O_{5+d}$ layered perovskite had an ASR of 0.13 $\Omega \cdot cm^2$ at 650°C (Kim et al., 2009). However, the thermal shock and long-term stability of the Co substituted layered perovskite at high temperatures have been questioned due to the high thermal expansion coefficient (TEC) (Tietz, 1999; Pelosato et al., 2015).

Strategies to develop not only excellent cathode materials for IT-SOFCs by substituting various materials into layered perovskite, but also non-stoichiometric cathode materials synthesized by removing individual elements of layered perovskite are being pursued (Kostogloudis and Ftikos, 1999; Wang et al., 2014; Sun et al., 2016; Yi et al., 2016). Based on the composition $PrBaCo_2O_{5+d}$, $PrBa_{0.92}Co_2O_{5+d}$, in which 0.08 mol% of Ba was removed from the $A^{//}$-site, showed better electrochemical properties than the composition $PrBaCo_2O_{5+d}$. In particular, $PBa_{0.92}CO$ had an excellent ASR value of 0.166 $\Omega \cdot cm^2$ at 600°C (Idrees et al., 2019). It can be seen from this result that the electrochemical properties were enhanced in the non-stoichiometric composition in which the $A^{//}$-site is removed stepwise from the composition of layered perovskite $LnBaCo_2O_{5+d}$.

In the case of the composition of $PrBaCo_2O_{5+d}$ with partially removed $A^{/}$-site, not $A^{//}$-site, the concentration of oxygen vacancies inside the crystal structure increased as the Pr-deficiency level increased. Especially, the $Pr_{0.95}BaCo_2O_{5+d}$ composition showed ASR values of 0.113, 0.054, and 0.028 $\Omega \cdot cm^2$ at 600, 650, and 700°C (Jiang et al., 2014). As another example, the oxygen content of $PrBaCo_2O_{5+d}$ was 5.74 and the value of $Pr_{0.92}BaCo_2O_{5+d}$ was reduced to 5.62 when the amount of Pr removed increased. In addition, $Pr_{0.92}BaCo_2O_{5+d}$ was found to have excellent ASR values of 0.081 and 0.041 $\Omega \cdot cm^2$ at 700 and 750°C (Zhang et al., 2016). Therefore, in the case of the non-stoichiometric composition of the layered perovskite, excellent electrochemical properties can be obtained when the lanthanide element is controlled. In summary, oxygen vacancies in the lattice of layered perovskite can be activated through non-stoichiometry of the $A^{/}$-site, thereby promoting the ORR reaction.

The goal of this research is to investigate the phase synthesis characteristics of $Sm_{1-x}BaCo_2O_{5+d}$ ($x = 0$, 0.01, 0.02, 0.03, 0.04, 0.05, 0.10, and 0.15) showing non-stoichiometric compositions in which samarium (Sm) elements were stepwise removed at the $A^{/}$-site of a $SmBaCo_2O_{5+d}$ layered perovskite by using solid state reaction. Significantly, the electrochemical properties of $Sm_{1-x}BaCo_2O_{5+d}$ oxide systems were also investigated to apply this material as cathode material for direct application to IT-SOFCs.

EXPERIMENTAL SECTION

Synthesis

$Sm_{1-x}BaCo_2O_{5+d}$ ($x = 0$, 0.01, 0.02, 0.03, 0.04, 0.05, 0.10, and 0.15) oxide systems having layered perovskite structure were synthesized using Solid State Reaction (SSR). The starting materials were Sm_2O_3 (smarium oxide, Alfa Aesar, 99.9%), $BaCO_3$ (barium carbonate, Samchun, 99.0%), and Co_3O_4 (cobalt oxide, High Purity Chemicals, 99.9%); an electronic balance (WBA-320) was use for accurate weighing to the third decimal place.

In this study, two calcinations were performed for more accurate synthesis of single phase. The weighed materials were mixed and calcined for 6 h at 1,000°C in air. After the first calcination into uniform and small particles, wet ball milling was performed at room temperature for about 1 day to make the composite powder. The powder after ball milling was again calcined at a rate of 5°C/min in air, and secondary calcination was performed at 1,100°C for 8 h. Resulting materials after the two calcinations were pulverized to form fine powders. The compositions and abbreviations are summarized in **Table 1**.

Sample Preparation

$Ce_{0.9}Gd_{0.1}O_{2-d}$ (CGO91, Solvay) powders were used as the electrolyte of symmetrical half cells ($Sm_{1-x}BaCo_2O_{5+d}$/CGO91/$Sm_{1-x}BaCo_2O_{5+d}$). After weighing 2.5 g of CGO91, it was put into a metal mold and compression molding was performed by applying a force of 2×10^3 kg/m^2. After that, sintering was performed at 1,450°C for 6 h in air. Cathode ink made using a-terpieal(Kanto Chemical), Butvar(Sigma Aldrich), and acetone with cathode powder; composite ink was also prepared by mixing electrolyte powder and cathode material at a weight ratio of 50:50. Both sides of the sintered electrolyte support were printed' with the prepared cathode ink, and the printed cell was sintered at 1,000°C for 1 h in the air condition. After the sintering, surface area of both sides of cathode was measured and found to be 0.785 cm^2. To confirm the electrical conductivity characteristics of the composites as identified through XRD analysis, a sample was prepared and the electrical conductivity was measured. After making a bar-type sample with dimensions of ~2.8 × 5.5 × 23 mm through compression molding, sample was sintered at 1,100°C for 3 h in air.

TABLE 1 | Abbreviations of $Sm_{1-x}BaCo_2O_{5+d}$ ($x = 0$, 0.01, 0.02, 0.03, 0.04, 0.05, 0.10, and 0.15) compositions.

Composition	Abbreviation
$SmBaCo_2O_{5+d}$	SBCO_1
$Sm_{0.99}BaCo_2O_{5+d}$	SBCO_0.99
$Sm_{0.98}BaCo_2O_{5+d}$	SBCO_0.98
$Sm_{0.97}BaCo_2O_{5+d}$	SBCO_0.97
$Sm_{0.96}BaCo_2O_{5+d}$	SBCO_0.96
$Sm_{0.95}BaCo_2O_{5+d}$	SBCO_0.95
$Sm_{0.90}BaCo_2O_{5+d}$	SBCO_0.90
$Sm_{0.85}BaCo_2O_{5+d}$	SBCO_0.85

Characterizations

To understand the crystal structure of the cathode powder synthesized by SSR method, X-ray diffraction analysis was used. The experimental equipment was an X-ray Diffractometer (Model: SmartLab/Rigaku), operated using a Cu Kα filter under conditions of 9 kW, 45 kV, and 200 mA. A range of 10–140° (2θ) was employed with steps of 0.02°. Microstructural properties of $Sm_{1-x}BaCo_2O_{5+d}$ ($x = 0$, 0.01, 0.02, 0.03, 0.04, 0.05, 0.10, and 0.15) oxide systems were examined using a field-emission scanning electron microscope (FESEM/Hitachi SU5000). To measure the electrical conductivity, a bar-type sample was prepared and the electrical conductivity was measured through the DC 4-probe method. A Keithley 2400 Source meter was used as measuring device; after connecting the sample with Pt-wire, the electrical conductivity was measured by increasing the temperature in steps of 50°C in a temperature range of 50–900°C. Additionally, the current range was measured from 0 to 1A through steps of 0.05A, and the limit of voltage was set to 20V.

Impedance measurement was performed to confirm the electrochemical properties of the synthesized $Sm_{1-x}BaCo_2O_{5+d}$ ($x = 0$, 0.01, 0.02, 0.03, 0.04, 0.05, 0.10, and 0.15) oxide systems. According to existing literature, $SmBaCo_2O_{5+d}$ does not react with $Ce_{0.9}Gd_{0.1}O_{2-d}$ (CGO91), so there is no problem to use it with CGO91 (Kim et al., 2009). Therefore, the symmetrical half cell (SBCO_X/CGO91/SBCO_X) after the sintering was connected using Pt mesh, and the impedance was measured in a temperature range of 500–750°C in an air atmosphere. Frequency range was 0.05 Hz to 2.5 MHz.

The area specific resistance (ASR) of the synthesized composition was calculated using the impedance results obtained through electrochemical analysis. Using the impedance results with ohmic resistance removed, ASR was calculated according to the difference between the low intercept and high intercept of the real X-axis. Impedance was measured using a multi-channel electrochemical analyzer (Model nStat, HS Technologies).

RESULTS AND DISCUSSION

Figure 1 summarizes the XRD results of $Sm_{1-x}BaCo_2O_{5+d}$ (x = 0, 0.01, 0.02, 0.03, 0.04, 0.05, 0.10, and 0.15) calcined at 1,100°C for 8 h to investigate the synthesis characteristics of these oxide systems with respect to the non-stoichiometric compositions. In addition, indicators for $BaCoO_{2.6}$ phase (▼) and CoO (▼) were added to all XRD results. The characteristic XRD patterns discovered in the vicinity of 23.4°, 33.0°, 40.4°, 46.7°, 59.1°, 69.2°, 78.1°) indicate that the $Sm_{1-x}BaCo_2O_{5+d}$ oxide systems were synthesized as a single phase from the stoichiometric $SmBaCo_2O_{5+d}$ (SBCO) composition in which Sm was not removed and the non-stoichiometric composition in which 0.01, 0.02, 0.03, and 0.04 mol% of Sm (SBCO_0.99, SBCO_0.98, SBCO_0.97, and SBCO_0.96) were partially removed. However, when Sm was removed at 0.05 mol% or more, $BaCoO_{2.6}$ phase appeared (SBCO_0.95, SBCO_0.90). Especially, when Sm was removed 0.15 mol%, CoO phase was additionally identified (SBCO_0.85).

Supplementary Figure 1 summarizes the SEM images of the $Sm_{1-x}BaCo_2O_{5+d}$ (x = 0, 0.01, 0.05, and 0.10) oxide systems. Overall particle size decreases from (A) to (C), which results in porous microstructures as the non-stoichiometry composition increases. Especially, the particular microstructural characteristics can be seen in **Supplementary Figures 1C,D**. For example, in **Supplementary Figure 1D**, in which a part of SBCO_0.95 is magnified, white crystals can be seen protruding like arrowheads on the cathode surface. Particle size of arrowheads is very small, so it was impossible to carry out EDS (Energy-Dispersive x-ray Spectroscopy) analysis. However, as mentioned in the XRD results, it is known that the white arrowheads are formed by crystal structure of $BaCoO_{2.6}$. In other words, it can be thought that a small amount of secondary phase particles was generated on the cathode surface. For the SBCO_0.90 composition, which further increased the non-stoichiometry, as can be seen in **Supplementary Figures 1E,F**, particles like pebbles can be seen attached to the cathode surface. It is found that the particle size increased as the concentration of $BaCoO_{2.6}$ increased via the increase of the non-stoichiometry.

Figures 2A,B show that the overall ASR value decreases as the tendency toward non-stoichiometric composition increases (= the removal amount of Sm increases). For example, the ASRs of SBCO_1, SBCO_0.95, and SBCO_0.90 were about 0.301, 0.147, and 0.119 $\Omega \cdot cm^2$ at 600°C. These ASR values are closely related to the composition because the lowest ASR value was observed for the SBCO_0.90 composition. However, in the composition of SBCO_0.85 with an increased non-stoichiometric condition, the ASR value measured at 600°C was 0.179 $\Omega \cdot cm^2$, which is relatively higher than the ASR values of SBCO_0.95 and SBCO_0.90 measured at 600°C. That is, from the non-stoichiometric compositions of $Sm_{1-x}BaCo_2O_{5+d}$, the characteristics of the percolation composition showing the lowest ASR value in the chemical composition of $Sm_{0.90}BaCo_2O_{5+d}$ can be found. This tendency can also be confirmed in the layered perovskite composition of $LnBaCo_2O_{5+d}$ in which Pr was substituted into the $A^{/}$-site of the layered perovskite (Zhang et al., 2016; Idrees et al., 2019).

For example, according to the literature on ASR characteristics caused by non-stoichiometric composition of $Pr_{1-x}BaCo_2O_{5+d}$ (x = 0–0.1), $PrBaCo_2O_{5+d}$ (PBCO) and $P_{0.92}BaCo_2O_{5+d}$ (PBCO_0.92) exhibit ASR values of about 0.097 and 0.081 $\Omega \cdot cm^2$ at 700°C (Zhang et al., 2016). In the case of electrochemical properties related to the non-stoichiometric composition that reduce the amount of Pr in $Pr_{1-x}BaCo_2O_{5+d}$ oxide systems, when the degree of non-stoichiometry of the $A^{/}$-site increased, the ASR tended to decrease; at the same time, the percolation composition was also exhibited.

As the degree of non-stoichiometry of the $A^{/}$-site increases in the $Sm_{1-x}BaCo_2O_{5+d}$ oxide systems, the value of the activation energy tends to decrease. This trend can also be confirmed in works in the literature that have studied the electrochemical properties of similar layered perovskite structure composition in which the $A^{/}$-site is partially removed (Jiang et al., 2014; Yi et al., 2016). As a result of calculating the activation energy values, as shown in **Figure 2A**, $Sm_{0.98}BaCo_2O_{5+d}$ and $Sm_{0.96}BaCo_2O_{5+d}$ compositions have slightly increased activation energy values, but overall activation energy showed a tendency to decrease. For example, the activation energy of $SmBaCo_2O_{5+d}$ was 1.094 eV. As degree of non-stoichiometry of $A^{/}$-site increases, the activation energy decreases. The values of $Sm_{0.95}BaCo_2O_{5+d}$ and $Sm_{0.90}BaCo_2O_{5+d}$ were calculated and found to be 0.970 and 0.948 eV. In addition, the value (0.987eV) of $Sm_{0.85}BaCo_2O_{5+d}$ increased slightly compared to that of $Sm_{0.90}BaCo_2O_{5+d}$. When comparing the activation values of the $Sm_{1-x}BaCo_2O_{5+d}$ oxide systems synthesized in this experiment with those of recently reported cathode materials showing excellent electrochemical reaction, it can be determined that $Sm_{1-x}BaCo_2O_{5+d}$ oxide systems have relatively lower activation energy (Clematis et al., 2019; Anbo et al., 2020). In general, the activation energy indicates the strength of the energy barrier that must be overcome when oxygen ions move through the oxygen vacancies (Kaur and Singh, 2020).

For example, as mentioned above, Jiang et al. reported on the compositions of PBCO and $P_{0.95}BCO$; these compositions showed activation energy values of 1.19 and 0.98 eV (Jiang et al., 2014). This activation energy phenomenon was caused by the increase of concentration of pathways through which oxygen ions could move because the deficiency of Pr in $A^{/}$-sites resulted in many more oxygen vacancies in the PrO layer. The activation energy value was an 0.948 eV, excellent even when compared with those of other compositions of layered perovskite (Jiang et al., 2014; Yi et al., 2016). In addition, as shown in **Figure 2B**, $Sm_{0.90}BaCo_2O_{5+d}$ had the lowest ASR values in this experiment, showing values of 0.119, 0.061, and 0.035 $\Omega \cdot cm^2$ at 600, 650, and 750°C, respectively.

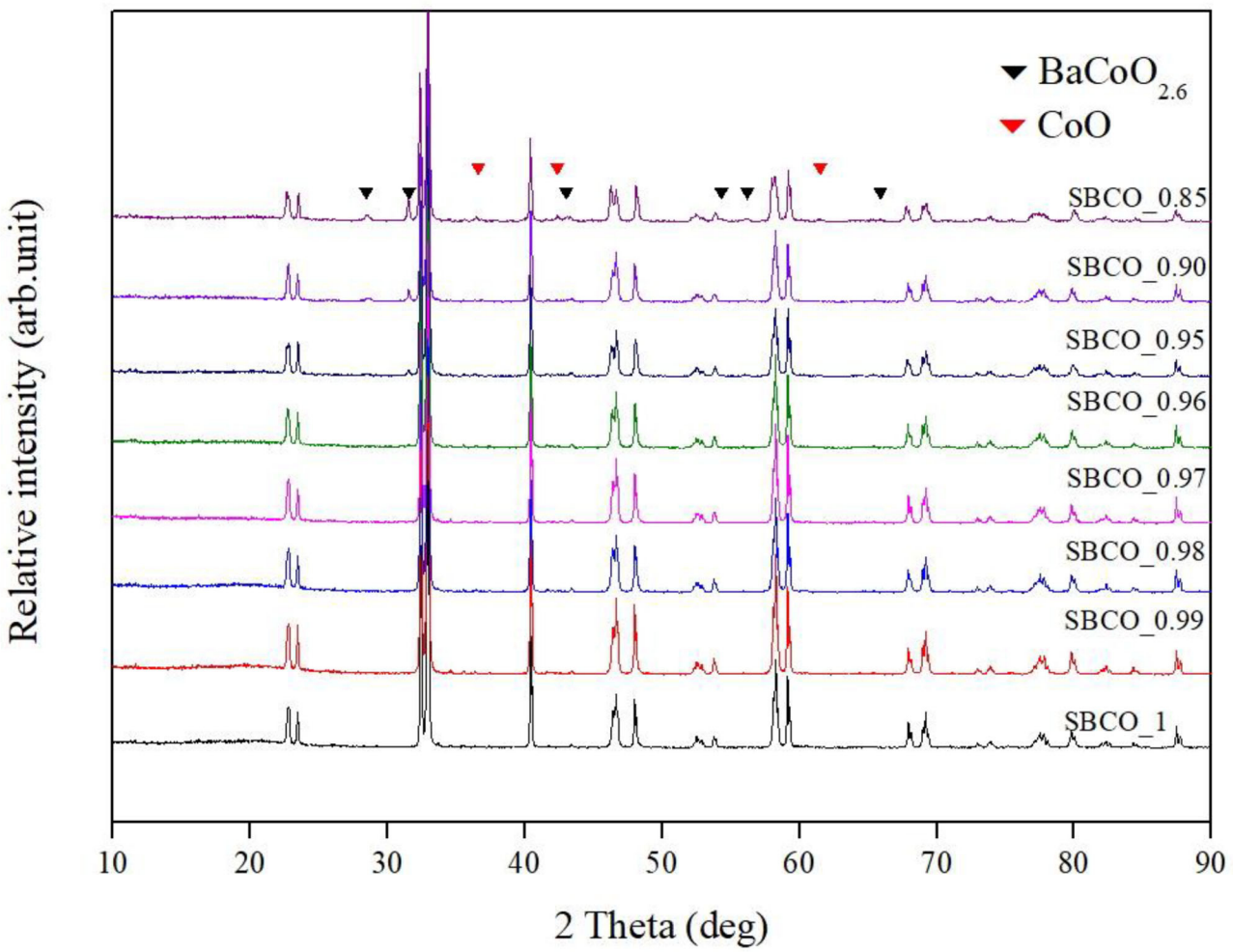

FIGURE 1 | X-ray diffraction (XRD) patterns of $Sm_{1-x}BaCo_2O_{5+d}$ ($x = 0$, 0.01, 0.02, 0.03, 0.04, 0.05, 0.10, and 0.15) oxide systems calcined at 1,100°C for 8 h.

The results of an equivalent circuit of SBCO_0.90 are given in **Table 2** and **Figure 3** to confirm the rate determining step (RDS). In **Table 2**, the impedance results measured at 600°C using the $Sm_{1-x}BaCo_2O_{5+d}$ oxide systems were divided into R_1, R_2, and R_3.

In general, the impedance results of SOFC cathode materials can be classified by the frequency range (Murray et al., 1998). In equivalent circuits, the resistance from the high frequency (HF, 10^3 Hz∼) is directly related with the charge transfer (R_1) when oxygen ions move across the interface between the cathode and the electrolyte. The resistance from the middle frequency (MF, 10^2∼1 Hz) range is attributed to the resistance (R_2) that occurs when oxygen ions move inside the bulk of the cathode. The lower frequency (LF, below 1 Hz) arc is ascribed to oxygen dissociation and bulk or surface oxygen diffusion process (R_3). Therefore, ASR results were analyzed by subdividing them into R_1, R_2, and R_3.

In **Figures 3A–C**, the results for an equivalent circuit consisting of R_1, R_2, and R_3 and the impedance results measured directly for the SBCO_0.90 composition at 550, 600, and 650°C are summarized. **Figure 3D** presents the impedance results of SBCO_0.90 measured in the temperature range of 500∼750°C, as well as the values R_1, R_2, and R_3 separating these results, obtained using an equivalent circuit.

As can be seen from **Figures 3A–C**, R_2 takes up the largest proportion of the total resistance. These results are also summarized in **Table 2**. In addition, all the compositions of $Sm_{1-x}BaCo_2O_{5+d}$ ($x = 0$, 0.01, 0.02, 0.03, 0.04, 0.05, 0.10, and 0.15) applied in this experiment showed the same results. For example, R_2 of SBCO_1 was calculated and found to be 0.2162 $\Omega \cdot cm^2$, which is about 72% of the total ASR; however, R_1 (0.074 $\Omega \cdot cm^2$) and R_3 (0.0104 $\Omega \cdot cm^2$) occupied only 28% of the total resistance. This trend does not change with increasing degree of non-stoichiometry of compositions and the R_2 values of SBCO_0.95 and SBCO_0.90 are 0.1112 and 0.0847 $\Omega \cdot cm^2$, with proportions of about 75 and 71% of the total resistance. Therefore, it can be

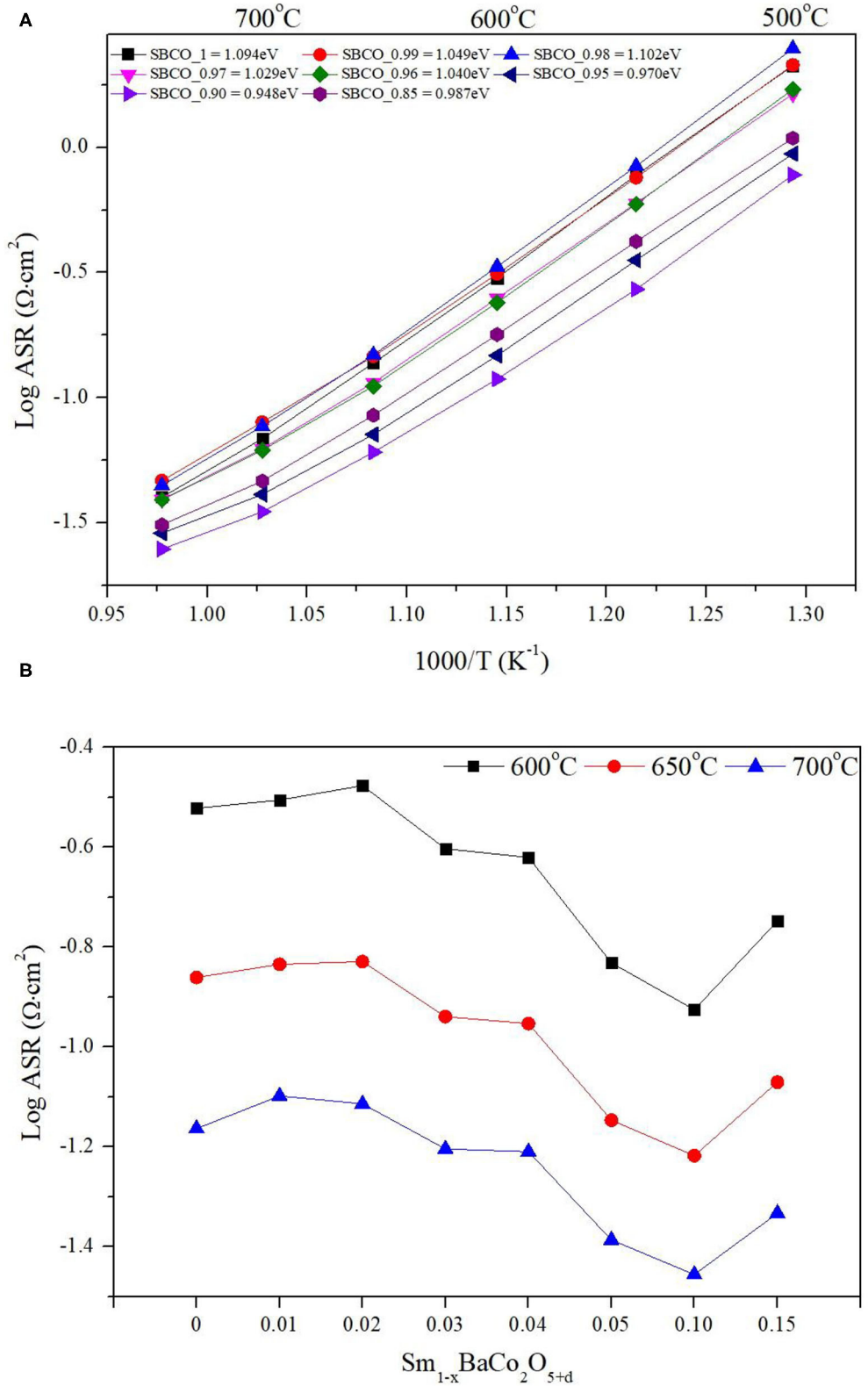

FIGURE 2 | Area specific resistance (ASR) results of **(A)** $Sm_{1-x}BaCo_2O_{5+d}$ oxide systems with respect to temperature, and **(B)** ASR dependence of cathodic polarization with respect to compositions at 600, 650, and 700°C.

TABLE 2 | ASR results of symmetrical half cells comprised of $Sm_{1-x}BaCo_2O_{5+d}$/CGO 91/$Sm_{1-x}BaCo_2O_{5+d}$ ($x = 0$, 0.01, 0.02, 0.03, 0.04, 0.05, 0.10, and 0.15) oxide systems measured at 600°C.

Composition	R_1(2.5 MHz–100 Hz) Ω·cm^2	R_2(100 Hz–1 Hz) Ω·cm^2	R_3(1 Hz–0.05 Hz) Ω·cm^2
SBCO_1	0.0741	0.2162	0.0104
SBCO_0.99	0.0550	0.2405	0.0167
SBCO_0.98	0.0558	0.2628	0.0152
SBCO_0.97	0.0550	0.1826	0.0118
SBCO_0.96	0.0559	0.1702	0.0135
SBCO_0.95	0.0279	0.1112	0.0082
SBCO_0.90	0.0250	0.0847	0.0091
SBCO_0.85	0.0317	0.1355	0.0115

determined that the RDS of $Sm_{1-x}BaCo_2O_{5+d}$ ($x = 0$, 0.01, 0.02, 0.03, 0.04, 0.05, 0.10, and 0.15) oxide systems tested is R_2, which is the resistance when oxygen ions move in the cathode bulk. In addition, in **Table 2**, all R_1, R_2, and R_3 ASR values decreased as the non-stoichiometry compositions increased. Especially for the SBCO_0.95 composition, ASR decreases rapidly. The reason for the rapid decrease in ASR results for SBCO_0.95 is the effect of $BaCoO_{2.6}$ phase, as described in the above XRD and SEM results. In the case of the SBCO_0.90 composition, which showed increased concentration of $BaCoO_{2.6}$, the ASR value was lower than that of SBCO_0.95.

According to Qi et al., who studied the composition of the perovskite structure $BaCo_{0.6}Zr_{0.4}O_{3-\delta}$ (BZC-BC) in nanocomposite form, advanced electrochemical properties were reported when a secondary phase of $BaCo_{0.96}Zr_{0.04}O_{3-\delta}$ transformed into $BaZr_{0.82}Co_{0.18}O_{3-\delta}$ main phase. For example, single-phase $BaZr_{0.80}Co_{0.20}O_{3-\delta}$ (BZC2) showed a power density of 33 mW·cm^{-2} at 750°C. However, the BCZ-BC oxide system containing the secondary phase ($BaCo_{0.96}Zr_{0.04}O_{3-\delta}$) showed a value of about 1,530 mW·cm^{-2}, an increase of 46 times compared to the case of using single phase at the same temperature; this implies that the composition BZC-BC including secondary phase exhibited excellent properties. In addition, in the case of multi-phase cathode materials mixed with various compositions containing Ba and Co based oxide, it was reported that $BaCoO_{3-x}$ generates a large number of oxygen vacancies that promote the oxygen reduction reaction (ORR) by assisting the movement of reduced oxygen ions (Qi et al., 2020). Therefore, the composition of SBCO_0.90 applied in this experiment, which has the lowest ASR characteristics, is affected by activated ORR caused by $BaCoO_{2.6}$.

Figure 4 summarizes the impedance results of the $Sm_{1-x}BaCo_2O_{5+d}$ ($x = 0$, 0.05, 0.10, and 0.15) oxide systems measured at 600°C. ASR values decrease as the effect of degree of non-stoichiometry composition increased. However, in the SBCO_0.85 composition, the R_2 value increased sharply and the total ASR increased. From these results, it can be determined that the CoO phase found in the composition of SBCO_0.85, shown in **Figure 1**, somewhat limits the movement of oxygen ions in the bulk state of the cathode.

Additionally, electrochemical analysis was carried out using composite cathodes prepared by mixing CGO91 powder and SBCO_0.90. For the fabrication of the composite cathodes, the synthesized SBCO_0.90 was mixed with CGO91 at a weight ratio of 1:1. The summarized ASR results of the composite cathodes are given in **Figure 5** and **Table 3**. As can be seen in **Figure 5**, the two cathode materials of single phase SBCO_0.90 and composite phase exhibited similar ASR values over the entire measured temperature range. For example, the composite cathode showed ASR values of 0.031 and 0.024 $\Omega \cdot cm^2$ at 700 and 750°C; it showed a slight difference of only 0.004 $\Omega \cdot cm^2$ compared to the ASR value of SBCO_0.90. In the general case of composite cathodes, ASRs measured from the composite cathode tend to decrease. However, a large amount of CGO91 could rather interfere with the movement of oxygen ions in the bulk and on the surface of the cathode, and so composite did not significantly affect the reduction of resistance of the composite cathode applied in this experiment.

From these results, it can be confirmed that the effect of the composite cathode is not significant for the non-stoichiometric composition state in which the quantitative composition of the A/-site of the layered perovskite changes. However, the thermal expansion problem of the SOFC cathode operating at high temperature range can be solved when the composite cathode concept is applied. In other words, thermal stability can be secured by lowering the thermal expansion coefficient (TEC). Co-based materials have high TEC of 20–25 $\times$ 10^{-6}K^{-1} when SOFC is operated in high temperature operating temperature range; however, CGO91 has a relatively low TEC of 12–13.1 $\times$ 10^{-6}K^{-1} (Kim et al., 2009). Therefore, the high TEC value generated from the cathode material substituted with Co can lower the coefficient of thermal expansion through composite cathodes.

Kim et al., who synthesized the composition of $SmBaCo_2O_{5+d}$ through in a composite with CGO91 at an ∼50:50 ratio, reported that the TEC of 20.2 $\times$ 10^{-6}K^{-1} decreased by about 66% to 13.3 $\times$ 10^{-6}K^{-1} (Kim et al., 2009). By mixing the electrolyte materials and cathode materials, the thermal stability increases while the TECs rapidly decrease. Therefore, it is suitable to use a composite cathode with excellent electrochemical properties and relatively lower TEC when applying single phase SBCO_0.90 at a relatively high temperature (650°C∼). However, it is desirable to use a single phase cathode when using at a relatively lower temperature range.

The ASRs of $Sm_{1-x}BaCo_2O_{5+d}$ ($x = 0$, 0.01, 0.02, 0.03, 0.04, 0.05, 0.10, and 0.15) applied in this study were 0.083, 0.095, 0.088, 0.074, 0.075, 0.041, 0.035, and 0.045 $\Omega \cdot cm^2$, respectively, at 700°C. All compositions can be sufficiently used as cathode materials at 700°C because these ASR results are all 0.15 $\Omega \cdot Cm^2$ or less (Steele, 1996). The ASRs of SBCO_0.97, SBCO_0.96, SBCO_0.95, and SBCO_0.85 are 0.130, 0.129, 0.072, and 0.085 $\Omega \cdot cm^2$ at 650°C. Especially, the SBCO_0.90 composition has an ASR of 0.130 $\Omega \cdot cm^2$, and can thus be used as a cathode material at a relatively low temperature of 600°C.

The electrical conductivity results of the $Sm_{1-x}BaCo_2O_{5+d}$ ($x = 0$, 0.01, 0.02, 0.03, 0.04, and 0.05) oxide systems are

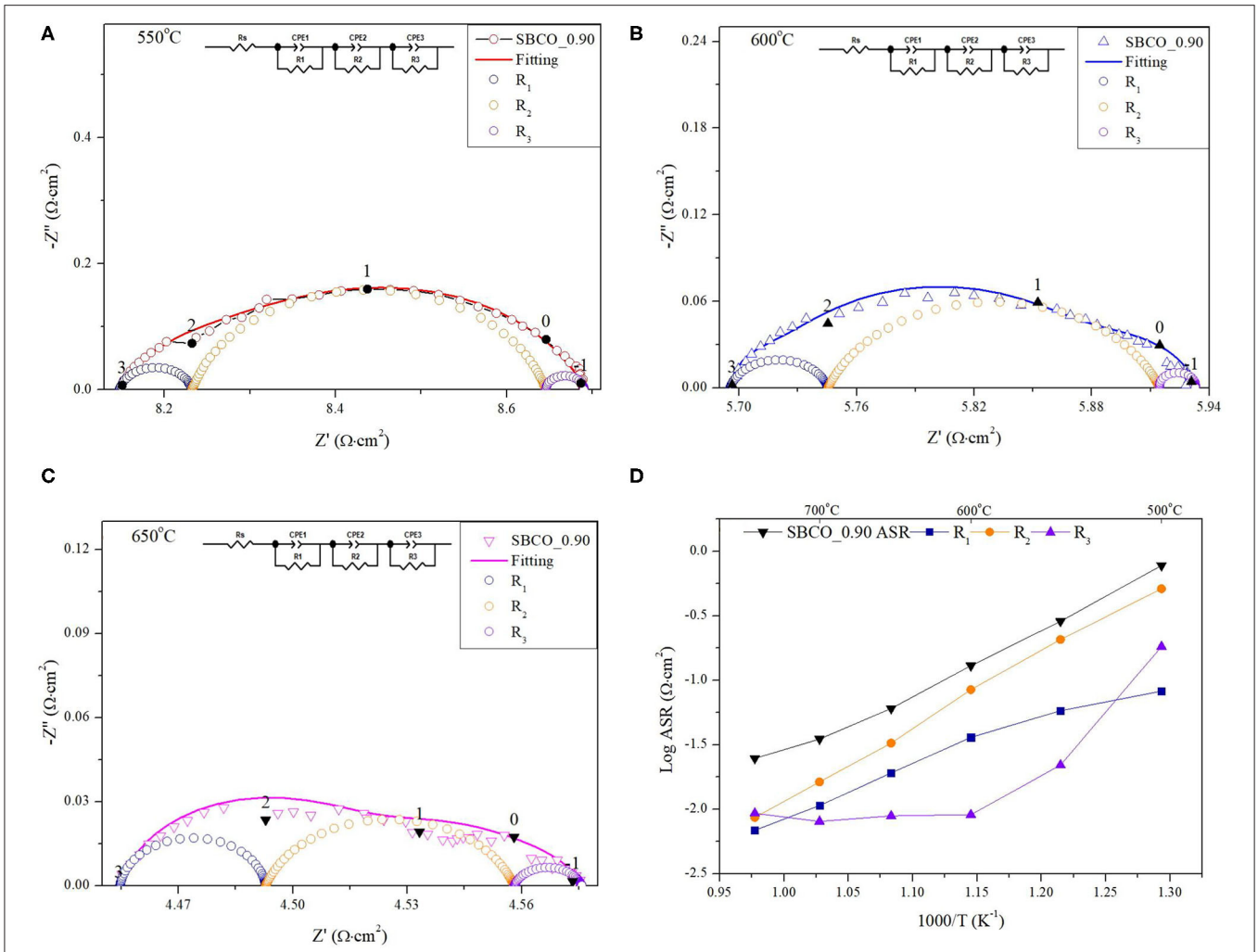

FIGURE 3 | Impedance plots of $Sm_{0.90}BaCo_2O_{5+d}$ measured at **(A)** 550°C, **(B)** 600°C, and **(C)** 650°C with equivalent circuit in inset. **(D)** shows ASR calculated from R_1 (■), R_2 (●), and R_3 (▲) of equivalent circuit; total ASRs are shown as (▼).

summarized in **Figure 6A**. According to the literature related to the electrical conductivity behavior of $SmBaCo_2O_{5+d}$ (SBCO, in this study SBCO_1), SBCO showed a maximum electrical conductivity value (570 S/cm) in the range of 200–250°C; then, the electrical conductivity started to decrease from 250°C, indicating Metal Insulator Transition (MIT) behavior (Kim et al., 2009). The electrical conductivity tendency of MIT in the $LnBaCo_2O_{5+d}$ system is influenced by various factors, such as small degree of polaron hopping and oxygen content (Maignan et al., 1999; Moon et al., 2001).

However, in **Figures 6A,B**, it can be seen that the temperature at which the change in electrical conductivity occurs is directly related to the non-stoichiometric composition. For the compositions of SBCO_1, SBCO_0.99, SBCO_0.98, and SBCO_0.97, which are relatively less influenced by the non-stoichiometric composition, the electrical conductivity value increases from 50°C and then begins to decrease at 200°C. For the SBCO_0.96 and SBCO_0.95 compositions, which show increased influence of the non-stoichiometric composition in the A/-site, the electrical conductivity began to decrease at 250°C, as shown in **Figure 6A**. On the other hand, the electrical conductivity of SBCO_0.90 decreased from 650°C and the electrical conductivity values of SBCO_0.85 began to decrease at 450°C, as shown in **Figure 6B**.

From these results, it can be concluded that when the influence of the non-stoichiometric composition increases, temperature of the MIT behavior increases. The electrical conductivities of materials having non-stoichiometric compositions, namely the $Sm_{1-x}BaCo_2O_{5+d}$ (x = 0, 0.01, 0.02, 0.03, 0.04, 0.05, 0.10, and 0.15) oxide systems, are summarized in **Figure 6C** for the intermediate temperature range (500–750°C). The values of electrical conductivity increase as the effect of non-stoichiometric composition increases ($x \leq 0.05$). That is, the electrical conductivity increases when a relatively small amount of Sm is removed in the range of $Sm_{1-x}BaCo_2O_{5+d}$ ($x = 0$, 0.01, 0.02, 0.03, 0.04, and 0.05). Especially the SBCO_0.95 composition

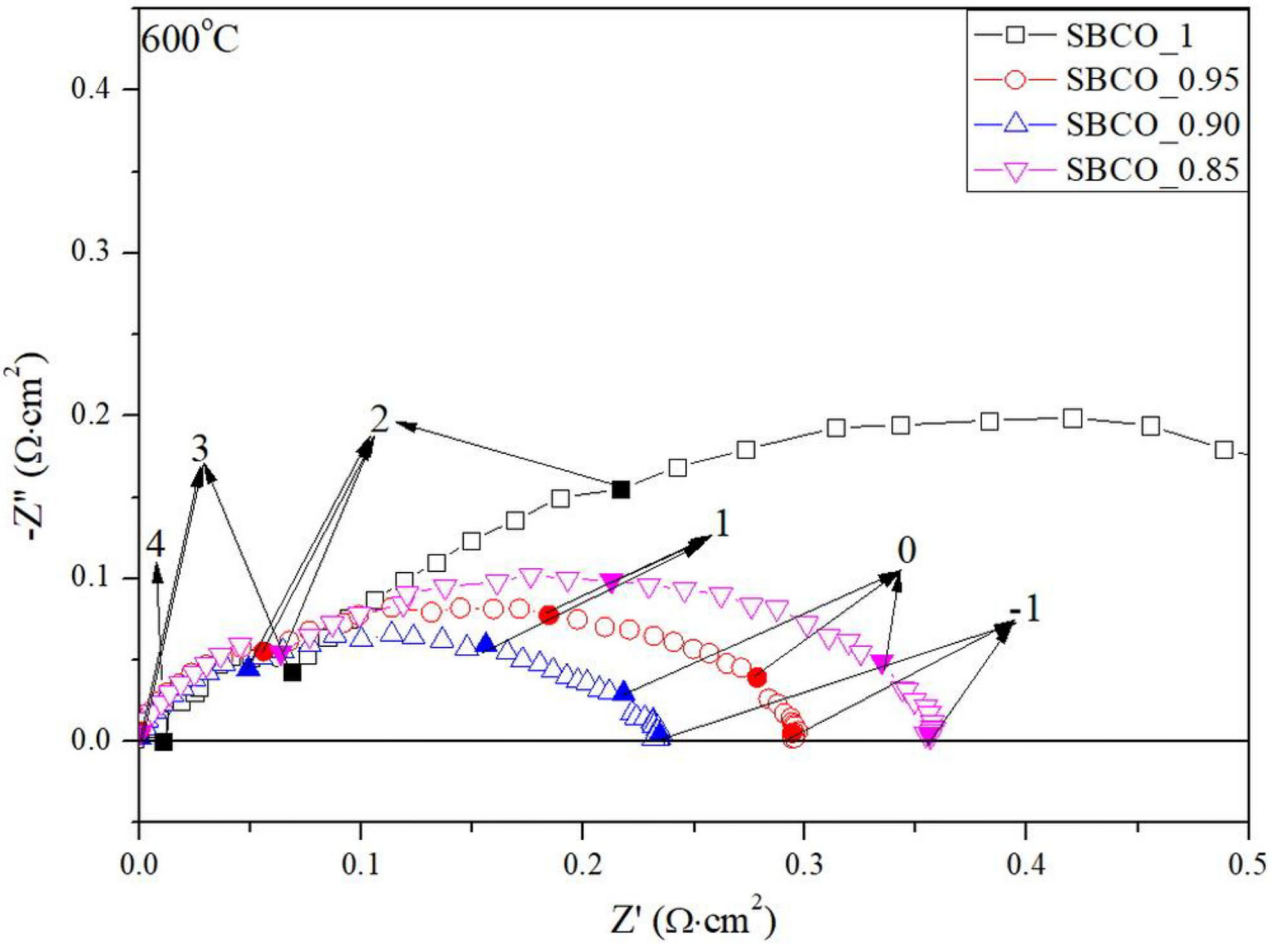

FIGURE 4 | Impedance results of $Sm_{1-x}BaCo_2O_{5+d}$ ($x = 0$, 0.05, 0.10, and 0.15) measured at 600°C. For exact comparisons of ASRs, ohmic resistances were removed in these results; inset numbers denote logarithm of measuring frequency.

exhibited electrical conductivity values of about 917 and 732 S/cm at 500 and 600°C and showed the highest electrical conductivity values among the measured compositions. However, when the non-stoichiometric composition increased from $x = 0.05$ in the $Sm_{1-x}BaCo_2O_{5+d}$ ($x = 0$, 0.01, 0.02, 0.03, 0.04, 0.05, 0.10, and 0.15) oxide systems, the electrical conductivity value decreased. It can be concluded that this is because a large amount of $BaCoO_{2.6}$ phase activates the conductivity of ions but inhibits the transfer of charge carriers (Chen et al., 2011; Liu et al., 2011).

Therefore, it can be seen that a percolation phenomenon that affects the electrical conductivity according to the non-stoichiometry is found in the $Sm_{1-x}BaCo_2O_{5+d}$ ($x = 0$, 0.01, 0.02, 0.03, 0.04, 0.05, 0.10, and 0.15) oxide systems. In addition, the conductivity characteristics found in the non-stoichiometric compositions exceeding $x = 0.04$ can be determined by the influence of the secondary phase. However, the detailed influence of the $BaCoO_{2.6}$ composition for electrical conductivity in $SmBaCo_2O_{5+d}$ oxide systems is not discussed now and will be reported later.

Therefore, it can be determined that as the deficiency level of $A^{/}$-site increases, the electrical conductivity behavior conditions in this experiment changed. In addition, the lowest conductivity value in the IT range was 169 S/cm, a value exceeding 100 S/cm. This is a value that exceeds the standard that must be satisfied for material to be used as cathode for SOFC; therefore, all compositions can be suitable for use as cathode material for IT-SOFC (Tu et al., 1997). In addition, SBCO_0.95, having the highest electrical conductivity values in the IT ranges, also showed electrical conductivity values higher than those of $NdBaCo_2O_{6-d}$ and the compositions of $LnBaCo_2O_{5+d}$ (Ln = La, Pr, Nd, Sm, Gd, Y) (Kim and Manthiram, 2015; Yi et al., 2016). Especially SBCO_0.90, which shows excellent electrochemical properties, also showed a high electrical conductivity value of 500 S/cm or more in the IT range.

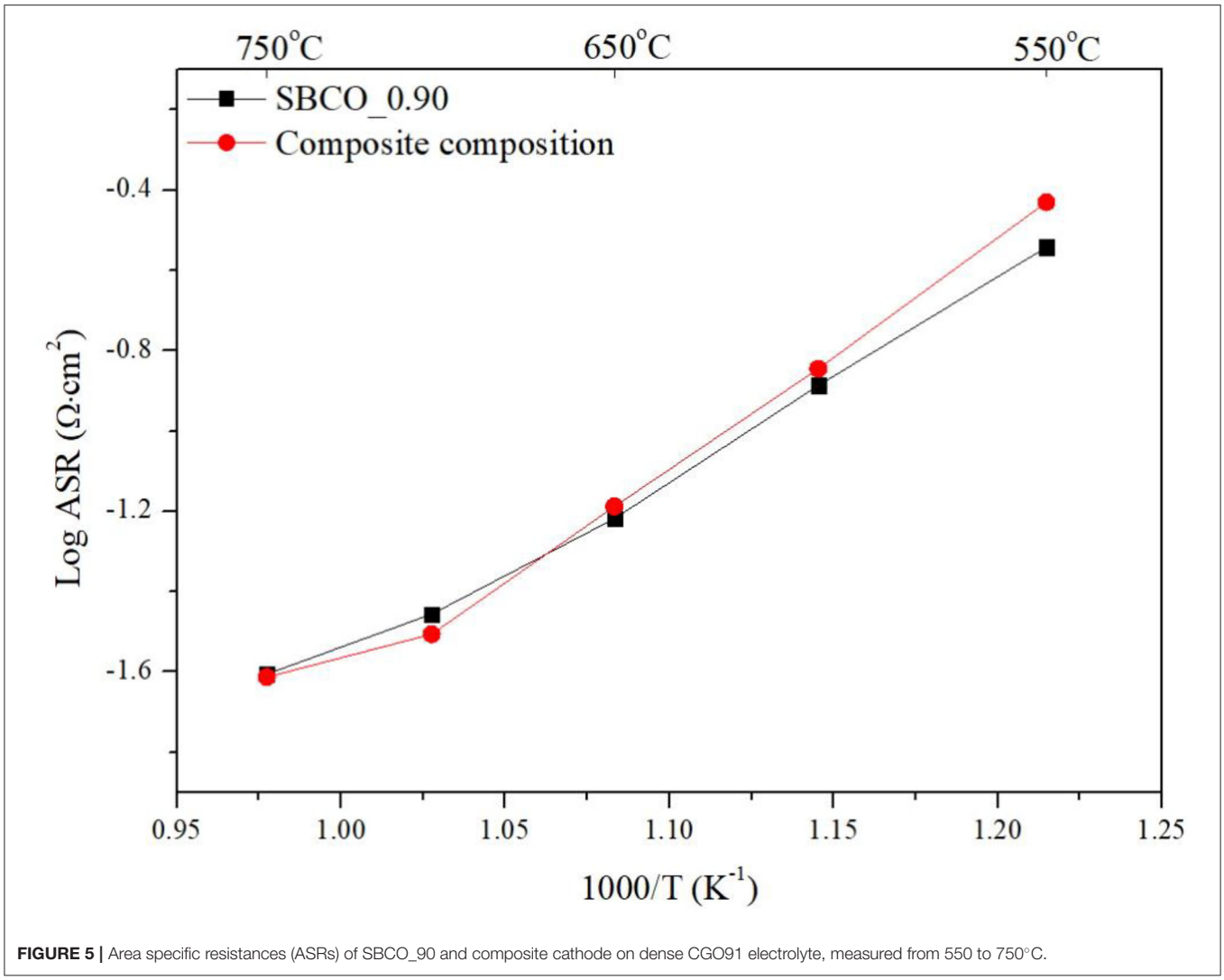

FIGURE 5 | Area specific resistances (ASRs) of SBCO_90 and composite cathode on dense CGO91 electrolyte, measured from 550 to 750°C.

TABLE 3 | ASR comparisons of single phase cathode SBCO_0.90 and composite cathode measured from 550 to 750°C.

Composition	550	600	650	700	750	T(°C)
SBCO_0.90	0.271	0.119	0.061	0.035	0.025	$\Omega \cdot cm^2$
Composite	0.349	0.139	0.056	0.031	0.024	$\Omega \cdot cm^2$

CONCLUSION

The electrochemical properties of materials having non-stoichiometric compositions in which Sm of the A/-site was partially removed in $SmBaCo_2O_{5+d}$ oxide systems were studied for direct application of these materials as cathodes for IT-SOFC. In the case of the $Sm_{1-x}BaCo_2O_{5+d}$ (x = 0, 0.01, 0.02, 0.03, 0.04, 0.05, 0.10, and 0.15) oxide systems synthesized by SSR, single phase composition was confirmed for $Sm_{0.96}BaCo_2O_{5+d}$ (SBCO_0.96). However, secondary phase of $BaCoO_{2.6}$ was found for compositions of $Sm_{0.95}BaCo_2O_{5+d}$, (SBCO_0.95) in $Sm_{1-x}BaCo_2O_{5+d}$ oxide systems. Additional phase of CoO appeared for the SBCO_0.85 composition.

All of the synthesized compositions showed excellent electrochemical properties, with ASR values $< 0.15\ \Omega \cdot cm^2$ at 650°C. The $Sm_{0.90}BaCo_2O_{5+d}$ (SBCO_0.90) showed the lowest ASR characteristics, with values of 0.119, 0.061, and 0.035 $\Omega \cdot cm^2$ at 600, 650, and 700°C. Additionally, the ASRs of the composite cathodes prepared by mixing with an electrolyte using CGO91 and SBCO_0.90 were 0.139 and 0.056 $\Omega \cdot cm^2$ at 600 and 650°C. All compositions exhibit electrical conductivity values of more than 100 S/cm over the temperature range (500–750°C) for IT-SOFC. It was also confirmed that the behavior conditions of MIT change as the non-stoichiometry composition of the A/-site increases. SBCO_0.90 composition, which had the best electrochemical properties, showed the maximum (568 S/cm)

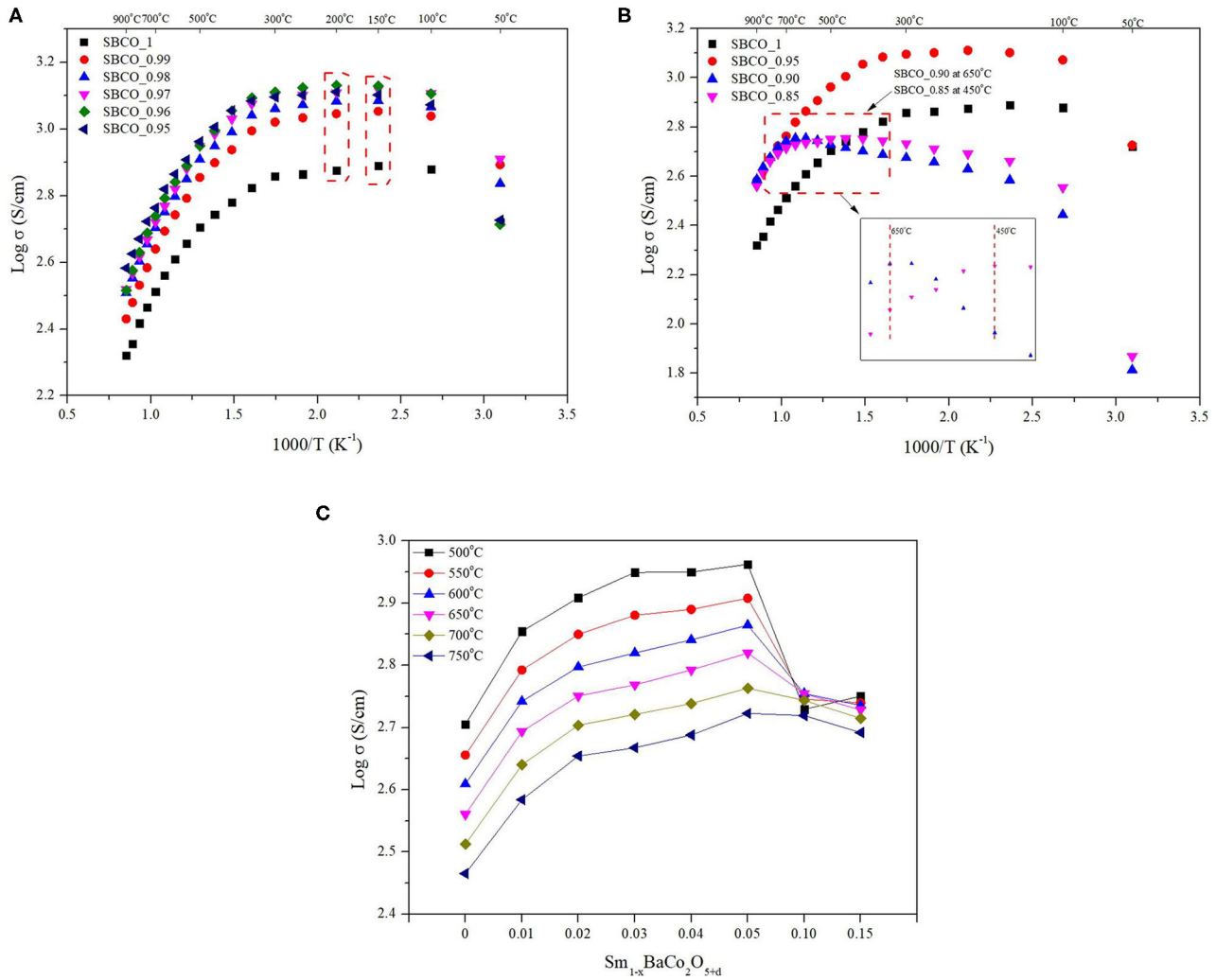

FIGURE 6 | Electrical conductivity results of $Sm_{1-x}BaCo_2O_{5+d}$ oxide systems cathode materials for each condition. **(A)** Electrical conductivity results of $Sm_{1-x}BaCo_2O_{5+d}$ ($x = 0$, 0.01, 0.02, 0.03, 0.04, and 0.05) from 50 to 900°C in air. **(B)** Electrical conductivity results of $Sm_{1-x}BaCo_2O_{5+d}$ ($X = 0$, 0.05, 0.10, and 0.15) 50–900°C in air. **(C)** Electrical conductivity results of $Sm_{1-x}BaCo_2O_{5+d}$ ($x = 0$, 0.01, 0.02, 0.03, 0.04, 0.05, 0.10, and 0.15) from 500 to 750°C in air.

and minimum (387 S/cm) electrical conductivity values in the temperature range of 500–900°C.

DATA AVAILABILITY STATEMENT

The original contributions presented in the study are included in the article/**Supplementary Material**, further inquiries can be directed to the corresponding author/s.

AUTHOR CONTRIBUTIONS

CK was responsible for conducting all experiments, analyzing experimental data, and writing papers. SW teaches experimental methods and informs questions about results. KS, S-WB, HK, and WC helped to write the manuscript. KS provided additional help in thesis publication. Finally, JK coordinated the overall experimental design, direction, and schedule. In addition, he reviewed the paper and gave direction. All authors contributed to the article and approved the submitted version.

FUNDING

This work was supported by a National Research Foundation of Korea (NRF) grant funded by the Korean Government (MSIT) (No. 2019R1A2C1087534) and the research fund of Hanbat National University in 2019.

SUPPLEMENTARY MATERIAL

The Supplementary Material for this article can be found online at: https://www.frontiersin.org/articles/10.3389/fchem.2021.633868/full#supplementary-material

REFERENCES

Akahoshi, D., and Ueda, Y. (2001). Oxygen nonstoichiometry, structures, and physical properties of $YBaCo_2O_{5+x}$ ($0.00 \leq x \leq 0.52$). *J. Solid State Chem.* 156, 355–363. doi: 10.1006/jssc.2000.9006

Anbo, Y., Tian, X., Liping, S., Qiang, L., Lihua, H., and Hui, Z. (2020). Effects of rare earth doping on electrochemical properties of $NdBaCo_2O_{6-\delta}$ cathode materials. *J. Alloys Compd.* 837:155563. doi: 10.1016/j.jallcom.2020.155563

Chen, L., Lu, C. H., Zhao, Y. Z., Zhang, W. Y., Ni, Y. R., and Xu, Z. Z. (2011). The electrical conductivity and infrared properties of Ba-doped $SmCoO_{3-\lambda}$ composite oxides. *Adv. Mater. Res.* 239–242, 687–690. doi: 10.4028/www.scientific.net/AMR.239-242.687

Clematis, D., Barbucci, A., Presto, S., Viviani, M., and Carpanese, M. P. (2019). Electrocatalytic activity of perovskite-based cathodes for solid oxide fuel cells. *Int. J. Hydrog. Energy* 44, 6212–6222. doi: 10.1016/j.ijhydene.2019.01.128

Ding, H., and Xue, X. (2010). $PrBa_{0.5}Sr_{0.5}Co_2O_{5+\delta}$ layered perovskite cathode for intermediate temperature solid oxide fuel cells. *Electrochim. Acta* 55, 3812–3816. doi: 10.1016/j.electacta.2010.01.104

Frontera, C., García-Muñoz, J. L., Llobet, A., Mañosa, L., and Aranda, M. A. G. (2003). Selective spin-state and metal-insulator transitions in $GdBaCo_2O_{5.5}$. *J. Solid State Chem.* 171, 349–352. doi: 10.1016/S0022-4596(02)00232-3

Hoad, D. (2015). Reflections on small island states and the international climate change negotiations (COP21, Paris, 2015). *Isl. Stud. J.* 10, 259–262. Available online at: http://www.islandstudies.ca/sites/islandstudies.ca/files/ISJ-10-2-Hoad.pdf

Idrees, A., Jiang, X., Liu, G., Luo, H., Zhang, Q., Jiang, L., et al. (2019). An optimized synthesis route for high performance composite cathode based on a layered perovskite oxide of $PrBa_{0.92}Co_2O_{6-\delta}$ with cationic deficiency. *Int. J. Hydrog. Energy* 44, 4271–4280. doi: 10.1016/j.ijhydene.2018.12.183

Ingole, A. S., and Rakhonde, B. S. (2015). Hybrid power generation system using wind energy and solar energy. *Int. J. Sci. Res. Publ.* 5, 2250–3153. Available online at: http://www.ijsrp.org/digital-object-identifier.php

Jiang, X., Shi, Y., Zhou, W., Li, X., Su, Z., Pang, S., et al. (2014). Effects of Pr^{3+}-deficiency on structure and properties of $PrBaCo_2O_{5+\delta}$ cathode material-A comparison with Ba^{2+}-deficiency case. *J. Power Sources* 272, 371–377. doi: 10.1016/j.jpowsour.2014.08.091

Joung, Y. H., Kang, H., Choi, W. S., and Kim, J. H. (2013). Investigation of X-ray photoelectron spectroscopy and electrical conductivity properties of the layered perovskite $LnBaCo_2O_{5+d}$ (Ln = Pr, Nd, Sm, and Gd) for IT-SOFC. *Electron. Mater. Lett.* 9, 463–465. doi: 10.1007/s13391-013-0002-8

Kaur, P., and Singh, K. (2020). Review of perovskite-structure related cathode materials for solid oxide fuel cells. *Ceram. Int.* 46, 5521–5535. doi: 10.1016/j.ceramint.2019.11.066

Kim, G., Wang, S., Jacobson, A. J., Reimus, L., Brodersen, P., and Mims, C. A. (2007). Rapid oxygen ion diffusion and surface exchange kinetics in $PrBaCo_2O_{5+x}$ with a perovskite related structure and ordered a cations. *J. Mater. Chem.* 17, 2500–2505. doi: 10.1039/b618345j

Kim, J. H., Cassidy, M., Irvine, J. T. S., and Bae, J. (2010). Electrochemical investigation of composite cathodes with $SmBa_{0.5}Sr_{0.5}Co_2O_{5-\delta}$ cathodes for intermediate temperature-operating solid oxide fuel cell. *Chem. Mater.* 22, 883–892. doi: 10.1021/cm901720w

Kim, J. H., Kim, Y., Connor, P. A., Irvine, J. T. S., Bae, J., and Zhou, W. (2009). Structural, thermal and electrochemical properties of layered perovskite $SmBaCo_2O_{5+d}$, a potential cathode material for intermediate-temperature solid oxide fuel cells. *J. Power Sources* 194, 704–711. doi: 10.1016/j.jpowsour.2009.06.024

Kim, J. H., and Manthiram, A. (2015). Layered $LnBaCo_2O_{5+\delta}$ perovskite cathodes for solid oxide fuel cells: an overview and perspective. *J. Mater. Chem. A* 3, 24195–24210. doi: 10.1039/C5TA06212H

Kosnik, L. (2008). The potential of water power in the fight against global warming in the US. *Energy Policy* 36, 3252–3265. doi: 10.1016/j.enpol.2008.05.009

Kostogloudis, G. C., and Ftikos, C. (1999). Properties of A-site-deficient $La_{0.6}Sr_{0.4}Co_{0.2}Fe_{0.8}O_{3-\delta}$-based perovskite oxides. *Solid State Ionics* 126, 143–151. doi: 10.1016/S0167-2738(99)00230-1

Liu, Z., Cheng, L. Z., and Han, M. F. (2011). A-site deficient $Ba_{1-x}Co_{0.7}Fe_{0.2}Ni_{0.1}O_{3-\delta}$ cathode for intermediate temperature SOFC. *J. Power Sources* 196, 868–871. doi: 10.1016/j.jpowsour.2010.05.051

Maignan, A., Martin, C., Pelloquin, D., Nguyen, N., and Raveau, B. (1999). Structural and magnetic studies of ordered oxygen-deficient perovskites $LnBaCo_2O_{5+\delta}$, closely related to the "112" structure. *J. Solid State Chem.* 142, 247–260. doi: 10.1006/jssc.1998.7934

Minh, N. Q. (1993). Ceramic fuel cells. *J. Am. Ceram. Soc.* 76, 563–588. doi: 10.1111/j.1151-2916.1993.tb03645.x

Minh, N. Q. (2004). Solid oxide fuel cell technology - features and applications. *Solid State Ionics* 174, 271–277. doi: 10.1016/j.ssi.2004.07.042

Moon, J. W., Masuda, Y., Seo, W. S., and Koumoto, K. (2001). Influence of ionic size of rare-earth site on the thermoelectric properties of $RCoO_3$-type perovskite cobalt oxides. *Mater. Sci. Eng. B Solid-State Mater. Adv. Technol.* 85, 70–75. doi: 10.1016/S0921-5107(01)00645-6

Murray, E. P., Tsai, T., and Barnett, S. A. (1998). Oxygen transfer processes in $(La,Sr)MnO_3/Y_2O_3$-stabilized ZrO_2 cathodes: an impedance spectroscopy study. *Solid State Ionics* 110, 235–243. doi: 10.1016/S0167-2738(98)00142-8

Pelosato, R., Cordaro, G., Stucchi, D., Cristiani, C., and Dotelli, G. (2015). Cobalt based layered perovskites as cathode material for intermediate temperature solid oxide fuel cells: a brief review. *J. Power Sources* 298, 46–67. doi: 10.1016/j.jpowsour.2015.08.034

Qi, H., Zhao, Z., Wang, X., Tu, B., and Cheng, M. (2020). Self-assembled cubic-hexagonal perovskite nanocomposite as intermediate-temperature solid oxide fuel cell cathode. *Ceram. Int.* 46, 22282–22289. doi: 10.1016/j.ceramint.2020.05.307

Rodman, L. C., and Meentemeyer, R. K. (2006). A geographic analysis of wind turbine placement in Northern California. *Energy Policy* 34, 2137–2149. doi: 10.1016/j.enpol.2005.03.004

Steele, B. C. H. (1996). Survey of materials selection for ceramic fuel cells: II. Cathodes and anodes. *Solid State Ionics* 86–88, 1223–1234. doi: 10.1016/0167-2738(96)00291-3

Sun, J., Liu, X., Han, F., Zhu, L., Bi, H., Wang, H., et al. (2016). $NdBa_{1-x}Co_2O_{5+\delta}$ as cathode materials for IT-SOFC. *Solid State Ionics* 288, 54–60. doi: 10.1016/j.ssi.2015.12.023

Tietz, F. (1999). Thermal expansion of SOFC materials. *Ionics* 5, 129–139. doi: 10.1007/BF02375916

Tu, H. Y., Takeda, Y., Imanishi, N., and Yamamoto, O. (1997). $Ln_{1-x}Sr_xCoO_3$ (Ln = Sm, Dy) for the electrode of solid oxide fuel cells. *Solid State Ionics* 100, 283–288. doi: 10.1016/S0167-2738(97)00360-3

Wang, J., Meng, F., Xia, T., Shi, Z., Lian, J., Xu, C., et al. (2014). Superior electrochemical performance and oxygen reduction kinetics of layered perovskite $PrBa_xCo_2O_{5+\delta}$ (x = 0.90-1.0) oxides as cathode materials for intermediate-temperature solid oxide fuel cells. *Int. J. Hydrog. Energy* 39, 18392–18404. doi: 10.1016/j.ijhydene.2014.09.041

Wigley, T. M. L. (1998). The kyoto protocol: CO_2, CH_4 and climate implications. *Geophys. Res. Lett.* 25, 2285–2288. doi: 10.1029/98GL01855

Yi, K., Sun, L., Li, Q., Xia, T., Huo, L., Zhao, H., et al. (2016). Effect of Nd-deficiency on electrochemical properties of $NdBaCo_2O_{6-\delta}$ cathode for intermediate-temperature solid oxide fuel cells. *Int. J. Hydrogen Energy* 41, 10228–10238. doi: 10.1016/j.ijhydene.2016.04.248

Zhang, L., Yao, G., Song, Z., Niu, B., Long, W., Zhang, L., et al. (2016). Effects of Pr-deficiency on thermal expansion and electrochemical properties in $Pr_{1-x}BaCo_2O_{5+\delta}$ cathodes for IT-SOFCs. *Electrochim. Acta* 212, 522–534. doi: 10.1016/j.electacta.2016.07.014

Zhou, W., Lin, C. T., and Liang, W. Y. (1993). Synthesis and structural studies of the perovskite-related compound $YBaCo_2O_{5+x}$. *Adv. Mater.* 5, 735–738. doi: 10.1002/adma.19930051010

Conflict of Interest: The authors declare that the research was conducted in the absence of any commercial or financial relationships that could be construed as a potential conflict of interest.

frontiers in Chemistry

ORIGINAL RESEARCH
published: 27 May 2021
doi: 10.3389/fchem.2021.627699

Simulation of the Electrochemical Impedance in a Three-Dimensional, Complex Microstructure of Solid Oxide Fuel Cell Cathode and Its Application in the Microstructure Characterization

Vishwas Goel[1], *Dalton Cox*[2], *Scott A. Barnett*[2] *and Katsuyo Thornton*[1]*

[1]Department of Materials Science and Engineering, University of Michigan, Ann Arbor, MI, United States, [2]Department of Materials Science and Engineering, Northwestern University, Evanston, IL, United States

Electrochemical impedance spectroscopy (EIS) is a powerful technique for material characterization and diagnosis of the solid oxide fuel cells (SOFC) as it enables separation of different phenomena such as bulk diffusion and surface reaction that occur simultaneously in the SOFC. In this work, we simulate the electrochemical impedance in an experimentally determined, three-dimensional (3D) microstructure of a mixed ion-electron conducting (MIEC) SOFC cathode. We determine the impedance response by solving the mass conservation equation in the cathode under the conditions of an AC load across the cathode's thickness and surface reaction at the pore/solid interface. Our simulation results reveal a need for modifying the Adler-Lane-Steele model, which is widely used for fitting the impedance behavior of a MIEC cathode, to account for the difference in the oscillation amplitudes of the oxygen vacancy concentration at the pore/solid interface and within the solid bulk. Moreover, our results demonstrate that the effective tortuosity is dependent on the frequency of the applied AC load as well as the material properties, and thus the prevalent practice of treating tortuosity as a constant for a given cathode should be revised. Finally, we propose a method of determining the aforementioned dependence of tortuosity on material properties and frequency by using the EIS data.

Keywords: electrochemical impedance spectroscopy (EIS), tortuosity, 3D microstructure, solid oxide fuel cells, Adler-Lane-Steele model, Gerischer impedance

OPEN ACCESS

Edited by:
Dong Ding,
Idaho National Laboratory (DOE), United States

Reviewed by:
Yanxiang Zhang,
Harbin Institute of Technology, China
Francesco Ciucci,
Hong Kong University of Science and Technology, Hong Kong

****Correspondence:***
Katsuyo Thornton
kthorn@umich.edu

Specialty section:
This article was submitted to Electrochemistry, a section of the journal Frontiers in Chemistry

Received: *10 November 2020*
Accepted: *26 April 2021*
Published: *27 May 2021*

Citation:
Goel V, Cox D, Barnett SA and Thornton K (2021) Simulation of the Electrochemical Impedance in a Three-Dimensional, Complex Microstructure of Solid Oxide Fuel Cell Cathode and Its Application in the Microstructure Characterization. Front. Chem. 9:627699. doi: 10.3389/fchem.2021.627699

INTRODUCTION

With rising CO_2 levels in the atmosphere, low emission energy technologies for energy conversion and storage are needed to mitigate further increases in the global temperature. Such technologies in active research and development include, Li-ion batteries (Nitta et al., 2015), supercapacitors (Zhang L. et al., 2018), and several types of fuel cells like polymer electrolyte membrane fuel cells (PEMFC) (Wang et al., 2020), solid acid fuel cells (SAFC) (Lim et al., 2020), biofuel cells (BFC) (Shakeel et al., 2019), and solid oxide fuel cells (SOFC) (Mahato et al., 2015). In particular, SOFCs can be used to

produce electricity or, when used in reverse (as a solid oxide electrolyzer cell), to produce fuel, depending upon their applied polarization. Specifically, anodically polarized cells act as low-emission fuel-flexible electrochemical engines, and cathodically polarized cells store energy in the form of stable chemical bonds in H_2, CO, or CH_4 through electrolysis (Chen and Jiang, 2016; Mogensen et al., 2019). However, conventional high temperature SOFCs run at 800–1000°C, which makes their operation and maintenance highly cost-ineffective (Gao et al., 2016). The operating temperature has been reduced by the use of electrocatalytically active mixed ion-electron conducting (MIEC) cathodes such as (La,Sr) $(Co,Fe)O_{3-\delta}$ (LSCF) (Hwang et al., 2005; Liu et al., 2013; Niania et al., 2020) and $Sr(Ti,Fe)O_{3-\delta}$ (STF) (Yoo and Bouwmeester, 2012; Perry et al., 2015; Nenning et al., 2017), wherein the oxygen evolution reactions (OERs) and oxygen reduction reactions (ORRs) occur over the entire surface. To take advantage of this behavior, SOFC cathodes are designed to have complex and porous microstructures with a large specific surface area; however, such designs result in a high degree of tortuosity for ion transport, which limits the performance of SOFCs. Thus, it is important to accurately determine the tortuosity of a cathode microstructure and optimize it to enable high performance at low operating temperatures.

Several methods have been reported in the literature for determining the tortuosity of a porous electrode. These methods include: a) porosity-tortuosity relations, such as Bruggeman's relations (Bruggeman, 1935); b) calculations of the tortuous path length either through the distance propagation method (Chen-Wiegart et al., 2014) or the shortest path search method (Çeçen et al., 2012); and c) calculations of tortuosity based on the effective diffusivity (Wilson et al., 2006). Bruggeman's relations are known to be less suitable for a domain with connected solid phases and complex porous networks (as in a MIEC cathode) (Tjaden et al., 2018). The methods involving the calculations of tortuous path length or the effective diffusivity require the three-dimensional microstructural data as input, which is obtained through tomography (Wilson et al., 2006; Cooper et al., 2016). Unfortunately, availability of the necessary equipment to obtain tomographic data is not ubiquitous, sample preparation is time consuming, and the calculations are computationally expensive. Furthermore, these approaches provide tortuosity values associated with steady-state diffusion, yielding a single value and do not generally describe the tortuosity relevant to oscillating load or when surface reaction is present. Therefore, there is a need for alternate methods for determining tortuosity of a given SOFC electrode. Yu et al. (Yu et al., 2020) reported that tortuosity can be extracted from the diffusional impedance data; in particular, they showed that in systems limited by only bulk diffusion, the diffusional impedance data can be used to characterize a given microstructure in terms of tortuosity and the area of the loading boundary. They also showed that tortuosity is a function of the AC load frequency, which they define as effective tortuosity. Such use of impedance data to characterize the microstructure of a SOFC cathode is valuable to SOFC researchers since they widely use electrochemical impedance spectroscopy (EIS) to test SOFC performance.

In this study, we show that the EIS data of a SOFC MIEC cathode can be used to determine the tortuosity of the solid phase within the cathode. In particular, we consider a statistically representative (Scott Cronin et al., 2012) portion of an experimentally determined complex three-dimensional microstructure of an unbiased SOFC cathode. In the microstructure, we solve for the amplitude of the concentration-response to an applied AC load under the influence of surface reaction and bulk diffusion, and subsequently, use the solution to determine the impedance behavior. We investigate the effect of different material properties (bulk diffusion coefficient and reaction rate constant) on the impedance behavior, and on the effective tortuosity of the microstructure. From our simulations, we find that, due to the presence of surface reaction, the amplitude of oscillations in the oxygen vacancy concentration at the pore/solid interface of the cathode is lower than the amplitude within the bulk of the solid phase. Moreover, the difference between the two concentration amplitudes increases with an increase in the ratio between the reaction rate constant and the bulk diffusion coefficient. Such a difference is not taken into account by the widely used Adler-Lane-Steele (ALS) model, a macrohomogeneous model developed by Adler, Lane and Steele to predict the impedance data of a SOFC MIEC cathode (Adler et al., 1996; Adler, 1998). Thus, we propose a modification to the ALS model to account for the aforementioned difference.

Furthermore, we develop a method of extracting the effective tortuosity from the impedance data. Specifically, we compare the macrohomogeneous (modified ALS) and 1D Finite Length Gerischer relations for the impedance to determine the effective tortuosity. Our calculations for tortuosity determination reveal that the effective tortuosity is a function of the microstructure, frequency of the applied AC load, and the material properties such as the reaction rate constant and bulk diffusion constant. Additionally, the effective tortuosity of a microstructure in the low-frequency regime (where the tortuosity approaches the DC value) decreases with an increase in the ratio between the reaction rate constant and the bulk diffusion coefficient due to a decreased penetration depth of the electrode reactions. This finding suggests that the prevalent practice of using a single tortuosity value for a given electrode for extracting the material properties by employing the ALS model (Adler, 1998; Zhang S.-L. et al., 2018; Zhang S.-L. et al., 2019) should be reviewed and revised. Additionally, the finding suggests that, both the intrinsic material properties and the microstructure should be considered concurrently in designing a cathode with enhanced performance. Our findings open a new array of applications for the EIS technique in characterizing and optimization of the microstructure of a SOFC cathode.

All the previous reports primarily consider artificially generated microstructures (Rüger et al., 2007; Haffelin et al., 2013; Pereira et al., 2014), which are designed to match given macrohomogeneous properties and thus may not be representative of the local microstructural morphologies and topologies. Only a few three-dimensional impedance calculations have been reported with a consideration of

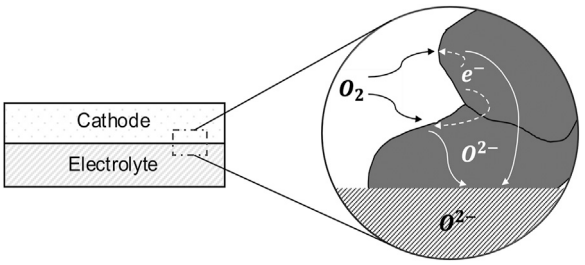

FIGURE 1 | A schematic of oxygen transport withing the solid phase (gray region) of a MIEC SOFC cathode; the schematic is based on Kreller, (Kreller, 2011).

experimentally determined microstructures that are statistically representative of the cathode (Kreller et al., 2011; Lynch et al., 2013). The report by Kreller et al. (Kreller et al., 2011) only explicitly considered the three-dimensional microstructure near the electrode/electrolyte interface and assumed a one-dimensional macrohomogeneous domain beyond a certain distance from the interface. On the other hand, the investigation by Lynch et al. (Lynch et al., 2013) focused on the method of calculating impedance in a microstructure where the ORR occurs either through bulk or surface pathways. However, it did not propose the utilization of the calculated impedance data for characterizing the microstructure nor did it consider the difference between the concentration amplitudes at the pore/solid interface and within the bulk of the solid, which are the two focuses of this paper.

METHODS

Model Equations for Impedance Calculation

MIEC cathodes are known to have much higher electronic conductivity as compared to the ionic conductivity (Jung and Tuller, 2009); thus, we ignore any impedance contribution due to electronic resistance. Moreover, due to the high electronic conductivity, it is reasonable to assume that the electrostatic potential of the solid phase is spatially invariant. Thus, in the absence of any gas phase transport limitation, the cathode impedance can be entirely attributed to the reduction of oxygen at the pore/solid interface and the transport of the resulting oxygen ions through the solid in the cathode, which is shown in **Figure 1**. The oxygen ions diffuse inside the solid phase of the cathode through a vacancy mechanism. Hence, the ionic current can be calculated from the flux of the oxygen vacancies. The mass transport equation for the oxygen vacancies inside the cathode can be written as

$$\frac{\partial C_v}{\partial t} = \nabla \cdot \left(AD_v \nabla C_v\right) \in \Omega, \tag{1}$$

where C_v represents the concentration of oxygen vacancies, A represents the thermodynamic factor, which is defined by Adler, Lane, and Steele (Adler et al., 1996) as a factor relating the oxygen vacancy concentration to the partial pressure of oxygen gas in the pore phase, $A = (1/2)\partial \ln(P_{O_2})/\partial \ln(C_v)$. The diffusivity of the vacancies inside the cathode is denoted by D_v, whereas t represents time, and Ω represents the solid phase region within the cathode where the vacancy transport takes place. The reaction at the pore/solid interface within the cathode can be modeled as a first-order chemical reaction as

$$-AD_v \nabla C_v = \kappa^{3D}\left(C_v - C_v^0\right) \in \delta\Omega, \tag{2}$$

where κ^{3D} is the reaction rate constant, C_v^0 is the equilibrium vacancy concentration and $\delta\Omega$ represents the pore/solid interface.

We employ the smoothed boundary method (SBM) (Yu et al., 2012) to solve **Eq. 1** within an experimentally determined, complex microstructure of the MIEC cathode, along with the boundary condition set in **Eq. 2**. Using SBM, these equations can be reformulated as

$$\psi \frac{\partial C_v}{\partial t} = \nabla \cdot \left(\psi A D_v \nabla C_v\right) - \left|\nabla \psi\right| \kappa^{3D}\left(C_v - C_v^0\right), \tag{3}$$

where ψ is a domain parameter that represents the geometry of the complex microstructure. Within the pores, ψ has a value of zero, and within the solid phase, it has a value of one. At the pore/solid interface, it smoothly transitions between zero and one. Further details about the process of obtaining ψ for a complex microstructure can be found in our previous work (Yu et al., 2020).

The application of an AC load causes the vacancy concentration, C_v, to oscillate about C_v^0. The oscillating perturbation is denoted by ΔC, and thus, the relation between C_v, C_v^0, and ΔC can be written as

$$C_v = C_v^0 + \Delta C. \tag{4}$$

Since C_v^0 is constant throughout space at a given temperature, the spatial variation of C_v can be described entirely in terms of ΔC as

$$\psi \frac{\partial \Delta C}{\partial t} = \nabla \cdot \left(\psi A D_v \nabla (\Delta C)\right) - \left|\nabla \psi\right| \kappa^{3D} \Delta C. \tag{5}$$

Furthermore, AD_v can be assumed to be a constant for a MIEC cathode at a given temperature and for a small value of ΔC (Mizusaki et al., 1993). Therefore, **Eq. 5** can be written as

$$\psi \frac{\partial \Delta C}{\partial t} = AD_v \nabla \cdot \left(\psi \nabla (\Delta C)\right) - \left|\nabla \psi\right| \kappa^{3D} \Delta C. \tag{6}$$

Eq. 6 can be further simplified by expressing the time dependent part of the oscillations as complex exponential functions, i.e.,

$$\Delta C = \frac{\tilde{C} e^{i\omega t} + \tilde{C}^* e^{-i\omega t}}{2}, \tag{7}$$

where $\tilde{C}$ is a complex quantity that varies in space with $\tilde{C}^*$ as its complex conjugate, ω is the frequency of the AC load, and i is the imaginary unit. Let C_R and C_I be the real and imaginary components of $\tilde{C}$. Upon the substitution of **Eq. 7** into **Eq. 6**, the subsequent collection of real and imaginary terms, and the cancellation of the exponential functions, we obtain

$$AD_v \nabla \cdot \left(\psi \nabla C_R\right) - \left|\nabla \psi\right| \kappa^{3D} C_R = -\psi \omega C_I, \tag{8a}$$

TABLE 1 | Sets of boundary conditions applied to the system of equations, **Eq.12a**,**12b**.

Set of BCs\Location	$\hat{x} = 0$	$\hat{x} = \hat{L}$
Blocking current collector (BCC) BC	$C_R = 1$, $C_I = 0$	$\partial C_R/\partial \hat{x} = 0$, $\partial C_I/\partial \hat{x} = 0$
Transmissive current collector (TCC) BC	$C_R = 1$, $C_I = 0$	$C_R = 0$, $C_I = 0$

$$AD_v\nabla\cdot\left(\psi\nabla C_I\right) - \left|\nabla\psi\right|\kappa^{3D}C_I = \psi\omega C_R. \tag{8b}$$

The above pair of equations is then solved to determine the C_R and C_I as functions of space and ω. Once C_R and C_I are known, the impedance, $Z(\omega)$, of the cathode can be calculated as (Jacobsen and West, 1995; Nielsen et al., 2011)

$$Z(\omega) = \frac{RTL}{\left(-n^2F^2D_vC_v^0\right)}\frac{\tilde{C}|_{x=0}/L}{\langle\partial\tilde{C}/\partial x|_{x=0}\rangle}, \tag{9}$$

where R is the universal gas constant, T is temperature, n is the number of moles of electrons consumed in the reaction, F is Faraday's constant, L is the thickness of the cathode, and $\langle\partial\tilde{C}/\partial x|_{x=0}\rangle$ is the gradient of the concentration amplitude in the primary diffusion direction, x, averaged over the loading boundary located at $x = 0$, which represents the electrolyte/cathode interface. Furthermore, the first term on the right-hand side of **Eq. 9** is the product of the material resistivity and thickness of the cathode, and it can be defined as Z_0. Therefore, **Eq. 9** becomes

$$Z(\omega) = Z_0\frac{\tilde{C}|_{x=0}/L}{\langle\partial\tilde{C}/\partial x|_{x=0}\rangle}. \tag{10}$$

For numerically solving **Eqs 8a**,**b**, we chose to make them nondimensional by defining a length scale, l; then, $\hat{\nabla} = l\nabla$. Hereafter, the circumflex ($\hat{\cdot}$) symbol denotes that the associated operator or quantity is nondimensional. Substituting $\hat{\nabla}/1$ in place of ∇, and multiplying both sides with $(l^2/(AD_v))$ gives

$$\hat{\nabla}\cdot\left(\psi\hat{\nabla}C_R\right) - \left|\hat{\nabla}\psi\right|\kappa^{3D}\frac{l}{AD_v}C_R = -\psi\omega\frac{l^2}{AD_v}C_I, \tag{11a}$$

$$\hat{\nabla}\cdot\left(\psi\hat{\nabla}C_I\right) - \left|\hat{\nabla}\psi\right|\kappa^{3D}\frac{l}{AD_v}C_I = \psi\omega\frac{l^2}{AD_v}C_R. \tag{11b}$$

By defining $\hat{\kappa}^{3D} = \kappa^{3D}l/(AD_v)$ and $\hat{\omega} = \omega l^2/(AD_v)$ we obtain

$$\hat{\nabla}\cdot\left(\psi\hat{\nabla}C_R\right) - \left|\hat{\nabla}\psi\right|\hat{\kappa}^{3D}C_R = -\psi\hat{\omega}C_I, \tag{12a}$$

$$\hat{\nabla}\cdot\left(\psi\hat{\nabla}C_I\right) - \left|\hat{\nabla}\psi\right|\hat{\kappa}^{3D}C_I = \psi\hat{\omega}C_R, \tag{12b}$$

which are solved for two different sets of boundary conditions (BCs) as listed in **Table 1**.

The two sets of the BCs differ only in those at the cathode/current collector interface ($\hat{x} = \hat{L}$), as shown in **Table 1**. The blocking current collector (BCC) BC represents the case of a foil-like current collector, which blocks all the ionic current at the cathode/current collector interface. This condition is more representative of the SOFC cathodes and is also used by the ALS model (Adler et al., 1996). However, in some reports (Boukamp et al., 2003; Boukamp et al., 2006; Holtappels et al., 2006) the impedance behavior of MIEC oxides has also been fit with the relation that is applicable to the transmissive boundary condition. Under this boundary condition, the vacancy concentration is set to be zero at the cathode/current collector interface, and we will refer to this as transmissive current collector (TCC) BC, which may correspond to a porous or mixed conducting current collector. We simulate the impedance behavior for both of these sets of boundary conditions to cover all the scenarios reported in the literature. The results for TCC BC are provided in **Supplementary Material**. Moreover, a list of all the variables and symbols used in this article is provided in **Table 2**.

Numerical Implementation

The choice of SBM enabled the use of a standard Cartesian grid and the finite difference method to solve the above pair of equations (**Eqs 12a,b**). We used the center difference scheme to discretize the domain, which consists of $352 \times 642 \times 594$ grid points. A uniform grid spacing ($h = 0.0272$, non-dimensional) was selected to ensure the presence of at least 3 grid points across the pore/solid interface ($\lambda = 0.0817$). The selection of the numerical parameters is discussed in **Supplementary Material** in detail. The Alternating-Direction Line-Relaxation (ADLR) method (Hofhaus and Van de Velde, 1996) was employed to solve the equations. The ADLR method utilizes a tridiagonal matrix solve to obtain the values of the solutions individually along the x, y, and z directions. To simultaneously solve **Eqs 12a**,**b**, an iterative scheme was developed, in which the ADLR method was first used to calculate C_R for a given RHS of **Eq. 12a**, and the resulting values were then used to update the RHS of **Eq. 12b**. Subsequently, C_I was obtained using **Eq. 12b** with the updated value of C_R. This procedure was repeated until both C_R and C_I numerically converged. We defined the convergence metric as the ratio between the absolute value of the sum of all elements of the change matrix (obtained by taking the difference between the updated concentration and previous concentration) and the sum of all elements of the old concentration matrix. The solution was deemed converged when the metric became less than a specified threshold value. We deduced the value by progressively reducing the value and observing the change in the resulting solution. We found that solution did not change appreciably between the threshold values of 10^{-10} and 10^{-11}. Thus, we selected a value of 10^{-10} as the criteria the numerical convergence of our solution.

We chose $l = 0.46$ μm as the length scale for the non-dimensionalization. The reader is referred to our previous work (Yu et al., 2020) for more details on the selection of l. Finally, a wide range of values for AD_v and κ^{3D} are reported in the literature (Zhang L. et al., 2018) because of the use of different

TABLE 2 | List and description of the variables and symbols used in the model equations.

Symbol	Description
C_v	Concentration of oxygen vacancies
A	The thermodynamic factor relating the oxygen vacancy concentration to the partial pressure of oxygen gas in the pore phase, $A = (1/2)\partial \ln(P_{O_2})/\partial \ln(C_v)$
D_v	Diffusivity of the oxygen vacancies within the solid bulk
Ω	Solid phase region within the cathode
$\delta\Omega$	Pore/solid interface
κ^{3D}	Reaction rate constant
ψ	Domain parameter that represents the geometry of the complex microstructure. Within the pores, ψ has a value of zero, and within the solid phase, it has a value of one
ΔC	Perturbation in the oxygen vacancy concentration caused by the applied AC load
$\tilde{C}$	Complex quantity that varies in space
$\tilde{C}^*$	Complex conjugate of $\tilde{C}$
ω	Frequency of the AC load
i	Imaginary unit
C_R	Real component of $\tilde{C}$
C_I	Imaginary component of $\tilde{C}$
$Z(\omega)$	Impedance
R	Universal gas constant
T	Temperature
n	Number of moles of electrons consumed in the electrochemical reaction
F	Faraday's constant
L	Thickness of the cathode
Z_0	Product of the material resistivity and thickness of the cathode
$\hat{(\cdot)}$	The circumflex symbol denotes that the associated operator or quantity is nondimensional
Z^{3D}	Impedance of a finitely thick MIEC SOFC cathode
R_{chem}	Characteristic resistance describing the chemical contributions to the cathode impedance; as defined in the ALS model
t_{chem}	Relaxation time related to the chemical processes of solid-state diffusion and oxygen surface exchange; as defined in the ALS model
δ	Characteristic distance related to the chemical processes of solid-state diffusion and oxygen surface exchange; as defined in the ALS model
ϵ	The microstructure porosity
τ	The microstructure tortuosity
κ	Surface exchange coefficient; as defined in the ALS model
a	Interfacial surface area per unit cathode volume
C_{mc}	The oxygen site concentration in the mixed conductor (mc)
κ^{1D}	Macrohomogeneous reaction rate constant
Z^{FLG}	The FLG impedance
C_v^s	Oxygen vacancy concentration at the pore/solid interface
ΔC^s	The concentration oscillation at the pore/solid interface
α	The ratio between the interface and the bulk concentration oscillations
$\langle\alpha\rangle$	Volume averaged α
$\langle\alpha_0\rangle$	DC value of $\langle\alpha\rangle$

cathode materials and operating temperatures (600–800°C). We chose three values of $\hat{\kappa}^{3D}$ for our study in order to cover this wide range and simulated the impedance behavior for the frequency values, $\hat{\omega}$, between 0 and 2.672. It should be noted that the value of $\hat{\kappa}^{3D}$ is affected by the values of both AD_v and κ^{3D}.

Derivation for Impedance Expressions and Transcendental Equation for Tortuosity

Adler, Lane, and Steele proposed a macrohomogeneous model to predict the impedance, Z^{3D}, of a finitely thick MIEC SOFC cathode, which is commonly known as the ALS model (Adler et al., 1996; Adler, 1998). The model gives the impedance response for a symmetric cell with two identical cathodes. Since we consider a half cell with a single cathode in our investigation, the ALS impedance expression is divided by 2. Thus,

$$Z^{3D} = \frac{R_{\text{chem}}}{\sqrt{(1+i\omega t_{\text{chem}})}} \coth\left(\frac{L}{\delta}\sqrt{(1+i\omega t_{\text{chem}})}\right), \tag{13a}$$

$$R_{\text{chem}} = \frac{RT}{4F^2}\sqrt{\left(\frac{\tau^2}{(1-\varepsilon)C_v^0 D_v a\kappa C_{\text{mc}}}\right)}, \tag{13b}$$

$$t_{\text{chem}} = \frac{C_v^0(1-\varepsilon)}{Aa\kappa C_{\text{mc}}}, \tag{13c}$$

$$\delta = \sqrt{\left(\frac{C_v^0 D_v(1-\varepsilon)}{a\tau^2\kappa C_{\text{mc}}}\right)}, \tag{13d}$$

where τ is the microstructure tortuosity, ε is the microstructure porosity, κ is the surface exchange coefficient, a is interfacial surface area per unit cathode volume, C_{mc} is the oxygen site concentration (in the unit of mol/m^3) in the mixed conductor (mc). The ALS model defines the reaction rate as $A\kappa C_{\text{mc}}\Delta C/C_v^0$, whereas we define it as $\kappa^{3D}\Delta C$ (**Eq. 2**). Therefore, κ and κ^{3D} are related as

$$\kappa^{3D} = \frac{A\kappa C_{mc}}{C_v^0}. \quad (14)$$

It should be noted that in the original ALS expression, τ is used for denoting tortuosity factor, whereas in this article we use τ for denoting tortuosity. These two quantities are related; the tortuosity factor is the square of the tortuosity.

The substitution of **Eqs 13b**,**c**,**d**, and **Eq. 14** into **Eq. 13a** gives

$$Z^{3D} = \frac{RTL}{4F^2C_v^0D_v}\frac{\tau^2}{1-\varepsilon}\frac{\coth\left(\tau L\sqrt{\frac{\frac{a\kappa^{3D}}{(1-\varepsilon)}+i\omega}{AD_v}}\right)}{\tau L\sqrt{\frac{\frac{a\kappa^{3D}}{(1-\varepsilon)}+i\omega}{AD_v}}}. \quad (15)$$

By defining $\kappa^{1D} = \kappa^{3D}a/(1-\varepsilon)$ as the macrohomogeneous reaction rate constant and by using the definition for Z_0 we obtain

$$Z^{3D} = Z_0\frac{\tau^2}{1-\varepsilon}\frac{\coth\left(\tau L\sqrt{\frac{\kappa^{1D}+i\omega}{AD_v}}\right)}{\tau L\sqrt{\frac{\kappa^{1D}+i\omega}{AD_v}}}. \quad (16)$$

Finally, by following the same methodology as described in the model equation section, **Eq. 16** can be made nondimensional as

$$\frac{Z^{3D}}{Z_0} = \frac{\tau^2}{1-\varepsilon}\frac{\coth\left(\tau\hat{L}\sqrt{\hat{\kappa}^{1D}+i\hat{\omega}}\right)}{\tau\hat{L}\sqrt{\hat{\kappa}^{1D}+i\hat{\omega}}}, \quad (17)$$

where the nondimensional quantities are defined as $\hat{L} = L/l$, $\hat{\kappa}^{1D} = \kappa^{1D}l^2/(AD_v)$, and $\hat{\omega} = \omega l^2/(AD_v)$.

The conversion of **Eq. 13** into **Eq. 17** enables a direct comparison of the impedance expression of a complex 3D microstructure with that of the standard expression for 1D Finite Length Gerischer (FLG) impedance. The 1D FLG element represents the impedance of a 1D MIEC domain where no microstructural effects are present and where the kinetics is co-limited by both surface reaction and bulk diffusion. The FLG impedance, Z^{FLG} for a 1D domain with the same macrohomogeneous reaction rate constant, $\hat{\kappa}^{1D}$, and thickness, $\hat{L}$, as the SOFC cathode under consideration can be written as

$$\frac{Z^{FLG}}{Z_0} = \frac{\coth\left(\hat{L}\sqrt{\hat{\kappa}^{1D}+i\hat{\omega}}\right)}{\hat{L}\sqrt{\hat{\kappa}^{1D}+i\hat{\omega}}}, \quad (18)$$

It is evident from a comparison between **Eq. 17** and **Eq. 18** that the microstructure affects the impedance response of a SOFC cathode in two ways. First, the microstructure increases the cathode impedance by a factor of $\tau^2/(1-\varepsilon)$. Second, the effective thickness of the cathode is increased by a factor of τ. These effects can be exploited in the following way to determine the value of τ using the value of Z^{3D}, which is experimentally known.

A ratio between **Eq. 17** and **Eq. 18** gives

$$\frac{Z^{3D}}{Z^{FLG}} = \frac{\tau}{1-\varepsilon}\frac{\coth\left(\tau\hat{L}\sqrt{\hat{\kappa}^{1D}+i\hat{\omega}}\right)}{\coth\left(\hat{L}\sqrt{\hat{\kappa}^{1D}+i\hat{\omega}}\right)}. \quad (19)$$

By taking the modulus (which is analytically unnecessary but numerically required) and after some rearrangement, **Eq. 19** can be written as

$$\left|\tau\coth\left(\tau\hat{L}\sqrt{\hat{\kappa}^{1D}+i\hat{\omega}}\right)\right| = \left|\frac{Z^{3D}}{Z^{FLG}}\left((1-\varepsilon)\coth\left(\hat{L}\sqrt{\hat{\kappa}^{1D}+i\hat{\omega}}\right)\right)\right| \quad (20)$$

where terms containing τ are collected on the left-hand side of the equation, yielding a transcendental equation for τ. The nondimensional macrohomogeneous reaction rate constant, $\hat{\kappa}^{1D} = \kappa^{1D}l^2/(AD_v) = al^2\kappa^{3D}/((1-\varepsilon)AD_v)$, is dependent on material properties, namely κ^{3D} and AD_v, which can be determined from the literature for standard materials, as well as on microstructural characteristics, namely a and ϵ, both of which can be determined experimentally (e.g., using Mercury intrusion porosimeter (Rootare and Prenzlow, 1967). Therefore, with both $\hat{\kappa}^{1D}$ and Z^{3D} known, **Eq. 20** can be solved to determine the effective tortuosity. However, before implementing this method, we need to make a modification to the ALS model as described in the following section.

SIMULATION RESULTS AND DISCUSSION

Modification to the ALS Model

The ALS model (Adler et al., 1996; Adler, 1998) is derived using the volume averaged form of the mass conservation equation (**Eqs 2** and **3**), which can be written as

$$(1-\varepsilon)\frac{\partial C_v}{\partial t} = \frac{AD_v(1-\varepsilon)}{\tau^2}\frac{\partial^2 C_v}{\partial x^2} - a\kappa^{3D}(C_v^s - C_v^0). \quad (21)$$

where C_v^s is the oxygen vacancy concentration at the pore/solid interface. **Eq. 21** can be written in term of ΔC by using the relation described by **Eq. 4** as

$$(1-\varepsilon)\frac{\partial \Delta C}{\partial t} = \frac{AD_v(1-\varepsilon)}{\tau^2}\frac{\partial^2 \Delta C}{\partial x^2} - a\kappa^{3D}\Delta C^s. \quad (22)$$

The ALS model assumes the concentration oscillations at the pore/solid interface, ΔC^s, and within the bulk of the solid, ΔC, to be equal. However, in reality, the amplitude of the concentration oscillation, $\tilde{C}$, is smaller at the interface than the amplitude within the bulk because of the surface reaction. We demonstrate this phenomenon by considering a model microstructure with solid cylindrical domain surrounded by the pore phase, as shown in **Figure 2A**. The dimensions of the microstructure are also shown in the figure, and the primary diffusion direction of the model microstructure is along the x-axis. The reaction occurs at the pore/solid interface, i.e., at the surface of the cylinder. Using this model geometry, we determine C_R and C_I within the cylinder for $\hat{\omega} = 0.5$ and for two different values of $\hat{\kappa}^{3D}$ by solving **Eqs 12a**, **12b**, which are subject to the BBC BC at $\hat{x} = 1$. **Figures 2B,C** show the distribution of C_R and C_I along the radius of the cylinder at different positions along the x-axis for $\hat{\kappa}^{3D} = 0.02$ and $\hat{\kappa}^{3D} = 0.2$, respectively. The solution values outside the cylinder ($|\hat{y}| > 1$) have no physical meaning as the domain parameter, ψ, is zero there, and therefore are not included in the plots. As can be seen,

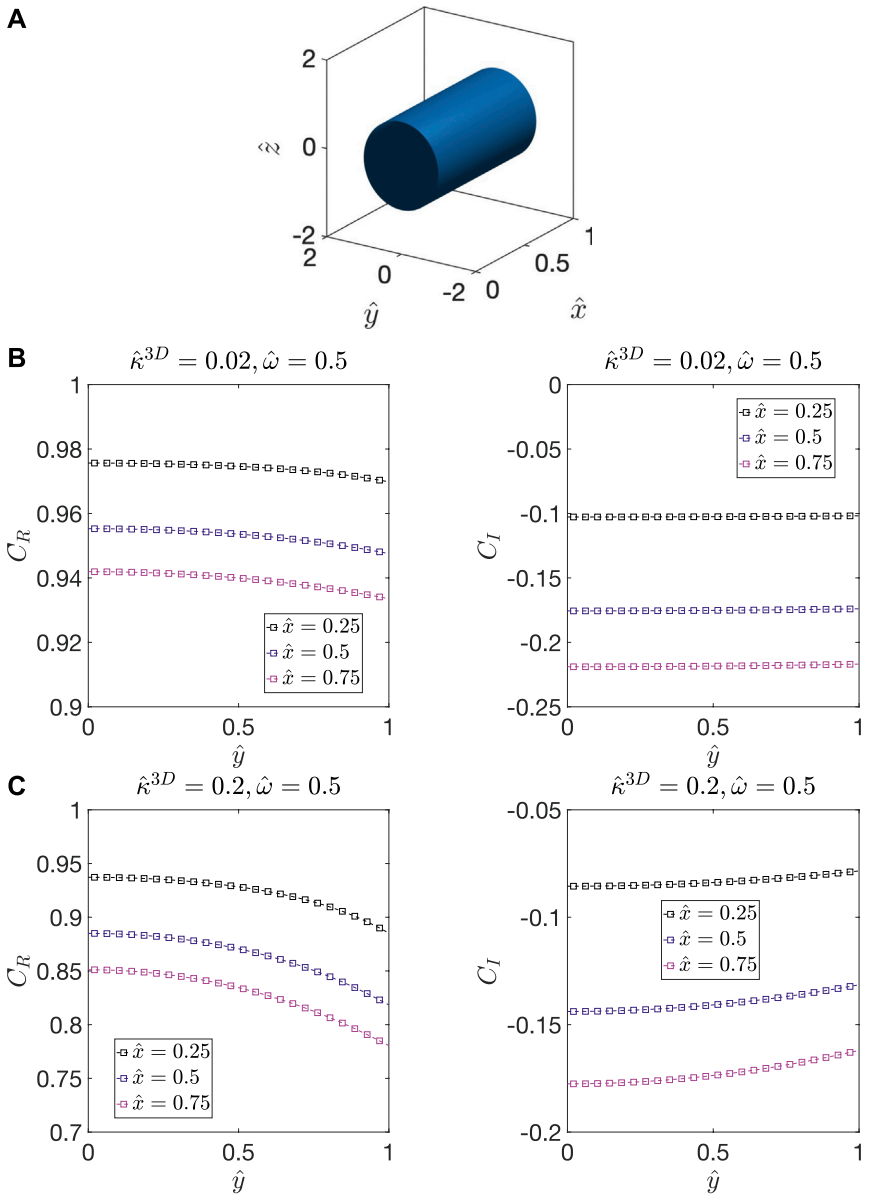

FIGURE 2 | (A) The model microstructure, which contains a cylindrical solid domain with unit radius and length surrounded by pore phase. The distribution of C_R and C_I along the radial axis of the cylinder at different $\bar{x}$ positions for $\bar{\omega}$= 0.5 for **(B)** $\bar{\kappa}^{3D}$= 0.02, and **(C)** 0.2. The solution values outside the cylinder ($|\bar{y}| > 1$) have no physical meaning as the domain parameter, ψ, is zero there, and therefore are not included in the plots. Due to the radial symmetry of the cylinder, results are only shown for $\bar{y}$ between zero and one.

for a small value of $\bar{\kappa}^{3D}$, 0.02, the magnitude of C_R at $\bar{y} = 0$ and $\bar{y} = 1$ are similar (**Figure 2B**), whereas for a larger value of $\bar{\kappa}^{3D}$, 0.2, the magnitude of C_R is significantly smaller at $\bar{y} = 1$ than at $\bar{y} = 0$, as shown in **Figure 2C**. The larger extent of spatial variation in C_R for higher $\bar{\kappa}^{3D}$ is caused by the greater magnitude of $\bar{\nabla} C_R$ at the interface, which is directly proportional to $\bar{\kappa}^{3D}$. In other words, a large $\bar{\kappa}^{3D}$ suggests that the rate of diffusion is slower than the reaction rate, which causes C_R to be smaller in magnitude at the interface than within the bulk. This spatial variation is observed throughout the cylinder, and a similar trend is seen for C_I as well.

It is evident from the above model case that the difference between the amplitude of the oscillations at the interface and within the bulk cannot be neglected. Thus, we now consider a modification to the ALS model. Let α be the ratio between the interface and the bulk concentration oscillations, i.e., $\alpha = \Delta C^s / \Delta C$. Therefore, **Eq. 22** becomes

$$(1-\varepsilon)\frac{\partial \Delta C}{\partial t} = \frac{AD_v(1-\varepsilon)}{\tau^2}\frac{\partial^2 \Delta C}{\partial x^2} - a\kappa^{3D}(\alpha \Delta C). \qquad (23)$$

Eq. 23 suggests that the effect of α can be incorporated into the ALS model by appropriately modifying $\bar{\kappa}^{3D}$. However, this cannot be done as straightforwardly because $\langle \alpha \rangle$ varies in space. Nonetheless, the complexity can be reduced by considering the

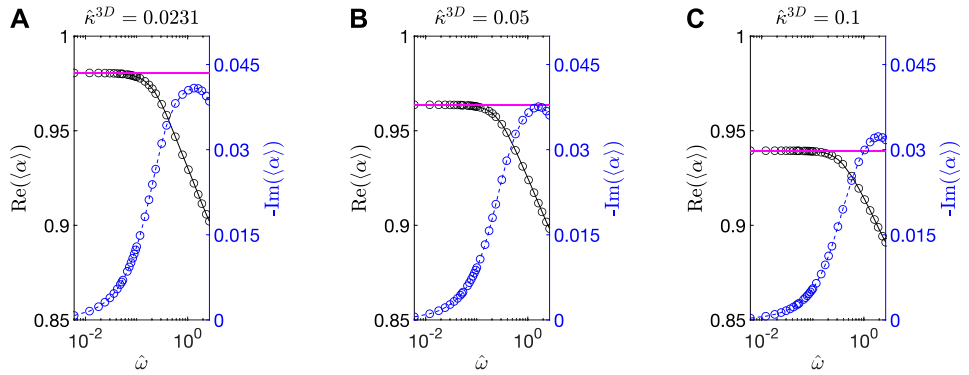

FIGURE 3 | Calculated $\langle\alpha\rangle$ vs. $\hat{\omega}$ (BCC BC) at **(A)** $\hat{\kappa}^{3D} = 0.0231$, **(B)** 0.05, and **(C)** 0.1. The real component (black solid curve) and the imaginary component (blue dashed curve) of $\langle\alpha\rangle$ are plotted on the left and right *y*-axes, respectively. The circles indicate the calculated data point. The DC values of $\langle\alpha\rangle$ are shown with horizontal magenta dotted lines as a reference.

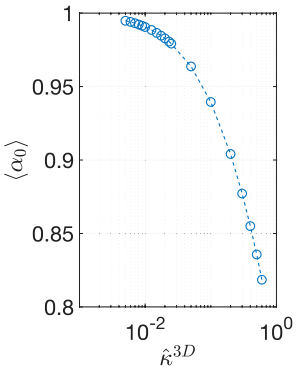

FIGURE 4 | DC value of $\langle\alpha\rangle$, $\langle\alpha_0\rangle$, as a function of $\hat{\kappa}^{3D}$.

volume averaged α, or $\langle\alpha\rangle$, to modify the value of κ^{3D}. The quantity $\langle\alpha\rangle$ is defined as the ratio between average interface and average bulk concentration amplitudes, i.e.,

$$\langle\alpha\rangle = \frac{\int \tilde{C}|\hat{\nabla}\psi|d\hat{V}}{\int |\hat{\nabla}\psi|d\hat{V}} \cdot \left(\frac{\int \tilde{C}\psi\, d\hat{V}}{\int \psi d\hat{V}}\right)^{-1}, \tag{24}$$

where the integral is over the entire volume of the cathode microstructure.

To characterize $\langle\alpha\rangle$, we first determined its dependence on $\hat{\omega}$ for the three values of $\hat{\kappa}^{3D}$. The results are summarized in **Figure 3**. Note that examination of the numerical accuracy is presented in **Supplementary Material**, and it has been shown that the error in the results is within 2%. It can be seen that, for a particular value of $\hat{\kappa}^{3D}$, $\langle\alpha\rangle$ has much higher real component than the imaginary component at all $\hat{\omega}$ values. Moreover, the real component remains constant with increasing $\hat{\omega}$ before transitioning into a regime where it decreases with increasing $\hat{\omega}$. The $\hat{\omega}$ value where this transition occurs increases with the value of $\hat{\kappa}^{3D}$. Furthermore, since $\langle\alpha\rangle$ remains constant for a fairly wide range of frequency values, we made a further simplifying assumption by approximating $\langle\alpha\rangle$ by its DC value, $\langle\alpha_0\rangle$. We calculated $\langle\alpha_0\rangle$ for 19 values of $\hat{\kappa}^{3D}$ ranging from 5×10^{-3} to 6×10^{-1} and summarized the results in **Figure 4**. The value of $\langle\alpha_0\rangle \approx 1$ for small values of $\hat{\kappa}^{3D}$, and it monotonically decreases with increasing $\hat{\kappa}^{3D}$. Both of these characteristics are expected because small values of $\hat{\kappa}^{3D}$ suggest that the reaction rate is lower than the diffusion rate, and thus there is little difference between the interface and bulk concentration amplitudes. However, for large values of $\hat{\kappa}^{3D}$, the reaction rate is much larger than the diffusion rate, which causes the concentration amplitude at the pore/solid interface to be lower than the bulk.

Using $\langle\alpha_0\rangle$ as a function of $\hat{\kappa}^{3D}$, to capture the difference between the surface and bulk concentration amplitudes, we propose a modified macrohomogeneous reaction rate constant, $\hat{\kappa}^{1D}$, in the ALS expression as

$$\frac{Z^{3D}}{Z_0} = \frac{\tau^2}{1-\varepsilon} \frac{\coth\left(\tau\hat{L}\sqrt{\langle\alpha_0\rangle\hat{\kappa}^{1D} + i\hat{\omega}}\right)}{\tau\hat{L}\sqrt{\langle\alpha_0\rangle\hat{\kappa}^{1D} + i\hat{\omega}}}. \tag{25}$$

Thus, the expression for calculating the effective tortuosity can be modified as

$$\left|\tau\coth\left(\tau\hat{L}\sqrt{\langle\alpha_0\rangle\hat{\kappa}^{1D}+i\hat{\omega}}\right)\right| = \left|\frac{Z^{3D}}{Z^{FLG}}\left((1-\varepsilon)\coth\left(\hat{L}\sqrt{\langle\alpha_0\rangle\hat{\kappa}^{1D}+i\hat{\omega}}\right)\right)\right|. \tag{26}$$

Simulated Impedance and Tortuosity Calculation

Figure 5 shows the impedance spectra of the experimentally obtained microstructure for three values of $\hat{\kappa}^{3D}$, along with the impedance spectra obtained from the analytical expression for the 1D FLG impedance in **Eq. 18**. As expected, the two curves for the same value of $\hat{\kappa}^{3D}$ deviate significantly, with the FLG curve underestimating the impedance value. To enable a better visualization of the difference a few iso-frequency points, on both the curves, are marked with magenta triangles. We note that the discussion below is for a fixed cathode thickness provided in the numerical implementation section. The effect of cathode thickness on the impedance and tortuosity is discussed qualitatively in **Supplementary Material**.

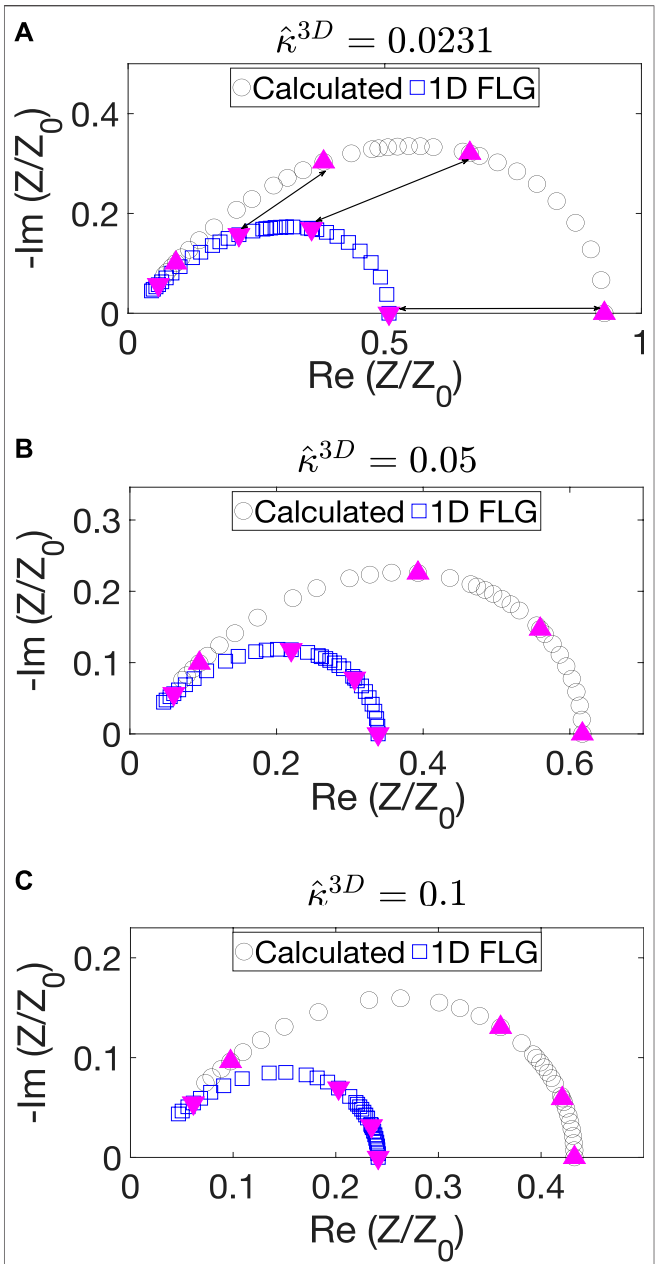

FIGURE 5 | Nyquist plots obtained from 3D calculations for the BCC BC (black curve) and 1D FLG model (blue curve) for **(A)** $\hat{\kappa}^{3D}$ = 0.0231, **(B)** 0.05, and **(C)** 0.1. The iso-frequency points are marked with upright magenta triangles on the black curves and inverted magenta triangles on the blue curves. Three iso-frequency points are connected with arrows in a).

By solving **Eq. 26**, we calculated τ for the three values of $\hat{\kappa}^{3D}$ over the entire frequency range examined. The results are shown in **Figure 6**. From this comparison, three trends can be observed in the tortuosity data. First, for a given value of $\hat{\kappa}^{3D}$, τ remains almost a constant before it begins to decrease with an increase in $\hat{\omega}$. The relation between τ and $\log(\hat{\omega})$ at high frequencies can be represented by a linear function with a slope of −0.1033, as shown by black dashed line in **Figure 6**. Second, the low frequency value of τ decreases with an increase in $\hat{\kappa}^{3D}$. Finally, all three τ vs. $\hat{\omega}$ curves coincide at high frequencies.

To provide further insights, **Figure 7** shows the distribution of C_R and C_I in the complex microstructure at a low value of $\hat{\omega}$, 0.018, which is close to the DC case, for three different $\hat{\kappa}^{3D}$ values. For the low value of $\hat{\kappa}^{3D}$, 0.0231, the gradient in the concentration amplitude is non-zero in much of the microstructure thickness, as shown in **Figure 7A**. However, with an increase in the value of $\hat{\kappa}^{3D}$, the gradient spans lesser and lesser of the microstructure at the same frequency, as qualitatively shown in **Figures 7B,C**. Thus, it is evident that the penetration depth of the diffusing species (oxygen vacancies) at the same frequency of the AC load decreases with an increase in $\hat{\kappa}^{3D}$. Furthermore, **Figure 8** shows the distribution of C_R and C_I in the microstructure for three values of $\hat{\kappa}^{3D}$ at a higher frequency value, $\hat{\omega}$ = 1.038. As can be seen, the gradient in the concentration amplitude is mostly confined to a small region near the electrolyte/cathode interface for all values of $\hat{\kappa}^{3D}$ at the high frequency regime. Therefore, the penetration depth for each case at the high frequency value is much smaller than at the low frequency value. Moreover, at $\hat{\omega}$ = 1.038 the penetration depth is similar for all three values of $\hat{\kappa}^{3D}$. This shows that the penetration depth is a function of both $\hat{\kappa}^{3D}$ and $\hat{\omega}$. Since the effective tortuosity of a microstructure is directly influenced by the penetration depth (Yu et al., 2020), it is evident that the effective tortuosity is also a function of both $\hat{\kappa}^{3D}$ and $\hat{\omega}$. Therefore, it can be inferred that, for a porous medium, where the rate kinetics is co-limited by both the bulk diffusion and surface reaction, the tortuosity is a function not only of the microstructural characteristics but also of $\hat{\kappa}^{3D}$, which is a combination of material property. In addition, it also depends on the frequency, as was found in the case for diffusional impedance case (Yu et al., 2020). The observed behavior of the

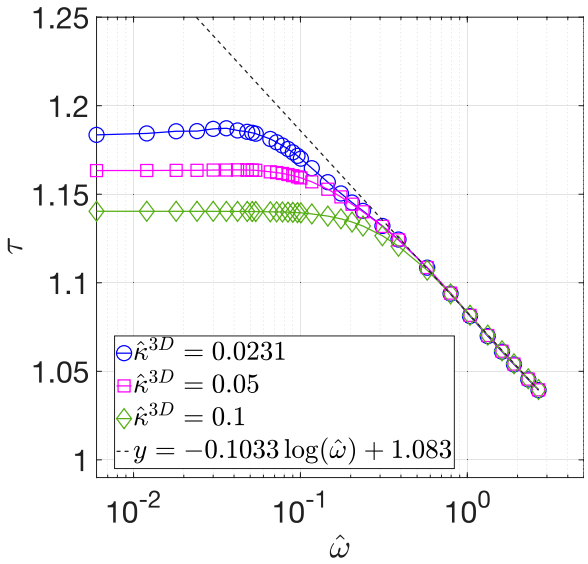

FIGURE 6 | Calculated τ vs. $\hat{\omega}$ relations (BCC BC) for $\hat{\kappa}^{3D}$ = 0.0231 (blue circles), 0.05 (magenta squares), and 0.1 (green diamonds). The black dashed line represents the fit with a linear function at high frequencies.

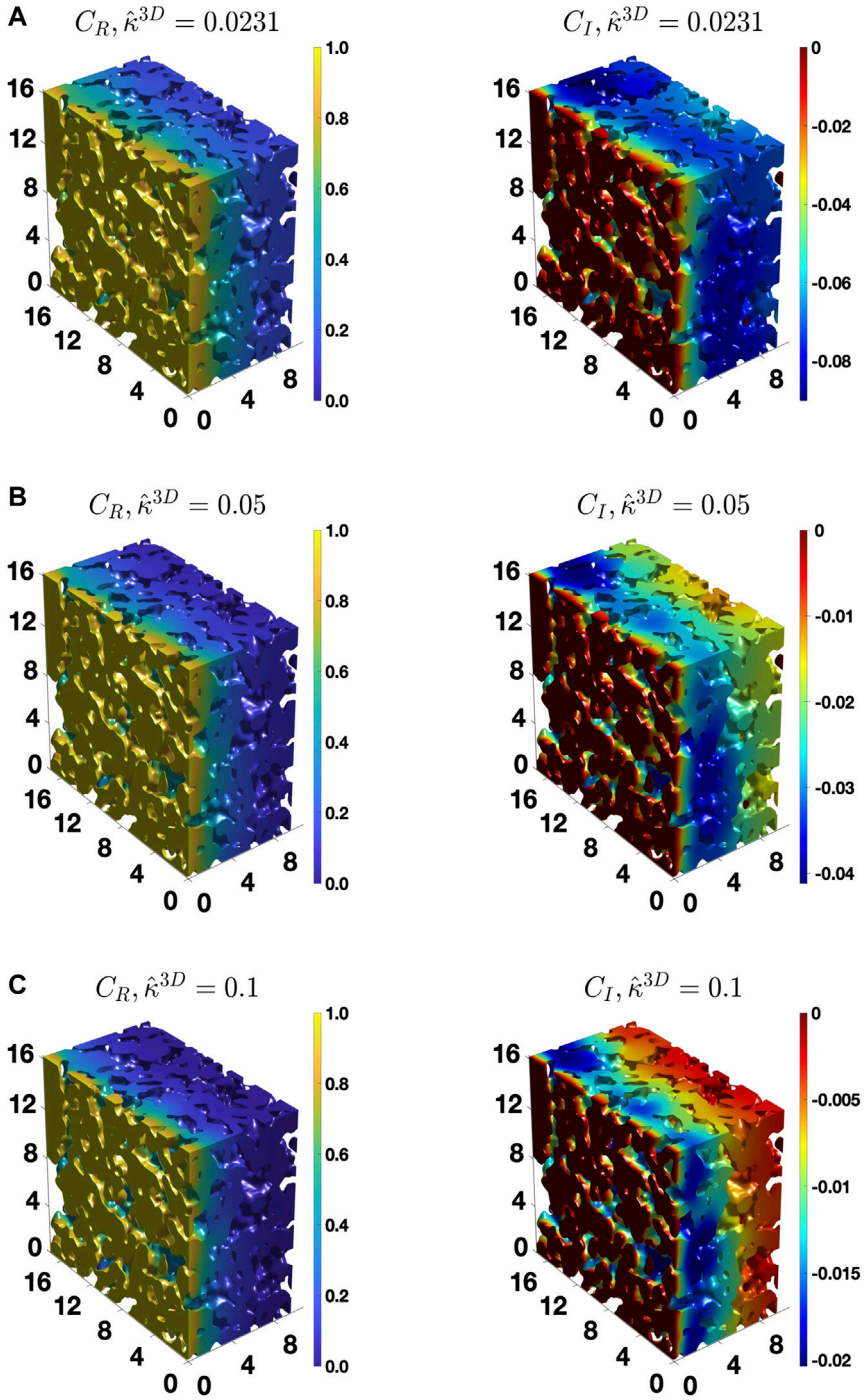

FIGURE 7 | The distribution of the real and imaginary components of the concentration amplitude calculated for the BCC BC, $\hat{\omega} = 0.018$ and **(A)** $\hat{\kappa}^{3D} = 0.0231$, **(B)** 0.05, and **(C)** 0.1.

effective tortuosity could also be observed from the distribution of reaction-diffusion streamlines (Zhang Y. et al., 2019), which is a 3D visualization of the flux. As the penetration depth decreases, the streamlines or the trajectories of the oxygen vacancies begin to straighten. The resulting decrease in the deviation from a straight path causes the effective tortuosity to decrease.

We note that there exists an error of up to 9% in the calculated impedance value at high frequencies, as described in **Supplementary Material**. The error arises because the accuracy of numerical approximations of the gradients in the concentration amplitudes decreases at high frequencies, as our numerical implementation employs fixed grid resolution

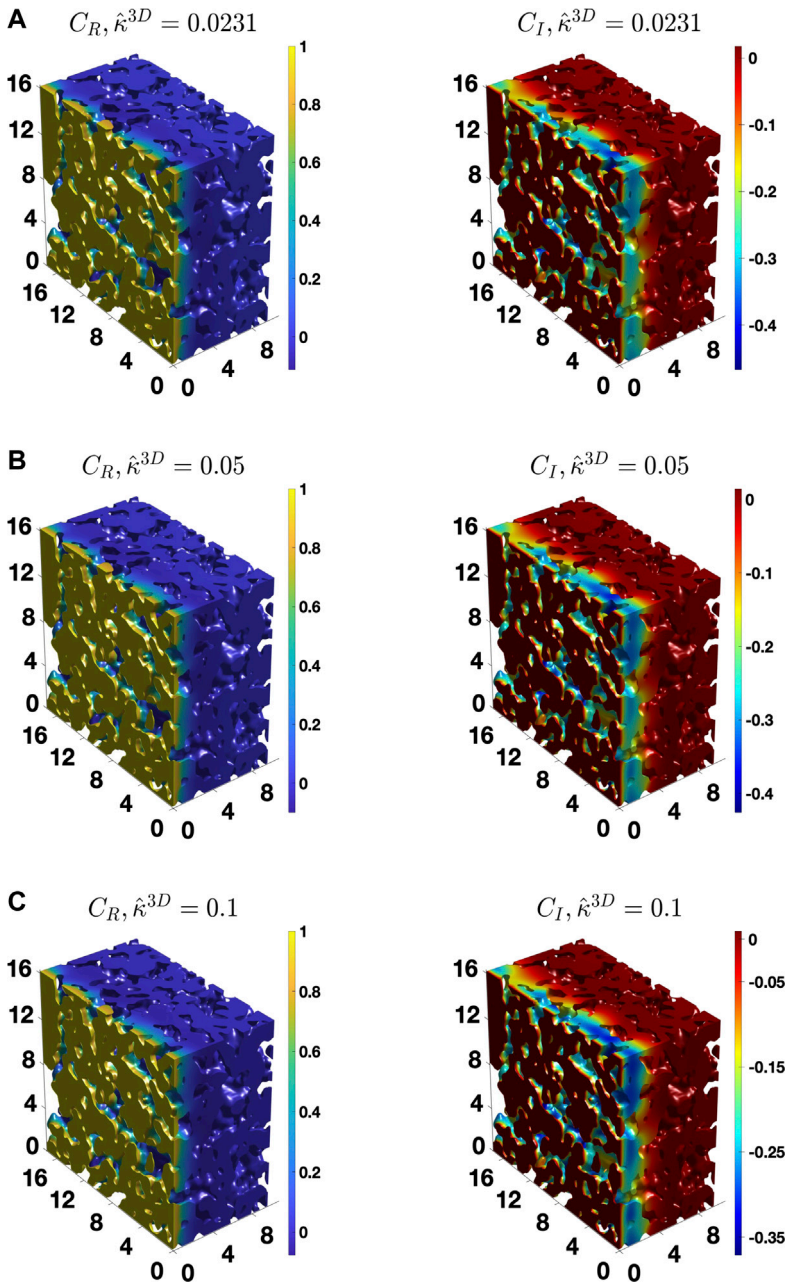

FIGURE 8 | The distribution of the real and imaginary components of the concentration amplitude calculated for the BCC BC, $\hat{\omega} = 1.038$ and **(A)** $\hat{\kappa}^{3D} = 0.0231$, **(B)** 0.05, and **(C)** 0.1.

throughout the simulation domain. Although this error can be reduced by doubling the grid resolution, such calculations become computationally expensive (as discussed in **Supplementary Material**) without providing additional insights. In fact, the error does not affect the observed qualitative behavior of the effective tortuosity, which is the one of the two main focuses of this work. Thus, the numerical results presented here are sufficiently accurate for demonstrating the dependence of the effective tortuosity on $\hat{\kappa}^{3D}$ and $\hat{\omega}$. In the future, we plan to implement the model into a finite element framework with adaptive-mesh capability such as PRISMS-PF framework (Aagesen et al., 2018; DeWitt et al., 2020), in which SBM is already implemented, to increase the computational efficiency of the calculations at high frequencies.

Finally, to further evaluate the accuracy of approximating $\langle \alpha \rangle$ with $\langle \alpha_0 \rangle$ in the modified ALS model, we compared the tortuosity results with and without this approximation, latter of which include the frequency dependence of $\langle \alpha \rangle$. A comparison between the two sets of τ value obtained for the three values of $\hat{\kappa}^{3D}$ is provided in **Figure 9**, which show good agreement.

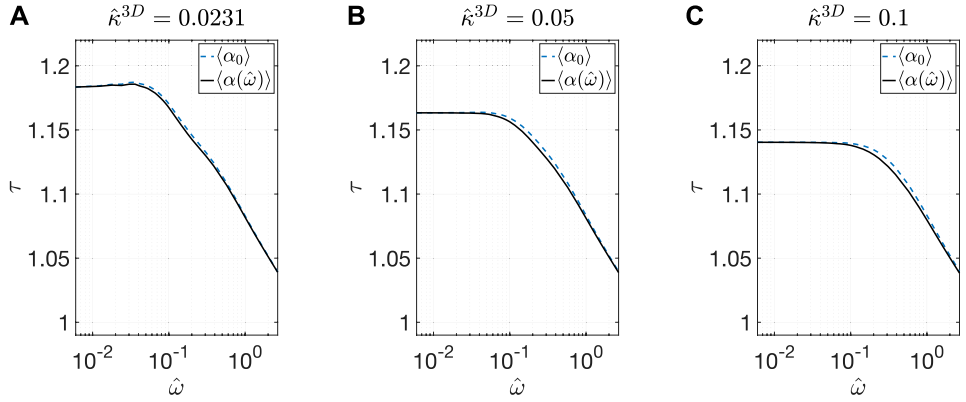

FIGURE 9 | Comparisons of the calculated τ vs. $\hat{\omega}$ relations (BCC BC) by using $\langle\alpha_0\rangle$ (blue curve) and $\langle\alpha\rangle$ (black curve) for **(A)** $\hat{\kappa}^{3D}$ = 0.0231, **(B)** 0.05, and **(C)** 0.1.

Hence the use of $\langle\alpha_0\rangle$ as the correction factor is sufficiently accurate for calculating the effective tortuosity of a MIEC SOFC cathode using the EIS data.

SUMMARY

In this study, we simulated the impedance behavior of a statistically representative portion of an experimentally determined complex three-dimensional microstructure of an unbiased MIEC SOFC cathode under two different boundary conditions. Our investigation generated two key insights. First, due to the presence of surface reaction, the amplitude of oscillations in the vacancy concentration is lower at the pore/solid interface than within the solid bulk of the cathode. This difference between the interface and bulk amplitude increases with an increase in the ratio between the reaction rate constant and the bulk diffusion coefficient. Therefore, to account for this difference, we proposed a modification to the ALS model in terms of the ratio of the surface and bulk concentration amplitudes at zero frequency, $\langle\alpha_0\rangle$, and provided numerically evaluated $\langle\alpha_0\rangle$ as a function of the reaction rate coefficient, $\hat{\kappa}^{3D}$. Second, through the examination of the three-dimensional distribution of the vacancy concentration amplitude, we showed that the penetration depth of the oxygen vacancies is a function of $\hat{\kappa}^{3D}$ and the frequency of the applied AC load, $\hat{\omega}$. Due to the direct dependence of the effective tortuosity on the penetration depth, the effective tortuosity also becomes a function of $\hat{\kappa}^{3D}$ and $\hat{\omega}$ in addition to the microstructure. Furthermore, we developed a method, which utilizes the EIS data, for determining τ as a function of $\hat{\kappa}^{3D}$ and $\hat{\omega}$ for a cathode with known material properties (such as the reaction rate constant and bulk diffusion constant), pore surface area, and porosity.

DATA AVAILABILITY STATEMENT

The data for all the figures in this paper can be downloaded from the following link: https://doi.org/10.13011/m3-ywxf-yw20.

AUTHOR CONTRIBUTIONS

VG: Methodology, Software, Formal analysis, Visualization, and Writing - original draft. DC: Formal analysis and Writing–original draft. SB: Conceptualization, Formal analysis, Writing–review and editing. KT: Conceptualization, Methodology, Formal analysis, Writing–review and editing, Supervision, Project administration, and Funding acquisition.

FUNDING

This study is supported by the United States National Science Foundation, Division of Material Research under the grant numbers DMR-1912151 and DMR-1912530. Computational resources were provided by the Extreme Science and Engineering Discovery Environment (XSEDE (Towns et al., 2014)) (allocation No. TG- DMR110007), which is supported by the United States National Science Foundation under grant number ACI-1053575, by the National Energy Research Scientific Computing Center (NERSC), a DOE Office of Science User Facility supported by the Office of Science of the United States Department of Energy under Contract No. DE-AC02–05CH11231.

ACKNOWLEDGMENTS

The authors would like to acknowledge Prof. Hui-Chia Yu, who was involved in the development of the simulation code used in this work and provided associated information. The authors also thank Dr Beck Andrews for helpful discussions.

SUPPLEMENTARY MATERIAL

The Supplementary Material for this article can be found online at: https://www.frontiersin.org/articles/10.3389/fchem.2021.627699/full#supplementary-material

REFERENCES

Aagesen, L. K., Adams, J. F., Allison, J. E., Andrews, W. B., Araullo-Peters, V., Berman, T., et al. (2018). PRISMS: An Integrated, Open-Source Framework for Accelerating Predictive Structural Materials Science. *JOM* 70, 2298–2314. doi:10.1007/s11837-018-3079-6

Adler, S. B., Lane, J. A., and Steele, B. C. H. (1996). Electrode Kinetics of Porous Mixed-Conducting Oxygen Electrodes. *J. Electrochem. Soc.* 143, 3554–3564. doi:10.1149/1.1837252

Adler, S. B. (1998). Mechanism and Kinetics of Oxygen Reduction on Porous La1−Sr CoO3− Electrodes. *Solid State Ionics* 111, 125–134. doi:10.1016/s0167-2738(98)00179-9

Boukamp, B., Bouwmeester, H. J. M., Boukamp, B. A., and Bouwmeester, H. J. M. (2003). Interpretation of the Gerischer Impedance in Solid State Ionics. *Solid State Ionics* 157, 29–33. doi:10.1016/s0167-2738(02)00185-6

Boukamp, B., Verbraeken, M., Blank, D., and Holtappels, P. (2006). SOFC-anodes, Proof for a Finite-Length Type Gerischer Impedance?. *Solid State Ionics* 177, 2539–2541. doi:10.1016/j.ssi.2006.03.002

Bruggeman, D. A. G. (1935). Berechnung verschiedener physikalischer Konstanten von heterogenen Substanzen. I. Dielektrizitätskonstanten und Leitfähigkeiten der Mischkörper aus isotropen Substanzen. *Ann. Phys.* 416, 636–664. doi:10.1002/andp.19354160705

Çeçen, A., Wargo, E. A., Hanna, A. C., Turner, D. M., Kalidindi, S. R., and Kumbur, E. C. (2012). 3-D Microstructure Analysis of Fuel Cell Materials: Spatial Distributions of Tortuosity, Void Size and Diffusivity. *J. Electrochem. Soc.* 159, B299–B307. doi:10.1149/2.068203jes

Chen, K., and Jiang, S. P. (2016). Review-Materials Degradation of Solid Oxide Electrolysis Cells. *J. Electrochem. Soc.* 163, F3070–F3083. doi:10.1149/2.0101611jes

Chen-Wiegart, Y.-c. K., Demike, R., Erdonmez, C., Thornton, K., Barnett, S. A., and Wang, J. (2014). Tortuosity Characterization of 3D Microstructure at Nano-Scale for Energy Storage and Conversion Materials. *J. Power Sourc.* 249, 349–356. doi:10.1016/j.jpowsour.2013.10.026

Cooper, S. J., Bertei, A., Shearing, P. R., Kilner, J. A., and Brandon, N. P. (2016). TauFactor: An Open-Source Application for Calculating Tortuosity Factors from Tomographic Data. *SoftwareX* 5, 203–210. doi:10.1016/j.softx.2016.09.002

DeWitt, S., Rudraraju, S., Montiel, D., Andrews, W. B., and Thornton, K. (2020). PRISMS-PF: A General Framework for Phase-Field Modeling with a Matrix-free Finite Element Method. *Npj Comput. Mater.* 6, 1–12. doi:10.1038/s41524-020-0298-5

Gao, Z., Mogni, L. V., Miller, E. C., Railsback, J. G., and Barnett, S. A. (2016). A Perspective on Low-Temperature Solid Oxide Fuel Cells. *Energy Environ. Sci.* 9, 1602–1644. doi:10.1039/c5ee03858h

Häffelin, A., Joos, J., Ender, M., Weber, A., and Ivers-Tiffée, E. (2013). Time-Dependent 3D Impedance Model of Mixed-Conducting Solid Oxide Fuel Cell Cathodes. *J. Electrochem. Soc.* 160, F867–F876. doi:10.1149/2.093308jes

Hofhaus, J., and Van de Velde, E. F. (1996). Alternating-Direction Line-Relaxation Methods on Multicomputers. *SIAM J. Sci. Comput.* 17, 454–478. doi:10.1137/S1064827593253872

Holtappels, P., Verbraeken, M., Vogt, U., Blank, D., and Boukamp, B. (2006). Preparation and Electrochemical Characterisation of Supporting SOFC-Ni-YZT Anodes. *Solid State Ionics* 177, 2029–2032. doi:10.1016/j.ssi.2006.06.018

Hwang, H. J., Moon, J.-W., Lee, S., and Lee, E. A. (2005). Electrochemical Performance of LSCF-Based Composite Cathodes for Intermediate Temperature SOFCs. *J. Power Sourc.* 145, 243–248. doi:10.1016/j.jpowsour.2005.02.063

Jacobsen, T., and West, K. (1995). Diffusion Impedance in Planar, Cylindrical and Spherical Symmetry. *Electrochimica Acta* 40, 255–262. doi:10.1016/0013-4686(94)E0192-3

Jung, W., and Tuller, H. L. (2009). Impedance Study of SrTi1−xFexO3−δ (x=0.05 to 0.80) Mixed Ionic-Electronic Conducting Model Cathode. *Solid State Ionics* 180, 843–847. doi:10.1016/j.ssi.2009.02.008

Kreller, C., Drake, M., Adler, S. B., Chen, H.-Y., Yu, H.-C., Thornton, K., et al. (2011). Modeling SOFC Cathodes Based on 3-D Representations of Electrode Microstructure. *ECS Trans.* 35, 815–822. doi:10.1149/1.3570062

Kreller, C. R. (2011). Measurement and Modeling of Material and Microstructural Factors Governing Performance of Solid Oxide Fuel Cell Cathodes. *ProQuest Diss. Theses*. Available at: https://proxy.lib.umich.edu/login?url=https://www.proquest.com/dissertations-theses/measurement-modeling-material-microstructural/docview/865807958/se-2?accountid=14667.

Lim, D.-K., Plymill, A. B., Paik, H., Qian, X., Zecevic, S., Chisholm, C. R. I., et al. (2020). Solid Acid Electrochemical Cell for the Production of Hydrogen from Ammonia. *Joule* 4, 2338–2347. doi:10.1016/j.joule.2020.10.006

Liu, Z., Liu, M., Nie, L., and Liu, M. (2013). Fabrication and Characterization of Functionally-Graded LSCF Cathodes by Tape Casting. *Int. J. Hydrogen Energ.* 38, 1082–1087. doi:10.1016/j.ijhydene.2012.10.048

Lynch, M. E., Ding, D., Harris, W. M., Lombardo, J. J., Nelson, G. J., Chiu, W. K. S., et al. (2013). Flexible Multiphysics Simulation of Porous Electrodes: Conformal to 3D Reconstructed Microstructures. *Nano Energy* 2, 105–115. doi:10.1016/j.nanoen.2012.08.002

Mahato, N., Banerjee, A., Gupta, A., Omar, S., and Balani, K. (2015). Progress in Material Selection for Solid Oxide Fuel Cell Technology: A Review. *Prog. Mater. Sci.* 72, 141–337. doi:10.1016/j.pmatsci.2015.01.001

Mizusaki, J., Yasuda, I., Shimoyama, J. i., Yamauchi, S., and Fueki, K. (1993). Electrical Conductivity, Defect Equilibrium and Oxygen Vacancy Diffusion Coefficient of La1 − X Ca X AlO3 − δ Single Crystals. *J. Electrochem. Soc.* 140, 467–471. doi:10.1149/1.2221070

Mogensen, M. B., Chen, M., Frandsen, H. L., Graves, C., Hansen, J. B., Hansen, K. V., et al. (2019). Reversible Solid-Oxide Cells for Clean and Sustainable Energy. *Clean. Energ.* 3, 175–201. doi:10.1093/ce/zkz023

Nenning, A., Volgger, L., Miller, E., Mogni, L. V., Barnett, S., and Fleig, J. (2017). The Electrochemical Properties of Sr(Ti,Fe)O3-Δfor Anodes in Solid Oxide Fuel Cells. *J. Electrochem. Soc.* 164, F364–F371. doi:10.1149/2.1271704jes

Niania, M. A. R., Rossall, A. K., Van den Berg, J. A., and Kilner, J. A. (2020). The Effect of Sub-surface Strontium Depletion on Oxygen Diffusion in La0.6Sr0.4Co0.2Fe0.8O3−δ. *J. Mater. Chem. A.* 8, 19414–19424. doi:10.1039/d0ta06058e

Nielsen, J., Jacobsen, T., and Wandel, M. (2011). Impedance of Porous IT-SOFC LSCF:CGO Composite Cathodes. *Electrochimica Acta* 56, 7963–7974. doi:10.1016/j.electacta.2011.05.042

Nitta, N., Wu, F., Lee, J. T., and Yushin, G. (2015). Li-ion Battery Materials: Present and Future. *Mater. Today* 18, 252–264. doi:10.1016/j.mattod.2014.10.040

Pereira, J. M. C., Navalho, J. E. P., Amador, A. C. G., and Pereira, J. C. F. (2014). Multi-scale Modeling of Diffusion and Reaction-Diffusion Phenomena in Catalytic Porous Layers: Comparison with the 1D Approach. *Chem. Eng. Sci.* 117, 364–375. doi:10.1016/j.ces.2014.06.028

Perry, N. H., Kim, J. J., Bishop, S. R., and Tuller, H. L. (2015). Strongly Coupled Thermal and Chemical Expansion in the Perovskite Oxide System Sr(Ti,Fe)O3−α. *J. Mater. Chem. A.* 3, 3602–3611. doi:10.1039/c4ta05247a

Rootare, H. M., and Prenzlow, C. F. (1967). Surface Areas from Mercury Porosimeter Measurements. *J. Phys. Chem.* 71, 2733–2736. doi:10.1021/j100867a057

Rüger, B., Weber, A., and Ivers-Tiffee, E. (2007). 3D-Modelling and Performance Evaluation of Mixed Conducting (MIEC) Cathodes. *ECS Trans.* 7, 2065–2074. doi:10.1149/1.2729320

Scott Cronin, J., Muangnapoh, K., Patterson, Z., Yakal-Kremski, K. J., Dravid, V. P., and Barnett, S. A. (2012). Effect of Firing Temperature on LSM-YSZ Composite Cathodes: A Combined Three-Dimensional Microstructure and Impedance Spectroscopy Study. *J. Electrochem. Soc.* 159, B385–B393. doi:10.1149/2.053204jes

Shakeel, N., Ahmad, A., Ahamed, M. I., Inamuddin, and Asiri, A. M. (2019). Kraton Based Polymeric Nanocomposite Bioanode for the Application in a Biofuel Cell. *Enzyme Microb. Technol.* 127, 43–49. doi:10.1016/j.enzmictec.2019.04.003

Tjaden, B., Brett, D. J. L., and Shearing, P. R. (2018). Tortuosity in Electrochemical Devices: a Review of Calculation Approaches. *Int. Mater. Rev.* 63, 47–67. doi:10.1080/09506608.2016.1249995

Towns, J., Cockerill, T., Dahan, M., Foster, I., Gaither, K., Grimshaw, A., et al. (2014). XSEDE: Accelerating Scientific Discovery. *Comput. Sci. Eng.* 16, 62–74. doi:10.1109/MCSE.2014.80

Wang, Y., Ruiz Diaz, D. F., Chen, K. S., Wang, Z., and Adroher, X. C. (2020). Materials, Technological Status, and Fundamentals of PEM Fuel Cells - A Review. *Mater. Today* 32, 178–203. doi:10.1016/j.mattod.2019.06.005

Wilson, J. R., Kobsiriphat, W., Mendoza, R., Chen, H.-Y., Hiller, J. M., Miller, D. J., et al. (2006). Three-dimensional Reconstruction of a Solid-Oxide Fuel-Cell Anode. *Nat. Mater* 5, 541–544. doi:10.1038/nmat1668

Yoo, C.-Y., and Bouwmeester, H. J. M. (2012). Oxygen Surface Exchange Kinetics of SrTi1−xFexO3−δ Mixed Conducting Oxides. *Phys. Chem. Chem. Phys.* 14, 11759–11765. doi:10.1039/c2cp41923h

Yu, H.-C., Adler, S. B., Barnett, S. A., and Thornton, K. (2020). Simulation of the Diffusional Impedance and Application to the Characterization of Electrodes with Complex Microstructures. *Electrochimica Acta* 354, 136534. doi:10.1016/j.electacta.2020.136534

Yu, H.-C., Chen, H.-Y., and Thornton, K. (2012). Extended Smoothed Boundary Method for Solving Partial Differential Equations with General Boundary Conditions on Complex Boundaries. *Model. Simul. Mater. Sci. Eng.* 20, 075008. doi:10.1088/0965-0393/20/7/075008

Zhang, L., Hu, X., Wang, Z., Sun, F., and Dorrell, D. G. (2018). A Review of Supercapacitor Modeling, Estimation, and Applications: A Control/management Perspective. *Renew. Sustain. Energ. Rev.* 81, 1868–1878. doi:10.1016/j.rser.2017.05.283

Zhang, S.-L., Cox, D., Yang, H., Park, B.-K., Li, C.-X., Li, C.-J., et al. (2019). High Stability SrTi1−xFexO3−δ Electrodes for Oxygen Reduction and Oxygen Evolution Reactions. *J. Mater. Chem. A.* 7, 21447–21458. doi:10.1039/c9ta07548h

Zhang, S.-L., Wang, H., Lu, M. Y., Zhang, A.-P., Mogni, L. V., Liu, Q., et al. (2018). Cobalt-substituted SrTi0.3Fe0.7O3−δ: a Stable High-Performance Oxygen Electrode Material for Intermediate-Temperature Solid Oxide Electrochemical Cells. *Energ. Environ. Sci.* 11, 1870–1879. doi:10.1039/c8ee00449h

Zhang, Y., Yan, F., Ma, J., Yan, M., Ni, M., and Xia, C. (2019). In Operando Monitoring of Reaction-Diffusion Streamlines and Uncovering of Electrochemo-Structural Interactions in Electrodes. *J. Mater. Chem. A.* 7, 10256–10263. doi:10.1039/c9ta01784d

Conflict of Interest: The authors declare that the research was conducted in the absence of any commercial or financial relationships that could be construed as a potential conflict of interest.

Advantages of publishing in Frontiers

OPEN ACCESS
Articles are free to read for greatest visibility and readership

FAST PUBLICATION
Around 90 days from submission to decision

HIGH QUALITY PEER-REVIEW
Rigorous, collaborative, and constructive peer-review

TRANSPARENT PEER-REVIEW
Editors and reviewers acknowledged by name on published articles

Frontiers
Avenue du Tribunal-Fédéral 34
1005 Lausanne | Switzerland

Visit us: www.frontiersin.org
Contact us: frontiersin.org/about/contact

REPRODUCIBILITY OF RESEARCH
Support open data and methods to enhance research reproducibility

DIGITAL PUBLISHING
Articles designed for optimal readership across devices

FOLLOW US
@frontiersin

IMPACT METRICS
Advanced article metrics track visibility across digital media

EXTENSIVE PROMOTION
Marketing and promotion of impactful research

LOOP RESEARCH NETWORK
Our network increases your article's readership